DESIGN AND OPTIMIZATION OF HYBRID RENEWABLE ENERGY SYSTEMS FOR OFF-GRID CONTINUOUS OPERATIONS

Oluwamayowa O. Amusat

A dissertation submitted in partial fulfilment
for the award of the degree of

DOCTOR OF PHILOSOPHY
Chemical Engineering

Faculty of Engineering Sciences
University College London

June 2017

Declaration

I, Oluwamayowa O. Amusat, confirm that the work presented in this thesis is my own. Where information has been derived from other sources, I confirm that this has been indicated in the thesis.

Amusat, O.O.

Abstract

The mining industry accounts for a significant portion of the energy demand by the industrial sector. The rising demand for metals around the world, coupled with the depletion of readily accessible ore deposits, has led to mining operations moving to more remote locations with no grid supply of energy. As a result, the operations require transport of fuel over large distances, leading to a significant increase in the overall mining cost. Renewable energy is considered to be the most promising solution to the mining industry energy problem. This work investigates the possibility of operating remote mines on local generation from renewables.

A survey of recent literature revealed that while a lot of research had been done on hybrid renewable energy systems design and sizing, little thought had been given to accounting for the stochastic nature of renewable resources in the sizing process. Previous works focused on the sizing of PV-wind-battery systems; other potential generation and storage technologies were largely ignored. The challenge of intermittency in the power output of renewable generation systems had also largely been ignored. This thesis extends the state of the art on hybrid systems sizing by developing models and methodologies to address these challenges.

A novel hybrid energy system integrating thermal and electrical renewable generation options with multiple large scale energy storage options is considered in this thesis. Models are developed for the different components of the energy system, with dynamic models incorporated for the material and energy balances of the storage alternatives, leading to a system of nonlinear differential algebraic equations (DAEs). The temporal nature of the renewable resources is accounted for by considering multiple stochastic renewable input scenarios generated from probability distribution functions (PDFs) as inputs into the system model. A reliability measure to quantify the impact of weather-based variability, called the modified loss of power supply probability, is developed.

A bi-criteria sizing methodology which allows for the stochastic nature of renewable resources to be accounted for is presented. The approach combines the time series approach to reliability evaluation with a stochastic simulation model. Two approaches for mitigating the impact of intermittency in power outputs of renewable generation technologies are also developed. The first approach is based on system redesign, while the second approach is based on the introduction of an instantaneous response storage option. Case studies were presented to demonstrate the various methodologies.

The results show that climate-based variability can have a significant impact on the cost and performance of hybrid energy systems and should always be accounted for in the sizing process. Intermittency needs to be accounted for in some form at the design stage as it can have an impact on the choice of technologies. The integration of thermal and electrical power generation and storage options provide a way to reduce hybrid system costs.

The methodologies developed in this thesis are applicable to any location and can easily be extended to incorporate other generation and storage alternatives. They provide the decision maker with necessary information for making preliminary sizing decisions.

Acknowledgements

I would like to thank God for being a source of strength and inspiration.

I would like to thank Professor Eric Fraga and Dr Paul Shearing for their support and for providing me with solid guidance and direction throughout the program.

I would also like to acknowledge funding from the Nigerian Universities Commission (NUC) through the PRESSID scheme, without which this work would not have been possible.

Finally, I would like to say a big thank you to my family, especially my parents. Without their unconditional support and guidance I would never have made it to the university, much less be working towards a doctorate degree in Chemical Engineering.

Contents

List of Figures

List of Tables

List of Algorithms

List of Symbols

Roman Symbols

Symbol	Description	Units
A_c	Area of heliostats	[m^2]
A_p	Installed area of photovoltaics	[m^2]
A_{wt}	Wind turbine swept area	[m^2]
A_{tank}	Area of salt storage tanks	[m^2]
C	Capacity of unit (Nominal or storage)	[W;Wh]
CC	Capital cost	[€]
U	Unit cost	[€/m^2; €/MW; €/MWh]
C_p	Heat Capacity	[J/kgK]
$\dot{D}$	Instantaneous demand	[MW]
DOD	Battery depth of discharge	[%]
$EENS$	Expected Energy Not Supplied	[Wh]
E_τ^{ext}	External energy requirement in time interval τ	[Wh]
EIR	Energy Index of Reliability	
$\dot{E}$	Rate of electrical energy	[W]
$\dot{G}^o$	Extraterrestrial irradiance	[W/m^2]
$\dot{G}^{tot}$	Global Horizontal Irradiance	[W/m^2]
g	Gravitational Acceleration	[m/s]
H	Wind turbine hub height	[m]
k_b	Beam transmittance	
k	Set of salt storage tanks	
k_t	Clearness index	
$LPSP$	Loss of Power Supply Probability	
$\overline{LPSP}_m$	Modified loss of power supply probability	

m	Accumulated mass	[kg]
$\dot{m}$	Mass flow rate	[kg/s]
n	Polytropic exponent	
n_g	Number of renewable generation options	
N	Number of renewable input scenarios	
n_s	Number of energy storage options	
n_t	Number of discrete time intervals	
N_T	Number of wind turbines	
$\overline{OP}$	Selected operating scheme	
N_{pop}	Population size for genetic algorithm	
P_R	Rated power of wind turbines	[W]
p	Air pressure	[bar]
p_z	Probability of renewable scenario z	
$\hat{q}_{BAT}$	Battery charge level	[Ah]
$\dot{Q}$	Rate of thermal energy	[W]
$\hat{q}_{BAT}^{nom}$	Nominal charge capacity of battery	[Ah]
R_i	Reliability in scenario i	
$\overline{R}$	Reliability over a number of scenarios	
R_A	Specific gas constant	[J/kgK]
SOC	State of charge of battery	
S	Energy accumulation in storage	[Wh]
T	Temperature	[K]
T_{cell}	Photovoltaic module cell temperature	$[^oC]$
t	Continuous time	[s]
U_k^{loss}	Overall heat loss coefficient for storage tank k	$[\mathrm{Wm^{-2}K^{-1}}]$
U_{bat}	Battery bank voltage [Volts]	
V	Volume	$[\mathrm{m}^3]$
$\bar{X}$	Vector of optimal designs $\bar{x}$	
$\overline{x}$	Design	
z	Reservoir height difference	[m]

Abbreviations

Symbol	Description	Units
AA-CAES	Advanced Adiabatic Compressed Air Energy Storage	
ac	Alternating current	
BAT	Battery	
CDF	Cumulative Distribution Function	
CT	Cold tank, salt storage	
dc	Direct current	
DG	Diesel generator	
DHI	Direct Horizontal Irradiance	
DNI	Direct Normal Irradiance	
ECDF	Empirical Cumulative Distribution Function	
GHI	Global Horizontal Irradiance	
HT	Hot tank, salt storage	
MBE	Mean Bias Error	
MTS	Molten salt Thermal Storage	
PDF	Probability Distribution Function	
pb	Power block	
PT	Power tower	
PHES	Pumped Hydraulic Energy Storage	
PV	Photovoltaics	
RES	Renewable Energy System	
RMSE	Root Mean Square Error	
TES	Thermal Energy Store	
VRFB	Vanadium Redox Flow Battery	
WT	Wind Turbine	

Greek Symbols

Symbol	Description	Units
α	Scale parameter for Weibull distribution	[m/s]
β	Shape parameter for Weibull distribution	

η	Efficiency	
κ	Rate of battery self-discharge	[%/day]
μ	Mean	
$\dot{\phi}$	Unmet load demand	[W]
ρ	Density	[kg/m^3]
σ	Standard deviation	
θ_z	Solar zenith angle	[rad]
τ	Discrete time	[s,h]
υ	Windspeed	[m/s]

Subscripts

Symbol	**Description**	**Units**
i	Generation unit	
inv	Inverter	
j	Storage unit	
wt	Wind turbine	

Superscripts

Symbol	**Description**	**Units**
$c, comp$	Compressor	
d	Direct to plant	
el	Electrical	
gen	Generation from renewable option	
h	Storage tank heat loss	
in	Input to storage	
out	Output from storage	
s	Storage	
th	Thermal	

Chapter 1.

INTRODUCTION

1.1. Background

1.1.1. Mining as an energy intensive process

Industrialization and rapid population growth have led to a steady rise in the demand for energy. The total primary energy consumption of the World in 2014 was 572EJ, representing a 5% rise in energy consumption over five years [73]. The global energy demand is expected to rise by between 30% and 40% by 2040 [112, 167]. The industrial sector is the chief consumer of energy, demanding 42.5% of the world's electricity generation in 2014, along with significant quantities of coal, natural gas and oil [111].

The mining industry accounts for a significant portion of the energy demand by the industrial sector. Mining operations involve several energy intensive processes such as drilling, excavation and blasting. In 2007-08, mining consumed 11% (450 PJ) of the total energy generated in Australia [22]. More than 80% of the electricity generated in Northern Chile is consumed by Copper mining operations [165]. Vale mine is the largest single electricity consumer in Brazil, accounting for 4% of the total electricity consumed in the country. The mining industry consumes 6% of all the energy generated in South Africa, and 3% in the United States [151]. In Canada, it is estimated that 58-143 kWh of energy is consumed per tonne of ore mined [9]. About 180 GWh of energy is required to produce one million tonnes of base metal a year [156].

Energy costs have been shown to represent between 15-21% of the total cost of production in the mining industry [151, 223].

1.1.2. The energy challenge for mining

The rising demand for metals around the world, coupled with the depletion of readily accessible ore deposits, has led to mining operations moving to more remote locations. Mining operations located in remote regions face significant energy problems since grid electricity is usually unavailable in such locations. Such mines resort to the use of diesel generators, leading to a significant increase in the overall mining cost. The fuel is transported over large distances using trucks, raising safety concerns. The use of diesel generators also leads to significant greenhouse emissions, translating to high carbon

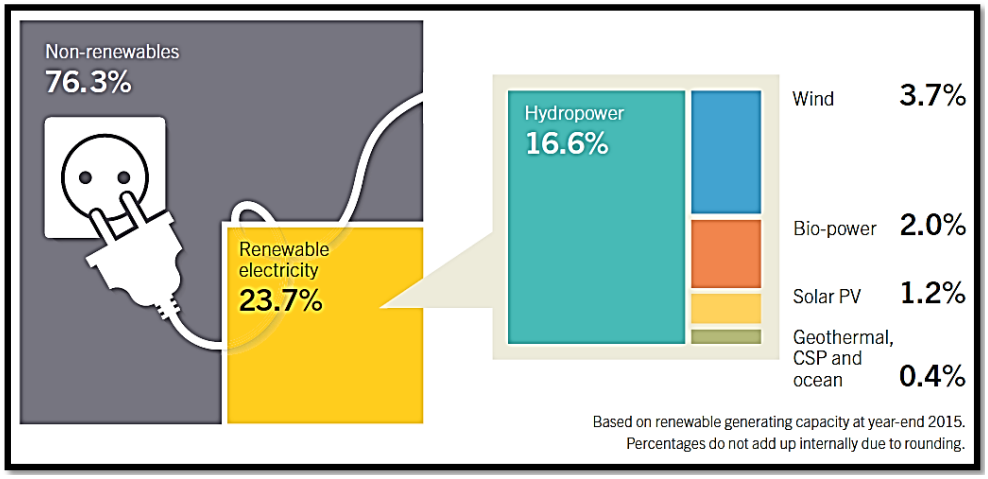

Figure 1.1.: Estimated Renewable Energy Use for Electricity Generation in 2015 [190]

footprints. For example, mining operations in Australia are responsible for about 20% of greenhouse emissions [72].

Mines connected to the electrical grids are also facing energy challenges, with pressure from governments to reduce energy consumption and improve energy efficiency. In 2007, South Africa set an 8-year target of 15% reduction in energy demand for the mining industry [151]. Similar challenges are faced by mining industries in other countries with large mining sectors.

These challenges, along with the ever-rising fossil fuel costs, have driven mining operations to seek alternative sources of energy.

1.1.3. The renewables solution

Recent advancements in technology have made renewable energy the most promising solution to the mining industry energy problem. Renewable electricity contributed 23.7% of the world's total electricity generation in 2015, with most of the generation coming from hydropower (Figure 1.1). Remotely located mines usually have good access to land, no access to the electric-power grid, and are often located in regions with extreme climatic conditions; making them perfect for renewable energy use. The lower operating cost of electricity generation from renewables, as well as the possibility of earning tax credits, have made renewables particularly appealing to the mining industry [102, 176].

Some mining companies around the world have started incorporating wind and solar energy, with several projects planned for the near future [213]. Solar PV intallations are planned in the Atacama desert to supply the needs of the Copper mines in Northern Chile [176]. Some the energy needs of MSPL Ltd., one of the largest iron ore companies in India, is supplied by a 175MW wind farm[19]. El-Toqui mine in Chile operates an integrated wind-diesel-hydraulic energy generation system, with wind energy capable of meeting 23% of the plant demand [93].

A lot of research is still ongoing on the use of renewable energy for mining. Carvalho et al. [44] presented work on the optimization of polygeneration systems combining biomass

with conventional energy generation methods. Beath [27] and Eglinton et al. [72] published work on the potential use of solar energy in Australian mines.

1.1.4. Challenges of renewable energy use

Despite the recent interest in renewable energy use in mining operations, several challenges associated with renewable energy have limited its use in large scale continuous processes. Some of the challenges include:

- Variability and Intermittency of Resource: Generation from renewables is non-dispatchable and varies independently of demand, both daily and seasonally. This is a problem for continuous processes where high reliability is required. As such, the mines which have incorporated renewable generation maintain diesel generators as auxiliary back-up systems [176].
- High initial investment costs compared to diesel systems [176].
- Space demands: Renewable energy generation usually requires a lot of land. While space might not pose a challenge for remotely located mines, operations located closer to settlements are severely hindered.
- System Integration: The integration of conventional energy generation systems such as diesel generators into continuous operations is well understood. With little experience to draw on, the integration of renewable energy generation systems with continuous processes presents higher risks.

In order to increase the penetration of renewables generation into the mining sector, these issues need to be addressed.

1.2. Energy Storage Integration

Energy storage is seen as the key to increasing the reliability of renewable energy generation systems. Energy storage eliminates some of the challenges associated with renewable energy such as variability, intermittency and seasonality. Combining renewables generation with energy storage also reduces greenhouse emissions by eliminating the need for diesel generators as auxiliary back-ups. Energy storage therefore plays an important role in bridging renewable energy generation and demand, as well as meeting the carbon emissions reduction target. According to the International Energy Agency [110], an estimated 310 GW of additional grid-connected electricity storage capacity would be needed in the United States, Europe, China and India to meet the electricity sector decarbonisation target.

As a result, a lot of research is currently ongoing on the development of suitable energy storage options, with a wide range of storage techniques such as high speed flywheels, flow batteries and hydrogen storage under consideration [49, 65, 108]. The integration of storage options with renewable energy systems are also being demonstrated. However, very few energy storage options are currently at the maturity and reliability level required for large scale processes [110].

1.2.1. Systems Modelling of Energy Storage

Systems modelling is important in the development of suitable energy storage options. Most of the technologies under consideration are relatively new and require enormous capital investment. Hence, their economic, technological and commercial viabilities must be investigated before they are embarked upon. Reliable models are required to predict the behaviour of the process, especially with respect to process efficiency and possible technical challenges.

For mature storage technologies such as pumped hydro storage (PHES), recent modelling work has focused on grid-renewable-storage integration [13, 17, 40]. For less mature storage technologies, recent work has focused on cost evaluation, design and configuration improvements, and efficiency estimation [91, 116].

Some work has also been done on the design and sizing of standalone hybrid renewable energy systems. However, as will be seen later, the focus has been on hybrid systems design for small scale applications such as residential use. Little thought has been given to off-grid power generation for large scale continuous operations using system-integrated renewables. Also, the choices of storage technologies considered for systems integration have been limited to battery and hydrogen storage. In order to properly assess the potential of hybrid power systems for standalone applications, the possible advantages of integrating multiple storage technologies needs to be explored. This is particularly important for operations with large power and energy demands such as mines; small gains in performance can lead to significant savings in cost.

1.3. Research Objective

The aim of this research is to demonstrate the possibility of operating remotely located mines almost entirely on local generation from renewables. Operating mines entirely on renewable energy offers several advantages, including:

- energy security over mine lifetime,
- reduction in operating (fuel, emissions and transportation) costs,
- environmentally friendliness, and
- improvement of overall plant safety because of reduced need for transportation and storage of flammable compounds such as diesel and natural gas.

In order for this to be possible, the renewable energy system must be able to provide dispatchable power at all times of the day: energy storage is required. Models for standalone hybrid systems integrating generation and storage technologies will be developed and applied specifically to mining processes. An optimization-based approach will be adopted to determine the optimal configuration and sizes of the hybrid energy systems for individual mining operations based on factors such as mine location and renewables availability. The effect of daily, seasonal and climate-based variability on the sizing of the energy generation and storage units will also be considered.

Details about the key contributions of the thesis will be presented later (Section 2.3.1).

1.4. Scope of the Work

This work considers the preliminary design and sizing of off-grid energy systems for remote mining operations. For this, an energy superstructure containing potential generation and storage technologies will be developed. The sizes and capacities of the generation and storage units required for continuous operation are considered, as well as the effect of variability in renewable input conditions. The electrical and thermal demands of the mining process are considered. The plant is assumed to require low-to-mild grade process heat ($< 600\,\mathrm{K}$) which is typical for mining operations [27]. The heat provided is suitable for space heating, fluid heating and steam generation, all of which are useful in remote mines and beneficiation plants [72].

The work does not consider the actual detailed design of the units within the superstructure. The demands of any utility plants are assumed to be included in the total demand of the mine. The sizing of heat exchangers is not considered. The mining activities are not modelled, and energy efficiency of the mining operation is not considered. Due to the quality of heat considered, this work is not applicable to mineral processing plants which require high temperature direct heating for furnaces and kilns [27].

The work assesses the potential advantages of integrating thermal and electrical generation and storage technologies. It also shows how the variable and intermittent nature of power outputs from renewable generation technologies can be accounted for at the preliminary stage of the design process, and provides an insight into how these factors impact the cost, size, configuration and performance of hybrid energy systems.

The next chapter will present a review of literature on hybrid energy system sizing and highlights the areas to which this work will seek to contribute to the state-of-the-art. This will then be followed by a roadmap of the rest of the thesis.

Chapter 2.

LITERATURE REVIEW

This chapter presents a review of recent literature on the sizing of hybrid renewable energy systems. The concept of reliability is introduced, followed by an overview of sizing methodologies. The last part of the chapter will highlight potential areas of improvement and how this thesis will seek to advance the state of the art.

Optimum system sizing involves determining the most cost-effective and efficient way to combine renewable energy sources to provide a given level of performance. Oversizing the system incurs unnecessary cost; undersizing leads to unexpected system failure. It is therefore important to evaluate renewable energy systems in both economic (cost) and technical (performance) terms during design and planning [48]. These objectives are usually antithetical and therefore a balance (trade-off) between both requirements is desired.

This chapter presents a review of the state of the art literature and methodologies for optimal system sizing. First, the concept of reliability for the technical assessment of system performance is introduced. Next, a review of the different approaches to system sizing is presented. Finally, the previously unaddressed challenges which this work will seek to tackle will be identified.

2.1. Energy System Reliability

The need to characterize the performance of power systems leads to the concept of reliability. According to Osborn and Kawann [169], reliability refers to "*the ability of power system components to deliver electricity to all points of consumption, in the quantity and with the quality demanded by the customer*". It is a measure of the frequency, duration and extent to which a power system experiences failure (i.e. unable to satisfy demand) and therefore provides a basis on which the performance of different types of energy systems may be compared.

2.1.1. Review of commonly used performance metrics

Several performance indicators have been used in literature for the assessment of the reliability and feasibility of hybrid renewable energy systems. The most frequently used measures will be described briefly.

2.1.1.1. Loss of power supply probability

The loss of power supply probability, LPSP, is the probability that insufficient energy supply occurs when the hybrid system is unable to satisfy the load demand [143, 243]. It represents the fraction of the operating time T in which the energy supplied by the energy system $E_{supplied}$ is insufficient to meet the load demand E_{load} and may be written as [143]

$$LPSP = \frac{\sum_{t=1}^{T} \text{Power failure time } (E_{supplied}(t) < E_{load}(t))}{\text{Total time period of operation, } T} \tag{2.1}$$

It is the most frequently used measure for reliability analysis [143] has been considered both as a constraint to be satisfied in single-objective design [7, 240, 242] and an objective in multi-criteria design [3, 64, 170].

2.1.1.2. Expected energy not supplied

The expected energy not supplied, EENS, is an indicator which measures the amount of energy not supplied by the power system when the load exceeds available generation [48, 143]. The EENS (also called the loss of energy expectation, LOEE [124]) at any instant in time is given by the difference between the load level and total generation corresponding to that time instant [124],

$$EENS(t) = \begin{cases} E_{load}(t) - E_{supplied}(t) & \text{when } E_{load}(t) > E_{supplied}(t) \\ 0 & \text{otherwise} \end{cases} \tag{2.2}$$

From this, the EENS over the entire time period of operation can be evaluated [124],

$$EENS = \sum_{t=1}^{T} EENS(t) \tag{2.3}$$

EENS is a measure of the extent of failure of the energy system. The measure was used by Khatod et al. [124] for assessing the performance of hybrid PV-wind-diesel systems.

2.1.1.3. Energy index of reliability

The energy index of reliability (EIR) is the fraction of the demand satisfied by an energy system and is directly related to EENS [217],

$$EIR = 1 - \frac{EENS}{\sum_{t=1}^{T} E_{load}(t)} \tag{2.4}$$

Karaki et al. [119] and Tina et al. [217] used the measure for the assessment of the performance of standalone PV-wind systems.

2.1.1.4. Renewable energy fraction

The renewable energy fraction, REF, represents the fraction of the total energy delivered to the load that was generated from a renewable resource. It is typically used for renewables-based systems which possess diesel generators as backup to prevent power failure and is given mathematically by [7]:

$$REF = 1 - \frac{\sum_{t=1}^{T} E_{DG}(t)}{\sum_{t=1}^{T} E_{load}(t)} \tag{2.5}$$

where $E_{DG}(t)$ represents the energy supplied from diesel generators and the load demand respectively. The REF has been treated both as a constraint [7] and an objective to be maximized [247] in energy system sizing problems.

2.1.1.5. Demand satisfaction criteria

Often, the aim of the problem is to determine the minimum cost design which is guaranteed to meet the load demands throughout the year. For such design problems, a simple energy balance constraint over the entire time period of operation (also called the demand satisfaction criteria [144, 145] or demand-supply criteria [148]) can be used to guarantee performance. For hybrid energy systems, this is given by:

$$E_{supplied}(t) + E_{DG}(t) \geq E_{load}(t) \qquad \forall t \tag{2.6}$$

The constraint has been used in several works [146, 154, 211]. While this is clearly not a conventional reliability measure, it does limit the minimum acceptable performance of the system.

As can be seen from the measures presented, the reliability of an energy system is obtained by comparing the actual output of the system to the desired (required) demand level at every time instant. However, the actual output of a renewable energy system is uncertain as it is dependent on the amount of renewables available. We therefore need to be able to model the amount of renewable resource available (and by extension, the outputs of the generation technologies) at every time for the location of interest.

2.1.2. Reliability evaluation approaches

Two approaches have been adopted in literature for the evaluation of system reliability [217]: the probabilistic and chronological approaches.

2.1.2.1. Probabilistic (statistical) approach

In this approach, all variables participating in the energy conversion process are modelled as random variables [216]. The performance of the energy system is assessed analytically by combining the probability distribution functions (PDFs) of the variables [48].

Consider a standalone photovoltaic (PV) system. PV generation is dependent on the solar radiation u. If the solar resource is considered to be a randomly distributed variable with a PDF $f(u)$, then the output power of the PV system P_u will also be randomly distributed with a distribution function $\mathcal{F}(P_u)$. The probabilistic approach takes the whole distribution $\mathcal{F}(P_u)$ into account for the evaluation of reliability at each point in time, rather than a single realization of the solar radiation (and PV output power).

For systems with more than one renewable resource, the total output of the hybrid system is also random. The performance of the energy system must therefore be evaluated by generating the joint probability distribution function of all the renewable resources. This is known as the convolution approach. For example, for a PV-wind system, the total output of the system P is given by $P = P_u + P_v$ which is randomly distributed according to the joint PDF

$$\mathcal{F}(P) = \mathcal{F}(P_u) * \mathcal{F}(P_v) \tag{2.7}$$

where $*$ represents the convolution of the distribution functions for the wind and PV outputs. The joint PDF must be taken into consideration for performance assessment of the PV-wind system. A similar approach must be adopted when incorporating other renewable generation sources [172].

Karaki et al. [119] developed a probabilistic approach for the evaluation of PV-wind system performance. The PDFs for wind and solar radiation were discretized into states and all the possible solar-wind states for each time interval combined to obtain a measure of performance. A similar approach was adopted by Khatod et al. [124] for the sizing of a PV-wind-diesel system. Tina et al. [217] developed an approach for the probabilistic assessment of the EENS and EIR of hybrid PV-wind systems based on continuous distributions for solar and wind generation. A similar approach to performance evaluation was adopted by Gooding et al. [89] who considered normal and Weibull distributions for solar radiation and windspeed respectively.

The probabilistic approach has several advantages: it requires no chronological data and takes into account variability in the renewable resource [124, 217]. However, the approach has not been developed sufficiently to account for systems incorporating storage. Until recently, it was thought that the approach was unsuitable for the sizing of systems incorporating storage because it did not allow for the dynamics of such systems to be accounted for [48, 241]. As such, the approach was limited to sizing problems involving

generation technologies only [119, 124]. However, Paliwal et al. [173] recently developed a probabilistic battery state model which allowed for the approach to be used in the performance assessment of PV-wind-battery systems. It was then applied to systems sizing [172].

The probabilistic approach is also complex and cumbersome: it requires statistical knowledge of how to handle and manipulate probability distributions. This makes the approach unattractive.

2.1.2.2. Chronological (time series) simulation

In this approach, the amount of renewable resource available at a given time is modelled as a single value which is considered typical for that time instant. The resource availability over the entire period (typically a year) is therefore represented by time series data. Some of the types of time series data that have been used for performance evaluation in literature include:

- Historical data for a fixed period: This is the most frequently used approach. Actual meteorological data recorded for the location is supplied as input. The input year may be selected randomly [7], based on the statistical properties of the historical data [3], or based on averages over several years [179].
- Typical meteorological year (TMY) data, referring to selected data which represents the best characteristics of the weather patterns of the selected region [143]. This approach was used in Yang et al. [243] and Xu et al. [237].
- Mean values based on probability distribution functions: In some works, the time series formed by the means of the probability distributions representing the renewable resource at the various time steps is taken as the input into the model. For example, the mean solar radiation u_{avg} at a given time can be evaluated from its continuous probability distribution $f(u)$ as

$$u_{avg} = \int_0^\infty u \cdot f(u) \cdot \mathrm{d}u \tag{2.8}$$

  The vector of all u_{avg} values forms the time series input into the model.

  In a similar way, the average power output may also be considered as input into the model in place of the renewable resource. Thus, for a PV system, the average power $P_{u,avg}$ at any time could be modelled as

$$P_{u,avg} = \int_0^\infty P_u \cdot f(u) \cdot \mathrm{d}u \tag{2.9}$$

  The power profiles generated from this approach form the input profiles into the energy system for the chronological evaluation of reliability. This approach was used by Borowy and Salameh [36] and Mokheimer et al. [157].

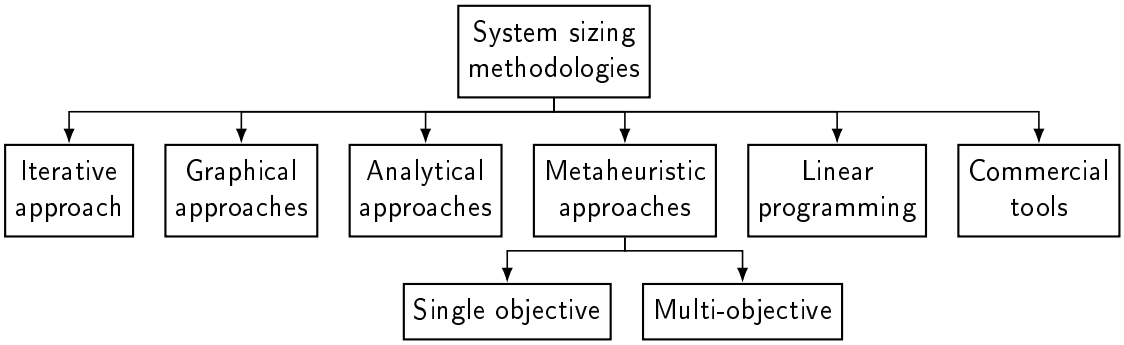

Figure 2.1.: Classification of sizing methodologies

The time series method is straightforward and is used in almost all works on system sizing, as will be seen later. It accounts for daily and seasonal variations in renewables availability. However, the approach assumes that resource availability is deterministic: it does not automatically account for the stochastic nature of renewable resources in performance evaluation [143, 217]. It also requires detailed chronological data which may not be available and is typically more time-consuming than the statistical approach [124, 217].

2.2. Review of Energy System Sizing Methodologies

A typical hybrid renewable energy system consists of the integration of a number of generation and storage alternatives to meet a set of load demands. Generation from the energy system will be dependent on the instantaneous availability of the renewable resources which are variable and often intermittent (depending on technology). Generation technologies are therefore typically represented by algebraic models. The behaviour of the storage system on the other hand is dynamic; it is dependent on the previous state of the system. For some technologies, a combination of different state variables such as mass, temperature and pressure may be necessary to properly characterize the system, causing nonlinearities. A typical sizing problem involves the determination of which generation and/or storage technologies are installed as well as their optimal capacities and orientations. Consideration must be given to optimizing both the cost and performance of the energy system. Thus, in its most general form, energy system sizing problems are typically non-linear, large-scale, dynamic, mixed-integer, multi-objective optimization problems with uncertainty.

Numerous works in literature have considered the sizing of integrated energy systems. The works may be categorized in terms of approach used for determination of the optimal configuration and unit sizes of the components. Figure 2.1 shows the classification of the different sizing methodologies which have been used in literature. While the probabilistic approach is often classified as a sizing methodology [48, 139], it is not considered as such here because it only returns values for system reliability; it must be combined with one of the methodologies shown in Figure 2.1 for system sizing.

The methodologies will be briefly described and a literature survey of works implementing each approach will be presented. Thus, the review will serve two purposes:

- The review of the methodologies will provide information about the strengths and weaknesses of each approach, as well as information on the types of problems (linear/non-linear, discrete/continuous) each method is suitable for. This will be useful in the selection of solution methodologies later in the thesis.
- The summary of the works implementing the different approaches will provide information on the characteristics of energy system sizing problems which have been considered previously: the locations, types of technologies, types of renewable input data (and by extension, variability), load demands, objectives and constraints. Such information will be useful in highlghting the areas of energy systems design yet to be explored adequately and how this work will contribute to the state-of-the-art.

Due to the large volume of works on the topic, the survey will focus on works integrating more than one renewable generation type (called hybrid renewable energy systems) with some form of storage. Except where necessary, works considering only one form of renewable generation and/or no storage will not be reviewed here. However, those works apply the same methodologies for system sizing.

Reviews of previous works on system sizing and sizing methodologies may be found in Chauhan and Saini [48], Luna-Rubio et al. [139] and Mahesh and Sandhu [143]. At the end of the literature survey, a table summarizing the characteristics of the different works reviewed will be presented (Table 2.4).

2.2.1. Iterative (exhaustive enumeration) approach

2.2.1.1. Description of the approach

The iterative approach[1] involves an exhaustive search, with every single design in the solution space considered one after another (iteratively). The method adopts a two-step approach to systems sizing. In the first stage, the reliabilities of all potential combinations of the energy system components are evaluated. This is achieved using an iterative program which linearly increases the capacities of the various components until all potential combinations and sizes have been considered. Evaluation of the reliabilities of the designs may be done with either the chronological or probabilistic approach, with the chronological approach more frequently used. The reliability of the system will increase as larger capacities are considered. Based on the results of the first stage, the costs of all the designs capable of satisfying the pre-set reliability target are evaluated and the minimum cost design chosen as optimal. The reliability target therefore acts as a constraint to determine the feasible designs.

[1] The iterative approach described is different from iterative solution algorithms in mathematical programming. "Iterative" here refers to the way exhaustive enumeration is done: by looping through all potential combinations of the capacities of the energy system components to be sized. While not necessarily accurate, it is the accepted name among researchers in energy systems sizing (see Chauhan and Saini [48] and Mahesh and Sandhu [143], for example).

Algorithm 2.1 Pseudocode for iterative approach to energy system sizing. Cost and reliability evaluation are performed separately.

Given: Range of acceptable PV capacities $[n_{pv,min} : n_{pv,step} : n_{pv,max}]$; Range of acceptable wind generation capacities $[n_{wt,min} : n_{wt,step} : n_{wt,max}]$, Allowable storage capacities in days $[n_{s,min} : n_{s,step} : n_{s,max}]$; Minimum acceptable reliability R_{min}.
Output: $\check{x}$, Optimal design at set reliability; $\check{C}_F$, cost of optimal design.

procedure OPTIMAL DESIGN
  function RELIABILITY SUB-MODEL
    for $n_s = n_{s,min} : n_{s,step} : n_{s,max}$ **do**
      for $n_{wt} = n_{wt,min} : n_{wt,step} : n_{wt,max}$ **do**
        for $n_{pv} = n_{pv,min} : n_{pv,step} : n_{pv,max}$ **do**
          $x = [n_s, n_{wt}, n_{pv}]$
          $R = \texttt{Perf-sim}(x)$ ▷ Evaluate reliability of current configuration
          if $R > R_{min}$ **then**
            $X \leftarrow x$ ▷ Keep designs which satisfy reliability condition
          end if
        end for
      end for
    end for
    return X ▷ First sub-model outputs all feasible designs
  end function
  function COST SUB-MODEL(X)
    for $x \epsilon X$ **do**
      $C_F = \texttt{Cost-sim}(x)$ ▷ Evaluate cost function for all feasible designs
    end for
    $\check{C}_F = \min(C_F)$ ▷ Determine minimum cost
    $\check{x} = x\,|_{\min(C_F)}$ ▷ Determine design corresponding to minimum cost
    return $\check{x}, \check{C}_F$
  end function
end procedure

A typical procedure for the iterative approach is shown in Algorithm 2.1. The first function (reliability sub-model) determines all the designs x capable of meeting the reliability target R_{min} by looping through all PV-wind-storage capacity combinations. The output of the submodel, X, contains all such designs. The costs of all the feasible designs are then evaluated in the second function (cost sub-model), with the design $\hat{x}$ with the minimum cost $\hat{C}_F$ returned as the optimal solution to the problem.

2.2.1.2. Summary of works implementing the iterative approach

Karaki et al. [119] developed a general probabilistic model for the sizing of autonomous solar-wind energy conversion systems. In the work, a probabilistic approach to reliability assessment was developed, with solar radiation modelled as beta distributions [96] and windspeed as Weibull distributions [192]. The authors accounted for potential hardware failure (failure of the PV modules) by representing the probability of failure as a Binomial distribution. The energy index of reliability was used to assess system performance. In order to evaluate reliability, the probability distributions for PV and wind generation

were discretized into states. The distributions were then combined using the convolution theorem to obtain a measure of the reliability. The use of the probabilistic approach meant that the battery system could not be sized independently. However, the upper limit on the battery size required was estimated based on the daily excess energy available to charge the battery.

To demonstrate how the probabilistic approach could be applied to system sizing, the design of a standalone energy system to meet a peak load of 45kW for one week in summer was considered via the iterative approach. The economic objective considered was the total capital cost of the PV-wind-battery system. The number of 50 m^2 PV modules (varied from one to five), 8 kW wind turbines (varied between four and eight) and battery capacity (varied from zero to the theoretical upper limit as determined by the available excess energy) were considered as the sizing variables. For each case, the cost and reliability was evaluated. The optimal design was then selected as the minimum cost design which satisfied the preset reliability norm of $EIR = 0.99$.

Yang et al. [243] used the iterative approach to analyze the complementary characteristics of solar and wind generation in Hong Kong. In their work, the potential of three different energy system configurations were investigated:

- Standalone PV-battery systems with 3 and 5 days of storage;
- Standalone wind generation-battery systems with 3 and 5 days of storage; and
- Hybrid PV-wind-battery systems with 1, 3 and 5 days of storage.

In each case, the wind power capacity was varied from 0.2-2 kW while the PV capacity was increased in steps of 50 W. The loss of power supply probability (LPSP), evaluated using the chronological approach for one year of hourly renewables input data, was the metric for the comparison of the performances of the different configurations. No economic objective was considered. The results from the study indicated that integrating wind and solar generation reduced the required generation and storage requirements, taking advantage of the complementary nature of solar and wind generation.

Diaf et al. [64] implemented the approach for design of standalone PV-wind-battery systems for three sites in Corsica island, France: Ajaccio, Calvi and Cape Corse. The LPSP was implemented as the reliability measure and was evaluated based on one year (8,760 h) of hourly historical data using the chronological approach. The cost function considered was the levelized cost of energy, LCE, given by

$$LCE = \frac{\text{PVC} \cdot \text{CRF}}{E_{tot}} \tag{2.10}$$

where PVC is the present value cost of the energy system (sum of capital, maintenance and replacement costs), CRF is the capital recovery factor which accounts for discount rates and the useful lifetime of the plant, and E_{tot} is the annual energy delivered by the PV and wind generation systems.

For each of the locations, the system size required to meet a 3 kWh/day load was investigated. The capacities of the wind generators and PV modules were varied from

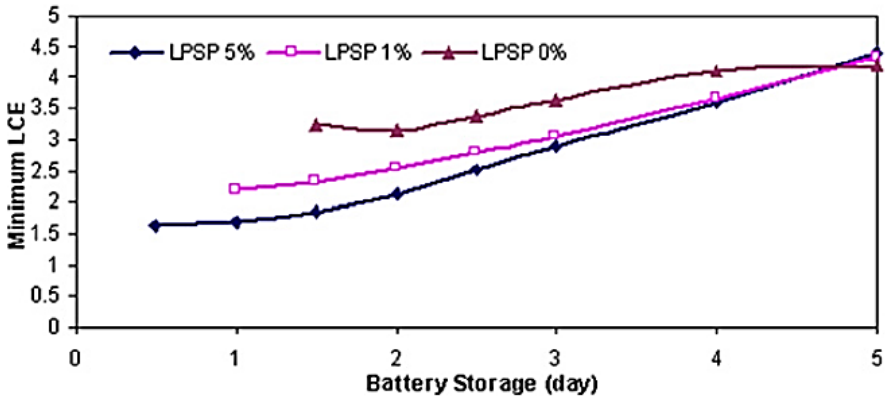

Figure 2.2.: Minimum levelized cost of energy vs battery capacity for different LPSP requirements [240].

zero to 3 kW, with 50 W steps for the PVs and 200 W increments for the wind generators. Up to 5 days of storage (at daily intervals) was considered. A range of reliability targets were considered (LPSP = 0 to 5%).

The results of the work suggested that the size of the system required was heavily influenced by the system reliability requirements, with high reliability requirements leading to considerable increases in the system size. Reducing the LPSP requirement from zero to 1% reduced the LCE by between 8% and 20% for all the sites. The results also indicated that smaller generation capacities were required as more storage days were allowed. The LCE was found to be most sensitive to the battery storage capacity, with 2 days of storage found to be best for $LPSP = 0$. The location with the highest wind potential (Cape Corse) was found to yield the designs with the lowest costs.

Yang et al. [240] considered the relationships between system reliabilities, system configurations and system cost in the sizing of a hybrid PV-wind-battery system for Guangdong, China. The LPSP and LCE were considered as performance and economic objectives as in the work by Diaf et al. [64]. The number of PV modules (ranging from 20-300, each of 50 W), rated wind turbine power (ranging from 0.5 kW to 10 kW) and number of storage days (ranging from zero to 5 days at half-day intervals) were considered as the design variables in the design of an energy system to meet a demand load of 1 kW. A range of reliability targets were considered (LPSP = 0 to 5%).

The results obtained from the work indicated that the designs with the lowest LCE tends to occur when the number of both the wind and PV installations are moderate. While the minimum storage requirement for the 100% reliable scenario was 1.5 days, the minimum cost configuration was obtained with 2 days of battery bank storage (Figure 2.2). It was concluded that increasing the number of PV panels and wind turbines made more sense than increasing battery storage capacity from a cost point of view.

Prasad and Natarajan [183] presented an iterative procedure for the sizing of a hybrid PV-wind-battery system for an Indian site. The capacities of the PV, battery and wind turbine were considered as the design variables. System performance was evaluated based on one year of daily solar and wind data using chronological simulation. The deficiency

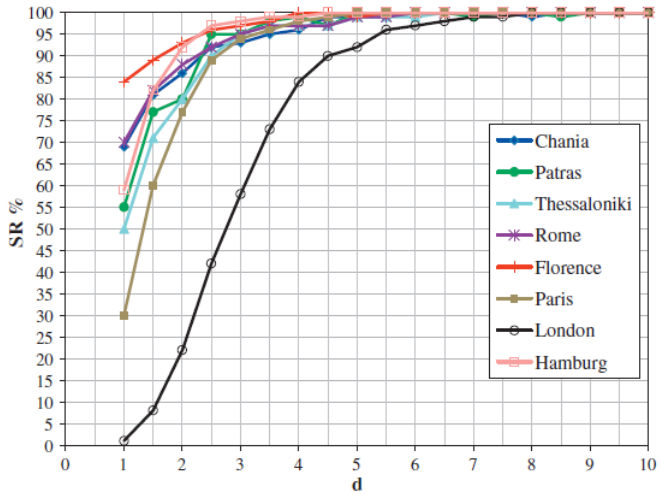

Figure 2.3.: Success rate vs days of autonomy for various European cities [118]

power supply probability (DPSP), defined as the LPSP evaluated on a daily (rather than hourly) basis, was considered as the reliability measure. Based on the results of the reliability submodel for the specified DPSP, two alternative approaches were presented for the selection of the optimal design capacities. First, the minimization of an economic objective (LCE) was considered for optimal design selection. The optimal design selected via this approach was found to generate 28% unutilized excess power (UEP, defined as the fraction of generated power not used or stored by the system) annually. Based on this, an alternative approach of minimizing the UEP was proposed for design selection. A reduction in the UEP to 14% was achieved, but the system cost increased by 1.5%.

Kaplani and Kaplanis [118] developed a methodology to account for the stochastic nature of solar radiation in PV-battery system sizing using the chronological approach. The number of days of autonomy(d), representing the number of days of battery back-up necessary for energy independence, was considered as the sole design variable. The PV and battery capacities were related to the days of autonomy with linear equations.

The number of days of autonomy was iteratively increased from one to ten. For each value, the performance of the energy system was evaluated for 100 synthetic monthly solar input scenarios. The scenarios were generated from probability distributions fitted to the daily historical data for the worst month of the year. In each scenario, the capability of the current design to meet 100% demand was evaluated using the chronological approach. The daily load was split into two: day loads to be met directly from PV generation; and night loads to be satisfied from the battery. Based on the performance over the 100 scenarios, a success rate (SR) for each value of d was defined as:

$$SR(\%) = \frac{\text{Number of scenarios where 100\% demand satisfaction occurs}}{\text{100 scenarios}} \tag{2.11}$$

Figure 2.3 shows the results obtained for several European locations. The authors concluded that system performance is latitude-dependent, with southern European cities

(such as Rome and Florence) requiring less days of autonomy than their northern counterparts (such as London). In the case of Patras (Greece), the results showed that 2.5 and 5 days of autonomy was sufficient to provide 95% and 99% success rates respectively. While the methodology presented in the work is not applicable to systems integrating wind generation, it provides an insight into how stochasticity in renewables availability may be accounted for with the chronological approach.

Kaabeche and Ibtiouen [114] implemented the iterative approach for the sizing of a PV-wind-battery-diesel hybrid system for Ghardaia, Algeria. The number of 160 W PV modules (varied from 35 to 55) and 1 kW wind turbines (varied from one to ten) were the decision variables considered in system sizing. The total energy deficit (TED), representing the fraction of total demand unmet over the total evaluation period, was implemented as the reliability measure and evaluated with the chronological approach. Full demand satisfaction (TED=0%) was demanded from the system, with any shortfalls from the PV-wind-battery system supplied by the diesel generator. The diesel generator was sized to meet peak demand. The net present cost [139] and the levelized cost of energy (given by Equation 2.10) were considered as the cost metrics for optimal design selection. The model was implemented in MATLAB and demonstrated by considering the load demand of ten residential houses in Algeria. One year of hourly time series data (2005) for the location was supplied as input into the model. Based on the set of solutions obtained for 0% TED, relationships between installed generation capacities, costs, diesel generator operating hours and CO_2 emissions were investigated.

The optimal solution was found to correspond to the design with the lowest number of wind turbines. This was attributed to the high solar potential at the location. The optimal design required 104 h of diesel generation annually. Hybrid systems incorporating diesel generation were shown to be more economical than PV-wind-battery systems.

Recently, a commercial software for the sizing of PV-wind-battery systems based on the iterative approach was developed by Belmili et al. [30]. The objectives included in the software are the LPSP for reliability and net present cost for economics. The software requires renewables input data, technical data on generation and storage technologies, and the desired LPSP as model inputs; it reports the optimal system configuration, actual LPSP and net present cost as output.

2.2.1.3. Advantages and limitations of the iterative approach

The iterative approach to energy systems sizing has several advantages: it is easy to code [48], and allows the relationships between the design parameters and the design objectives to be studied relatively easily [240]. It has been applied to discrete, single-objective, non-linear dynamic problems; the dynamic equations are discretized.

However, the approach is computationally expensive and is therefore only suitable for problems with few design parameters, typically no more than three [48, 241]. The method also has the potential to yield suboptimal solutions if the step sizes are too large [48, 241].

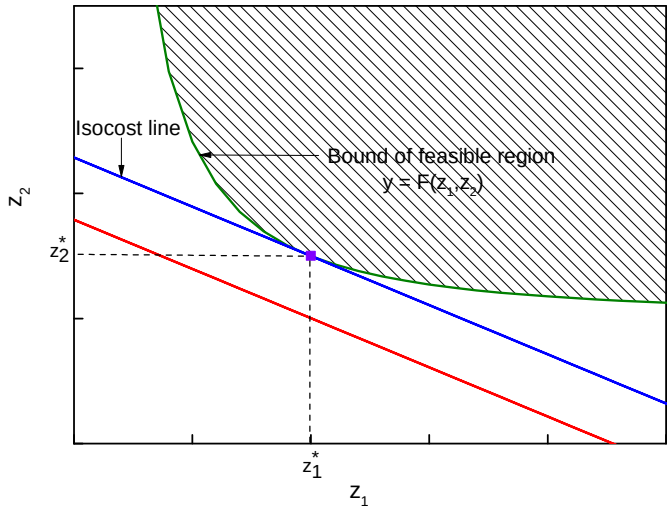

Figure 2.4.: Schematic representation of graphical approach to system sizing. The green line represents the sizing curve, the blue line is lowest feasible isocost line while the purple box corresponds to the optimal design point. Solutions which fall on lower isocost lines (like the red line) will be infeasible.

2.2.2. Graphical construction method

2.2.2.1. Description of the approach

In this approach, the optimal design point is determined using the graphical approach to cost minimization. Consider the cost minimization problem

$$\min c = a_1 z_1 + a_2 z_z \text{ subject to } y \geq F(z_1, z_2) \tag{2.12}$$

where a_1 and a_2 are unit costs of design parameters z_1 and z_2 respectively, and y represents a constraint to be satisfied (reliability in the case of systems sizing). The minimum cost of the system will occur at the point (z_1^*, z_2^*) such that the minimum cost of the system is given by $a_1 z_1^* + a_2 z_2^*$.

Figure 2.4 summarizes the graphical approach. The region on and above the curved green line contains all the solutions which satisfy the constraint $y \geq F(z_1, z_2)$. This is called the feasible region. The optimal design point must therefore lie on or above the curve. The straight lines represent isocost lines: $[z_1, z_2]$ pairings with the same cost. Rearranging the cost function in terms of z_1 gives the equation of the isocost lines as:

$$z_2 = \left(-\frac{a_1}{a_2}\right) z_1 + \left(\frac{c}{a_2}\right) \tag{2.13}$$

Equation 2.13 shows that all potential cost lines have the same slope $-a_1/a_2$. From the intercept of the equation, it is clear that isocost lines closer to the origin correspond to designs with lower costs. To minimize cost, the second term must be as small as possible.

The cost minimization problem is to determine the pair of points $[z_1, z_2]$ which is feasible for the constraint y (meaning it must be on or above the $z_1 - z_2$ curve) that costs as little as possible (meaning it must be on the lowest possible isocost line). The isocost line for

the minimum cost will therefore be tangential to the $z_1 - z_2$ curve as shown in Figure 2.4. Lower isocost lines (such as the one in red) do not satisfy the reliability constraint. The minimum cost will occur be at the point of tangency of the isocost line and the $z_1 - z_2$ sizing curve (represented by the purple box).

Thus, given the unit costs of the design parameters ($a_{1,}, a_2$), the optimal (minimum cost) design is at the point on the sizing curve at which the slope of the tangent is equal to the ratio slope $-a_1/a_2$.

2.2.2.2. Summary of works implementing the graphical approach

Borowy and Salameh [36] applied the methodology to the optimum sizing of a battery bank and PV array for a standalone hybrid wind/PV system. Two design parameters were considered: the number of PV modules (N_{pv}) and the number of batteries (N_{batt}). The wind turbine capacity was considered to be fixed at 15 kW. Long term data (30 years) for solar radiation and windspeed were used to generate hourly probability distribution functions. The Weibull distribution was considered for windspeed modelling, while Beta and Weibull distributions were considered for solar radiation modelling. The power output available from the generation options at each hour were taken as the weighted average of the power available at all the potential states over the time period (Equation 2.9). These formed the input profiles into the energy system for the chronological evaluation of performance.

A reliability submodel similar to the one described in Algorithm 2.1 was used to evaluate the performance of all potential $N_{pv} \times N_{batt}$ configurations. The LPSP was considered for performance assessment, with the target set at $LPSP = 3 \times 10^{-4}$ (equivalent to one day of failure in 10 years). By plotting all potential solutions capable of satisfying the reliability target, the sizing curve of the $N_{pv} \times N_{batt}$ solution space was determined. A tangent to the curve based on the cost function (similar to Equation 2.12) was then drawn to determine the minimum cost and optimal PV and battery capacities. Thus, the cost of the optimal design (and by extension, the optimal design itself) was determined graphically, unlike in the iterative approach where the costs of all the feasible designs would need to be evaluated (see Algorithm 2.1).

A similar method was applied by Mokheimer et al. [157] for the sizing of a hybrid PV-wind-battery-diesel system for Dhahran, Saudi Arabia. Three potential wind turbine capacities of 500 W, 1000 W and 1500 W were considered. The same renewable input models, reliability evaluation approach and reliability constraints used by Borowy and Salameh [36] were adopted. The LCE was considered as the cost objective. The load of a typical house in the region (average load of 473 W, peak load of 1231 W) was considered. For each wind turbine capacity, the $N_{pv} \times N_{batt}$ sizing curve was plotted. The tangents to the curves based on the cost function were then used to determine the optimal designs and costs for each wind generation scenario. The effect of adding a 2.6 kW diesel generator to the system was also investigated.

The authors found that that increasing the number of wind generators led to a reduction

in the LCE of the system as less batteries and PVs were required to obtain the same performance. The results also showed that small changes in the battery and PV capacities led to significant changes in the LPSP and LCE. Introducing diesel generation was found to be a beneficial way to reduce the LCE value while keeping the system reliability intact. The cost of storage was concluded to be the major economic constraint for standalone applications. The methodology was validated by comparing the results obtained for each wind turbine case against the results from commercial software.

Markvart [148] developed a technique for finding the optimum solar/wind combination of a hybrid system using graphical construction. The two design variables were considered: the sizes of the PV generator (a_s) and wind generator (a_w). Monthly average solar energy (S) and wind energy (W) values were considered as input into the model. 100% reliability was demanded of the energy system by applying demand-supply criteria: generation for each month was constrained to exceed the monthly demand of $d = 1\,\mathrm{kWh/day}$. The sizing problem was therefore defined as

$$\begin{aligned} \underset{a_s,a_w}{\text{minimize}} \quad & cost = c_w a_w + c_s a_s \\ \text{subject to} \quad & d \leq W_i a_w + S_i a_s \qquad i = \text{Jan,Feb} \ldots, \text{Dec} \end{aligned} \tag{2.14}$$

where c_s and c_w represent the unit costs of the PV and wind generators.

The entire problem was solved graphically. First, the twelve constraints were plotted to obtain the feasible region, with the sizing curve formed by the topmost lines. The optimal configuration was then determined as the point on the sizing curve where the slope of the tangent was $-c_w/c_s$.

2.2.2.3. Limitation of the graphical approach

The graphical approach is difficult to implement for problems with more than two design parameters [48, 241], making it unsuitable for complex system sizing problems.

2.2.3. Analytical approaches

2.2.3.1. Description of the approach

In analytical approaches, the potential of several alternative system architectures are assessed independently. For each energy system configuration, the most attractive design is determined based on the cost and performance objectives. The subproblems may be solved using the iterative approach previously described or using a metaheuristic approach. The best configuration of the energy system is then determined by comparing the cost and/or performance indices of the "best" designs of the different configurations analyzed [47, 139].

While the analytical approach depends on other solution approaches for solving its sub-problems, it is usually considered a separate energy system sizing methodology because it provides information that is usually not available with the iterative or metaheuristic

approaches. In addition to the information about the "optimal" solution which is provided by all the sizing methodologies, the analytical approach also provides information about the best available solutions for different configurations of the system. This additional information is useful because it can often influence decision-making. For example, consider the sizing of a typical PV-wind-battery system. The analytical solution not only provides information about the best PV-wind-battery solution, but also about the best results obtainable for other configurations such as PV-battery and wind-battery systems. Thus, it not only provides information about the optimal design, it also gives information about *how much better* the optimal solution is when compared to the best results of other potential configurations. Such information allows the decision maker to choose designs based on considerations beyond the cost alone. For example, a decision-maker may prefer to choose a slightly more expensive sub-optimal configuration which would be easier to operate and require significantly less time to build. Such considerations may be taken into account in decision-making when the analytical approach is used, unlike with the other approaches which return only the cost-optimal result.

2.2.3.2. Summary of works implementing the analytical approach

Koutroulis et al. [129] proposed a methodology to select, from among a list of commercially available systems, the optimal configuration and sizes of PV-wind-battery units which minimize the total system cost. Ten design variables were considered in the problem: the type and number of PV modules, type and number of wind generators, type and nominal capacity of the battery system, type and number of battery chargers, the wind turbine installation height and the PV tilt angle. Two types of PVs, wind generators, batteries and battery chargers of different capacities and costs were made available for selection in the energy system.

The sizing problem was solved in two stages as shown in Figure 2.5. First, optimal sizing problems were solved for all potential configurations of the energy system. It was assumed that only one type of each technology could be selected, meaning 16 potential energy system configurations were possible. For each configuration, an optimization problem to determine the sizes of the components required to minimize the total system cost while ensuring full demand satisfaction was solved using a genetic algorithm. The chronological approach to performance evaluation was adopted. Based on the results of the first stage which yielded 16 potential designs of different costs, the optimal system design was selected in the second stage as the configuration with the lowest system cost.

The methodology was demonstrated by considering the power demands of a residential household located in the area of the Technical University of Crete (TUC), with historical daily solar radiation hourly wind speed data for 2003 supplied as model inputs. The results indicated that hybrid PV/wind systems were cheaper than designs which featured WG or PV sources exclusively. PV-based systems were also found to be twice as expensive as wind-based systems.

Dufo-Lopez et al. [69] investigated the economics of integrating hydrogen generation and

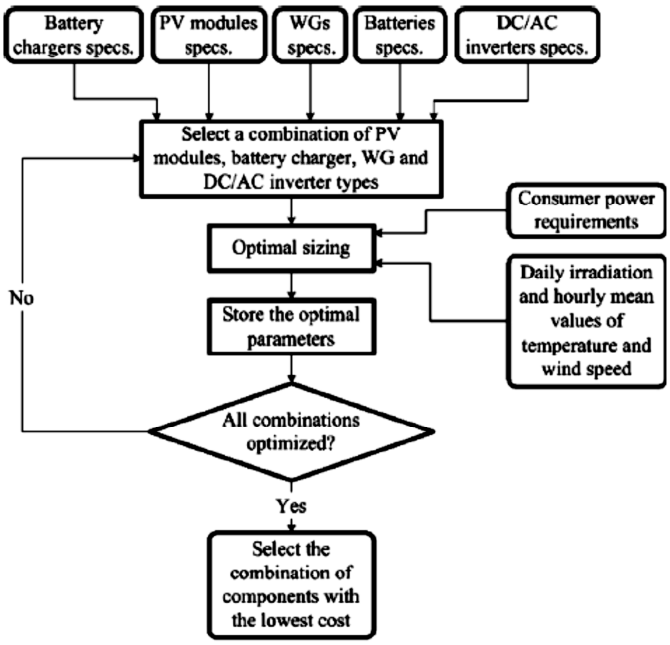

Figure 2.5.: Flowchart for sizing methodology proposed by Koutroulis et al. [129]

storage into grid-connected hybrid PV–wind systems in Spain. Three potential system configurations were considered:

1. PV-wind systems for the generation of electrical energy to be sold to the grid: In this scenario, the objective was to sell all energy generated to the grid. No energy storage was available.
2. PV-wind generation integrated with an electrolyzer: In this scenario, excess generation not required by the grid was used for hydrogen production via electrolysis. The hydrogen was sold for external use.
3. PV-wind generation coupled with an electrolyzer, hydrogen storage and a fuel cell: In this scenario, the hydrogen generated with excess power was temporarily stored to be used in a fuel cell. The fuel cell was used to generate electricity to be sold to the grid when renewable generation was insufficient to meet the grid demand.

For each configuration, the net present value (NPV) was maximized subject to constraints on the available land area and initial investment cost. The chronological approach to performance evaluation was adopted using hourly solar and wind data. Three potential wind availability levels (low, medium and high) were considered. Table 2.1 shows the total number of potential combinations considered for each configuration of the system. For each configuration, the NPV of all potential combinations were evaluated and the optimal design selected as the combination with the lowest cost objective.

The results indicated that PV-wind systems without hydrogen production were the most profitable for locations with low-to-medium windspeed levels. For locations with high windspeed availability, hydrogen production for external sale was found to be the best scenario. Generation from fuel cells was found to be unprofitable under any windspeed conditions at the current electricity prices in Spain.

Table 2.1.: Potential technology combinations for three system configurations considered by Dufo-Lopez et al. [69]

Type	Configuration	Alternatives available	Number of combinations
1	PV-wind system	6 types of PV generators of different sizes, 1 type of wind turbine with 21 possible sizes	126
2	PV - wind - electrolyser	Type 1 + 6 different electrolyzers of capacities between 0-10 MW	756
3	PV - wind - electrolyser - fuel cell	Type 2 + 6 fuel cells of capacities between 0-6 MW	4536

Khatod et al. [124] developed an analytical approach for the sizing of PV-wind-diesel systems based on the probabilistic evaluation of system performance. The problem considered was the maximization of the annual operating cost of the energy system subject to generation and demand constraints. Four potential system configurations were considered for the integration of renewables generation:

- 150 kW of diesel generation, considered as the base case,
- PVA added: PV generation ranging from zero to 150 kW added to base case,
- WTG added: Wind generation ranging from zero to 150 kW added to base case, and
- PVA + WTG added: PV and wind generation ranging from zero to 150 kW added to base case, with the capacity evenly split between both renewable generation options in equal amounts.

The study period of one year was divided into 12 months, with each month further subdivided into 24 segments, each referring to a particular hour of the month. Solar radiation and wind speed data for all the hours of the months were represented with discretized beta and Weibull distributions respectively, while an empirical discrete distribution was created for the load (peak demand of 60 kW, average demand of 36.82 kW). The maximum wind penetration was set at 40%. Two reliability measures were considered: loss of energy expectation (LOEE, defined as the total unmet load in the year) and the loss of load expectation (LOLE, defined as the number of hours with unmet load in the year).

For each of the configurations, the reliabilities, annual operating costs and annual fuel savings of all potential capacity combinations were evaluated. Figure 2.6 shows how the reliability (LOLE) and fuel savings vary with installed capacity for the three scenarios incorporating renewables generation. Initially, the system reliability improves with addition of renewable energy sources. Beyond a point however, the system becomes saturated and the addition of renewable energy sources causes no substantial improvement in the system reliability. As expected, the hybrid systems produced the best system performance. The wind-integrated systems were found to outperform PV-integrated systems because of their day-round generation capabilities.

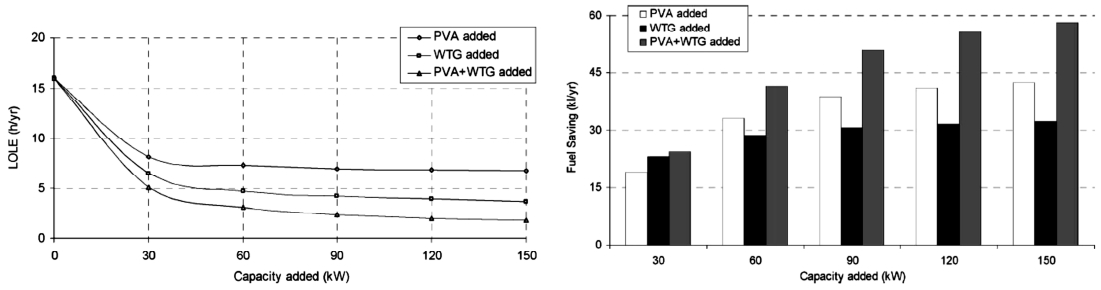

(a) LOLE (b) Fuel savings

Figure 2.6.: Variation in reliability (LOLE) and fuel savings with renewables generation capacity for different system configurations considered by Khatod et al. [124].

Table 2.2.: Alternative system configurations and energy costs for PV-wind-diesel-battery systems investigated by Merei et al. [154] for Aachen, Germany. Three types of batteries were considered: lead-acid (Pb), Vanadium redox flow (V) and Lithium-ion (Li) batteries.

Configurations	Available technologies	Selected technologies	Energy cost (€/kWh)
I	Pb, V, Li, Diesel	V, Diesel	0.65
II	Pb, V, Li	Pb, V, Li	1.35
III	Diesel	Diesel	0.91
IV	Pb, Diesel	Pb, Diesel	0.68
V	V, Diesel	V, Diesel	0.65
VI	Li, Diesel	Li, Diesel	0.72

For the PV-diesel and hybrid-diesel systems, increasing the installed capacities of renewables led to increased fuel savings. For pure wind-diesel systems however, the observed improvement in the fuel savings was marginal after 60 kW due to the wind penetration constraint. The hybrid-diesel systems provided the highest fuel savings over the entire capacity range. Based on the cost and reliability assessments, installation of between 30 kW and 60 kW of renewables generation to supplement the diesel generation was recommended. The authors also showed that the analytical approach to reliability evaluation produced results within 5% of those obtained from Monte-Carlo simulations while requiring significantly less computational time.

Merei et al. [154] applied the analytical approach to the sizing of a hybrid energy system integrating PV-wind-diesel generation with different battery technologies. Three batteries types were considered: Lead acid (Pb), Lithium ion (Li) and a Vanadium redox-flow (V). Six potential energy system configurations were considered as shown in Table 2.2. For each configuration of the system, the 20-year total system cost was minimized using a genetic algorithm. The chronological approach was adopted for performance evaluation, with full demand satisfaction ensured using the generation-demand constraint similar to Equation 2.6. During operation, the order of battery discharge was determined by the operating cost: the battery with lowest operating cost was discharged first.

The model was implemented in MATLAB and demonstrated for two locations: Aachen,

Table 2.3.: Alternative system configurations and energy costs for PV-wind-diesel-battery system investigated by Al-Shamma'a and Addoweesh [7]. The costs are based on a diesel price of \$0.1/L.

Configurations	Available technologies	LCOE (\$/kWh)
I	PV/WT/Batt/DG	0.1396
II	PV/Batt/DG	0.1749
III	WT/Batt/DG	0.1480
IV	PV/WT/DG	0.1487
V	WT/DG	0.1748
VI	DG	0.1378
VII	PV/WT/Batt	0.2919
VIII	WT/Batt	0.5355
IX	PV/Batt	0.7769

Germany and Quneitra, Syria. Ten years of historical data was supplied as input for the German case, while one year of historical data (2005) was used in the Syrian case. The load of a telecommunications station ($2750\,\mathrm{W} \pm 6\%$) was considered. The results for Aachen are shown in Table 2.2. The minimum cost scenario for both locations involved the integration of renewables generation with a redox flow battery (scenario I), with diesel generation providing 22% of the energy in the German case and 56% in the Syrian case. Incorporating batteries into the hybrid system made the system about 30% cheaper compared to the diesel only case. However, the elimination of diesel generation was found to be uneconomically unfavourable (scenario II).

Combining several battery technologies was found to provide no particular advantage when diesel generation was an alternative. However, a combination of the three battery technologies was found to be the optimal solution for the hybrid system when diesel generation was unavailable. The authors concluded that combining batteries with the renewable generation technologies was effective, economical and environmentally friendly.

Al-Shamma'a and Addoweesh [7] also applied the analytical approach to the design of PV-wind-diesel-battery hybrid systems. Nine potential configurations of the system were considered as shown in Table 2.3. Three decision variables were considered: the number of PV modules, number of wind turbines and the number of batteries. The diesel generator was sized to meet the peak load demand. The levelized cost of energy (Eq. 2.10) was considered as the cost objective. Two reliability measures were considered: the LPSP and the renewable energy fraction (REF), representing the fractional contribution of renewables to load satisfaction. The load of a village in Saudi Arabia was considered, with hourly solar and wind data for 2010 supplied as data input into the model for chronological performance evaluation. For each configuration, the minimum cost design required to provide an LPSP of zero was determined using a genetic algorithm. Fifteen different types of wind turbines were considered in the work.

The results showed pure diesel generation to be the most economic solution for power supply. However, for the systems integrating renewables, the hybrid system (scenario I) was found to be the most cost-effective option. Battery integration was found to impact

the LCE positively by reducing the annual diesel consumption. The type of wind turbine selected was also found to be influenced by the desired reliability. The authors found that meeting about 65% of the annual load demand from renewables provided a balance between cost and surplus energy generation.

Paliwal et al. [172] developed an analytical technique for the sizing of PV-wind-battery-diesel systems using the probabilistic approach to reliability evaluation. Seven potential configurations were considered:

- Configuration-1: Diesel generating units only
- Configuration-2: Wind turbines and diesel generating units only
- Configuration-3: Photovoltaics and diesel generating units only
- Configuration-4: Wind turbines with battery storage
- Configuration-5: Photovoltaics with battery storage
- Configuration-6: Wind turbines and photovoltaics and diesel generating units
- Configuration-7: Wind turbines and photovoltaics with battery storage

The probabilistic battery state model developed in their previous work [173] was used for the representation of the battery system, along with Beta and Weibull distributions for solar radiation and wind speed respectively. For each configuration of the system, the LCE was minimized subject to environmental and technical constraints using particle swarm optimization. A peak load of 70 kW was considered. Two reliability constraints were used to evaluate performance:

- Percentage of risk state probability, defined as the percentage of operational time in which generation was inadequate to supply load, indicating 'risk' state.
- Percentage of healthy state probability, defined as the percentage of operational time in which system has adequate reserves to satisfy laid down reserve criteria, indicating 'healthy' state.

For each configuration, sensitivity of the system performance to small variations in the component sizes around the optimal solution was investigated. The PV-wind-battery system (configuration 7) was found to have the lowest LCE and was chosen as optimal system configuration. The results showed that using larger storage helped reduce the replacement costs, and the addition of RES based units contributed significantly to reducing operating costs. It was also found that system oversizing did not always imply increased costs. The development of a probabilistic battery model allowed the use of a probabilistic approach to be used for the sizing of systems incorporating storage for the first time.

2.2.3.3. Advantages and limitations of the analytical approach

The analytical approach allows for the effect of a given technology choice to easily be determined by comparing to other potential configurations. It also allows for the final design decision to be made on factors other than cost alone.

However, the procedure is tedious [48] and often the entire design space is not explored, meaning that the best solution may not be found. For example, the work by Khatod et al. [124] only considers equal amounts of wind and solar generation for the hybrid system, ignoring potentially better solutions which may occur with uneven amounts of wind and solar generation. Similarly, Koutroulis et al. [129] assumed that only one type of each technology could be selected. In reality, a combination of different types and capacities of the same technology may have produced a better solution. Paliwal et al. [172] did not consider a configuration incorporating PV-wind-battery with diesel generation.

2.2.4. Metaheuristic approaches

2.2.4.1. Description of the approach

Metaheuristic algorithms are stochastic solution approaches which start from random points and explore the solution space based on simple guiding rules. They typically combine random and local search techniques to ensure that good solutions are found. Metaheuristic algorithms are typically problem-independent, make no assumptions about the problem being optimized, require no gradient information and can easily jump out of local optima [34, 186]. For these reasons, they tend to produce better solutions and require smaller computational time than classical optimization methods for large problems [186].

Several metaheuristic algorithms have been applied to system sizing problems in recent times, as will be shown later. However, the most frequently used techniques are genetic algorithms (GA), simulated annealing (SA), and particle swarm optimization (PSO).

Genetic algorithms are population-based optimization methods based on the evolutionary process of biological organisms [77]. The key to forming new solutions in GAs are two evolution operators: mutation and crossover. In crossover, two members of the population (called parents) are combined (reproduce) in some way to form a new offspring solution. In mutation, a part of an existing solution is changed (mutates) randomly to form a new solution. The mutation operation allows the algorithm to get out of local optimums. Selection of solutions for crossover and mutation are based on the quality of the solution – "good" solutions reproduce more frequently. It is expected that better solutions are found with each new generation.

Particle swarm optimization is also a population-based optimization technique and is based on the movement of birds and swarms. In PSO, each solution is considered to be a particle (bird) moving in the search space. The position of each particle (each solution) is improved by taking into account its current position (representing the current solution), its previous best position (representing the best solution attained by the particle so far), and the position of the optimum particle (representing the current best known solution to the problem). Thus, all the particles (swarm) move toward the best solutions.

Simulated annealing is a probabilistic optimization technique based on the concept of metal annealing – the heating and gradual cooling of metals. Unlike GA and PSO which

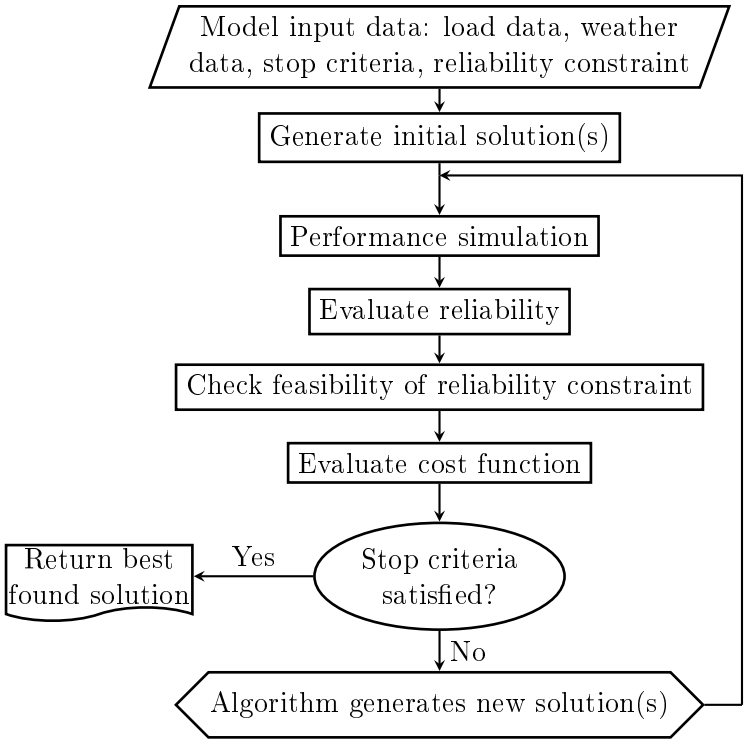

Figure 2.7.: Flowchart of typical single-objective metaheuristic solution methodology

are population-based, simulated annealing only considers a single solution. The algorithm starts with a single random solution. In SA, a temperature variable is used to simulate the cooling process. The temperature variable is initially set high in the algorithm and then gradually reduced. The probability of new solutions being accepted is dependent on the temperature variable. Initially, the high temperature allows the algorithm to accept new solutions worse than the current solution. This gives the algorithm the capability to jump out of local optimums early on. As the temperature variable is reduced, so does the frequency with which worse solutions are accepted. Thus, the algorithm starts by accepting solutions from all over the search space and narrows in on the neighbourhood of the current solution as the temperature variable is decreased.

Further information about these and other metaheuristic algorithms which have been applied to system sizing problems may be found in Erdinc and Uzunoglu [77].

Metaheuristic approaches have been applied for single and multi-objective system design and sizing problems.

2.2.4.2. Summary of sizing works based on metaheurisic approaches

Single objective design With single-objective problems, the reliability is treated as a constraint to be satisfied in the optimization process. The function of the algorithm is to improve on the cost objective by randomly and/or systematically exploring the solution space while ensuring the feasibility of the reliability constraint. A typical solution methodology is shown in Figure 2.7. At the end of the optimization process, the algo-

rithm returns the best found (but not necessarily optimal) solution which satisfied the imposed reliability constraint.

Xu et al. [237] proposed an optimal sizing method for PV-wind-battery systems using a genetic algorithm (GA). Five integer decision variables were considered: the number of 50 W PV modules, PV tilt angle, type of wind turbines (5 alternatives were provided), number of wind turbines and the number of 200 Ah batteries. The objective was to minimize the total capital cost of the energy system subject to a constraint on the LPSP, with the LPSP target set at 1%. The chronological approach to performance evaluation was adopted, with one year of hourly TMY data for Daggett, California supplied as input. A constant load of 2 kW was considered. The optimal design found by the GA had a storage capacity of 1.5 days and an LPSP of 0.996%. The authors concluded that the GA converged well and suggested that they are suitable for energy system sizing applications.

Similarly, Yang et al. [241] and Yang et al. [242] considered the sizing of a hybrid PV-wind system employing battery banks for a telecommunications station located in Guangdong, China using a genetic algorithm. The LPSP was considered as the reliability objective. The annualized cost of system (ACS) was considered as the cost objective, given by

$$ACS = C_{acap} + C_{arep} + C_{amain} \tag{2.15}$$

where C_{acap}, C_{arep} and C_{amain} represent the annualized capital, replacement and maintenance costs respectively.

Five decision variables were considered included in the optimization process: the number of PV modules, number of wind turbines, number of batteries, PV tilt angle and the wind turbine installation height. System performance was evaluated based on one year (1989) of hourly solar and wind data using chronological simulation. The load demand was assumed to be constant at 1500 W throughout the year. A population size of 10 was used for the genetic algorithm. The sizing of systems to meet LPSP targets of 1% and 2% were considered.

The authors found that a hybrid system with 3–5 days of battery storage was sufficient to meet reliability targets of 1-2%. Increasing the reliability required from the system resulted in optimal configurations with higher costs. Systems limited to only one generation option (either PV or wind) were also found to be more expensive than hybrid systems for the same level of reliability.

Kumar et al. [131] demonstrated the use of a biogeography based optimization (BBO) algorithm for the sizing of hybrid PV-wind-diesel-battery systems. Four design variables were considered, one to represent the capacity of each system component. The total system cost was considered as the cost objective based on a project life of 25 years. The reliability of the system was defined based on a parameter R_{max} representing the maximum permissible fraction of the unmet power. Based on this parameter, the

generation-demand relationship over the entire period of operation was constrained:

$$P_{PV}(t) + P_{WT}(t) + P_{DG}(t) + P_{Batt}(t) \geq (1 - R_{max}) \cdot P_{load}(t) \qquad \forall t \qquad (2.16)$$

The methodology was demonstrated for Jaipur, India. One year of hourly time series data (2010) for the location was supplied as input into the model. The performance of the BBO algorithm was compared to other evolutionary algorithms such as GA and PSO, as well as commercial system sizing softwares such as HOMER[2]. The daily load was assumed constant at 2263 kWh/day.

The results showed that the BBO performed better than the other evolutionary algorithms, comfortably and rapidly approaching the optimal solution. The design obtained also from the BBO significantly improved on the results obtained from HOMER while cutting the simulation time required for the system from 15h to 0.87 h. Wind integration was found to reduce the battery bank and diesel requirements. Sensitivity of the results to windspeed variability was then investigated by adjusting the windspeed level at every hour by ±17.5%. Increasing the windspeed was found to reduce the cost by 11.6% while windspeed reduction led to an 8% cost increase.

Askarzadeh [20] also proposed a new algorithm for the sizing of hybrid PV-wind-battery systems called discrete chaotic harmony search-based simulated annealing (DCHSSA). The algorithm combined the advantages of three metaheuristic optimization approaches: chaotic search (CS), harmony search (HS) and discrete simulated annealing (DSA). The objective of the optimization problem was to minimize the total annual cost subject to full demand satisfaction. Three design variables were considered: the number of PV modules, wind turbines and batteries. Hourly PV and wind generation profiles for a single day were supplied as input data for the model.

The performance of the proposed algorithm was compared to two other algorithms: discrete simulated annealing (DSA) and discrete simulated annealing combined with harmony search (DHSSA – also developed by the authors). Fifty independent runs were carried out with the three algorithms for different starting points. The new algorithm (DCHSSA) was found to yield better solutions than the two alternatives and was suggested to be a good alternative to GAs for optimum hybrid system sizing problems.

Amer et al. [11] considered the sizing of a similar hybrid system to meet the load demands of a residential house. The objective of the optimization problem was to minimize the levelized cost of energy (given by Equation 2.10) subject to full demand satisfaction. The model was implemented in MATLAB and was solved using particle swarm optimization. A similar problem was solved by Tegani et al. [211] using a genetic algorithm, with the total system cost considered as the objective to be minimized.

Maleki and Askarzadeh [144] evaluated the performance of different metaheuristic algorithms in the optimal sizing of PV/wind/H_2 and PV/wind/battery systems. Four algorithms were compared in terms of accuracy and computational cost: particle swarm optimization (PSO), tabu search, simulated annealing and harmony search. The ob-

[2]Hybrid Optimization Model for Electric Renewables, <http://www.homerenergy.com>

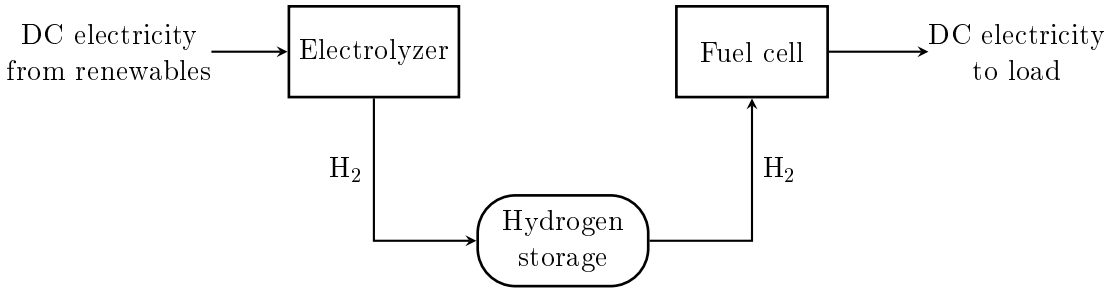

Figure 2.8.: Schematic representation of hydrogen storage. The system consists of three components: an electrolyzer for hydrogen generation, a storage tank for hydrogen storage, and fuel cells for hydrogen to power conversion. Each component of the system must be sized separately .

jective considered was the minimization of the total annual cost subject to constraints on full demand satisfaction. The system models and algorithms were implemented in MATLAB. One year of hourly solar and wind time series data for Iran was supplied as input into the model. Fifty independent runs of each algorithm were performed for performance comparison. Different potential system configurations (PV/H_2, wind/H_2, PV/battery, and wind/battery) were also considered.

The results of the simulations showed the wind/battery system to be the best choice economically. PSO was found to yield better results than the other algorithms. It was also found to be the most robust based on the low standard deviation of the cost values obtained over the fifty runs. It was however found to require the most computational time, with tabu search requiring the least. The authors concluded that PSO was the most promising approach for energy systems sizing.

Maleki and Pourfayaz [145] considered the design of hybrid PV-wind-diesel-storage systems for a set of residential houses in Iran using discrete harmony search (DHS) algorithm. Two storage types were considered: battery storage and hydrogen storage. A schematic representation of hydrogen storage is shown in Figure 2.8. The aim of the optimization problem was to minimize the total annualized cost of each system type subject to full demand satisfaction. The model was implemented in MATLAB and one year of hourly solar and wind time series data for Rafsanjan, Iran was supplied as input into the model. The results obtained from the DHS algorithm were found to be similar to those obtained with simulated annealing and HOMER. Battery-integrated systems were found to be more cost-effective and more environmentally friendly than hydrogen storage, with the authors concluding that further reductions in the costs of electrolyzers and fuel cells are required before hydrogen storage can become economically feasible.

Tito et al. [218] investigated the effects of socio-demographic factors on the sizing of PV-wind-battery systems. Six different load profiles were considered, each representing a different type of electricity user. The aim of the work was to generate optimal designs for each type of user by minimizing the total system cost subject to a constraint on the LPSP, with the LPSP target set at zero. One year of hourly solar and wind time series data for

Auckland, New Zealand was supplied as input into the model. The solution methodology implemented combined the iterative and metaheuristic approaches to system sizing. The genetic algorithm was used to obtain good solutions to the sizing problem, which were then used to generate bounds for the iterative approach.

The implemented hybrid approach was found to obtain the same results as a pure GA in a shorter amount of time. The cost was of the optimal designs for the different load types were found to be influenced significantly by the magnitude and temporal positions of the peak demand. The authors concluded that energy system costs could be reduced by accounting for the socio-demographic profile of the electricity consumer during design.

Multi-objective design In multi-objective solution approaches, the aim is to generate a set of non-dominated (Pareto-optimal) designs which trade-off between a number of objectives, two of which typically are the cost and the system reliability. A solution is non-dominated if no other solution exists which improves on one objective without worsening another objective. The preferred configuration and/or size of system components is then selected from the list of alternative optimal designs.

Dufo-Lopez and Bernal-Agustin [68] proposed a novel approach for the triple multi-objective design of isolated PV-wind-diesel-hydrogen-battery systems. The objective was to minimize, simultaneously, objectives related to cost, reliability and environmental impact. The net present cost (NPC), annual unmet load (%) and annual CO_2 emissions (kg/year) were considered as the three objectives to be minimized. The chronological approach to performance evaluation was adopted.

Two types of variables were optimized in the work: seven design variables to define the configuration of the system (three variables for each component required in the hydrogen storage system as shown in Figure 2.8, and one for each of the other system components), and ten control variables (such minimum battery level and minimum generator output power) to control the operation of the system . The optimization problem was solved by combining a multi-objective evolutionary algorithm (MOEA) with a genetic algorithm as shown in Figure 2.9. The design variables were optimized by the MOEA, while the genetic algorithm optimized the control variables. The performance of each design generated in the MOEA was evaluated for several potential control strategies in the secondary GA, and the best operating strategy selected based on minimum NPC.

The method was demonstrated by considering one year of hourly time series data for Zaragoza, Spain as input into the model. The results of the study suggested that battery storage was more efficient than hydrogen storage, with most of the solutions in the final generation incorporating only battery storage. While the method was unable to generate the full Pareto front due to the large solution space (less than 0.001% of the solution space was explored), the authors concluded that methodology developed was useful for recognizing non-dominated solutions based on which sizing and operational decisions could be made.

Katsigiannis et al. [121] proposed a method for the bi-objective design of small autonomous hybrid power systems (SAHPS) for cost and environmental impact. The lev-

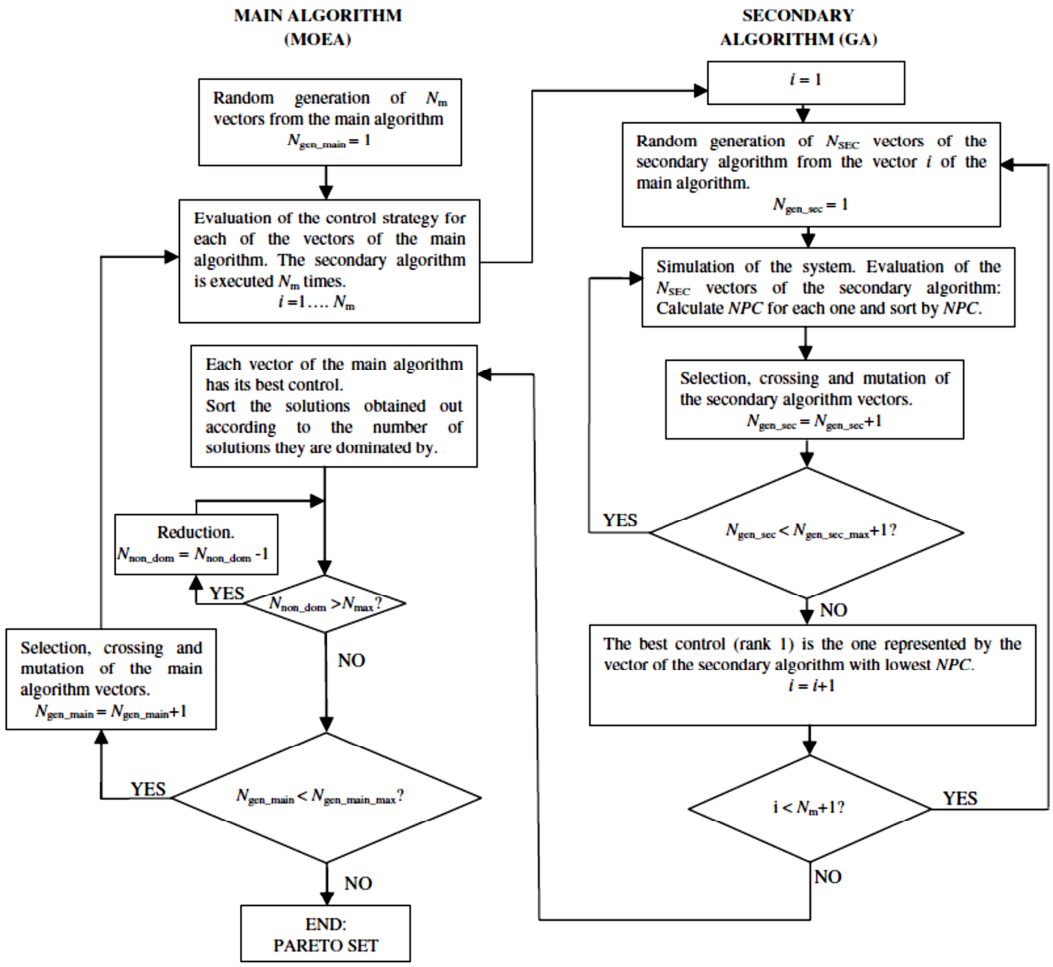

Figure 2.9.: Solution methodology implemented by Dufo-Lopez and Bernal-Agustin [68], called the strength Pareto evolutionary algorithm (SPEA). The method combines two algorithms: a multi-objective evolutionary algorithm (MOEA) to optimize the configuration of the system (shown left), and a genetic algorithm to optimize the control strategy (shown right).

elized cost of energy was considered as the cost objective while the total greenhouse gas emissions, evaluated using the life cycle analysis (LCA) approach, was used to quantify environmental impact. Two systems incorporating different storage options were considered:

- A hybrid system consisting of PV modules, wind turbines, diesel generators, biofuel generators, fuel cell with natural gas as fuel, and battery storage.
- A hybrid system consisting of PV modules, wind turbines, diesel generators, biofuel generators, fuel cell with hydrogen as fuel, and hydrogen storage.

Reliability was treated as a constraint by limiting the maximum allowable annual unmet load. The maximum acceptable initial cost of the system was also constrained. The order of dispatch of the generators and storage alternatives was predefined based on their operating costs.

The methodology was demonstrated for Chania, Greece. 10-minute solar, wind and

temperature time series data for the location was supplied as input into model. For each system, the Pareto front was generated using a multi-objective genetic algorithm combined with a local search procedure. The system incorporating battery storage was found to be cheaper and produce less emission than the hydrogen-based system. The ratio of the size of diesel to biofuel generators was also found to be the most significant factor affecting economic and environmental performance: selecting more biofuel generators reduced emissions but increased cost. The authors suggested that the optimal design be selected based on the financial impact of the greenhouse emissions.

Ould Bilal et al. [170] investigated the effect of load profile variation on the optimal configuration of PV-wind-battery systems for Potou, Senegal. Three qualitatively different load profiles with the daily same energy demand (94 kWh/day) were studied. The number of PV modules, wind turbines, batteries, inverters and regulators were considered as the decision variables. The LPSP and ACS (Equation 2.15) were treated as the reliability and economic objectives to be minimized. One year of hourly time series data was supplied for reliability evaluation. For each case, the Pareto front was generated using a multi-objective genetic algorithm. The results indicated that the load profile had a significant impact on the trade-off curve, with as much as 7% cost difference between the maximum reliability designs of the three load scenarios. The lowest ACS was observed for the demand profile with the most regular distribution of load throughout the day.

Perera et al. [179] considered the potential trade-offs between the levelized cost of energy (LCE), initial capital cost (ICC) and greenhouse gas emissions (GHG) in the design of PV-wind-diesel-battery systems for rural electrification. The system reliability, modelled as the unmet load fraction, was treated as a constraint. Ten design variables were considered, six related to the configuration of the system and four related to operating ranges of the battery and diesel generators. Hourly renewables input data for Hambonthota, Sri Lanka based on the averaging of three years of historical data (1995,1997 and 1998) was supplied as input into the model. The problem was solved using a steady ε-state evolutionary algorithm. The 3D Pareto front was generated. 2D projections of the ICC-LEC and LEC-GHG fronts were also presented to make the decision making process simpler. The sensitivity of the trade-off curve to variations in unit costs, fuel costs and minimum unmet load fraction was also investigated.

Variations in the prices of equipment (PV and wind turbines) were observed to significantly affect the trade-offs between the ICC and LCE. On the other hand, variations in the cost of diesel had more impact on the LEC-GHG front. Increasing the required reliability of the system by decreasing the maximum unmet load fraction was found to lead to higher emissions and capital costs. The authors recommended that stagewise integration of renewables be encouraged to help bear the high initial cost requirements of renewables. This was demonstrated by considering a possible six-stage pathway for renewables integration based on the solutions present on 3D-front.

Abbes et al. [3] also proposed a methodology for the tri-objective design of autonomous hybrid PV-wind-battery systems. Three design variables were considered: the installed area of photovoltaics (A_{pv}), the wind turbine swept area (A_{wt}) and the battery capacity

(C_{batt}). The life cycle cost (LCC) and LPSP were considered for cost and reliability. Environmental impact was modelled as an embodied energy (EE), defined as the total non-renewable energy consumed in all the processes associated with the production of the energy system components. This was represented mathematically as:

$$Em_{total} = Em_{pv}A_{pv} + Em_{wt}A_{pv} + Em_{batt}C_{batt} \tag{2.17}$$

where Em_i is the unit embodied energy in the production of system component i.

Half-hourly renewables input data for 9 years (2002-2010) was obtained from the National Wind Technology Centre, Colorado. The total wind potential for the years were computed and the year with the worst wind potential (2010) was selected as time series input for the model. The typical load of a residential house in Colorado (2193 $^{\text{kWh}}/_{\text{yr}}$ with monthly variations) was considered. The model was implemented in MATLAB/Simulink and solved using a controlled elitist multi-objective genetic algorithm. 3D and projected 2D representations of the Pareto front were presented.

Photovoltaics were found to be the largest contributors (49%) to the embodied energy. Batteries were also found to contribute significantly (40%) due to the need for replacement every 4 years. Cost variation between designs was found to increase with reliability, with a 30% difference observed in the costs of the designs with LPSPs of 1% and 5%. The optimal solution was selected based on a maximum LPSP criterion of 5%. The performance of the optimal solution in the other years (2002-2009) was then evaluated to ensure that LPSP criterion was satisfied in all the years.

Zhao et al. [247] considered the tri-criteria sizing of a PV-wind-diesel-battery system to meet the residential and commercial load demands of Dongfushan Island, China. The minimization of lifecycle cost, maximization of renewable energy source penetration (defined as the fraction of energy supplied by energy system generated from renewables) and the minimization of pollutant emissions were the three objectives considered in the design problem. Five design variables were considered. The weighted sum approach was applied to reformulate the tri-objective problem into a single objective problem,

$$\min f = \mu_1\lambda_1 + \mu_2\lambda_2 + \mu_3\lambda_3 \tag{2.18}$$

where $\lambda_1 - \lambda_3$ and $\mu_1 - \mu_3$ represent normalized values of the objective functions and objective function weights respectively, with $\mu_1 + \mu_2 + \mu_3 = 1$.

Hourly historical data for a typical year was supplied as input into the model. Seven cases of different values of the weights were considered. The single objective problems were solved using a genetic algorithm. The trade-off between renewables penetration and utilization was found to be a key issue for renewables integration. Oversized systems were found to dump power more frequently than desired, while undersized systems did not make the best use of the favorable potential of renewable resources. The renewables penetration level was found to vary between 55% and 62% for all the seven cases considered. The authors concluded that generation cost and the size of energy storage units need to be balanced in order to obtain an optimal level of renewables penetration.

The microgrid was also found to be economically superior to pure diesel generation.

Sharafi and ELMekkawy [202] presented a methodology for the triple multi-objective design of isolated PV-wind-diesel-hydrogen-battery systems using the ϵ-constraint method. Seven design variables relating to the capacities of the different energy system components were considered. The operating strategy was predefined, with the battery system prioritized over the hydrogen-based system during charging and discharging. Diesel generation was considered as the last resort for power generation. Three objectives were considered for minimization: the total system cost, CO_2 emissions and loss of load probability.

The ϵ-constraint method was employed, with the cost treated as the primary objective to be minimized. The LLP and maximum CO_2 emissions were treated as constraints with the limits varied between 0-5% and 1500-4500 kg/year respectively. The solution approach involved solving a series of single objective problems for the minimum cost design using particle swarm optimization (PSO) to generate different points on the 3D Pareto front.

The methodology was demonstrated using the same case study considered by Dufo-Lopez and Bernal-Agustin [68] for Zaragoza, Spain. Fifty non-inferior solutions were obtained. The optimization approach was found to yield designs with better costs than those obtained by Dufo-Lopez and Bernal-Agustin [68] for the same LLP and CO_2 emissions. The results also indicated that the total cost of the system was most sensitive to the allowable level of CO_2 emissions.

The improved fruit fly optimization algorithm (IFOA) was proposed by Zhao and Yuan [248] for bi-criteria sizing of stand-alone hybrid PV-wind-diesel-battery systems. The objective considered was to minimize, simultaneously, the total annual cost of the system and the annual CO_2 emissions while ensuring full demand satisfaction. Three decision variables were considered relating to the number of the PV modules, wind turbine and batteries. A 30 kW diesel generator was made available as backup to the renewable energy system. The model was implemented in MATLAB. The IFOA algorithm was demonstrated by considering single objective (cost only) and multi-objective sizing problems for Dongao Island, China. One year of hourly wind speed, solar radiation and ambient temperature data collected on the island, along with the typical daily load profile for the island, were supplied as inputs into the model. The hybrid system obtained by the algorithm for the single-objective problem was shown to be more economical than pure diesel generation for the site. The 2D Pareto front was also presented. Compared to the basic fruit fly optimization algorithm (FOA), the IFOA algorithm was shown to converge faster and possess stronger global research ability.

Shi et al. [203] developed a metaheuristic methodology for the tri-criteria sizing of hybrid PV-wind-battery-diesel systems using a preference-inspired co-evolutionary algorithm (PICEA). Three objectives were considered for minimization: annualized cost of system (Equation 2.15) for economics, LPSP for reliability and fuel emissions for environmental impact. One year of hourly solar, wind and load demand time series data for a remote area in Spain was supplied as input into the model.

One year of hourly solar, wind and load demand time series data for a remote area in Spain was supplied as input into the model for chronological performance evaluation. The renewables input data were obtained by averaging ten years of historical data. 3D and 2D projections of the Pareto front were presented. The authors concluded that PICEA showed better diversity and convergence performance to the 3D Pareto front than the SPEA algorithm used by Dufo-Lopez and Bernal-Agustin [68].

2.2.4.3. Advantages and limitations of metaheuristic algorithms

Metaheuristic algorithms have been used for all types of problems, including mixed integer and non-linear optimization problems. In addition to being suitable for finding good solutions to single and multi-objective problems, they are suitable for combinatorial optimization problems[3] and can easily handle problems with more than three variables; a significant advantage over the graphical and iterative approaches to energy systems sizing [48].They can also handle non-linear variations in the sizes of system components [48]. Thus, metaheuristic methods are considered to be the state-of-the-art approach for system sizing applications [48, 139, 241].

However, metaheuristic approaches have their drawbacks: they are comparatively more difficult to code and understand than the iterative approach, and provide no guarantee that the best solution will be found [34, 48]. All metaheuristic approaches incorporate some element of randomness, meaning that two identical runs may yield different solutions. This means that more than one run of the algorithm may be required to obtain a measure of confidence in amy solution obtained using a metaheuristic algorithm.

2.2.5. Linear programming

2.2.5.1. Description of the approach

With this approach, the objective function and constraints related to the energy system components are represented by linear expressions, leading to a linear programming (LP) or mixed integer linear programming (MILP) problem formulation. The problem can then be solved using any available deterministic LP or MILP method. Linear programming is a special case of mathematical programming. LP problems are easier to solve because the optimal solution will always lie at one of the vertices of the feasible region.

Solvers have been developed which solve LP problems to optimality. They are typically based on the simplex or interior point algorithms [71]. With the simplex method, the algorithm moves along the vertices of the feasible region formed by the constraints in a direction which improves the objective until the optimal solution is found. In interior point methods, the search moves through the interior of the feasible region [227]. MILP solvers combine the LP solution techniques with branch and bound algorithms [71].

[3] In general, combinatorial optimization problems refer to problems which involve finding good solutions to a problem from a finite or countably infinite set of solutions [34]. In energy system sizing problems, the combinatorial nature arises from the many potential combinations of technologies, sizes, configurations and operating schemes which may exist in the search space.

2.2.5.2. Summary of works based on linear programming

Malheiro et al. [146] developed a methodology for the sizing of PV-wind-diesel-battery systems using a linear programming approach. An MILP model to minimize the total life cycle cost subject to constraints enforcing full demand satisfaction was developed. Four design variables were considered, with the number of wind turbines, PV panels, and diesel generators modelled as integer variables and the storage capacity as a continuous variable. Binary variables were used to control the state of operation of the storage (charging, discharging or dormant) and diesel generation (on/off) units.

To demonstrate the methodology, the case study of Lisbon, Portugal was considered. Synthetic hourly meteorological data for a year obtained from commercial software was supplied as input into the model. The load profile of an industrial facility (power demands between 8 AM and at 7 PM only) was considered, with the same demand profile considered for every weekday of the year. The model was implemented in GAMS and solved with an MILP solver CPLEX for an optimality gap (difference between the best found and best possible solutions) of 5%. Sensitivity of the results to economic data, climate data and the demand profile were also investigated by solving multiple instances of the MILP optimization problem.

The results of the simulation showed the PV subsystem to be the main component of the hybrid system in terms of installed capacity and cost, with low amount of storage installed. This was attributed to the high correlation between the demand and solar radiation profiles (no night power requirements). Renewable energy was found to supply 90% of the annual demand, with 24% surplus energy generation. The diesel generators were only in use on winter evenings when PV generation was insufficient. The optimal capacities of the individual components were found to be strongly affected by the climate and cost data. The cost objective was found to be most sensitive to the PV cost, while the level of renewable penetration was most significantly impacted by the cost of diesel. Increasing the level of the wind or solar resource available was found to change the optimal capacities: higher wind resource meant more wind turbines were installed at the expense of PVs, and vice versa. Changes in the load profile were found to affect only the capacity of battery storage required.

A linear programming approach was also used by Saif et al. [198] for the sizing of a PV-wind-diesel-battery system for Masdar city, Abu Dhabi. Two objectives were considered for minimization: the total cost of the system and the annual CO_2 emissions. The emissions objective was evaluated using the life cycle analysis (LCA) approach. The reliability of the system was enforced by constraining the expected unserved energy (EUE). Each month was modelled as a single day to reduce the size of the problem, with hourly measurements of solar resource and windspeed supplied as input into the model. The multi-objective problem was converted into a series of single objective problems using the weighted sum approach. The single objective problems were solved using deterministic methods.

A wind-diesel-battery configuration was found to be optimal for the location. This was

attributed to wind generators having the lowest cost and emissions per kWh energy delivered. The least cost and least emissions solutions were found to be relatively close, with 1% and 3% differences in the cost and emissions respectively.

2.2.5.3. Advantages and limitations of the linear programming approach

Linear programming approaches are suitable for both discrete and continuous system sizing problems and provide an optimality guarantee, an advantage over the metaheuristic approaches. Recent improvements in MILP solvers allow for optimal or near optimal solutions to be found in short CPU times when compared to the computational times required by most metaheuristic algorithms. [146].

However, linear programming approaches are not applicable sizing problems involving generation or storage systems which cannot be represented with linear expressions, limiting their applicability. For such systems, non-linear mathematical programming (NLP) algorithms are required. While several NLP algorithms such as the penalty function method [71], reduced gradient method [66] and sequential quadratic programming [31] are available, they are yet to be applied successfully to energy system sizing problems. This is because the NLP approaches are sensitive to problem size and have difficulties solving large problems to optimality [188]. For this reason, only a few works on energy system sizing have adopted this approach.

Table 2.4 summarizes the key characteristics of the literature reviewed.

Table 2.4.: Summary of sizing studies involving multiple renewable generation options and some form of storage

Ref.	Year	Sized components	Sizing approach	Reliability metric	Reliability evaluation	Accounted for inter-year variability	Cost metric
Tito et al. [218]	2016	PV,WT,Bat	S-M	LPSP	Time series		TSC
Malheiro et al. [146]	2015	PV,WT,Bat	LP	DS	Time series		LCC
Shi et al. [203]	2015	PV,WT,Bat,DG	M-M	LPSP	Time series		ACS
Zhao and Yuan [248]	2015	PV,WT,Bat,DG	M-M	DS	Time series		TAC
Maleki and Pourfayaz [145]	2015	PV,WT,Bat,DG; PV,WT,H_2,DG	S-M	DS	Time series		TAC
Sharafi and ELMekkawy [202]	2014	PV,WT,Bat,H_2,DG	M-M	LLP	Time series		TSC
Zhao et al. [247]	2014	PV,WT,Bat,DG	M-M	REF	Time series		LCC
Abbes et al. [3]	2014	PV,WT,Bat	M-M	LPSP	Time series		LCC
Al-Shamma'a and Addoweesh [8]	2014	PV,WT,Bat,DG	A	LPSP, REF	Time series		LCE
Paliwal et al. [172]	2014	PV,WT,Bat,DG	A	P_H,P_R	Probabilistic	✓	LCE
Maleki and Askarzadeh [144]	2014	PV,WT,Bat; PV,WT,H_2	S-M	DS	Time series		TAC
Belmili et al. [30]	2014	PV,WT,Bat	I	LPSP	Time series		NPC
Kaabeche and Ibtiouen [114]	2014	PV,WT,Bat,DG	I	TED	Time series		NPC, LCE
Mokheimer et al. [157]	2014	PV,WT,Bat	G	LPSP	Time series		LCE
Tegani et al. [211]	2014	PV,WT,Bat	S-M	DS	Time series		TSC

Ref.	Year	Sized components	Sizing approach	Reliability metric	Reliability evaluation	Accounted for inter-year variability	Cost metric
Perera et al. [179]	2013	PV,WT,Bat,DG	M-M	AULF	Time series		CC, LCE
Amer et al. [11]	2013	PV,WT,Bat	S-M	DS	Time series		LCE
Askarzadeh [20]	2013	PV,WT,Bat	S-M	DS	Time series		TAC
Kumar et al. [131]	2013	PV,WT,Bat,DG	S-M		Time series		TSC
Merei et al. [154]	2013	PV,WT,Bat	A	DS	Time series		TSC
Kaplani and Kaplanis [118]	2012	PV,Bat	I	DS, SR	Time series	✓	-
Ould Bilal et al. [170]	2010	PV,WT,Bat	M-M	LPSP	Time series		ACS
Katsigiannis et al. [121]	2010	PV,WT,Bat,G; PV,WT,H_2,G	M-M	AULF	Time series		LCE
Khatod et al. [124]	2010	PV,WT,DG	A	LOLE, LOEE	Probabilistic	✓	AOC
Saif et al. [198]	2010	PV,WT,Bat,DG	LP	EUE	Time series		TSC
Dufo-Lopez et al. [69]	2009	PV,WT,H_2	A	-	Time series		NPC
Yang et al. [242]	2009	PV,WT,Bat	S-M	LPSP	Time series		ACS
Dufo-Lopez and Bernal-Agustin [68]	2008	PV,WT,Bat, H_2,DG	M-M	AULF	Time series		NPC
Yang et al. [241]	2008	PV,WT,Bat	S-M	LPSP	Time series		ACS
Diaf et al. [64]	2008	PV,WT,Bat	I	LPSP	Time series		LCE
Yang et al. [240]	2007	PV,WT,Bat	I	LPSP	Time series		LCE

Ref.	Year	Sized components	Sizing approach	Reliability metric	Reliability evaluation	Accounted for inter-year variability	Cost metric
Koutroulis et al. [129]	2006	PV,WT,Bat	A	DS	Time series		TSC
Prasad and Natarajan [183]	2006	PV,WT,Bat	I	DPSP	Time series		LCE
Xu et al. [237]	2005	PV,WT,Bat	S-M	LPSP	Time series		CC
Yang et al. [243]	2003	PV,WT,Bat	I	LPSP	Time series		-
Karaki et al. [119]	1999	PV,WT	I	EIR	Probabilistic	✓	CC
Markvart [148]	1996	PV,WT	G	DS	-		CC
Borowy and Salameh [36]	1996	PV,Bat	G	LLP	Time series		CC

KEY

- **Sized components**

  PV = Photovoltaics; WT = Wind turbines; Bat = Battery storage; H_2 = Hydrogen storage; DG = Diesel generators.

- **Sizing approach**

  A = Analytical; G = Graphical; I = Iterative; M-M = Multi-objective metaheuristic; S-M = Single objective metaheuristic.

- **Reliability metric**

  AULF = Allowable unmet load fraction; DS = Full demand satisfaction; EIR = Energy Index of Reliability; EUE = Expected unserved energy; LLP = Loss of load probability; LPSP = Loss of power probability; P_R = Percentage of risk state probability; P_H = Percentage of healthy state probability; REF = Renewable energy fraction; TED = Total energy deficit.

- **Cost metric**

  ACS = Annual cost of system; AOC = Annual operating cost; CC = Capital cost; LCE = Levelized cost of energy; LCC = Life cycle cost; NPC = Net present value; TAC = Total annual cost; TSC = Total system cost.

2.3. Summary of Literature Review

Most of the works focused on the sizing of PV-wind-battery and PV-wind-battery-diesel hybrid systems. This makes sense as they were designed for applications with small load demands such as residential applications. A variety of objectives have been considered, with cost, reliability and emissions-related objectives the most prominent. Different time frames of operation have been considered for sizing, from one day per month [36, 198] to hourly profiles for the entire year [144, 146]. The relationships between system reliabilities, system configurations and cost have been investigated [64, 240]. The effect of load demand profiles on optimum sizing has also been considered [170, 218].

Solution methodologies have evolved over the years, starting with the graphical approach in the mid 1990's. Metaheuristic approaches have become the preferred method for systems sizing due to advancements in computing technology and parallelization. The advancements have also allowed for multi-objective design problems to be considered. Some of the recent works have focused on the development of more efficient metaheuristic algorithms for system sizing [131, 203, 248]. Mathematical programming is promising and may be the preferred method in the future because it provides an optimality guarantee. However, only linear programming approaches have been demonstrated so far [146, 198].

While a lot of important work has been done in sizing, there are several areas which are yet to be explored adequately.

Accounting for stochastic nature of renewable resources: One of the major challenges associated with renewable energy use is the variable nature of the resource, with availability changing within and between seasons.

As can be seen from Table 2.4, most of the works use the time series approach for reliability evaluation, meaning that the renewable input profiles for the year were considered to be known with certainty. While this approach accounts for diurnal and seasonal variability, it does not account for climate-based variability (variability in renewable input level between years). The availability of renewables can be markedly different between years, and this can lead to significant deviations from the predicted performance [241]. The design of renewable energy systems without taking into account the stochastic nature of the resource generates systems which, while optimal for the scenario for which they are designed, may perform sub-optimally under other possible input scenarios. In order to account for climate-based variability with the time series method, it must be combined with a stochastic sampling approach such as Monte Carlo simulation [124, 217]. This approach was adopted for PV-battery sizing by Kaplani and Kaplanis [118]. However, the methodology developed by Kaplani and Kaplanis [118] is not applicable to systems integrating wind generation and did not account for the dynamic behaviour of storage systems. While a number of other works considered the sensitivity of model results to the input scenarios [7, 131, 146], they do not account for variability in systems sizing.

Works which adopted the probabilistic approach to reliability evaluation intrinsically accounted for climate-based variability. However, the works by Karaki et al. [119] and

Khatod et al. [124] do not consider optimal storage sizing at all, while the methodology developed by Paliwal et al. [172] is only useful for systems with battery storage and is not applicable to systems incorporating other storage alternatives.

Thus, no generalized methodology has been developed for accounting for climate-based variability in hybrid systems sizing.

Integration of thermal and electrical energy generation technologies: The focus of optimal sizing problems have been on hybrid systems integrating electrical generation options (PVs, wind and biodiesel and diesel). However, very little thought has been given to solar thermal generation as a potential power generation alternative. Solar thermal generation has been shown to be a viable alternative for large scale power generation [99], with several works already suggesting the technology as an alternative to photovoltaics. A cost analysis by Hernandez-Moro and Martinez-Duart [98] revealed that solar thermal technologies were more appropriate than PVs for low latitude locations. Similarly, Peters et al. [180] suggested the exploitation of the location-specific strengths of PV and solar thermal technologies as a way of cost and efficiency improvement. Some countries such as Chile have begun to adopt solar thermal generation as alternatives to photovoltaics [207]. This suggests that solar thermal generation technologies should be considered as alternatives in hybrid systems as they have the potential to provide renewable solutions with better cost and performance metrics than conventional PV-wind systems. However, no work on the sizing of such hybrid systems has been done.

Similarly, all of the works have considered electrical loads only; the sizing of hybrid systems to meet both thermal and electrical demand loads has not been considered.

Choice and integration of storage technologies: With the exception of works by Dufo-Lopez and Bernal-Agustin [68] and Sharafi and ELMekkawy [202] which considered hydrogen storage, all the works on system sizing have focused on battery storage. While they may be suitable for small scale operations, their high initial cost and need for replacement (and frequent maintenance) make battery systems vulnerable and thus unattractive for processes with high energy demands [143]. For large scale operations located in remote regions where land area is not a significant constraint, other technologies typically considered for grid scale storage may be more suitable. While such technologies have been considered for integration with either standalone wind [13, 127, 141] or PV systems [141], little consideration has been given to their integration into hybrid systems.

Also, while the possibility of integrating generation technologies has been considered extensively, the integration of multiple storage technologies has not been suitably explored. Evans et al. [78] suggested that a combination of storage technologies is necessary to ensure maximum power reliability. Other works in literature [110, 140] have also suggested that it may be necessary to incorporate more than one storage type for systems which provide large amounts of energy in order to meet all the technical requirements for power system operations. The integration of multiple storage alternatives promises several advantages, the most important of which are operational flexibility and cost reduction.

However, this has not been explored adequately in previous hybrid systems sizing works.

Accounting for fluctuations in renewables generation: A key feature of renewables generation is the intermittent nature of the power generated. For systems wholly dependent on renewables, the power fluctuations can be a serious issue depending on the response time of the storage type incorporated into the system.

The intermittent nature of the wind resource has been accounted for in planning and sizing of energy systems integrating only wind generation [40, 51, 221]. The works constrain the maximum fraction of the load which can be met directly from wind generation. However, the problem has not been addressed explicitly in the sizing of hybrid energy systems. Almost all the hybrid system works reviewed incorporate battery storage: the instantaneous response times of batteries meant that the problem of power fluctuations did not need to be considered separately during sizing. For most other storage types (such as hydrogen storage) however, this is not the case and the problem of power quality needs to be addressed explicitly during sizing. This has yet to be done. One of the conclusions of the recent review paper by Mahesh and Sandhu [143] was that that more attention needs to be paid to the intermittency issue during design and sizing if the energy share of renewables is to increase.

2.3.1. Key contributions of the thesis

This thesis will extend the state of the art on systems sizing by addressing the shortcomings highlighted in section 2.3.

The design and sizing of a novel hybrid energy system which will integrate thermal and electrical renewable generation options with multiple large scale energy storage options will be considered in this thesis. The hybrid system will be expected to service the thermal and electrical loads of a typical mine.

A sizing methodology which allows for the stochastic nature of renewable resources to be accounted for will be developed. The approach will combine the chronological approach to reliability evaluation with a stochastic simulation model and will be applicable to hybrid systems integrating any type of generation or storage technology. A reliability metric which accounts primarily for inter-year variability will be introduced.

Power quality management strategies which allow for fluctuations in renewables generation to be accounted for during sizing will also be developed. Two approaches will be considered. The approaches will demonstrate alternative methods that may be employed to ensure that unscheduled fluctuations in renewable power generation due to sudden changes in weather do not lead to shortfalls in power supply to the plant. The first approach will be based on including additional constraints which impact on how the system can be operated. The second approach will involve the introduction of a new storage alternative to the handle transitions between power supply modes. The two approaches were considered to demonstrate fundamentally different concepts for handling the intermittency challenge: the first approach demonstrates how intermittency can be mitigated

simply by *controlling system operation*, while the second approach demonstrates how it may be mitigated by *changing system design*.

2.3.2. Thesis structure

The structure of the rest of the thesis will be as follows:

Chapter 3 will focus on the development of the integrated energy system model. An overview of storage technologies, along with the relevant models for the different generation and storage technologies, will be presented. The capabilities of the model will be demonstrated for a simple optimum sizing problem.

Chapter 4 will focus on the development of a methodology for the generation of synthetic renewables scenarios for the stochastic evaluation of reliability. A review of the standard methods for solar radiation and windspeed simulation will be presented. A novel approach to solar radiation modelling will be presented.

A multi-objective sizing methodology for hybrid energy systems incorporating variability in Chapter 6.

Chapter 7 will focus on the development of power quality management strategies to mitigate the effects of the dynamic nature of renewables generation.

Chapter 3.

INTEGRATED ENERGY GENERATION AND STORAGE SYSTEM DESIGN

This chapter focuses on the integrated energy system considered in this work. The first part presents an overview of energy storage in general and a review of the storage alternatives selected for this work. A description of the integrated energy system is then presented, along with details about relevant models for the system components. A description of the cost function is then presented. A simple case study to demonstrate the capabilities of the model concludes the chapter.

Renewable energy sources such as wind and solar are immediate forms of energy which must be used as available. They cannot be stored in their original forms. In order for renewables to be used as primary energy sources for continuous processes, the energy must be converted and stored in a different form to be dispatched when required. Storage options integrated with renewables need to be able to serve three main purposes in order provide smooth and uninterrupted power:

Load shifting: Load shifting involves storing excess power available during off-peak periods for use during peak demand times [78]. This is important for applications in which the load profile varies significantly with time, such as household energy consumption.

Standby reserve: Standby reserves are power sources which can take over from the main power source when it is unavailable or unable to supply sufficient power for long periods of time[244]. This is particularly important given the variable and intermittent nature of the primary energy sources (renewables). Standby reserves need to be able to operate for days without interruption [78].

Power quality management: Renewables generation is susceptible to sudden changes in power output levels. As such, suitable storage options must be able to respond quickly

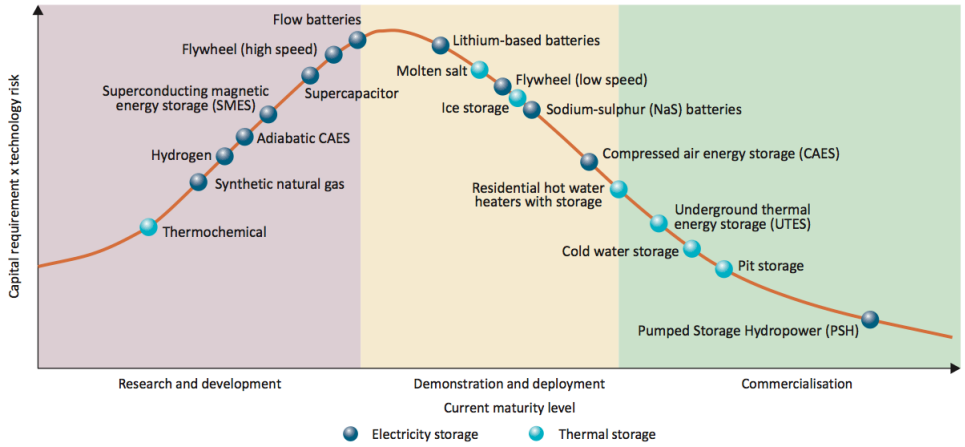

Figure 3.1.: Storage Technologies and their level of development [110]

to such sudden drops or spikes in the supply from the primary energy source. This requires the storage option to have very fast response rates for charging and discharging, typically milliseconds [78, 244].

The focus of this chapter will be on the design of a renewables-based energy system with storage incorporated to address the challenges of load shifting and standby reserve provision. The challenge of power quality management will be addressed later.

3.1. Selection of Storage Alternatives

A wide range of technologies are currently being considered for energy storage. These storage technologies have been reviewed in detail by several authors [49, 107, 108, 140]. Figure 3.1 shows the level of maturity of the most promising storage technologies.

Three of these technologies at different stages of maturity are considered in this work: pumped hydraulic energy storage (PHES), molten salt thermal storage (MTS) and advanced adiabatic compressed air energy storage (AA-CAES). The storage alternatives considered were selected from the large number of alternatives available based on practical considerations such as:

1. Scale of storage and dispatch: Mining operations are energy intensive, with the power requirements of most mines being over 10 MW_e. As such, the energy storage option must be capable of storing and delivering power on the MW scale. The storage option must also have the capability to discharge for long periods (typically hours) at the rated power. Several works suggest that the only electrical storage options currently capable of storing energy and discharging power at such scales are pumped hydro storage, conventional compressed air energy storage (and by extension AA-CAES) and flow batteries [65, 108, 140, 239, 244]. Thermal storage in molten salt has already been demonstrated to be operable at such size and time scales [42, 70, 108].
2. Technology lifespan: The average lifetime of a remote mine typically about 15-20

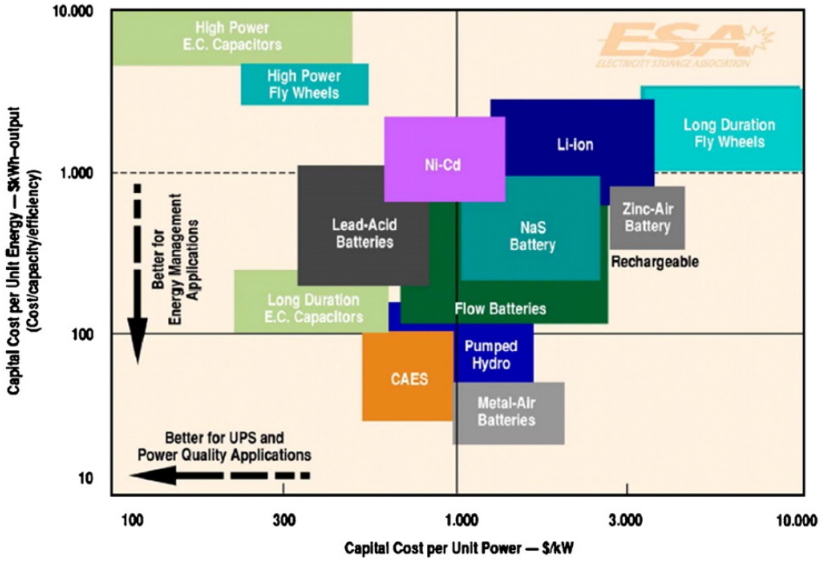

Figure 3.2.: Cost comparison for altervative electrical storage technologies [108]

years [44, 175]. The storage alternatives considered need to be able to operate throughout the lifetime of the mine. Pumped hydro energy storage and CAES systems (both conventional and adiabatic) have the longest lifetimes and are the only electrical storage options with depreciation times well over of 20 years [65, 140]. The design life for solar thermal generation and storage systems is expected to be about 25-30 years [38, 168].

3. Potential for renewables integration: Previous technology assessments of potential storage alternatives for renewable energy [60, 78] have suggested PHES, conventional CAES (and potential variants), and high-temperature thermal energy storage as the technologies with the most potential for integration with renewable generation. Evans et al. [78] suggested PHES and CAES systems as the ideal options for stand-by reserve and thermal energy storage as the ideal option for load shifting.
4. Suitable storage duration: The storage options must be capable of storing energy for durations ranging from minutes to months.
5. Comparatively low capital and operating costs: PHES and CAES systems are two of the cheapest electrical storage technologies per unit of energy (Figure 3.2). The annual operation and maintenance costs of both technologies are also low relative to other storage technologies [140].
6. High cycle efficiency.
7. Ease of operation and process integration.

3.1.1. Advanced adiabatic compressed air energy storage (AA-CAES)

Compressed air energy storage involves use of available or excess electricity in the compression of air. As such, electrical energy is converted to potential energy. In conventional

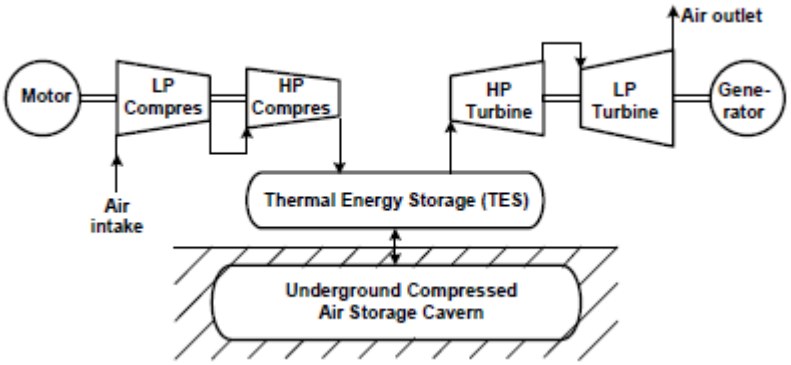

Figure 3.3.: Schematic representation of the AA-CAES system [136]

CAES, the heat generated by the compression process is lost during cooling. As such, conventional CAES is usually combined with fossil fuel combustion. Classical CAES systems, along with pumped hydraulic storage, are the only electricity storage technologies in commercial operation able to provide large-scale deliverability (50 to 300MW) for the use in the whole sale market [136].

AA-CAES involves storage of both thermal and potential energy by incorporation of a thermal store for the heat generated by compression (Figure 3.3). In AA-CAES, the heat generated by the compression process is collected and stored as thermal energy, and is used in reheating of the gas before expansion in the turbines. This increases the storage efficiency of the process. The incorporation of a thermal energy store (TES) also eliminates the use of fossil fuels, making it a standalone environmentally-friendly system. Several thermal storage options have been suggested for incorporation into the AA-CAES system, such as hot water storage [17], concrete thermal storage [208], and oil storage. However, Zunft et al. [249] suggests pre-stressed concrete be the most favourable option based on cost and efficiency. It is generally predicted that adiabatic CAES systems will have efficiencies of around 70% [76, 97, 127, 136], improving on the peak efficiency of 50% obtained for conventional CAES systems [76, 127].

Conventional CAES is considered mature technology. Three conventional CAES plants are currently in commercial operation. Huntorf CAES plant, located in Germany, was commissioned in 1978 and is the world's largest CAES plant rated at 290MW. The plant has a total cavern volume of 310,000m^3 and operates at air pressures between 48 and 70 bar, with 29% storage efficiency [76, 208]. The McIntosh CAES plant, located in Alabama, operates at air pressures between 50 and 78 bar, with 36% storage efficiency and is rated at 110MW. A 2 MW,500 MWh near-isothermal CAES plant started operation in Gaines, Texas in 2012. The deployment of CAES systems has been hindered by its high geographic dependence for storage of the compressed gas (salt caverns). However, previous assessments of energy storage technologies applied to renewables (particularly wind generation) have suggested CAES as the most likely storage technology due to its comparatively lower cost compared to non-PHES technologies (such as batteries) and the higher likelihood of suitable sites compared to PHES [59].

Table 3.1.: Costs and emissions of possible grid/wind/CAES combinations. The case study considered the campus of University of Salerno, Italy, with an average power demand of 1 MW_e [17].

Test Case	Daily cost (€/day)	CO_2 emissions (kg/kWh)
Wind+CAES+Grid power	284	0.054
Wind + Grid power	524	0.087
CAES + Grid power	2224	0.503
Grid power only	2968	0.527

AA-CAES systems however are still under development. The construction of the first commercial scale AA-CAES plant, a 200MW plant with 5 hours of storage, began in 2013 in Sachsen-Anhalt (Germany). The compression mode of the plant will be powered by wind energy [140]. The major challenges of AA-CAES systems are the effectiveness and economics of the heat exchangers associated with the process [65].

Since no plants have been built, the specific costs for installation of AA-CAES systems are uncertain. However, current assessment of the technology estimate capacity-specific and energy-specific costs of €600-1200 per kW and €10-120 per KWh respectively [127, 244]. The costs are expected to be higher than conventional CAES systems (which cost about €500-800 per kW [127]) due to thermal storage.

Previous works involving renewables integration and system sizing Due to the level of development of the technology, most of the modelling work done on AA-CAES systems have focused on efficiency estimation and the determination of the best configuration for the system [76, 92, 97, 125, 208]. While some researchers have highlighted the compatibility of AA-CAES systems with wind generation [65, 208], little modelling work has been done to investigate its performance in stand-alone renewable energy applications. There have however been a few works on the systems design of energy systems incorporating wind generation with conventional CAES.

Arsie et al. [17] investigated the effect of different grid power/wind generation/CAES combinations on the daily operating cost and suggested that the integration of wind generation and a conventional CAES system into the electrical grid reduced the daily operating cost and CO_2 emissions by up to 90% and 89% respectively. The work also highlighted the importance of storage in wind-integrated systems, with the daily operating cost reducing by 50% on CAES integration (Table 3.1).

Denholm and Sioshansi [59] examined the potential cost implications of co-locating wind and CAES systems in energy arbitrage. The work considered two scenarios for the energy system (Figure 3.4). In the first scenario the wind farm and the CAES are located and operated independently of each other, with storage attached to the energy grid. In the second scenario the storage plant is co-located with wind generation, with both operated in concert and co-optimized to maximize the net profits from energy arbitrage. For both cases, the profit from energy arbitrage and the energy transmission costs were evaluated. The results showed that co-locating the wind and storage plants reduced the

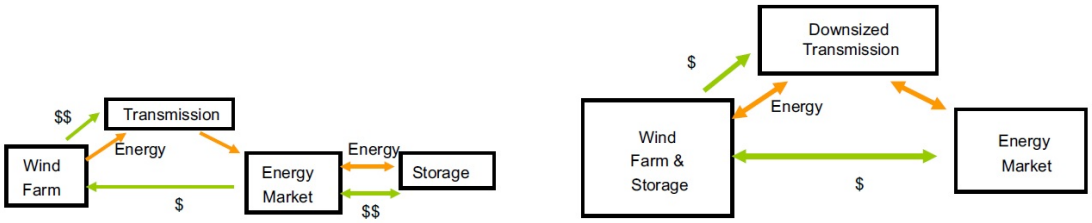

(a) Independent wind and storage (b) Wind and CAES co-located

Figure 3.4.: Alternative wind/CAES configurations for energy arbitrage [59]

plant revenue by up to 18%. However, in most of the cases evaluated, the reduction in transmission costs when the plants were co-located more than made up for the reduced revenue. The results suggested that the optimal size of the storage system be less than 25% of the rated wind farm capacity. The authors also suggested that remotely sited CAES experience fewer constraints and can take advantage of alternatives to natural gas such as coal or biomass for heating during power generation.

Hessami and Bowly [101] compared the economic advantages for integrating large-scale storage with a 195 MW_e wind farm located in Melbourne, Australia. Three energy storage systems compared in the work: pumped hydro energy storage (PHES), compressed air energy storage (CAES), and thermal energy storage in solid media. For each of the scenarios, an optimization problem was solved to determine the storage capacity which maximised the rate of return on capital investment. The results presented suggested CAES to be the most profitable storage option for the wind farm and grid with a rate of return of 15.4%, with the authors suggesting that the choice heavily influenced by the availability of natural underground caverns at the location.

These works found that integrating conventional CAES into renewables-based systems reduced operating and energy transmission costs as well as emissions. Replacing conventional CAES with an adiabatic CAES in such systems would likely increase cost and emissions savings even further since the dependence on gas for reheating the air before expansion will be eliminated [136].

3.1.2. Molten salt thermal storage

In molten salt thermal storage, thermal energy is stored in the form of sensible heat of salts. This storage system consists of two tanks containing molten salts at different temperatures and fill levels. When energy is required, stored heat is transferred to steam which is used to power a turbine for energy generation. Sensible heat storage in salts is attractive because heat transfer occurs by forced convection [132], therefore heat transfer is not a severely limiting factor for the system. This storage method is particularly favoured in solar thermal applications because of the extremely high operating efficiencies, with round-trip efficiencies of greater than 97% recorded [38, 99].

There are two types of molten salt thermal storage: indirect and direct systems (Figure 3.5). In indirect storage (Figure 3.5a), the molten salt is heated and cooled by heat

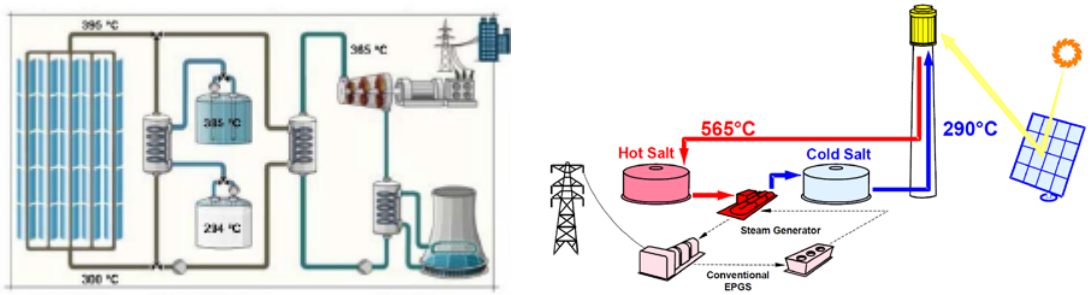

(a) Indirect operation (b) Direct operation

Figure 3.5.: Schematic representations of indirect and direct molten tank storage [26, 42]

exchange with the heat transfer fluid, usually thermal oil or therminol. Thus, the molten salt acts as storage media only. This method has been commercially applied in parabolic trough plants, with numerous plants incorporating this system, particularly in Spain [70, 132, 214]. The maximum temperatures attainable are determined by the thermal properties of the heat transfer fluid. Lower temperatures are usually attained, usually less than 400°C.

In the direct system (Figure 3.5b), the molten salt acts as both the heat transfer and storage fluid. The heated salt is stored in a hot tank, and sensible heat is charged or discharged depending on available solar irradiation and electric power demand. This method allows for much higher temperatures to be reached, with the lower and upper temperature limits defined by the freezing and degradation temperatures of the salt respectively[132, 246]. This method is applicable to central receiver systems/power tower plants, where the temperature difference is about three times that obtained in a parabolic trough system. This reduces the size of the storage system and increases the efficiency of the steam turbine [26]. The direct system is considered emerging technology. Gemasolar power plant in Seville (originally named Solar TRES) was the first solar power plant to demonstrate the active direct storage system commercially in 2011[42, 70]. The hot and cold tanks operate at 565°C and 288°C respectively, and the plant was designed for 15 hours of storage with a capacity of 600MWh. Crescent Dunes solar energy project became the largest commercial power tower plant with storage in 2016, with a net output of 110 MW and 10 hours of storage [163].

Reviews of molten salt thermal storage technology, comparison between direct and indirect storage, and commercial applications of molten tank storage may be found in numerous literature [26, 70, 87, 99, 132, 153, 214].

Previous works involving renewables integration and system sizing Most of the modelling work around molten salt thermal storage have revolved around heat loss evaluation [246], solar-thermal performance and efficiency evaluation[10, 86, 196], and storage sizing [100, 130, 142]. All of these works are based on the simulation of annual system performance with solar thermal generation. Other works which consider tank storage in other media such as thermal oil [4, 182, 206] will not be discussed since the sizing and

storage performance are fundamentally different.

One of the earliest modeling work on indirect storage in molten salts was done by Hermann et al. [100]. The work carried out a feasibility study and economic assessment on using molten salts for heat storage in 50MW parabolic trough plants. The feasibility study found no barrier to the use of thermal salts, while the economy of the process was observed to improve for large storage capacities (greater than 6 hours of storage). A plant with 12 hours of storage was found to reduce the levelized cost of electricity (LEC) by about 10%. The results agreed with those published in a previous work [184], in which a similar cost vs performance trade-off for parabolic trough plants with storage was done. In that work, incorporation of 6 hours of storage was found to increase the annual solar-to-electric efficiency from 12.4% to 13.2%. However, the power block efficiency was found to decrease by about 0.4%. The incorporation of storage increased the capital cost of the process, but also increased the energy production.

In Madaeni et al. [142], a systems model for the economic analysis of thermal energy storage for CSP plants was presented. An MIP model was developed to maximize the revenues of a parabolic trough plant by regulating the distribution of generated thermal energy from the solar plant to the TES store and power block. The solar generation of the plant was supplied as an input from Systems Advisor Model (SAM). The scheme optimized the dispatch of the plant over 48 hours. A fixed heat loss rate and round trip efficiency was used. The results of the model indicated that adding 12 hours of storage to a CSP plant increased the revenue by between 35% and 44%. An overall economic performance assessment indicated that maximum return on investment is observed with TES storage capacities of three to four hours. The results also suggest that the use of molten salt thermal storage gives the system the ability to provide power at a constant rate despite significant disturbances in the amount of solar radiation.

Kueh et al. [130] considered the sizing of MTS storage systems for solar thermal power plants to prevent unscheduled reductions in power output. The model accounted for diurnal, seasonal and weather-based variability by considering ten years of historical time series data for chronological simulation. Six sites in the United States and Australia with good solar resource were considered. For different storage capacities ranging from zero to 350 h, the probability of unscheduled power failure was evaluated. The results showed that massive oversizing of the storage system relative to the capacity required during periods of good solar resource was required to achieve near continuous power supply, with between four and ten days of storage required for the six locations. The required storage capacity for near-continuous output was shown to depend strongly on the efficiency of storage. It was also found that the peak capacity of the generation system had to be an order of magnitude larger than the power block to avoid unscheduled failure. It was concluded that while storage integration provides benefits to solar thermal systems, the benefits provided became negligible for storage capacities beyond 12 hours. Hybridization with other generation and storage technologies was suggested as a cost-effective way to achieve continuous power supply.

The other works involving the modelling of molten salt thermal storage have focused on

simulating the performance of existing plants with the aim of facilitating the prediction of the gross and net electric power generation of plants during design and operation. Garcia et al. [86] attempted to reproduce Andasol 2 power plant, a 50MW_e parabolic trough plant with 7.5 hours of storage situated in Spain. The simulation results agreed closely with the actual data, with a maximum variation of 8% observed for the total daily gross electric energy over 42 days. The work by Amadei et al. [10] investigated the potential for solar thermal generation in China by considering the hypothetical relocation of Gemasolar plant to different Chinese areas suitable for CSP technology.

The works reviewed suggest molten salt thermal storage as a feasible energy storage alternative. An added advantage of the solar-thermal generation route when integrated with tank storage is that the system is capable of handling sudden drops in generation due to factors such as cloud cover [142, 182]. This is because the plant and the storage system are typically both served by the same thermal conversion unit (steam turbine). As a result, the system requires less ancillary support than other renewable generation options such as wind and PV[142].

3.1.3. Pumped hydraulic energy storage

The fundamental principle of pumped hydraulic energy storage (PHES) is to store excess electrical energy in the form of gravitational potential energy. During periods of low demands or excess generation, available electricity is used in pumping water to an upper reservoir, while during times of high demand, water is released from the upper reservoir to power a turbine. Pumped hydraulic storage is considered mature technology with little scope for improvement, and is currently the most used for high-power applications, representing over 99% of installed large scale energy storage [110]. PHES systems have round-trip efficiencies between 65% and 80%, depending on the characteristics of the system [24, 108].

Grid-connected PHES facilities help with the regulation of baseload generation and provide flexibility by acting as arbitrage systems. Pumped hydraulic systems have a response time of seconds when in spinning mode, making them ideal for use as control reserves [127]. The storage capacity is dependent on two factors: the capacity of the upper reservoir and the height difference between the reservoirs. Bath County pumped storage station, located in the United States, is the world's largest battery system with a rated capacity of 3 GW [140]. Charging is done in off-peak periods using power from coal, nuclear and other power plants.

The main shortcoming of this technology is its geographic dependence on sites with suitable elevation differences [49, 55, 108]. This has limited the deployment of this technology in recent years, as many of the suitable sites are thought to have been used. However, work by Connolly et al. [52] suggested that several suitable sites may be available. The work presented a model which determined the possible locations for PHES plants within specified sites, and the model found five potential sites with an estimated total storage capacity of 8634MWh within a region of 800 km^2 in Ireland. Also, recent advancements

Table 3.2.: Operating Strategies for an integrated wind/fossil fuel/PHES system [40, 41]

Strategy	Reservoir Charging		Reservoir Discharging		% Renewables	Unit cost (€/kWh)
	Load	HP Pumps	Load	HP Pumps		
1	PS,FF	WP	PS,FF	WP	66.3	0.0746
2	FF	WP	PS	WP	65.6	0.0750
3	WP,PS,FF	WP	WP,PS,FF	WP	69.2	0.0686
4	WP,FF	WP	WP,PS	WP	68.4	0.0692
5	FF	WP	WP,PS	WP	69.4	0.0708
6	WP,FF	WP	PS	WP	64.2	0.0735

*WP =Wind power; PS = Pumped storage; FF = Conventional fossil fuel

in technology have led to more PHES projects being planned around underground reservoirs such as flooded mine shafts, open and deep mining structures, underground caves and and oceans [181, 244]. One such project is the Mount Hope project in New Jersey which aims to use an inactive mine as the lower reservoir [140].

Projects coupling PHES storage with wind and/or solar power generation are also being developed. One such project is the Ikaria Island power station in Greece which plans to integrate 2.7MW_e windfarm with a PHES facility [140, 181].

The investment cost for PHES systems is highly dependent on the location of the facility, with capacity specific costs of between €470/kW and €2170/kW [244]. Energy costs typically range between €10/kWh and €60/kWh.

Previous works involving renewables integration and system sizing Due to the high level of maturity of this technology, most of the modeling work on PHES systems involve comparison and integration with other energy storage options, regulatory policies, power grid integration and arbitrage revenue optimization [81, 107, 127, 174]. System models involving PHES integration with renewables generation have also been developed by many researchers. A few of the works will be reviewed here.

Bueno and Carta [40] presented a systems model for the integration of wind generation and pumped hydraulic energy storage with conventional fossil fuel generation. Electricity generated from a wind farm was used for operating pumps for the PHES reservoir and/or meeting load demands, with a conventional fossil fuel plant as an alternative when the PHES system was charging. Due to the variable nature of wind energy, a variable to set the maximum wind penetration was incorporated. Several alternative operating strategies for the hydropower/wind/fossil fuel system were considered (Table 3.2). An optimization model determined the optimum strategy and system configuration which minimized cost per unit energy and maximized the use of renewables for each of the alternative strategies. In Bueno and Carta [41], the model was applied to the Island of El-Hierro, with the maximum wind penetration was set at 30%. The results indicated that 69% of the Island's electrical demands could be met by renewable energy when wind energy is allowed to supply both the plant and the PHES system. The model indicated that the best operational strategy would be to run the fossil fuel plant and

Table 3.3.: Economic comparison for alternative energy schemes for a remote island in Hong Kong [141]

Strategy	Energy scheme	LCRES ($/kWh)
1	PV+advanced deep cycle battery	3496
2	PV + conventional battery	4530
3	PV + battery + PHES	1916
4	PV + PHES	1160

PHES system together, with wind energy used to meet a fraction of the load demand at all times (Strategy 3). However, due to the operational complexity of the solution, the authors suggested that the fossil fuel and hydropower plants be alternated (Strategy 4). The results also indicated that renewables could be used exclusively to meet demand for as long as two months.

Work by Connolly et al. [53] investigated the technical and economic implications of integrating wind generation with large scale storage into the Irish energy system. For storage, two configurations of the PHES system (single and double penstock systems) were considered, along with alternative technologies such as domestic heat pumps and district heating with combined heat and power (CHP). The results obtained suggested that the double penstock PHES system enabled up to 60% wind penetration into the Irish energy system. This is a significant improvement on the 30% instantaneous load limit for wind set by Ireland's electricity supply board [230]. The results also suggested that while the alternative technologies offered similar savings to the PHES system, the PHES option improved the security of supply more significantly because of the lower dependence on fuel prices, interest rates and wind power production.

The optimal design and sizing of a standalone renewable energy system integrating pumped hydro storage and battery storage for an isolated island in Hong Kong was investigated by Ma et al. [141]. The work compared four generation/storage configurations (shown in Table 3.3) using the using the life-cycle cost approach. The cost metrics for comparison used in the work were the lifecycle cost (LCC) and the levelized cost for renewable energy storage system (LCRES), which is the ratio of the total capital cost of the energy system to its storage capacity. The results obtained showed that the economic benefit was greatest in the case in which pure PHES storage was integrated. The researchers however suggested that the combination of PHES with battery storage would be the optimal choice if technical factors such as power supply stability, energy conservation and technology implementability were considered along with the cost objective.

Several other works also investigate the possibility of renewables integration with pumped hydro storage. Tuohy and O'Malley [221] investigated the effects of increasing wind energy penetration on power systems when combined with pumped storage and concluded that there was no advantage to storage integration until wind penetrations of greater than 40% was reached on the system examined. Work by Anagnostopoulos and Pa-

pantonis [13] focused on the determination of the optimum pumping configuration for maximizing the annual wind-to-hydraulic efficiency of a grid-integrated wind-PHES hybrid system. In Kaldellis et al. [115], a methodology for the sizing of PHES systems based in the storage of grid-rejected wind energy was presented.

From these works, it can be seen that PHES storage has the potential to play a major role in the integration of renewables generation into both standalone and grid-based energy systems.

3.2. Superstructure Description

Figure 3.6 shows the proposed energy superstructure for the mine given the available renewables generation options and the selected storage alternatives.

Three renewable energy generation alternatives are considered: electricity generation via photovoltaics (PV) and wind turbines (WT), and thermal energy generation from power towers (PT).

Photovoltaics convert solar energy into electricity. The photovoltaic system consists of two components: solar panels, which generate electricity in the form of direct current, and power-point tracking inverter(s) which convert from direct to alternating current. Photovoltaics are stationary and make use of global horizontal irradiance (GHI, $\dot{G}^{tot}$), which is the total irradiance received from the sun by a surface horizontal to the ground.

Wind turbines convert the kinetic energy available in wind into electrical energy.

Power towers (also called the central receiver system) convert solar energy into heat. The system consists of two main components: the heliostats (collectors) and the absorber. The sun-tracking heliostats reflect the direct portion of solar radiation which hits its surface onto the absorber where the concentrated thermal energy is transferred to the operating fluid (molten salt). The hot salt can then used for electricity generation through heating of steam for a turbine. Central receiver technology was selected over parabolic trough technology for thermosolar generation because of the higher temperatures and thermodynamic efficiencies attainable [26, 42]. A review of central receiver technology may be found in Behar et al. [28].

Excess electrical generation is stored in the CAES and/or PHES systems, while excess thermal energy is stored in the MTS system. The storage alternatives are fundamentally different in use and losses. The PHES system generates only electricity and incurs use-dependent losses. The AA-CAES system can supply both heat and electricity but incurs hourly (thermal) losses. Together, the options should be able to cater for the requirements of the process.

The integrated energy system allows for the electrical demands to be met directly from generation or from any of the storage options, while the thermal demands of the plant must be met from either the power tower, AA-CAES or molten salt systems. Both AA-CAES and molten salt systems are capable of supplying mild-temperature heat ($<300^{o}$C) because of the operating temperatures of their thermal storage, with several authors

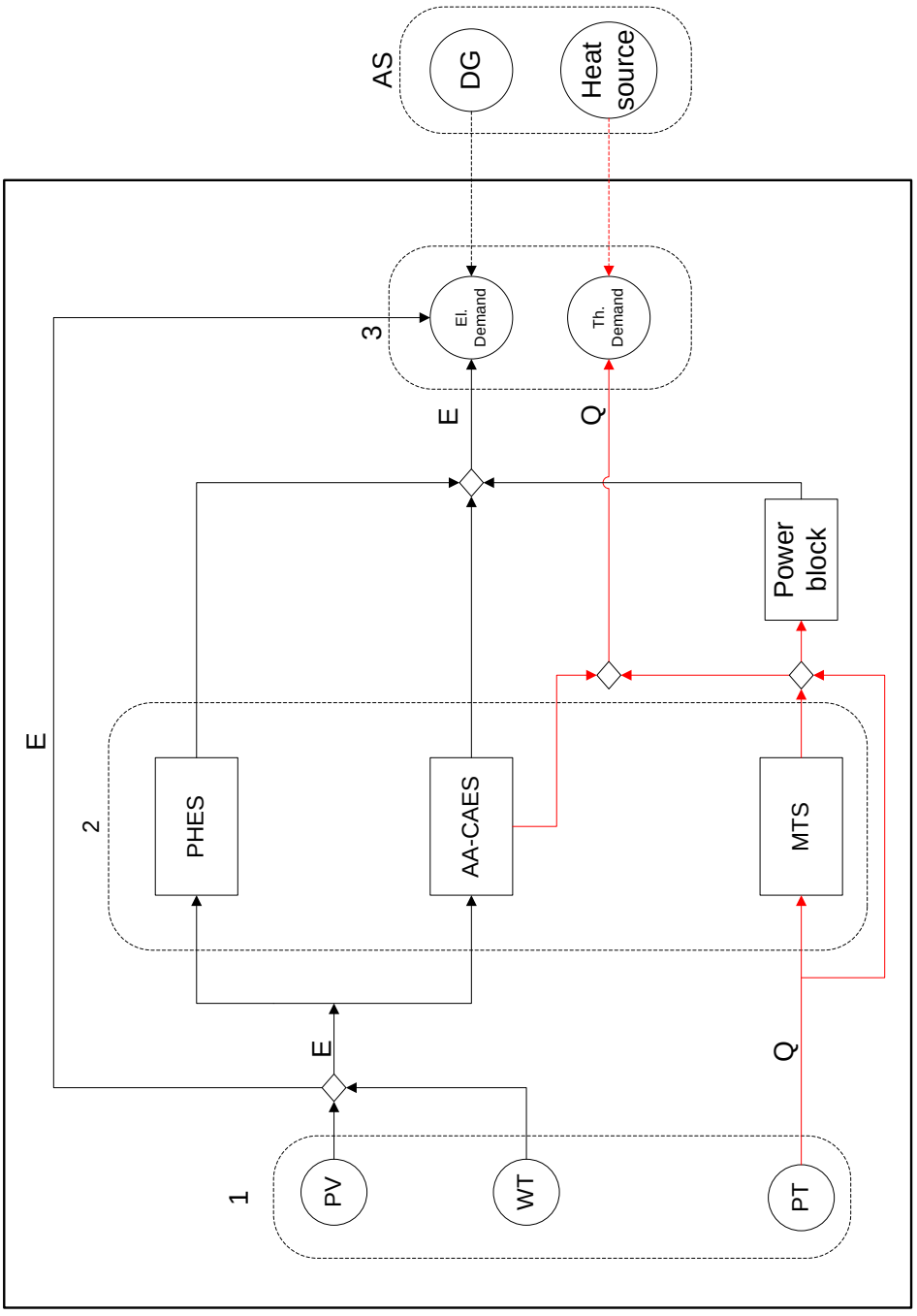

Figure 3.6.: Proposed energy superstructure for the mine. The numbered system boxes (represented with dashed lines) show the three main parts of the primary energy system: renewables generation (1), storage (2), and demand satisfaction (3). Ancilliary support (AS) for power (diesel generators) and heat is available in the event of failure of the primary energy system. The black lines represent electricity (E) while the red lines represent heat (Q).

suggesting that concentrated solar power would be suitable for medium grade heating in mining operations[27, 72]. The heat can be used for applications such as space heating, fluid heating and steam generation, all of which would be useful applications in remote mines and beneficiation plants [72]. Other heat sources would be required for applications requiring higher temperatures.

Ancillary support is available as back-up for the mine when the primary energy system is unable to meet the demands of the mine. This consists of diesel generation for power demands and electrical boilers (and heaters) for thermal demands.

3.3. Energy System Model

The relevant models implemented for the energy system components are presented in this section. Standard models available in literature have been used. Where more than one modelling technique is available for any system component, the alternative modelling approaches are presented and the most suitable approach selected based on the characteristics of the models. Only the core system models and constraints are presented here, with constraints related to specific case studies presented when required.

Dynamic models describe the behaviour and changing states of the energy generation and storage systems. The equations described below are valid over the entire time interval of operation $t \in [0, t_{final}]$. In the equations presented below, C represents the capacities of units, $\dot{E}$, $\dot{Q}$ and $\dot{D}$ represent electricity, heat and demand rates [MW], while S represents stored energy [MWh]. Subscript i refers to energy generation options (PV, WT, PT) and j for the storage options (PHES, AA-CAES, MTS). Superscripts gen, s, in, out, el and th represent generation, storage, input, output, electrical and thermal respectively. Subscript RES refers to the renewable energy system. Other notations used are described when introduced.

3.3.1. Generation models

3.3.1.1. Photovoltaic generation

Two approaches are available in literature for the modelling of photovoltaic cells.

The first approach, called the single diode model or the four-parameter approach, involves solving the I-V characteristic equation for the output current (I) and voltage (V) from the photovoltaic cell. The method is based on the equivalent circuit of a simple solar cell consisting of a current source, a parallel diode and a series resistor [187]. The I-V characteristic equation gives the continuous relationship of current as a function of voltage as [50]:

$$I = I_L - I_0 \left[\exp\left(\frac{q\left(V + IR_s\right)}{\gamma \kappa T_c} \right) - 1 \right] \tag{3.1}$$

where I_L and I_0 are the light current and saturation current, and γ, κ, R_s and T_c are the shape factor, Boltzmann constant, cell series resistance and cell temperature respectively.

For any given PV module, I_0, γ, κ, R_s and T_c are constant, while the light current I_L is dependent on the available solar irradiance. For a given irradiance, the non-linear implicit equation must be solved numerically to obtain the current and voltage which give the maximum output power $\left(\dot{E}_{PV}^{gen} = I \cdot V\right)$ over the entire voltage range [50]. While the model provides detailed information about the performance of the module under any given input condition, the cumbersome and module-dependent nature of the model, combined with the difficulty inherent in solving Equation 3.1 [50], mean that the modelling technique is not often used. More information about the four-parameter approach may be found in literature [50, 74, 187, 224, 245]. This approach was used by Xu et al. [237], Yang et al. [241] and Koutroulis et al. [129] in the optimal sizing of stand-alone hybrid solar-wind systems.

The alternative approach to PV modelling involves the evaluation of the instantaneous generation from the global horizontal irradiance $\dot{G}^{tot}$ [W/m²] and the installed area of photovoltaics A_p [m²]. The rate of energy generation is given by

$$\dot{E}_{PV}^{gen}(t) = \eta_{pv}(t)\eta_{inv}A_p\dot{G}^{tot}(t) \tag{3.2}$$

where η_{inv} is the inverter efficiency. The solar module efficiency η_{pv} is dependent on temperature and solar irradiance and is given by the Evans model [79, 166] as

$$\eta_{pv}(t) = 0.1244\left[1 - 0.0048\left(T_{cell}(t) - 25\right) + 0.12\log\left(\frac{\dot{G}^{tot}(t)}{1000}\right)\right] \tag{3.3}$$

for silicon solar cells. This approach is the most frequently used in energy systems modelling [3, 48, 64, 119, 144, 171] because of its linear nature and the ease of implementation and was therefore used in this work.

Equation 3.2 is based on the assumption that the solar panels are horizontally positioned, an assumption made in this work. When this is not the case, the energy output is based on the global irradiance on the inclined surface $\dot{G}_{\beta}^{tot}$ which is dependent on the GHI and the tilt angle β,

$$\dot{E}_{PV}^{gen}(t) = \eta_{pv}(t)\eta_{inv}A_p\dot{G}_{\beta}^{tot}(t) = \eta_{pv}(t)\eta_{inv}A_p\left[f\left(\beta\right)\cdot\dot{G}^{tot}(t)\right] \tag{3.4}$$

$f\left(\beta\right)$ is dependent on the tilt angle and the reflectance of the ground. Expressions for $f\left(\beta\right)$ may be found in Tina et al. [217] and Al-Rawahi et al. [6]. However, the tilted case is not considered in this work.

The nominal PV generation capacity C_{PV}^{gen} is calculated with Equation (3.2) using a solar irradiance level set at 1 kW/m²(irradiance level under standard test conditions for PV modules).

3.3.1.2. Wind generation

The calculation of the power output of a wind turbine requires two steps: generation of the wind profile at the hub height, and the calculation of wind turbine output.

Windspeed evaluation at hub height The first step in the evaluation of the wind turbine output is to generate the vertical profile of the windspeed at the hub height of the wind turbine. Two mathematical models are available for the adjustment of windspeed for height: the logarithm and the power laws [64, 149]. The logarithmic approach relates the windspeed at the hub height to the measured windspeed as

$$\left(\frac{\nu}{\nu_0}\right) = \frac{\ln\left(H/z\right)}{\ln\left(H_0/z\right)} \tag{3.5}$$

where ν and ν_0 are the windspeeds at heights H and H_0 respectively, and z is the roughness length.

The power law approach relates the windspeed at the hub height to the measured windspeed with a friction coefficient ξ,

$$\left(\frac{\nu}{\nu_0}\right) = \left(\frac{H}{H_0}\right)^{\xi} \tag{3.6}$$

A rough value of $\xi = 1/7$ is typically used for open terrain and well exposed sites [122, 149].

Both approaches have been used energy systems sizing, with the work by Dufo-Lopez and Bernal-Agustin [68] using the logarithmic approach and works by Diaf et al. [64] and Yang et al. [241] using the power law approach. However, the power law approach is the most widely used by researchers [64] was therefore used in this work.

Wind turbine power output Based on the adjusted windspeed calculated above, the power output of the wind generator can be calculated. Two approaches have been used in literature for the calculation of wind turbine output power.

The first approach, which is based on the kinetic energy equation $\left(K.E = \frac{1}{2}m\nu^2\right)$, models the power available in the wind and gives the electrical power output of a wind generator as a non-linear function of the windspeed [3, 149]:

$$\dot{E}^{gen}_{wind}(t) = \frac{1}{2}\eta_{wt}\rho A_{wt}\nu(t)^3 \tag{3.7}$$

where ρ is the air density, η_{wt} is the efficiency of the wind turbine (typically about 30% [3]) and A_{wt} is the total swept area of the turbine. Equation 3.7 may be obtained analytically from the kinetic energy equation by using the density-mass-volume relationship.

The second approach, which has been used in this work, involves the division of the windspeed regime based on the conceptual power curves of wind turbines. Typically, the power curve is subdivided four operating regimes. The power output in each region

linearly related to the rated power of the individual turbines P_R:

$$\dot{E}^{gen}_{wind}(t) = N_T \cdot \begin{cases} 0 & \text{for } \nu(t) < \nu_{c,in} \\ P_R \left(\frac{\nu(t) - \nu_{c,in}}{\nu_r - \nu_{c,in}} \right) & \text{for } \nu_{c,in} \leq \nu(t) \leq \nu_r \\ P_R & \text{for } \nu_r \leq \nu(t) \leq \nu_{c,out} \\ 0 & \text{for } \nu(t) > \nu_{c,out} \end{cases} \tag{3.8}$$

where N_T is the number of turbines, $\nu_{c,in}$ is the cut-in speed (the minimum speed at which the turbine can operate, $\nu_{c,out}$ is the cut-out speed (the maximum speed beyond which the turbine must be shut down for safety), and ν_r is the rated windspeed (the minimum windspeed at which the rated power can be generated). With this model, the power output of the turbines can be modelled if the cut-in speed, cut-out speed, rated speed and rated power are known [64]. This simplified approach has been shown to be more accurate [179] and is more frequently used in hybrid energy systems design [64, 119, 144, 217], although the first approach has also been used [3, 17].

The nominal capacity of installed wind is the product of the number of turbines and the rated power,

$$C^{gen}_{wind} = N_T \cdot P_R \tag{3.9}$$

3.3.1.3. Solar thermal (Power tower) generation

Modelling the power output of the power tower requires an energy balance which takes into account the optical losses from the collector during reflection (the heliostats) and the thermal losses from the absorber. Power towers generate heat from the direct portion of solar radiation which hits the heliostat surface, called direct normal irradiance (DNI, $\dot{G}^{DNI}$ [W/m^2]). Li et al. [137] and Ho and Iverson [104] give the thermal output of a power tower of collector area A_c as

$$\dot{Q}^{gen}_{PT} = \alpha \eta_{hel} A_c \dot{G}^{DNI} - \left(\dot{Q}^{conv} + \dot{Q}^{rad} \right) \tag{3.10}$$

where $\dot{Q}^{conv}$ and $\dot{Q}^{rad}$ are the rates of heat losses from the receiver via convection and radiation [MW] respectively; α the absorptivity; and η^{hel} the efficiency of the heliostat reflectors. The convective and radiative losses are given by Newton's law and the Stefan-Boltzmann equation respectively. The first term represents the energy output from the receiver and accounts for the optical losses from the system.

The minimum threshold value for the solar irradiance is the irradiance value $\dot{G}^{DNI}_{min}$ below which it is not viable to operate the power tower system [130]. The value is typically calculated as the point where the net heat output $\dot{Q}^{gen}_{PT} \geq 0$. Substituting into Equation 3.10 and rearranging gives

$$\alpha \eta_{hel} A_c \dot{G}^{DNI}_{min} \geq \dot{Q}^{conv} + \dot{Q}^{rad} \tag{3.11}$$

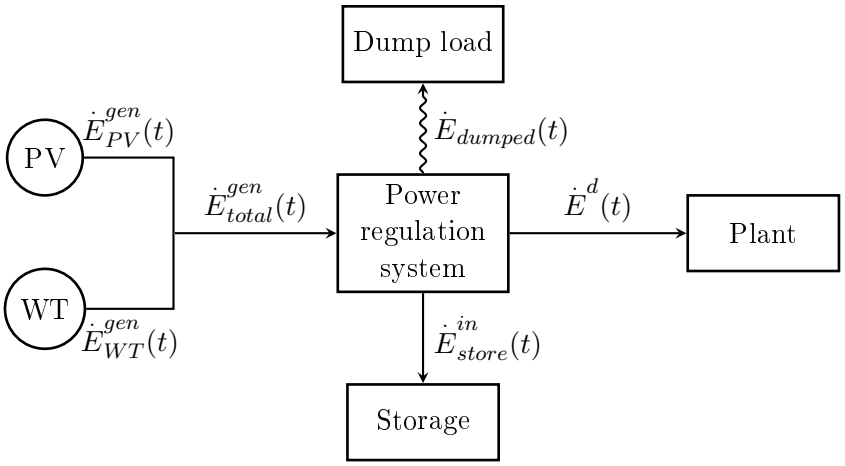

Figure 3.7.: Schematic model of electric power control system. Excess generation is diverted to a dump load.

With $\dot{Q}^{conv} + \dot{Q}^{rad} \approx \dot{Q}^{rad}$ because $\dot{Q}^{conv} \ll \dot{Q}^{rad}$, substituting the Stefan-Boltzmann equation into Equation 3.11 and rearranging the expression gives the minimum threshold solar irradiance as

$$\dot{G}^{DNI}_{min} \geq \frac{\sigma \varepsilon A_r T_r^4}{\alpha \eta_{hel} A_c} = \frac{\sigma \varepsilon T_r^4}{\alpha \eta_{hel} \tilde{C}} \tag{3.12}$$

where σ is the Stefan-Boltzmann constant $\left[5.67 \times 10^{-8}\,\mathrm{W/m^2K^4}\right]$, ε is the emissivity of the absorber, T_r is the absorber operating temperature in K, and $\tilde{C}$ is the concentration ratio and refers to the ratio of the collector to the absorber (A_c/A_r). For any power tower system, the emissivity, receiver temperature and concentration are constant [130]. Hence, the minimum threshold for solar irradiance is constant for any given system.

Combining Eqs. (3.10) and (3.12) gives the instantaneous thermal output for the power tower system when operated at full capacity as:

$$\dot{Q}^{gen}_{PT}(t) = \begin{cases} 0 & \text{for } \dot{G}^{DNI}(t) \leq \dot{G}^{DNI}_{min} \\ \alpha \eta_{hel} A_c \dot{G}^{DNI}(t) - \left(\dot{Q}^{conv}(t) + \dot{Q}^{rad}(t) \right) & \text{for } \dot{G}^{DNI}(t) > \dot{G}^{DNI}_{min} \end{cases} \tag{3.13}$$

The nominal power tower capacity C^{gen}_{PT} is calculated using the first term of Equation (3.10) using a design irradiance of $0.95\,\mathrm{kW/m^2}$ [161].

3.3.1.4. Energy balances for generation units

The total electrical output of the energy system is the sum of the wind and PV generation,

$$\dot{E}^{gen}_{total}(t) = \dot{E}^{gen}_{PV}(t) + \dot{E}^{gen}_{wind}(t) \tag{3.14}$$

Figure 3.7 shows a schematic model of the electric power control system. Often in power systems, generation exceeds the amount of energy that can be used and stored. The

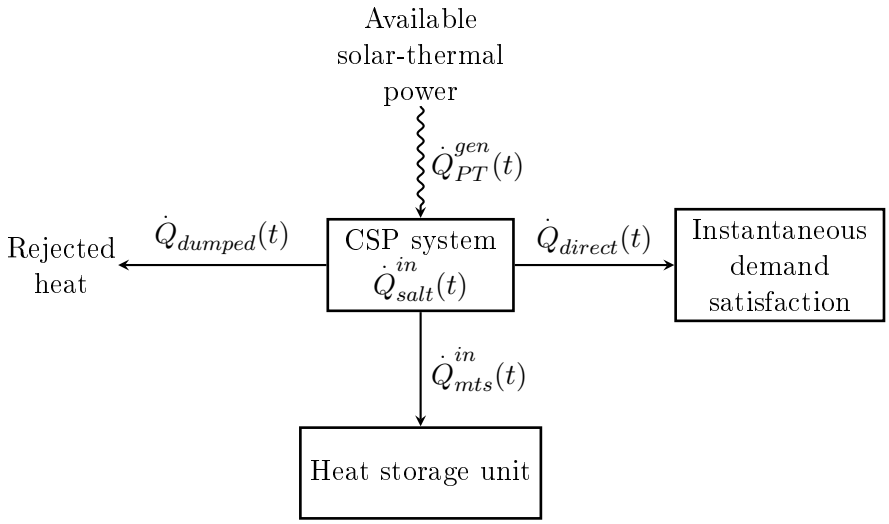

Figure 3.8.: Schematic model of power tower control system. Excess thermal energy is not collected by the CSP system. Adapted from Adinberg [4].

excess energy must therefore be dissipated (rejected) in some way. This process is called *energy dumping*. For PV and wind generation systems, dumping is achieved using a load diverting regulator which diverts the excess electricity to an alternate (dump) load such as a water heater [200, 220].

The energy into the system can either be used to satisfy immediate demand, sent to storage or rejected to the dump load. Thus,

$$\dot{E}_{total}^{gen}(t) = \dot{E}^{d}(t) + \dot{E}_{store}^{in}(t) + \dot{E}_{dumped}(t) \tag{3.15}$$

where $\dot{E}^{d}(t)$ is the electricity sent directly to the plant to satisfy immediate power needs, $\dot{E}_{store}^{in}(t)$ is the energy sent to the storage systems and $\dot{E}_{dumped}(t)$ is the rejected energy. For concentrated solar power (CSP) technologies, energy dumping occurs when the heat storage capacity is reached [130] and is achieved by defocusing the collectors (heliostats), thereby reducing the amount of energy that reaches the power tower [228]. Thus, the actual energy transferred to the salt $\dot{Q}_{salt}^{in}(t)$ may be less than the potential output from the power tower $\dot{Q}_{PT}^{gen}(t)$. Figure 3.8 shows the schematic model of the CSP control system. An energy balance around the system gives

$$\dot{Q}_{PT}^{gen}(t) - \dot{Q}_{dumped}(t) = \dot{Q}_{salt}^{in}(t) = \dot{Q}_{direct}(t) + \dot{Q}_{mts}^{in}(t) \tag{3.16}$$

3.3.2. Storage models

Since the MTS does not store electrical energy, all the excess electrical generation is split between the PHES and AA-CAES systems. Mathematically,

$$\dot{E}_{store}^{in}(t) = \dot{E}_{PHES}^{in}(t) + \dot{E}_{AA-CAES}^{in}(t) \tag{3.17}$$

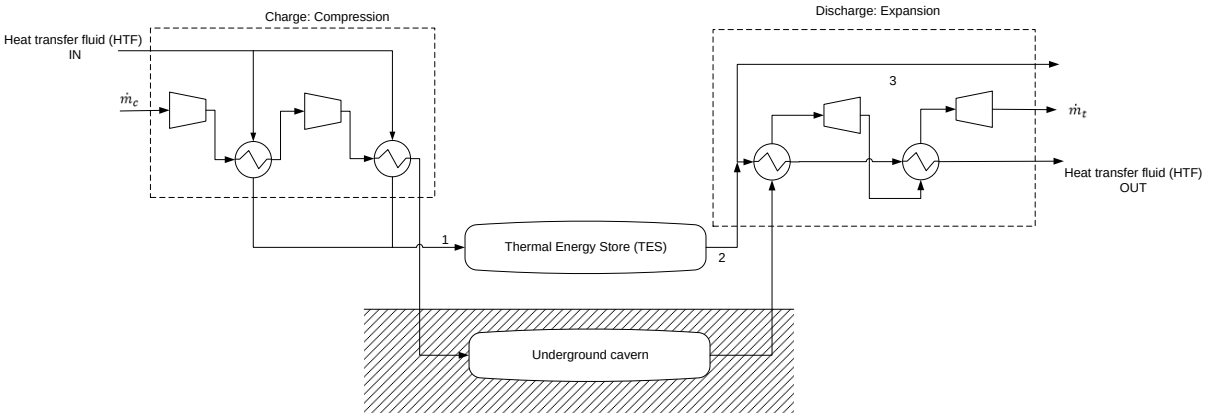

Figure 3.9.: Schematic diagram of the modelled AA-CAES system showing the charging and discharging phases. Streams 1 and 2 are material streams which carry heat into and out of the heat store. Stream 3 supplies thermal energy to the plant

3.3.2.1. Advanced adiabatic CAES (AA-CAES)

A schematic of the AA-CAES system is shown in Figure 3.9. The system consists of two polytropic compression and expansion stages. When in charging mode, excess electricity is used to power the two compressors with heat removed after each stage. During discharge, pre-heated high pressure air is expanded to generate power. Constant-pressure air storage is adopted [125]. Thermal energy for process heating can be withdrawn from the thermal energy store. Thermal energy storage in solid media has been suggested as the most technologically favourable option for integration into AA-CAES systems [249], and thus was used in this work.

The specific work $\dot{W}$ done on (or by) a gas during adiabatic compression (or expansion) from an inlet pressure p_{in} to an outlet pressure p_{out} is given by [136, 204]

$$\dot{W} = \frac{n}{n-1} R_A T_{in} \left(\left[\frac{p_{out}}{p_{in}} \right]^{\frac{n-1}{n}} - 1 \right) \tag{3.18}$$

where T_{in} is the inlet temperature into the compressor (or expander), n is the polytropic exponent and R_A is the specific gas constant (287 J·kg^{-1}·K^{-1} for air). Accounting for efficiency losses in the motor and compressors, introducing the polytropic law ($pv^n = c$), and accounting for the number of compression stages N_c [92, 97] gives rate of energy input for compression the charging process as:

$$\eta^{comp}\eta^{motor}\dot{E}^{in}_{AA-CAES}(t) = \frac{n}{n-1}\dot{m}_c(t) \cdot R_A \sum_{c=1}^{N_c} \Delta T^c \tag{3.19}$$

where $\dot{m}_c$ [kg·s^{-1}] is the air flowrate into the compressor c during charging, $\triangle T^c$ is the temperature difference between the compressor's inlet and outlet [K], η^{comp} is the compressor efficiency, and η^{motor} the motor efficiency.

Grazzini and Milazzo [92] and Hartmann et al. [97] give the relationship between the

polytropic exponent and the mechanical efficiencies of turbines and compressors as

$$\eta^{comp} = \frac{n}{n-1} \cdot \frac{\gamma - 1}{\gamma} = \frac{1}{\eta^{turbine}} \tag{3.20}$$

where γ is the specific heat ratio.

A similar expression to Equation 3.19 may be written for the electrical output from the turbines during discharge, taking into account the generator and turbine losses:

$$\frac{1}{\eta^{gen}\eta^{turbine}} \dot{E}^{out}_{AA-CAES}(t) = \frac{n}{n-1} \dot{m}_t(t) \cdot R_A \sum_{t=1}^{N_t} \Delta T^{turbine} \tag{3.21}$$

where $\dot{m}_t(t)$ is the air flowrate into the turbine $[kg \cdot s^{-1}]$, $\eta^{turbine}$ is the turbine efficiency, η^{gen} the generator efficiency and $\Delta T^{turbine}$ is the difference in inlet and outlet operating temperatures of the turbines [K].

Compressed air is added to the cavern during charging (storage) and removed during discharge (generation). The difference in the instantaneous flowrates of air in and out of cavern gives the rate of change of pressurized air within the cavern. For a stored mass of air $m^s_{AA-CAES}(t)$ [kg]:

$$\frac{\mathrm{d}}{\mathrm{d}t} m^s_{AA-CAES}(t) = \dot{m}_c(t) - \dot{m}_t(t) \tag{3.22}$$

The thermal energy store is charged with heat absorbed from compressed air during the charging phase. Energy removed from the TES via the heat transfer fluid can be used for two purposes: to re-heat the compressed gas for power generation or to supply process heat to the plant. An energy balance around the thermal energy store (TES) gives an expression for the temperature of the TES, $T^{TES}(t)$, as a function of the heat flow rates in, $\dot{Q}^{TES,in}(t)$, and out, $\dot{Q}^{TES,out}(t)$:

$$\rho c_p V_{TES} \frac{\mathrm{d}}{\mathrm{d}t} T^{TES}(t) = \left[\dot{Q}^{TES,in}(t) - \dot{Q}^{TES,out}(t) - \dot{Q}^{TES,loss}(t) \right] \tag{3.23}$$

The third term on the right hand side accounts for thermal losses from the heat store via convection and radiation [208]. The temperature of the TES is limited by the maximum operating temperature of the storage media:

$$T^{TES}(t) \leq T^{TES}_{max} \tag{3.24}$$

The energy accumulated within the system is calculated based on the mass holdup in the cavern and the operating conditions of the turbines,

$$\frac{\mathrm{d}}{\mathrm{d}t} S_{AA-CAES}(t) = \frac{n}{n-1} R_A \sum_{N_t} \triangle T^{turbine} \cdot \frac{\mathrm{d}}{\mathrm{d}t} m^s_{AA-CAES}(t) \tag{3.25}$$

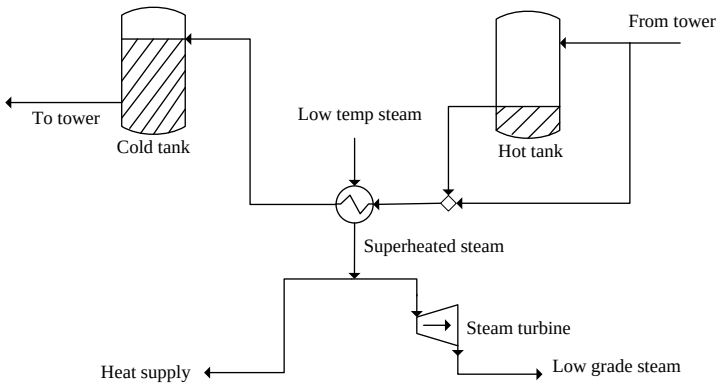

Figure 3.10.: Schematic representation of molten salt storage system

3.3.2.2. Molten salt thermal storage (MTS)

Figure 3.10 shows a schematic of the MTS system, with the molten salts acting as both the heat transfer fluid for the power tower and the heat storage medium. Salt from the cold tank is heated up solar energy collected by the power tower. Electrical and thermal demands of the plant may be met directly with heat from the generation plant or indirectly with heat from storage. The hot salt is heat exchanged with steam from which electricity may be generated to meet the electrical demands of the plant. This work considers two cylindrical tanks fitted with electric heaters and maintained at fixed storage temperatures as described in Bradshaw et al. [38] and Medrano et al. [153]. The hot and cold tanks are maintained at the outlet and inlet temperatures of the power tower absorber respectively [153, 246], both of which are dependent on the solidification and decomposition temperatures of the molten salt [246]. This is because the absorber temperature in a power tower system is always higher than the temperature of the heat transfer fluid [236]. The salt solidification temperature was also set as the reference temperature for the system. The methodology followed in this work for the modeling of the storage tanks is the same as those used in literature [86, 100, 182, 246].

The rate of change of salt mass within storage tank k is given by

$$\frac{\mathrm{d}}{\mathrm{d}t} m^{s}_{k,MTS}(t) = \dot{m}^{in}_{k,MTS}(t) - \dot{m}^{out}_{k,MTS}(t) \qquad k = \{CT, HT\} \tag{3.26}$$

where $\dot{m}^{in}_{k,MTS}(t)$ and $\dot{m}^{out}_{k,MTS}(t)$ are the flowrates of mass into and out of the storage tanks respectively. For the cold tank, mass flows out of the system to the tower for thermal energy collection while the inflow is from cooled salt exiting the heat exchanger. For the hot tank, mass is added from the power tower when excess thermal energy is generated and removed for demand satisfaction when generation is insufficient.

The rate of change of energy in the storage tanks $Q^{acc}_{k}(t)$ is given by

$$\frac{\mathrm{d}}{\mathrm{d}t} Q^{acc}_{k}(t) = \dot{Q}^{in}_{k}(t) - \dot{Q}^{out}_{k}(t) - \dot{Q}^{loss}_{k}(t) + \dot{E}^{h}_{k}(t) \qquad k = \{CT, HT\} \tag{3.27}$$

where $\dot{Q}^{in}_{k}(t)$, $Q^{out}_{k}(t)$, $\dot{Q}^{loss}_{k}(t)$ and $\dot{E}^{h}_{k}(t)$ refer to rates of thermal energy addition [W],

thermal energy removal [W], heat loss from the tank [W] and heat addition to tank via the heater [W] respectively. The electrical heating of the tank $\dot{E}_k^h(t)$ is required to maintain the tank temperature above the solidification temperature of the salt. This is key, especially if the system is to be used intermittently. The electrical heating requirement for the tanks will form a part of the total electrical demand and will need to be supplied from the electrical output of the renewable energy system.

Since only energy in the hot tank may supply the plant, the rate of change of stored thermal energy is the same as the rate of energy accumulation in the hot tank,

$$\frac{\mathrm{d}}{\mathrm{d}t}S_{MTS}(t) = \frac{\mathrm{d}}{\mathrm{d}t}Q_{HT}^{acc}(t) \tag{3.28}$$

Storage tank losses A thorough literature search revealed no appropriate expression for the evaluation of storage tank losses at the high operating temperatures attained by the power tower system. The work by Herrmann et al. [100] reports a heat loss expression for low temperature storage with molten salts, while Madaeni et al. [142] assumed a constant hourly heat loss rate of 0.015%. While the work by Zaversky et al. [246] gives insight into the most important factors to consider in estimating thermal losses from storage tanks, it develops no expression for heat loss evaluation. Rovira et al. [196] developed an empirical correlation for heat loss from storage tanks dependent on the salt level in the tank and the characteristic diameter of the storage tank. However, the correlation is only applicable to storage tanks with exactly the same geometric dimensionality, operating temperatures and thermal insulation [246]. The applicability of the correlation is also limited by its dependence on experimental information about the maximum and minimum heat loss rates. As such, a heat loss model for high temperature storage in molten salts had to developed in this work.

The heat loss from the tank has been shown to be dependent on the exposed surface area, the tank-to-ambient temperature difference and the fill level of the tank [196]. A nonlinear empirical heat loss expression incorporating both the temperature difference between the salt in the tank and ambient air (ΔT_k) and the salt fill level of the tank (χ_k) has been modelled as:

$$\dot{Q}_k^{loss}(t) = U_k^{loss} A_{tank} \Delta T_k \cdot \chi_k(t)^p \tag{3.29}$$

where U_k^{loss} and A_{tank} are the overall heat loss coefficient [$\mathrm{Wm^{-2}K^{-1}}$] and area of the storage tank [$\mathrm{m^2}$] respectively. The value of the exponential term (p) was calculated from recorded plant data for the Andasol-1 plant [189], with the exponent obtained as 0.3 when data from both the hot and cold tanks were used. This indicated that the exponent was independent of temperature. The overall heat loss coefficient for each of the tanks was then estimated using Equation 3.29 based on data recorded at the Solar-Two test project [38], a pilot power tower plant with molten salt tank storage. This yielded the overall heat loss coefficients as 0.335 $\mathrm{Wm^{-2}K^{-1}}$ and 0.364 $\mathrm{Wm^{-2}K^{-1}}$ for the cold and hot tanks respectively.

Further details about the development of the heat loss expressions may be found in Appendix A.

Power block efficiency The power block comprises of a conventional steam turbine and generator system operating a superheated rankine cycle [132]. The thermal power input into the power block $\dot{Q}_{MTS}^{power}(t)$ is given by the total heat from generation and storage less the energy removed for thermal demand satisfaction $\dot{Q}_{MTS}^{heating}(t)$,

$$\dot{Q}_{MTS}^{power}(t) = \dot{Q}_{direct}(t) + \dot{Q}_{HT,MTS}^{out}(t) - \dot{Q}_{MTS}^{heating}(t) \tag{3.30}$$

From this, the electrical output of the power block is given by

$$\dot{E}_{MTS}^{out}(t) = \eta^{pb} \cdot \dot{Q}_{MTS}^{power}(t) \tag{3.31}$$

where η^{pb} is the efficiency of the power block.

Most modelling works in literature [10, 130, 161] assume a constant power block efficiency with the values used ranging between $\eta^{st} = 0.33 - 0.425$. However, tests by Bradshaw et al. [38] suggest that the power block efficiency is heavily dependent on the input thermal power. Garcia et al. [86] gives an expression for estimating the theoretical heat-to-electricity efficiency based on the heat delivered to the power block Q as:

$$\eta^{pb} = A_1 + A_2 \exp\left(\frac{-Q}{A_3}\right) \tag{3.32}$$

where A_1, A_2 and A_3 are parameters. The exponential term is dependent on the input thermal power and actual turbine capacity and determines the efficiency of the turbine. Based on data fitting for the 50 MW_e turbine in use at Andasol 2 solar thermal plant in Spain, the parameters were obtained as $A_1 = 0.397$, $A_2 = 0.243$ and $A_3 = 28.23$ MW_t.

A similar expression is required for this work. However, Equation 3.32 cannot be used directly here because the expression is only valid for fixed steam turbine size ($50MW_e$). In order to be able to use the expression in this work, A_3 needs to be modelled as a function of the turbine thermal capacity at full power. Since the relationship between the thermal power input and A_3 is linear, A_3 was assumed to scale linearly the capacity of the turbine, that is

$$\left(\frac{A_3}{C_{MTS}^{out}}\right)_1 = \left(\frac{A_3}{C_{MTS}^{out}}\right)_2 \tag{3.33}$$

where subscript 1 refers to the values presented in Garcia et al. [86]. Combining Equations 3.32 and 3.33 and gives the efficiency for the power block as

$$\eta^{pb}(t) = A_1 + A_2 \exp\left(\frac{-\dot{Q}_{MTS}^{power}(t)}{0.5646 \cdot C_{MTS}^{out}}\right) \tag{3.34}$$

Equation 3.34 expresses the efficiency in terms of the peak electrical capacity of the turbine rather than in terms of a constant value (A_3) as is the case in Equation 3.32. The

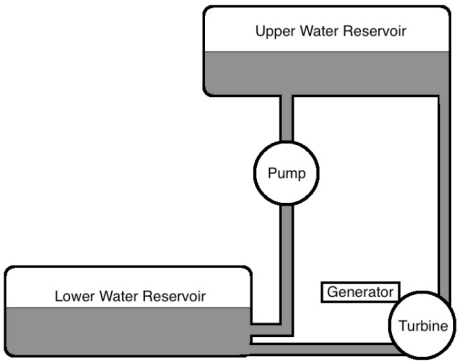

Figure 3.11.: Schematic representation of a double penstock PHES system. The system has two penstocks (separate pump and turbine) to ensure that charging and discharging can occur simultaneously. Source: Blonbou et al. [33]

expression can therefore be used for the evaluation of the efficiencies of steam turbines of various sizes.

3.3.2.3. Pumped hydro storage (PHES)

Figure 3.11 shows the schematic of a typical PHES system. The system was modelled as consisting of three major units: the pumping unit (pumps), the generating unit (water turbines), and the storage unit (water reservoirs). The driving force for PHES is the height difference between the upper and lower reservoir. The double penstock system was selected to allow for simultaneous pumping and discharge, as well as operational flexibility [53]. For a reservoir height difference z, the energy rate to the store during the charging phase $\left(\dot{E}^{in}_{PHES}(t)\right)$ and water flowrate $\dot{m}^{in}_{PHES}(t)\left[kg \cdot s^{-1}\right]$ pumped to the upper reservoir are related by the expression [52, 141]

$$\eta_{pump}\dot{E}^{in}_{PHES}(t) = gz \cdot \dot{m}^{in}_{PHES}(t) \tag{3.35}$$

where η^{pump} is the pump efficiency.

There is a similar expression for the electrical output of the turbine during discharge, taking into account the turbine losses η^{tur}:

$$\dot{E}^{out}_{PHES}(t) = \eta^{tur} gz \cdot \dot{m}^{out}_{PHES}(t) \tag{3.36}$$

The difference in the instantaneous flowrates of water into and out of around the upper water reservoir gives the rate of change of water accumulated in the reservoir:

$$\frac{\mathrm{d}}{\mathrm{d}t} m^{s}_{PHES}(t) = \dot{m}^{in}_{PHES}(t) - \dot{m}^{out}_{PHES}(t) \tag{3.37}$$

The rate of change of the energy stored in the PHES system is then

$$\frac{\mathrm{d}}{\mathrm{d}t} S_{PHES}(t) = gz \frac{\mathrm{d}}{\mathrm{d}t} m^{s}_{PHES}(t) \tag{3.38}$$

3.3.3. Capacity constraints

For each storage option, the energy accumulated at any point during operation is limited by the installed storage capacity,

$$S_j(t) \leq C_j^s \qquad \forall j \tag{3.39}$$

Similarly, the instantaneous electrical output from any storage option cannot exceed the nominal output capacity of the installed generation unit:

$$\dot{E}_j^{out}(t) \leq C_j^{out} \qquad \forall j \tag{3.40}$$

3.3.4. Renewable energy system output

The gross electricity output of the renewable energy system comprises of the power supplied directly from generation and the power output from the storage options:

$$\dot{E}^{RES}(t) = \dot{E}^{d}(t) + \sum_{j=1}^{3} \dot{E}_j^{out}(t) \tag{3.41}$$

It should be noted that the actual (net) electrical power available for supply to the plant may be slightly lower due to parasitic losses in the form of electrical heating requirements for the molten salt storage tanks.

Similarly, the total heat supplied from the energy system to satisfy thermal demands is

$$\dot{Q}^{RES}(t) = \dot{Q}_{AA-CAES}^{heating}(t) + \dot{Q}_{MTS}^{heating}(t) \tag{3.42}$$

Under ideal conditions, the net heat and electrical outputs of the renewable energy system satisfy the electrical demand $\dot{D}^{el}(t)$ and thermal demand $\dot{D}^{th}(t)$ of the mine. Primary energy system failure occurs when the net generation from the plant is insufficient to meet the demands of the mine. When this occurs, ancilliary support is used to meet the shortfall to ensure that the operation suffers no downtime due to power failure.

3.4. Energy System Cost

Several cost metrics have been used for renewables-based energy systems in literature, including the net present cost [68], the annualized system cost [241] and levelized cost of energy [7, 141]. A review of the costing approaches may be found in Chauhan and Saini [48].

Dufo-Lopez and Bernal-Agustin [68] classify the factors which must be considered in the costing of renewable energy systems into four categories:

1. The initial (investment) cost for the components (CC),
2. The cost of fuel consumed throughout the lifetime of the energy system (FC),

3. The operating and maintenance costs of the components over the system lifetime ($C_{O\&M}$), and
4. The cost of replacement of the system components (C_{Rep}).

The total energy system cost (TC) is given by:

$$TC = CC + FC + C_{O\&M} + C_{rep} \tag{3.43}$$

The system components of the primary energy system are the renewable generation and energy storage technologies. Photovoltaic arrays and wind turbines have lifetimes of 20 to 25 years [7, 241], while the lifetime of the power tower is expected to be between 20 and 30 years [103]. The storage technologies considered all have operating lifetimes of over 20 years [65, 140, 168]. Given that the average lifespan of a remote mine has been reported in literature to be about 15-20 years [44, 175], none of the system components is expected to need replacement. Thus, $C_{rep} = 0$.

None of the components of the primary energy system require fuel for operation, $FC = 0$.

Thus, the total cost of the renewable energy system is made up of just two components. The capital cost, which previously has been shown to be the major contributor to the cost of hybrid energy systems [117, 161, 179, 244], will be the focus of this work.

The capital cost of the primary energy system consists of the investment costs of the generation and storage technologies. Generation technologies are generally costed based on the nominal power output (C_i^{gen}). The capital cost of storage technologies is dependent on both the total energy capacity $\left(C_j^s\right)$ and the nominal discharge power $\left(C_j^{out}\right)$ [108, 127]. Given the unit costs of the generation, storage and delivery units (U_i^{gen}, U_j^s and U_j^{out}), the capital cost of any design may be evaluated as:

$$CC = \sum_{i=1}^{n_g} U_i^{gen} C_i^{gen} + \sum_{j=1}^{n_s} (U_j^s C_j^s + U_j^{out} C_j^{out}) \tag{3.44}$$

where n_g and n_s are the number of available generation and storage options respectively.

Equation 3.44 requires the unit costs in terms of power (for capacities) and energy (for storage). The cost of generation can also be expressed in terms of the installed area of generation units,

$$CC = \sum_{i=1}^{n_g} U_i^{gen} A_i^{gen} + \sum_{j=1}^{n_s} (U_j^s C_j^s + U_j^{out} C_j^{out}) \tag{3.45}$$

where U_i^{gen} in this case refers to the cost per unit area of the generation units. The areas costed in the equation are the installed area of solar panels (A_p) for photovoltaics, total swept area (A_{wt}) for wind turbines, and installed heliostat area (A_c) for the power tower.

The capital cost function described above assumes that the costs scale linearly with installed capacity over the entire capacity range. Most other works involving energy system sizing make a similar assumption [7, 141, 241]. However, more complex costing

schemes can easily be accommodated in the model.

Taken together, the equations presented in Sections (3.3) and (3.4) form the integrated energy system model and provide information about the performance of the individual generation and storage technologies for any instant in time. The model is generic, can be applied to any location, and can easily be extended to incorporate other generation and storage technologies.

A simple case study which demonstrates the capabilities of the model is presented in the next section.

3.5. Single Objective Design: Chilean Case Study

3.5.1. Case study description

The study considers Collahuasi mine (Lat. 22.3° S, Long. 68.9° W). Located in the Atacama region of Chile, the mine is jointly owned by Anglo American PLC (44%), Glencore Xstrata PLC (44%) and Japan Collahuasi Resources B.V (12%), and is one of the largest copper reserves in the world. Atacama receives one of the highest levels of solar radiation in the world annually. This study will focus on solar-based generation; it is assumed that power generation from wind is not an alternative. Chile currently has 537 MW of photovoltaics installed [207], while 730 MW of solar thermal generation is under construction [162].

The problem considered is the design of an integrated energy system for the off-grid operation of the mine. The aim is to generate a design which, under mean input conditions, will satisfy the thermal and electrical demands of the mine at the minimum cost. Solving this optimization problem should yield information about the optimal sizes of the generation and storage technologies as well as the distribution of energy at each time step, from generation to storage to demand satisfaction.

Electricity consumption data for the mine was obtained from the Chilean electricity dispatch authorities [45]. The average power requirements of the mine in July 2013, shown in Appendix B.3, was considered as the power demand data in this study. The configuration and performance of the energy system is dependent on two factors: the renewables availability data and the demand data. Keeping the same demand profile constant for all seasons eliminates any potential impacts of load variation between seasons, ensuring that the effect of solar variability between seasons on the size and performance of the energy system can be investigated in isolation. The thermal demands of the plant were assumed to be 10% of the electrical demands due to lack of data. With direct heating accounting for 13% of the mining industry's energy end-use [178], the assumption was considered reasonable.

Four days were considered in this study, with each day representative of a season. The middle months of the four seasons were considered: January for summer, April for autumn, July for winter and October for spring. Considering days from the four seasons

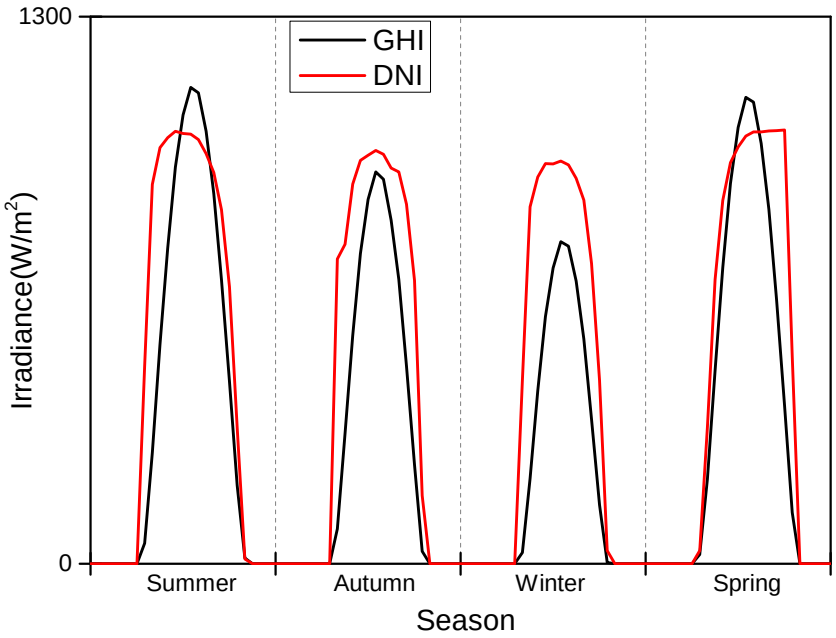

Figure 3.12.: Average Global Horizontal Irradiance (GHI) and Direct Normal Irradiance (DNI) for Chile.

ensures that we account for seasonal variability in the sizing process. For each of these months, the half-hourly averages over the ten years of historical data was computed to generate the mean GHI profile for the season. The corresponding DNI profiles were generated using the Louche model as described in Section 4.2.2.1. Figure 3.12 shows the resulting GHI and DNI profiles which served as input into the model.

3.5.2. Additional constraints

In order for the model to be fully defined and to obtain realistic results, some additional constraints are required.

Constraints ensuring demand satisfaction A necessary requirement is that the demands of the mine be satisfied. Figure 3.13 presents a schematic representation of the loads that must be met by the energy system. It must satisfy not only the requirements of the mine. but also the electricity requirements of the heaters of the MTS tanks. Constraints on the instantaneous thermal and electrical outputs are required to achieve this. These constraints be written mathematically as:

$$\dot{E}^{RES}(t) - \sum_{k} \dot{E}^{h}_{k}(t) \geq \dot{D}^{el}(t) \qquad k = \{CT, HT\} \tag{3.46}$$

$$\dot{Q}^{RES}(t) \geq \dot{D}^{th}(t) \tag{3.47}$$

Equation 3.46 constrains the power output of the primary energy system, ensuring that it is always sufficient to meet the electrical demands of the mine. The left hand side of the equation represents the net output of the renewable energy system after parasitic

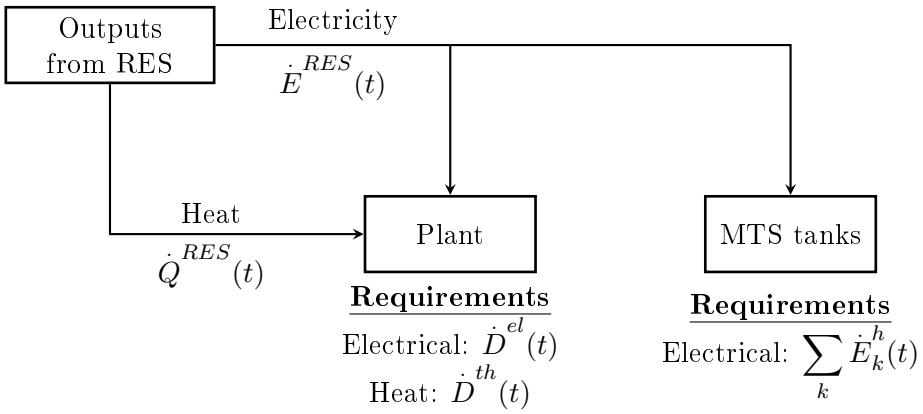

Figure 3.13.: Schematic representation of the energy requirements of the plant. Part of the electricity generated needs to be used to provide the electrical heating required by the two MTS storage tanks $k = \{CT, HT\}$. Such a load is referred to as a parasitic load [86] as it reduces the total energy available for plant demand satisfaction.

losses have been removed (see Figure 3.13). Equation 3.47 ensures that the thermal output of the energy system is sufficient to meet the thermal demands of the mine.

Boundary value constraints The problem described so far is an initial value problem. Two potential challenges arise when an attempt is made to solve the problem in its current form.

Firstly, attempting to solve the problem without further constraints may generate designs with large differences in the amounts of energy stored at the start and at the end of the operating period (24 h in this case study). This is possible because the objective function is dependent on the capacities of the units installed; energy available at the start of the process is not costed. Thus, the optimal solution when a relatively short time horizon (such as a few days) is considered may involve having as much "free" energy as possible at the start of the process, thereby reducing the need to generate such energy. This would reduce the capital cost of the energy system as storage is typically cheaper than generation. An example of the storage profile in such a case is shown in Figure 3.14. The only value that matters for the cost function is S_{max}. However, there is a difference δS between the energies available at the start and end of the operating time period. The difference represents energy which has been used within the operating period without being generated. This energy is therefore effectively available for free and means that a smaller generation capacity than is actually required can be installed. In practice however, such designs are unrealistic as it means the plant would eventually require external energy to resume operation.

Secondly, the problem in its current form allows the transfer of energy between successive days. This is not an issue when the system is solved for the full year but poses a challenge when representative days are used, as is the case with this study. The problem arises because of the large difference in renewables availability between the seasons (Figure

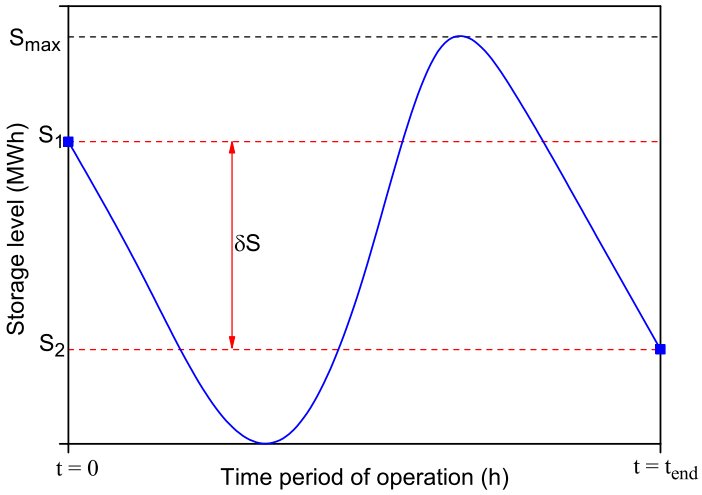

Figure 3.14.: Example of potential storage profile for the initial value problem. The cost function only takes into account the maximum storage capacity of the system S_{max}. However, the system uses "free" energy δS which is not generated during the operating time period $\delta t = t_{end}$.

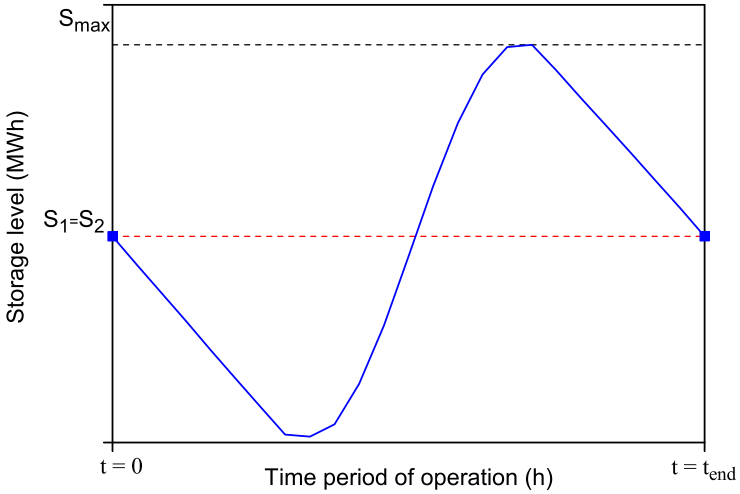

Figure 3.15.: Example of potential storage profile for the boundary value problem. In this case, the start and end states of the storage system are the same; $\delta S = 0$.

3.12) and the relatively short operation period. The "optimal" solution would involve transferring pockets of energy between days to reduce the size of the generation unit required. In practice, each day represents a season and as such the energy transferred between the representative days must be scaled up to account for the actual number of days in each season. The sizing of the storage systems do not account for this, making the design unrealistic.

In order to avoid these challenges, the problem is converted to a boundary value problem by imposing equality constraints on the endpoints of the system: the initial and final states of each storage options in each season must be the same, meaning that no net energy changes occur over the period of operation (Figure 3.15) . This is done by constraining the independent variables that determine the state of the storage systems.

For the PHES system, the constraint was placed on the mass of water accumulated in the upper reservoir. For each season,

$$m^s_{PHES}(0) = m^s_{PHES}(t) \tag{3.48}$$

For the molten salt system, the constraint was placed on the mass of salt accumulated in the hot tank. For each season,

$$m^s_{HT,MTS}(0) = m^s_{HT,MTS}(t) \tag{3.49}$$

For the AA-CAES system, both the mass of air in the cavern and the temperature of the thermal store were constrained. For each season,

$$m^s_{AA-CAES}(0) = m^s_{AA-CAES}(t_{final}) \tag{3.50}$$

$$T^{TES}(0) = T^{TES}(t_{final}) \tag{3.51}$$

Equations (3.48) - (3.51) ensure that each of the seasons is self-sufficient in terms of generation.

3.5.3. Model discretization: Backward Euler method

The model equations presented so far form a differential-algebraic system. In order to be able to solve the model with off-the-shelf optimization software such as GAMS, the system must be converted into a fully algebraic system.

For this study, the dynamic models were discretized using Euler's backward differencing technique. For an ordinary differential equation of the form:

$$\frac{\mathrm{d}y}{\mathrm{d}t} = f(t, y)$$

discretization with the backward Euler method gives the approximation at point λ as

$$y_\lambda = y_{\lambda-1} + f(t_\lambda, y_\lambda) \cdot \Delta t \tag{3.52}$$

The scheme was implemented with a uniform time step Δt. For each season, the time horizon, $t \in [0, t_{final}]$ is discretised into n_t intervals, $\Delta t = \frac{t_{final}}{n_t}$. We introduce $\tau = 0, \ldots, n_t$ as an index into the discretised time interval. All time dependent continuous variables in the model are replaced by corresponding time-step indexed discrete terms.

The backward Euler method is fully implicit and stable [191].

Discretization of the model, when combined with the incorporation of boundary value constraints, increases the complexity of the problem. This is because the algebraic system that results from discretization must be solved simultaneously for all time steps τ.

Table 3.4.: List of design constraints

Constraint type	Equation Number
Constraints on generation	3.2, 3.3, 3.6, 3.8, 3.9, 3.12-3.16
Constraints on storage	3.17, 3.19-3.25, 3.26-3.31, 3.34, 3.35-3.38
Capacity constraints	3.39, 3.40
Constraints on energy system output	3.41, 3.42

3.5.4. Problem definition for single-objective design

The nonlinear programming (NLP) optimization problem for the generation of the cost-optimal design may be stated as follows:

Given the solar input conditions for the location and the unit costs of the generation, storage and delivery units (U_i^{gen}, U_j^s and U_j^{out}), determine the optimal capacities of the units within the energy system (A_i^{gen}, C_j^s, and C_j^{out}) required to minimize the capital cost of the system

$$\begin{aligned} &\min\ CC = \sum_{i=1}^{n_g} U_i^{gen} A_i^{gen} + \sum_{j=1}^{n_s} (U_j^s C_j^s + U_j^{out} C_j^{out}) \\ &\text{subject to :} \\ &\qquad \text{Design constraints (Table 3.4)} \\ &\qquad \text{Demand satisfaction constraints (Eq. 3.46 - 3.47)} \\ &\qquad \text{Boundary value constraints (Eq. 3.48 - 3.51)} \end{aligned} \tag{3.53}$$

where n_g and n_s are the number of available generation and storage options respectively. The constraints on generation (Table 3.4) relate the instantaneous outputs of the generation units to solar availability and the installed generation areas. The capacity constraints relate the energy stored in and supplied from the storage units at any instant in time to the installed storage and output capacities. The demand satisfaction constraints ensure that the output of the energy system will be sufficient to meet the thermal ane electrical loads of the mine. Together, the constraints ensure that the performance observed for any given design of the energy system will be feasible.

3.5.5. Model implementation and solution strategy

The NLP optimization problem was implemented in GAMS 24.2 [84]. Information on the cost data and parameters used for the case study may be found in Appendix B. Hourly time steps were considered for the discretization of the entire model. The use of hourly time steps allows us to study the impact of the differences in the level of renewables availability throughout the day. For example, it allows us to compare how the system operates early in the morning when some (but not much) solar radiation is available to how it operates at midday when the solar availability is at the maximum. It also means that the behaviour of the storage system throughout the day can be studied in detail. The use of larger time steps would lead to some loss of information

(such as peak hour demands), increasing the possibility of potentially unrealistic designs being generated. Smaller time steps would increase the problem size without providing substantially more information. Hourly time steps provide a balance between information quality and problem complexity.

The optimization problem was solved using Baron 12.7.3, a solver based on the branch and bound algorithm [210]. Branch and bound methods divide the entire feasible region into smaller convex subregions which may be solved with local solvers. This usually requires the use of convex underestimating functions. Each subregion produces solutions which are global to the subregion but local to the entire interval [71]. This procedure is continued until all the subregions with potential solutions (called the candidate list) have been considered, and the best of the locally optimal solutions is reported as the optimum. Branch and bound methods guarantee optimal solutions to linear and nonlinear convex problems when carried out to completion [16, 71].

The major drawback of the branch and bound algorithm is the long time required to find optimal solutions due to the number of NLPs solved at the nodes [82]. This was a challenge encountered in this case study when an attempt was made to solve the optimization problem for the entire year (8760 h). Due to the large size of the model and the number of NLPs to be solved, the problem became intractable. This prompted the use of representative days for this study. The purpose of this case study is to verify that the model generates reasonable results; representative days are sufficient for this purpose. The case study is only an illustrative example; a more scalable approach will be presented later in the thesis. The relative gap was set at 0.005 for this study.

The model equations which represent the energy storage systems contain nonlinear equalities, making it difficult to ascertain whether the convexity conditions are satisfied [71]. This challenge, coupled with the lack of good starting points for several of the variables, motivated the use of Baron for this study.

A feature of the optimization procedure is that the operating scheme is determined by the optimizer. For the first time step for example ($\tau = 0$), the optimizer will decide on how energy is to be released from the storage options (such as whether discharge should occur from one or multiple storage options to meet the electricity demands, and whether the same storage option should be used to satisfy heating and electrical demands). Such decisions need to be made at every time step. The optimizer therefore determines how the integrated system should be operated on an hourly basis to best make use of the available generated and stored energy.

3.5.6. Results

The results obtained from the case study will be presented in two parts. First, the optimal design and the behaviour of the the energy system during the period of operation will be discussed. This will then be followed by a comparison of the design cost and performance with data available in literature.

Table 3.5.: Optimal design for single objective case study

Nominal PV capacity	C^{gen}_{PV}	1.6 MW_e
Nominal PT capacity	C^{gen}_{PT}	1195.6 MW_{th}
PHES storage capacity	C^{s}_{PHES}	2.8 MWh
PHES discharge capacity	C^{out}_{PHES}	1.3 MW_e
MTS storage capacity	C^{s}_{MTS}	5834.2 MWh
MTS discharge capacity	C^{out}_{MTS}	176.2 MW_e
Design Cost		€ 1182.5 M

3.5.6.1. Optimal Design and Energy System Performance

The capacities of the units within the optimal design is shown in Table 3.5. Solar thermal generation integrated with thermal storage is selected as the primary renewable option, satisfying all the thermal demands and a significant portion (>99%) of the electrical demands. A small PV installation is integrated with pumped hydro storage (PHES), with the AA-CAES system eliminated from the superstructure.

The choice of the power tower as the preferred generation option is due to the high ratio of the peak-to-nominal capacity obtained with the system in all seasons compared to that obtained with photovoltaics. The power tower is able to operate a fairly constant level throughout the year, taking advantage of the sun-tracking capabilities of the heliostats. In contrast, the low GHI available in winter (Figure 3.12) forces photovoltaics to operate at about 70% of the nominal capacity installed, meaning the cost of generation is almost doubled. This, combined with the higher solar-to-electrical efficiencies expected for a power tower (12-20% according to Romero et al. [194]) when compared with photovoltaics makes the power tower the preferred choice for electricity generation, despite the lower unit cost of photovoltaics.

Generation Figure 3.16 shows the generation profile of the power tower in the four seasons. The number of hours of generation varies from 11h in winter to 13h in the summer. No energy dumping occurs in winter, with the energy generated just about sufficient to satisfy the demands of the plant. This suggests that the winter season determined the generation capacity of the plant. Dumping of heat occurs in the other seasons and is highest in summer, the season with the highest potential generation (Table 3.6). The dumping of excess energy makes sense since storing the energy would have required extra storage capacity without any benefits to be had (since no energy transfer between seasons is allowed). The power tower is able to operate at close to its nominal capacity in all the seasons, with peak generation exceeding the nominal capacity in two of the four seasons.

Figure 3.17 shows the generation profile for the photovoltaics. The system performs poorly in winter and autumn, highlighting the chief challenge with PV generation. The number of hours of generation varies from 12h in winter to 14h in the summer. Little

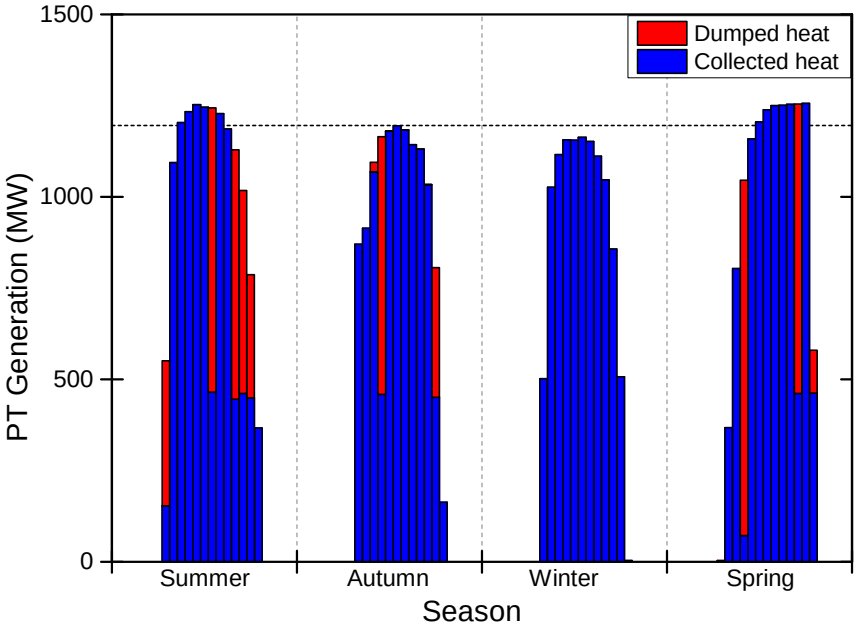

Figure 3.16.: Total thermal output from power tower system. Each bar represents 1 h. The blue bars represent the portion of energy actually collected, while the red bars show the portion dumped by defocusing the collectors. The horizontal line represents the nominal capacity of the system (1196 MW_{th}).

Table 3.6.: Seasonal power output behaviour of power tower system. Potential generation refers to the energy the power tower would generate from the solar resource available if it was operated at full capacity, while actual generation is the thermal energy that the system actually generates. The difference between the two terms provides information about the thermal energy dumped (see Figure 3.8).

	Summer	Autumn	Winter	Spring
Potential Generation [MWh]	13539	11881	10795	12668
Actual Generation [MWh]	10784	10790	10795	10780
Dumped Energy [MWh]	2755	1091	0	1888
Dumped Energy (%)	20.35	9.18	0.00	14.90

energy dumping occurs with the PV system.

Generation is the most significant contributor to the capital cost, accounting for 73% of the total cost of the design.

Storage The focus here will be on the performance of the MTS system.

Figure 3.18 shows the accumulation profile of the MTS system. The installed storage capacity provides 13.2 hours of storage at the nominal power of the steam turbine, suggesting that storage is required only for load-shifting purposes.

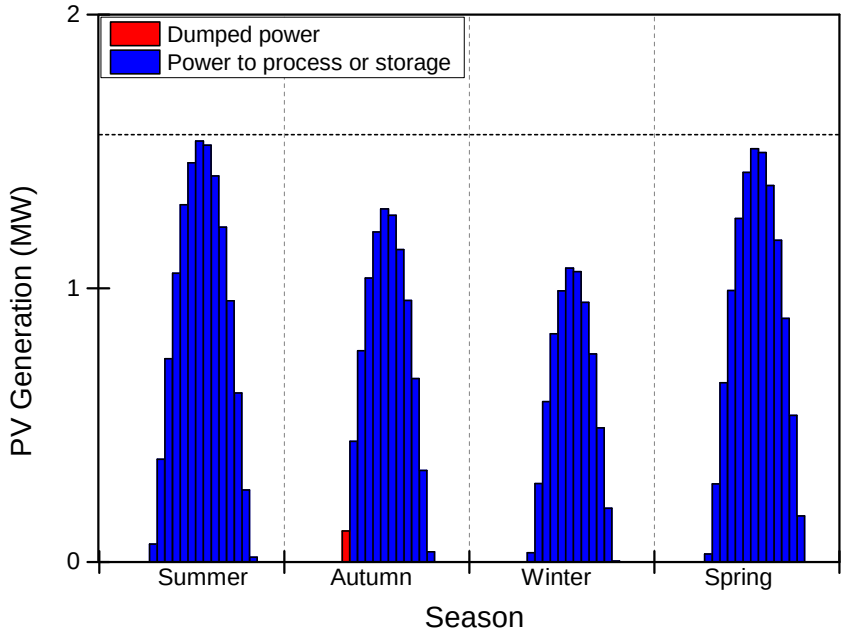

Figure 3.17.: Power output from photovoltaic system. Each bar represents 1 h. The blue bars represent the portion of output sent directly to the plant or to storage, while the red bars show the portion sent to the dump load. The horizontal line represents the nominal capacity of the system (1.56 MW_e).

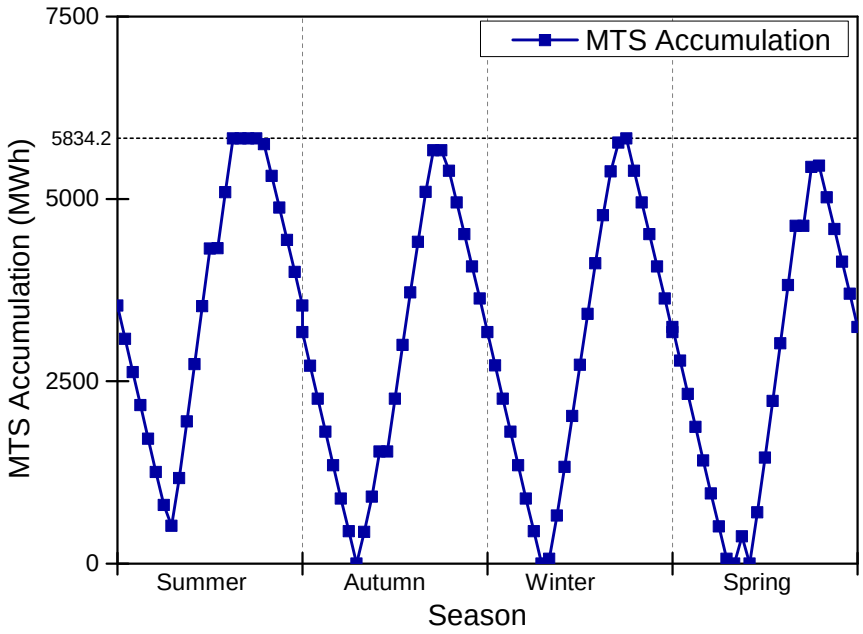

Figure 3.18.: Energy accumulation profile for MTS system. The horizontal line shows the storage capacity of the system (5835 MWh).

Winter is the only season where the storage system is in operation throughout the day. Time periods exist in the other seasons where the storage system is in standby mode: neither charging nor discharging. This is most easily observed in the summer profile in which the system is in standby mode for three consecutive hours.

Winter is also the only season in which full storage cycling (full to empty) is required.

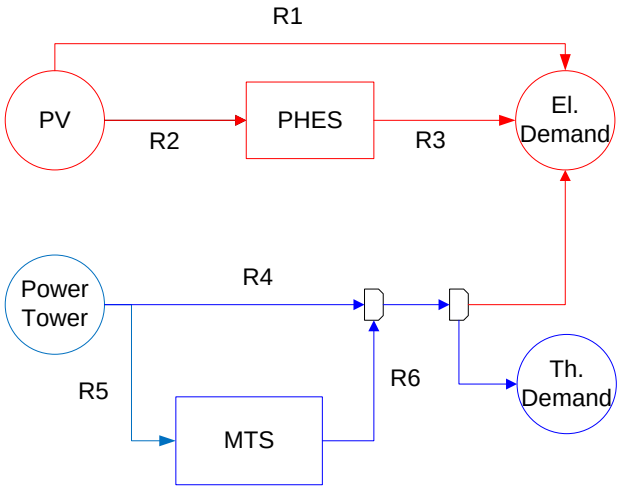

Figure 3.19.: Optimal energy system configuration with possible energy routes for Chile. The red and blue lines represent the electrical and thermal networks respectively.

Only partial cycling occurs in other months, with storage either only partially charged (spring and autumn) or partially discharged (summer). This occurs because larger portions of the plant demands can be satisfied directly from generation (bypassing storage) in the other seasons, meaning that less energy storage is needed. As such, the capacity of the system was determined by the winter storage requirements.

Power Output The installed capacity of the MTS steam generator is slightly less than the peak demand of 178 MW. Figure 3.19 shows the possible electricity supply routes within the system. The thermal system acts as the primary source of energy to the plant, with the power tower supplying during the day (R4) and the MTS system at night (R6).

For most time periods, the electrical demand of the mine is below the installed steam turbine capacity and demand can be fully satisfied from the thermal system. However, in some time periods, the electrical demand of the plant exceeds the installed capacity of the MTS steam generator, as is shown in Figure 3.20. At such times, the shortfall of energy is supplied by a combination of PV and PHES. The PHES system therefore acts as a secondary electricity source used in peak shaving in the hours with the highest electrical demands, taking advantage of its comparatively low generation cost. This is demonstrated most clearly in winter, where the PV and PHES systems are used in peak shaving only. This highlights the capability of the optimization procedure to identify the operating scheme that makes the best use of the available renewable resource.

In other seasons, energy from the PV and PHES systems not used in peak shaving is used randomly. The order and time the options are used matters little because of the excess energy available in those seasons.

The thermal demands are satisfied fully by the power tower and molten salt systems.

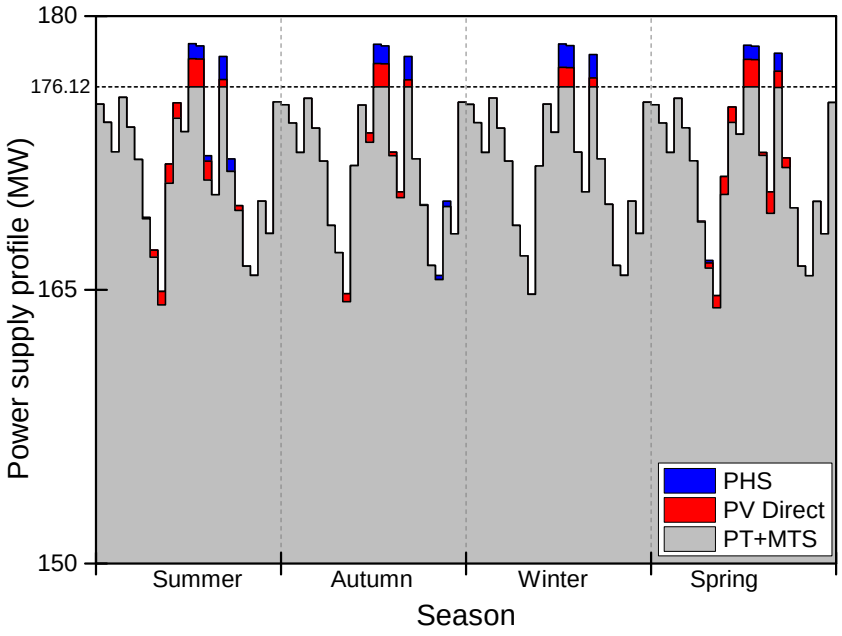

Figure 3.20.: Power supply profile for the energy system. The horizontal line shows the discharge capacity of the generator of the MTS system (176.122 MW_e).

3.5.6.2. Comparison with theoretical estimates

The capacities and costs obtained from the optimization process will be compared with theoretical estimates of the generation and storage requirements of the plant.

Generation Table 3.7 shows analytical estimates of the minimum photovoltaic and power tower capacities that would be required to meet the demands of the plant. The seasons with the highest (summer) and lowest (winter) solar availability were considered in the analysis. The minimum generation capacities that would be required for the technologies were estimated using their design equations, the peak efficiencies of the technologies, and available information about the daily load demands.

For the power tower (PT), the total plant demand (thermal and electrical) was converted into thermal form, assuming the peak efficiency of the available steam turbine for heat-electricity conversion (39.7%). The installed area of heliostats required to produce the thermal energy in both seasons was then evaluated using Eq. 3.10 assuming no thermal losses. Based on the area, the nominal PV capacity required to satisfy the demand was calculated using the design irradiance $0.95\,^{kW}/_{m^2}$.

For the photovoltaic (PV) system, the total plant demand (thermal and electrical) was converted into electrical form assuming 100% thermal to electrical energy conversion. The installed area of photovoltaics required to generate that electricity in both seasons was then evaluated using Eq. 3.2. Based on the area, the nominal PV capacity required to satisfy the demand was calculated using the standard design GHI level of $1\,^{kW}/_{m^2}$.

A comparison of the costs of the two technologies justifies the decision by the optimizer to supply most of the electricity (>99%) and all of the heat required by the plant via the

Table 3.7.: Analytical estimation of power tower and photovoltaic requirements for winter and summer. For the power tower system, the calculations are based on a heat to electricity conversion efficiency of 39.7%, and the thermal losses during generation have been ignored. For the PV system, it is assumed that that electrical to thermal energy conversion is 100% efficient. The key values (costs and capacities) are in bold for emphasis.

	Summer	Winter
Electrical demand (MWh)	4104.25	4104.25
Thermal demand (MWh)	410.425	410.425
Power tower		
Total demand as thermal (MWh)	10748.59	10748.59
Available DNI (W/m^2)	11180.10	8967.61
Area of heliostats (m^2)	1,599,140.30	1,993,681.84
Nominal Capacity (MW_{th})	913.33	**1138.67**
Estimated cost of PT (€ M)	**817.81**	
Photovoltaics		
Total demand as electrical (MWh)	4514.68	4514.68
Available GHI (W/m^2)	9059.60	5140.58
Area of PV modules (m^2)	4,216,707.10	7,431,398.55
Nominal Capacity (MW_e)	498.33	**878.24**
Estimated cost of PV (€ M)	**1290.09**	

thermal route: generation from the power tower is significantly (about 38%) cheaper. The cost of the PV system estimated here (with no storage) exceeds the cost of the entire energy system design obtained by the optimizer (Table 3.5).

The theoretical power tower size of 1139 MW_e is within 5% of the actual size obtained from the optimization process (Table 3.5). As expected, the installed size is the larger of the two: additional energy must be generated to offset the losses from not accounted for in the analytical sizing process (thermal losses during generation and parasitic electrical demands from the storage tanks).

The similarity between the results obtained by optimization and theoretical analysis for the generation capacity indicates that the model performs well in generation sizing.

Storage Table 3.8 shows the estimates of the minimum storage capacities required by the energy system in summer and winter. The thermal and electrical demands of the night periods were obtained by adding up the energy demands in the hours with no solar radiation. Based on the analysis, at least 5356 MWh of thermal energy storage will be required in order for the system to meet the nightly demand requirements. This is in the same region as the MTS storage capacity obtained from the optimization process (Table 3.5), with the installed capacity larger by 8%.

The installed MTS storage capacity is larger the analytical estimate for two reasons:

1. hours with low insolation (early mornings and late evenings) will require energy from storage to augment direct generation. This is not reflected in the analytical estimate since it only considers hours with zero solar radiation.

Table 3.8.: Analytical estimates of minimum thermal energy storage required to power the plant through the night in each season. The night period refers to the hours in which there is no solar radiation (GHI and DNI) available.

	Summer	Winter
Number of hours without solar radiation (h)	11	12
Peak electrical demand in night period (MW_e)	174.50	174.50
Total electrical demand in night period (MWh)	1876.90	2044.98
Total thermal demand in night period (MWh)	187.69	204.50
Total demand in night period if energy is stored as thermal (MWh)[a]	4915.38	**5355.58**

a - estimated with assumption of 39.7% thermal to electrical energy conversion

2. thermal losses are accounted for in the sizing of the actual system, unlike in the analytical estimate.

Even with these differences, the capacities obtained by both approaches are not significantly different. This indicates that the model performs well in storage sizing.

3.5.6.3. Comparison with results of other studies and projects

Solar thermal generation and storage (PT/MTS integrated system) account for a significant portion of the capital cost (99.6%) and power supply (>99%). As such, the cost and performance of the design will be compared to values reported in literature for similar solar thermal power projects.

Cost comparison The optimal design generated by the model has a total power discharge capacity of 177.40 MW_e and a capital cost of €1182.464 M. The unit cost of power is

$$\text{Unit cost of power} = \frac{€1182.464 \times 10^6}{177.40 \times 10^3 \text{ kW}} = 6,665 \text{ €/kW}$$

Table 3.9 shows some of the costs reported in literature for PT generation integrated with MTS storage. The values reported in literature show that the specific cost of a power tower plant is dependent on the location of the plant, the net output of the plant and size of the storage system. The unit cost obtained in the case study falls within the range of values reported in literature. The Crescent Dunes project is the most relevant comparison, given that it is the most recent, largest and only standalone (no fossil fuel backup) solar tower plant in operation [163, 238]. The 110 MW_e plant, located in Nevada, started operation in November 2015 and reportedly cost $983 million. Given that the Atacama region has an average solar resource of 3,343 kWh/m^2 [159] which is 20% higher than the solar resource in Nevada (2,685 kWh/m^2 at the plant location [163]), the capital cost of a similar plant located Chile can be expected to be significantly lower, as was observed in this work.

Table 3.9.: Comparison of estimated capital costs for power tower plants with storage.

Source	Plant site	Plant size (MW_e)	Storage Size (h)	Unit cost (€/kW_e)
Hinkley et al. [103]	Australia	100	6	4,352[a]
National Renewable Energy Laboratory, NREL [161]	United States	100	6	6,266[a]
Mancini et al. [147]	United States	100	9	7,178[a]
Konstantin and Kretschmann [128]	South Africa	100	9	6,382[a]
		100	12	7,493[a]
		50	15	9,409[a]
		100	15	8,701[a]
Crescent Dunes project [185]	United States	110	10	7,954*
Gemasolar plant [164]	Spain	19.9	15	11,557*

a - Theoretical estimates converted from dollars to euros (using \$1 = € 0.89).
* Cost estimates for existing plants

Efficiency comparison A key measure of performance for solar thermal power systems is the solar-to-electricity efficiency. This is a measure of how much of the solar radiation incident on the collector is converted into power [28]. Mathematically,

$$\text{Solar to electricity efficiency} = \frac{\text{Total power output}}{\text{Collector area x Total DNI input}} \tag{3.54}$$

The definition of the system efficiency assumes that the plant satisfies electrical demands only. The design generated in the case study satisfies both thermal and electrical demands, making the efficiency less straightforward to evaluate. For the purpose of comparison, it was assumed that all of the plant heat output was converted into power. Table 3.10 presents the plant efficiency in the different seasons. The plant has an annual efficiency of 20.3% and a peak efficiency of 22.8%. The annual efficiency obtained falls within the ranges reported by Kuravi et al. [132], Xu et al. [238] and Romero et al. [194], but is slightly higher than the values reported in Ortega et al. [168] and Behar et al. [28]. This is because the model does not account for some of the parasitic losses within the system such as pump efficiency losses, piping losses and power required by the heliostats for tracking [10].

The peak efficiency obtained falls within the ranges reported in literature (Table 3.11).

Storage capacity The results of the model suggest that 13.2 hours of storage is required for standalone operation of the plant. This is similar to the optimal storage size of 14 hours suggested for Chile by Starke et al. [207] for parabolic trough plants and is in good agreement with the planned storage capacities of projects currently under development in Chile [162].

Table 3.10.: Efficiency results for case study. All the energy supplied by the PT/MTS system was assumed to be converted to electricity.

Collector area:				2,093,372 m^2
	Summer	Autumn	Winter	Spring
Total DNI (Wh/m^2)	11,192	9,830	8,969	10,489
Potential generation (MW_{th})	23,429	20,579	18,775	21,957
Actual generation (MW_e)	4,281	4,284	4,286	4,279
Efficiency (%)	18.23	20.81	22.82	19.49

Table 3.11.: Values of power tower plant efficiencies reported in literature

Source	Annual efficiency (%)	Peak efficiency (%)
Behar et al. [28]	16-17	23-35
Kuravi et al. [132]	7-20	23-35
Ortega et al. [168]	18.1	-
Romero et al. [194]	12-20	16-23
Xu et al. [238]	10-22	-

The comparisons suggest that the model predicted reasonably well the cost, performance and size of the required plant for the study considered. The model can be used in the design of renewable energy systems for other geographies given adequate input data.

Summary

A description of the integrated energy system developed and the models used in this work have been presented in this chapter. The capabilities of the model were demonstrated by considering the single-objective design of a system for off-grid mining in Chile under fixed input conditions, and the results obtained were shown to agree well with both analytical size estimates and literature.

The case study considered assumed that the amount of solar radiation available hourly is fixed. In reality, this is not the case as renewables are by nature variable: no two years have exactly the same amount of wind and sunlight. Determining how much influence this variability may have on the required size and performance of energy systems will be the focus of the next few chapters.

Chapter 4.

MODELLING OF RENEWABLE RESOURCES

This chapter focuses on the development of a suitable methodology for the generation of renewables input data for the energy system model. The first two sections review the state-of-the-art techniques for wind and solar data modelling and forecasting. Descriptions of the selected modelling techniques are also presented. A methodology for the generation of renewable input scenarios is developed thereafter. In the final part of the chapter we show, via two case studies, that the synthetic renewable input profiles generated from the developed models have similar properties to historical data, making them suitable for reliability evaluation.

Variability in renewables input availability is a challenge that must be addressed in the design and sizing of stand-alone energy systems. A review of the main approaches to reliability evaluation (Section 2.1.2) showed chronological simulation as the state-of-the-art approach when the dynamic changing performance of the storage systems needs to be considered [48]. In order to account for climate-based variability in system sizing using the chronological approach however, multiple renewable input scenarios need to be considered. The accuracy of the reliability results obtained in the system sizing will depend on the range of input scenarios considered. Thus, large amounts of chronological data may be required to produce accurate and consistent results. In some cases, all the required data may be available in the form of historical measurements. More often than not however the historical data available is insufficient or incomplete, meaning part (or all) of the input data must be obtained by some other means. For such cases, there is a need to generate synthetic data with properties similar to what would be observed at the location under consideration. This will be the focus of this chapter.

The first two sections will focus on the review and selection of techniques for modelling renewables input data. Based on the techniques selected, a methodology for synthetic data generation will then be developed. In the final part of the chapter, we compare the results of the data generation models to historical data for two locations with different

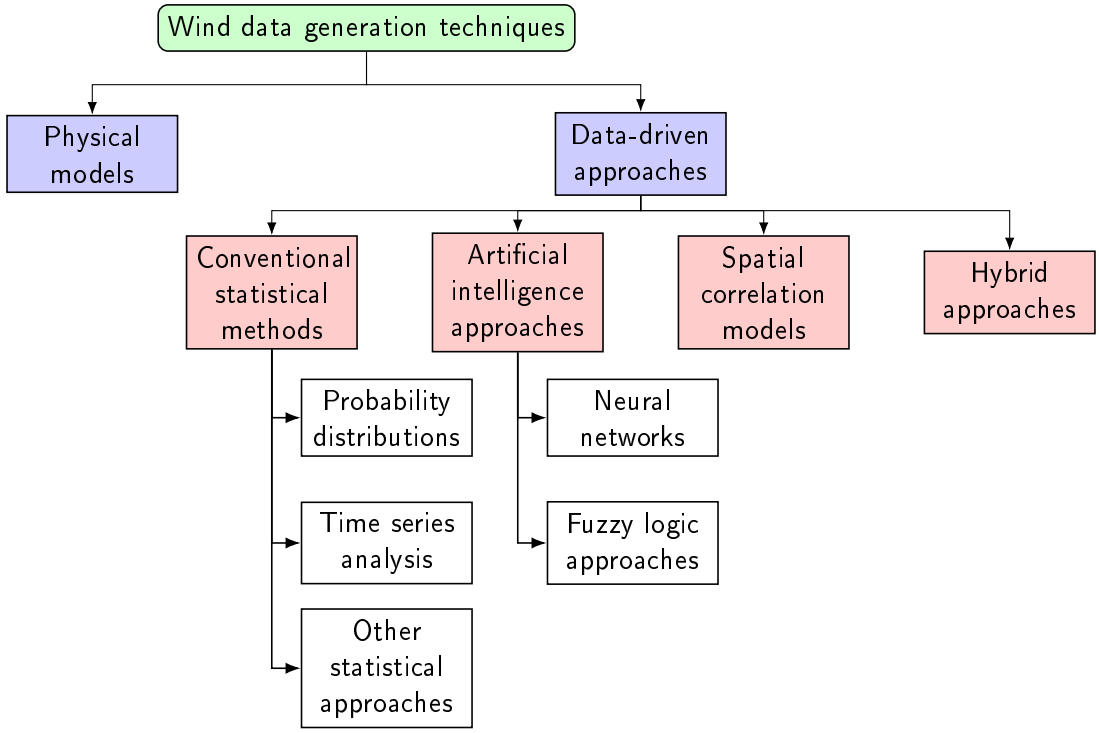

Figure 4.1.: Classification of available methods for windspeed simulation and forecasting. Based on work by Lei et al. [135]

levels of solar and wind variability. This is done to show that the models actually produce sufficiently good profiles that represent the locations. It also provides us with an understanding of the capabilities and limitations of the models.

4.1. Wind Resource Modelling

4.1.1. Review of available windspeed generation techniques

Several methods are available in literature for the modelling and simulation of wind velocity data. The methods may be classified into two categories: weather-based methods and data-driven approaches. Further sub-classifications are shown in Figure 4.1.

4.1.1.1. Numerical weather prediction (NWP) models

Numerical weather prediction models (also called physical models) use hydrodynamic atmospheric models which incorporate physical phenomena such as frictional, thermal and convective effects [122]. The inputs into the models are typically physical and meteorological information such as location, orography, topography and site elevation [135]. Physical models are typically complex, often requiring the numerical solution of conservation equations to obtain good results. Physical models perform well for long term data forecasting but perform poorly in short term predictions and are therefore typically combined with data-driven approaches [135]. A review of works involving physical models

may be found in Lei et al. [135].

4.1.1.2. Data-driven approaches

Data-driven approaches generate models and make windspeed predictions based solely on historical data. While there are different types of data-driven models available in literature, they may be broadly classified into four categories: conventional statistical approaches, artificial intelligence (AI) approaches, spatial correlation models and hybrid approaches.

Conventional statistical approaches make windspeed predictions based on historical wind speed data for the location of interest only. They will be discussed more extensively later as they are the most widely used for windspeed prediction.

In artificial intelligence approaches, historical weather data of variables such as windspeed, atmospheric pressure and temperature are used to train models to make predictions about future weather patterns. The approaches adopt machine learning methods such as neural networks and fuzzy learning approaches to analyze historical data with a good degree of accuracy [14, 135]. The process often involves temporal mining (identifying and learning from recurrent weather patterns) and a study of the interdependent nature of weather variables [94].

Spatial correlation models require the historical wind speed data of not just the site under consideration, but those of surrounding sites [135]. The models account for the location of the site relative to neighbouring sites and factor this into wind speed prediction.

Hybrid approaches combine two or more methods for wind speed prediction. For example, the work by Cadenas and Rivera [43] developed a model which combined time series analysis with artificial neural networks for wind speed forecasting in Oaxaca, Mexico.

Reviews and comparisons of performances of the various data-driven approaches may be found in several works [135, 201].

Conventional statistical approaches for windspeed prediction Conventional statistical approaches use only historical wind speed data recorded at the location to build statistical models from which predictions (or forecasts) can be made [122]. These methods may be classified based on the type of statistical analysis required for model development.

Time-series based approaches are the most frequently used approach for windspeed prediction. Time series methods work by identifying patterns and spotting trends present in historical data. Parameter estimation methods are then used to fit mathematical models to the trends observed in the data, based on which windspeed predictions can be made. The methods are based on a set of models originally proposed by Box and Jenkins [37]. Different classes of models which fall under this category which have been used in windspeed prediction include autoregressive (AR) models [5], autoregressive moving average (ARMA) models [54, 219] and autoregressive integrated moving average (ARIMA) models [32, 43, 122]. The simplest type of time-series method is the persistence model,

which forecasts that the average windspeed in the near future will remain at the same level as the current average windspeed,

$$v_{t+1} = v_t \tag{4.1}$$

Persistence models perform well in very short term prediction (minutes) and are therefore widely used in practice [135]. Persistence models are used to benchmark the accuracy of other time series approaches [122].

Time series models are continuously updated as actual windspeed realizations become available. They generally generate accurate results for short term forecasting (minutes to 1-2 days) and are therefore suitable for planning, scheduling and regulation purposes. Because of this, they are frequently combined with other data-driven approaches such as neural networks [43, 229]. They are however unsuitable for long term data generation because the accuracy of each prediction is dependent on the accuracy of the data available for the previous time step.

Data generation from probability distribution functions is another statistical approach which as been used in wind data modelling. The historical data is grouped based on the time step of measurement (usually hourly or half-hourly) and an appropriate probability distribution function (PDF) is fitted to the data. Based on the distribution for each time step, random windspeeds can be generated to form a windspeed dataset. The windspeeds generated at each step by this approach are independent of any previous predictions and are identically distributed [5]. The method is therefore fundamentally different from the time series approaches and is unsuitable for forecasting.

Different distribution types have been used in literature for modelling wind velocity in literature, some of which include normal distributions, lognormal distributions and Rayleigh distributions [5, 85]. However, the Weibull distribution is the most frequently used [21, 89, 215, 217].

Other statistical approaches have also been proposed for windspeed prediction, such as Markov chains [197] and wavelet approaches [5]. In the Markov chain approach, the winsdpeed is divided into several windspeed intervals, called "states". A transitioning matrix is then generated to represent the probabilities of transitioning between states. Each probability value in the matrix is based on how frequently such transitions occur the historical data. Based on the matrix, forecasts of the windspeed can be made.

A comparison of the performances of various statistical approaches may be found in Aksoy et al. [5].

The purpose of simulating wind input data in this work is to account for variability in design generation and selection. Thus, one of the most important factors in the selection of a wind prediction method for this work is the ability to generate multiple (distinct) years of data which are independent of each other and exhibit different properties (different types of profiles) while still taking into account historical behaviour. Time series and artificial intelligence approaches, developed specifically for operation planning and scheduling purposes, are designed to generate model predictions which maintain the

structure in the input data with very little perturbation of the system [5, 135]. This makes them unsuitable for this work as multiple runs of a given time series model will generate very similar wind profiles. Physical models, while being able to generate independent data, are very specific to the location and typically require input information which are not readily available [109].

Probability-based approaches predict windspeeds purely by random number generation from a distribution. This characteristic means that wind profiles with different structures can easily be generated. The approach is therefore the most suitable alternative for work in which variability in the generated wind profiles is desired. Because of this, it has been used in other works to account for wind variability in energy systems design [21, 89, 215, 217]. The approach will be adopted in this work.

The Weibull distribution is used, having been shown by Garcia et al. [85] and Tina and Gagliano [216] to outperform other distribution types in windspeed data fitting and prediction.

4.1.2. Weibull distribution

The probability density function (PDF) and cumulative distribution function (cdf) of a Weibull distribution are given by

$$f(\upsilon) = \frac{\beta}{\alpha}\left(\frac{\upsilon}{\alpha}\right)^{\beta-1} e^{-\left(\frac{\upsilon}{\alpha}\right)^{\beta}} \tag{4.2}$$

and

$$\mathcal{F}(\upsilon) = 1 - e^{-\left(\frac{\upsilon}{\alpha}\right)^{\beta}} \tag{4.3}$$

where υ is the wind speed, and β and α are the shape and scale parameters respectively.

The shape parameter β determines what the distribution will ultimately look like: whether the distribution will be exponential ($0 < \beta < 1$), positively skewed ($\beta < 2.6$), normally distributed ($2.6 < \beta < 3.7$) or left-skewed ($\beta > 3.7$). Gooding et al. [89] give the relationship between the mean μ, standard deviation σ, and shape parameter as

$$\beta = \left(\frac{\sigma}{\mu}\right)^{-1.086} \tag{4.4}$$

The scale parameter α determines the height and width (spread) of the distribution. Increasing the scale parameter stretches out the distribution to the right, thereby decreasing its height as shown in Figure 4.2b. Decreasing α pushes the distribution to the left, increasing its peak. The scale parameter can be evaluated from the mean of the data and the shape parameter,

$$\alpha = \frac{\mu}{\Gamma\left(1 + \frac{1}{\beta}\right)} \tag{4.5}$$

where Γ is the gamma function. Thus, given the mean and variance of a dataset, the two parameters for the weibull distribution can easily be evaluated.

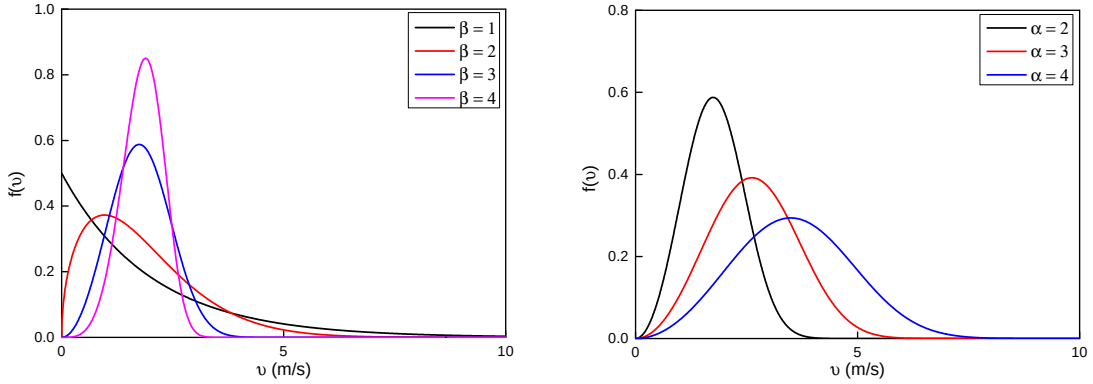

(a) Weibull PDF for various shape parameters with $\alpha = 2$

(b) Weibull PDF for various scale parameters with $\beta = 3$

Figure 4.2.: Effect of Weibull parameters on distribution

4.2. Solar Resource Modelling

Two types of solar radiation data are required as input into the energy system model: global horizontal irradiance (GHI) data for the PV system and direct normal irradiance (DNI) data for solar thermal generation.

4.2.1. Global horizontal irradiance (GHI) modelling

Several methods are available in literature for the modelling of GHI data, reviews of which may be found in Inman et al. [109] and Widen et al. [232]. As can be seen from Figure 4.3, the methods are similar to those for wind data modelling and have been discussed previously. Only the distribution-based approaches will be discussed here given that the other approaches have been shown to be unsuitable for this work for reasons previously presented.

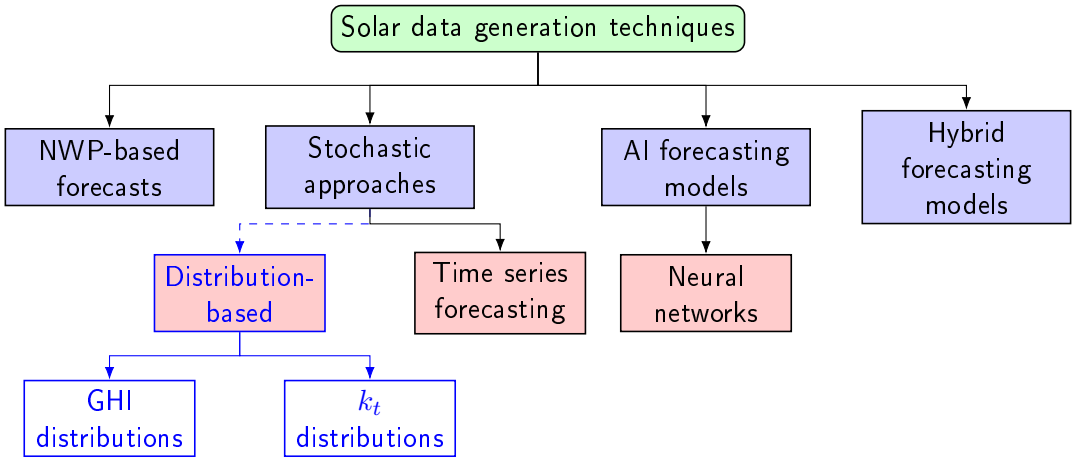

Figure 4.3.: Classification of available methods for solar data simulation and forecasting. Adapted from Inman et al. [109]. The parts in blue were not included in the original work which focused on forecasting approaches only.

4.2.1.1. Review of probabilistic approaches to GHI modelling

Two probabilistic approaches have appeared in literature for the modelling of GHI data. Both approaches will be discussed briefly.

Modelling of clearness index k_t

In this approach, the distribution is fitted to the hourly clearness index k_t. The clearness index is a measure of the atmospheric conditions that allow solar radiation through to the earth's surface [215] and is the ratio of the ground level irradiance $\dot{G}^{tot}$ to extraterrestrial irradiance $\dot{G}^{o}$,

$$k_t = \frac{\dot{G}^{tot}}{\dot{G}^{o}} \tag{4.6}$$

The extraterrestrial irradiance refers to the solar radiation level outside the earth's atmosphere [234] and is the theoretical upper limit of solar radiation at the earth's surface [67]. At any time, it is given by

$$\dot{G}^{o} = \dot{G}^{sc}\left(1 + 0.033\cos\frac{2\pi n}{365}\right)\cos\theta_z \tag{4.7}$$

where $\dot{G}^{sc}$ is the solar constant (1367 $\mathrm{W/m^2}$) and n is the day of the year.The solar zenith angle θ_z is dependent on the hour of the day, day of the year, and latitude of the site being considered [67]:

$$\cos\theta_z = \cos\phi\cos\delta\cos\omega + \sin\phi\sin\delta \tag{4.8}$$

where ϕ is the latitude of the site, δ is the declination which accounts for the day of the year, and ω is the hour angle represents the angle the sun makes with the local meridian due to the earth's rotation [67].

The value of the extraterrestrial irradiance is therefore time and location-specific, and accounts for the actual position of the sun.

To use this approach, historical GHI data are collected and the clearness index for each data point is calculated. The clearness index data is then fitted to an appropriate distribution. To generate a solar profile, random clearness indices are generated from the distributions and the corresponding GHI calculated using Equations 4.6 and 4.7.

Several distribution types have been developed specifically for fitting historical recordings of the clearness index, with the Hollands and Huget distribution [106] and the Gordon and Reddy distribution [90] the most commonly used. Tina et al. [217] compared both approaches and suggested that the Holland and Huget distribution is a better fit for the real data. Consequently, other works on hybrid energy system sizing adopting this modelling approach have used the Holland and Huget distribution for GHI data fitting [75, 215, 217].

Direct modelling of global horizontal irradiance $\dot{G}^{tot}$

In this approach, probability distributions are used to predict the GHI directly. Historical GHI data is grouped and appropriate probability distribution functions (PDF) are fitted to the data. Random solar radiation data can then be generated from the distributions if required. The approach is typically implemented on monthly basis. The method can be applied in two ways.

The first method involves fitting the discretized GHI data for each time step to an appropriate distribution. With half-hourly discretizations for example, 48 distributions will be required to represent each month. Predictions from each distribution will then be required to generate a full solar profile.

The second method involves fitting daily data for the month to an appropriate distribution. Each month is therefore represented by a single distribution. To generate hourly data, monthly predictions are made from the distribution and then discretized into hourly data using using a clear sky solar radiation model such as the CPRG model [95]. This method gives less reliable predictions because clear sky models predict smooth solar profiles and do not account for cloud cover. It also tends to produce conservative estimates of long-time process performance [215]. However, the approach is useful in situations where hourly data is unavailable.

The direct approach has used previously in energy systems design for both hourly and monthly GHI data modelling [88, 89, 118, 124].

Both GHI modelling approaches have been used previously in systems sizing. However, Gooding et al. [88] suggested that the second approach is better, concluding that the clearness index approach is flawed because it ignores the relative angle of the earth's surface to the sun which is the primary driver for solar irradiance. The Holland and Huget distribution also contains variables which are difficult to measure or obtain, making it difficult to implement [88, 89]. The second approach will therefore be used in this work.

The challenge with the second approach is the determination of the most suitable distribution type for GHI modelling. The work by Kaplani and Kaplanis [118] suggested the use of Weibull and extreme value distributions for monthly GHI data depending on the latitude of the site. Karaki et al. [119] and Khatod et al. [124] adopted beta distributions for the modelling of hourly solar irradiance. Gooding et al. [89] compared the performance of normal and Rayleigh distributions for hourly GHI data modelling and suggested that the normal distribution demonstrated better statistical correlation with real-world data. The authors however conceded that more appropriate distributions to characterize solar irradiance could almost certainly be found or developed, suggesting that a skewed distribution would make more sense because the actual output of the sun should theoretically provide a maximum which is then diminished by the atmospheric conditions such as cloud cover to produce a negative deviation.

From the above, it is clear that there is no consensus on the most suitable PDF representation for hourly GHI data. A new approach will therefore be proposed in this

work.

4.2.1.2. Direct modelling of GHI using the Pearson family of distributions

For the GHI, rather than pre-define a distribution type for the data, the discrete data for each time step is fitted to the most appropriate distribution type based on its statistical properties. This is achieved by considering the Pearson family of distributions [177].

The Pearson family of distributions were developed in an effort to model adequately skewed observations. They are based on the differential equation [192]

$$f'(x) = \frac{\mathrm{d}f(x)}{\mathrm{d}x} = \frac{(x-a)\cdot f(x)}{b_0 + b_1 x + b_2 x^2} \tag{4.9}$$

The equations for the parameters a, b_0, b_1 and b_2, which may be found in Lahcene [133], are dependent on two parameters: the skewness and the kurtosis, both of which are measures of the shape of the distribution. The skewness is a measure the lopsidedness of a distribution and is the normalized third central moment, given by [113, 192]

$$g_1 = \frac{m_3}{m_2^{3/2}} \tag{4.10}$$

where m_r is the rth moment about the mean, given for n data points of mean $\bar{x}$ by

$$m_r = \frac{1}{n}\sum (x - \bar{x})^r \tag{4.11}$$

Symmetric distributions, such as normal distributions, have a skewness of zero.

The kurtosis is a measure of the heaviness of the tail of the distribution and is dependent on the fourth moment around the mean [113, 231],

$$g_2 = \frac{m_4}{m_2^2} \tag{4.12}$$

The solutions $f(x)$ to Equation 4.9 are the density functions of the Pearson system.

The Pearson family of distributions are made up of seven parametric distributions: types I to VII. They cover any specified mean, standard deviation, skewness and kurtosis. Together, they form a 4-parameter family of distributions that cover the entire skewness-kurtosis region other than the impossible region [133], as shown in Figure 4.4. Each skewness-kurtosis pair corresponds to a unique member of the system [35].

Two methods currently exist for the determination of the best distribution type for a set of data: the method of moments and the method of maximum likelihood (ML). With the method of moments, the distribution type is selected based on the values of the kurtosis and skewness. Given the normalized third and fourth central moments (which can be estimated from the historical data), the coefficients of the terms in Equation 4.9 can be calculated, based on which the most appropriate type of distribution can be determined as shown in Table 4.1.

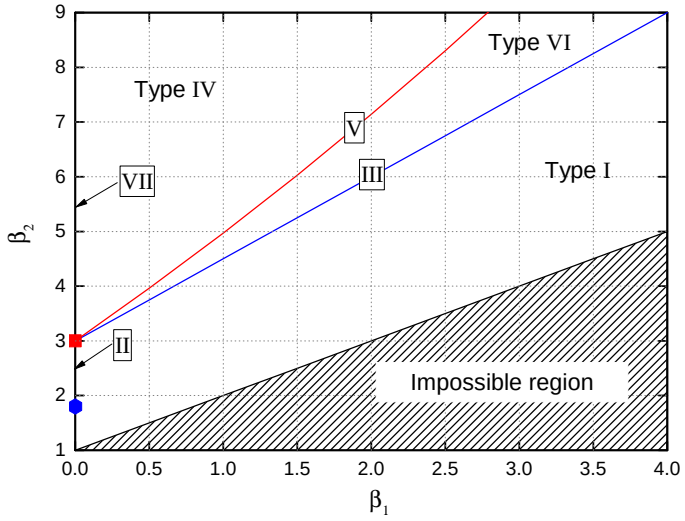

Figure 4.4.: Moment ratio diagram for Pearson family of distributions. β_1 represents the square of the skewness (g_1^2) while β_2 represents the kurtosis (g_2). The labels I-VII represent the areas covered by the seven distribution types. The red square shows the location of the normal distribution while the blue hexagon shows the location of the uniform distribution.

Table 4.1.: Determination of distribution family based on roots of Equation 4.9

Type	Characteristic(s)	Comments
0	$b_1 = \beta_1 = 0;\ \beta_2 = 3$	Normal distribution
I	$b_1^2/4b_0b_2 < 0$	Real roots for Eq. 4.9, opposite in sign
II	$b_1 = \beta_1 = 0;\ \beta_2 < 3$	Symmetric distributions with short tails, e.g. uniform distribution
III	$b_2 = 0,\ \beta_2 = 3 + 1.5\beta_1$	Gamma distribution, exponential distribution
IV	$0 < b_1^2/4b_0b_2 < 1$	Complex roots for Eq. 4.9
V	$b_1^2/4b_0b_2 = 1$	-
VI	$b_1^2/4b_0b_2 > 1$	Real roots with same sign for Eq. 4.9, e.g. lognormal distribution
VII	$b_1 = \beta_1 = 0;\ \beta_2 > 3$	Symmetric distributions with long tails, e.g. student's t-distribution

In the ML method, an attempt is made to fit all seven distribution types to the observed data. The parameters of the distribution types are selected in such a way as minimize the error between the fit and the input data. The best distribution type is then determined as the distribution type with the smallest error. While the ML method tends to produce better fits than the method of moments, it is more difficult to implement, requires more computational effort, does not guarantee a solution and yields poor results for small sample sizes [15, 58].

The Pearson family of distributions embody other distribution types such as the uniform distribution, normal distribution, extreme value distribution, beta distribution, Weibull

distribution, gamma distribution and exponential distribution among others. For example, the normal distribution has no skewness and a kurtosis of $g_2 = 3$. The uniform distribution has a skewness of zero and a kurtosis of $g_2 = 1.8$ [192] and is a special case of Type II.

The use of a family of distributions therefore allows us to model adequately the GHI input data, with the best distribution type determined on a case-by-case basis. This ensures that the simulated data mirrors the historical data, with any bias in the historical data also reflected in the simulated data. It also means that outliers in the data have a more significant effect on the shape of the distribution (through the kurtosis), as will be highlighted later.

4.2.2. Direct normal irradiance (DNI) modelling

Direct Normal Irradiance (DNI) data is required to calculate the instantaneous output of the power tower. However, the DNI available at any time is related on the GHI [67, 109],

$$\mathrm{GHI} = \mathrm{DHI} + \mathrm{DNI}\cos\theta_z \tag{4.13}$$

where DHI is the diffuse horizontal irradiance and θ_z is the solar zenith angle. DNI therefore cannot be modelled independently but must be calculated from the available GHI. Models linking both types of solar radiation must be used.

Several models exist in literature for the estimation of direct normal irradiance (DNI). The models fall into two categories: parametric and decomposition models [25, 234]. Wong and Chow [234] provide a review of both types of models. Parametric models (also called atmospheric transmittance models) require detailed information about atmospheric parameters such as atmospheric turbidity, cloud cover, fractional sunshine and precipitable water content [25, 234]. Decomposition models on the other hand use global irradiance information only to predict the direct and diffuse components [234]. Parametric models give better predictions, with a 6% root mean square error (RMSE) difference observed in the predictions of the most accurate decomposition and parametric models for Spain [25]. However, comparing the types of input information required by both models suggests that a decomposition model is more suited this work.

The Louche model, adjudged by Batlles et al. [25] and Wong and Chow [234] to be the most accurate decomposition model, was implemented.

4.2.2.1. Louche model

The Louche model [138] relates the clearness index k_t to the beam transmittance k_b (ratio of beam to extraterrestrial irradiance),

$$k_b = -10.627k_t^5 + 15.307k_t^4 - 5.205k_t^3 + 0.994k_t^2 - 0.059k_t + 0.002 \tag{4.14}$$

From the beam transmittance, the DNI may be calculated from [67]:

$$\dot{G}^{DNI} = \frac{k_b \cdot \dot{G}^o}{\cos\theta_z} \tag{4.15}$$

The angular displacement of the sun and the location of the site are accounted for in the calculation of the solar zenith angle (see Equation 4.8). Thus, given the latitude of the location and the GHI, the DNI can be calculated for any hour of any day of the year.

The previous two sections have focused on the development and selection of techniques for the modelling of renewables data. However, in order to evaluate the effect of inter-year variability, a methodology for the generation of multiple renewable input scenarios from historical data is required. This will be the focus of the next section.

4.3. Methodology for Renewables Input Scenario Generation

Four steps are involved in the generation of renewables input scenarios.

Pre-processing and calculation of monthly statistics The historical data for the site collected is grouped into monthly data. Monthly grouping of historical data ensures that a sufficient number of data points are available to develop an adequate stochastic representation of variability at the location. It also minimizes the effect of errors and outliers as the dataset is larger. It is a frequently used approach in renewables modelling [88, 118, 217].

Where the data available is in the local time of the location, time zone corrections are carried out. This is particularly important for the GHI data because the calculation of the DNI requires the solar zenith angle θ_z (Equation 4.15) which is a dependent on the GMT time.

For each time step of each month, the requisite statistical parameters are calculated: the shape and scale parameters for the wind velocity, and the mean, standard deviation, skewness and kurtosis for the GHI data.

Prediction of GHI and windspeed values and evaluation of DNI Random windspeed data was generated using an in-built MATLAB function `wblrnd` which generates random values from the Weibull distribution given the scale and shape parameters.

An in-built MATLAB function `pearsrnd` which implements the Pearson family of distributions based on the method of moments was used in the generation of random GHI data. The function requires the four moments as input, determines the appropriate distribution type, and generates a random number from the distribution while ensuring that the statistical properties are preserved in the simulated data.

Since the statistical properties of the historical data are evaluated on a monthly basis, a decision must be made on how the yearly data is generated. Two possible alternatives are:

1. Prediction of one solar profile for each month. With this technique, all days of the month are modelled to have exactly the same solar profile. The method assumes that all days of the month are similar to each other: the first day of January is exactly the same as the thirtieth day, for example. For any given month, the instantaneous renewable potential on day d, $\dot{R}_{d,\upsilon}$, may be represented mathematically as

$$\begin{aligned} \dot{R}_{d,\upsilon} &= f\left(r_\upsilon\right) \qquad d = 1; \upsilon = 1, 2 \ldots, n_s \\ \dot{R}_{d,\upsilon} &= \dot{R}_{1,\upsilon} \qquad d = 2 \ldots, n_{days}; \upsilon = 1, 2 \ldots, n_s \end{aligned}$$

   where $\upsilon = 1, 2 \ldots, n_s$ are the discrete time periods for the statistical data, r is the vector of statistical inputs for the month, and n_{days} represents the number of days in the month.

2. Prediction of different daily solar profiles. With this method, a different solar profile is generated from the distribution for each day. This method assumes that the days of the month are completely independent of each other; availability on consecutive days of the month are not linked in any way (no trend). Mathematically,

$$\dot{R}_{d,\upsilon} = f\left(r_\upsilon\right) \qquad d = 1; 2 \ldots, n_{days}; \upsilon = 1, 2 \ldots, n_s$$

In reality, while no two days are ever exactly the same, weather data typically exhibits a trend-like component (consecutive cloudy days or an extremely sunny month, for example). To mimic this, a linear combination of data generated from the two approaches described above is implemented in this work:

$$\begin{aligned} \dot{R}_{1,\upsilon} &= f\left(r_\upsilon\right) \qquad \upsilon = 1, 2 \ldots, n_s \\ \dot{R}_{d,\upsilon} &= \omega_d \cdot \dot{R}_{1,\upsilon} + (1 - \omega_d) \cdot f\left(r_\upsilon\right) \qquad \omega_d \epsilon [0, 1]; d = 2 \ldots, n_{days}; \upsilon = 1, 2 \ldots, n_s \end{aligned} \tag{4.16}$$

where is w_d a weighting factor which determines how much trend is expected in the data. A value of $w_d = 0$ indicates that no trend is expected. Thus, for each month, two sets of data need to be generated (one with each method) and the corresponding values combined. With this technique, we are able to retain the best properties of both schemes, with one dataset providing individuality and the other providing trend-like behaviour.

The approach assumes that the renewables availabilility in consecutive hours are independent: $\dot{R}_{d,\upsilon}$ is not influenced by $\dot{R}_{d,\upsilon-1}$. Other more complex approaches which account for trends in consecutive hours and/or days can also be developed.

Using this approach, yearly GHI and windspeed data (in discrete form) may be generated. The DNI corresponding to each GHI value can be calculated using the Louche model. The approach is repeated to generate the number of scenarios required for each renewable input type.

Each renewable input profile is made up of a number discrete values generated from probability distributions. Hence, the probability p_z of a profile z on any given day d of

the year is the product of the probabilities $p_{z,v}$ of the discrete values $\dot{R}_{d,v}$ for that day,

$$p_z = \prod_{\nu=1}^{n_s} p_{z,v} \tag{4.17}$$

Generation of continuous profile for renewables input data Discrete data are generated from the probability distributions. For probability distributions generated from historical data with n_s measurements at time intervals of Δk, the generated data may be written as

$$\dot{R}(t_\nu, d) = \dot{R}_{d,\nu} \qquad \nu = 1, 2 \ldots n_s;\ d = 1 \ldots, n_{days};\ t_\nu = \nu \cdot \Delta k \tag{4.18}$$

The renewable input profiles required for the generation models are continuous functions (see Section 3.3.1). The discrete data must therefore be converted into a function defined over the entire interval in some way. This is achieved using a simple piecewise step function, giving the function for each day as

$$\dot{R}_d(t) = \dot{R}_{d,\nu} \qquad t\epsilon[t_\nu, t_{\nu+1}];\ d = 1 \ldots, n_{days};\ \forall \nu \tag{4.19}$$

Other more complex methods, such as linear and spline interpolations, may also be used to generate the continuous profile.

Data pairing Once the required number of renewables input conditions have been generated, the next step is the generation of renewable input scenarios by pairing the solar and wind input conditions.

Ideally, all possible combinations of the generated profiles are considered: each solar input profile (n_s) generated is paired with each wind input profile (n_w) and vice versa. With this approach, the number of scenarios increases quadratically; $n_s \times n_w$ renewable input scenarios are created. The approach therefore requires significant computational expense to explore the renewable space sufficiently. This poses a problem as a large number of input profiles may be needed to represent renewables variability adequately. A sampling approach which allows space exploration while reducing the computational requirements is therefore required. This is achieved using the concept of stratified random sampling.

Stratification is the process of dividing members of a population into subgroups before sampling. With stratified random sampling, the population is first divided into a number of non-overlapping sub-regions (strata) based on a stratification criteria, with each strata then randomly sampled independently [39]. All the subgroups of the population are therefore represented by at least one member [152]. The biggest advantage of stratified random sampling is that it reduces selection bias, ensuring no segment of the population is over-represented or underrepresented. It also produces a sample population that is representative the entire population being studied, reduces sampling error and outperforms random sampling [152].

The criteria for stratification used here is the total renewables availability in the year.

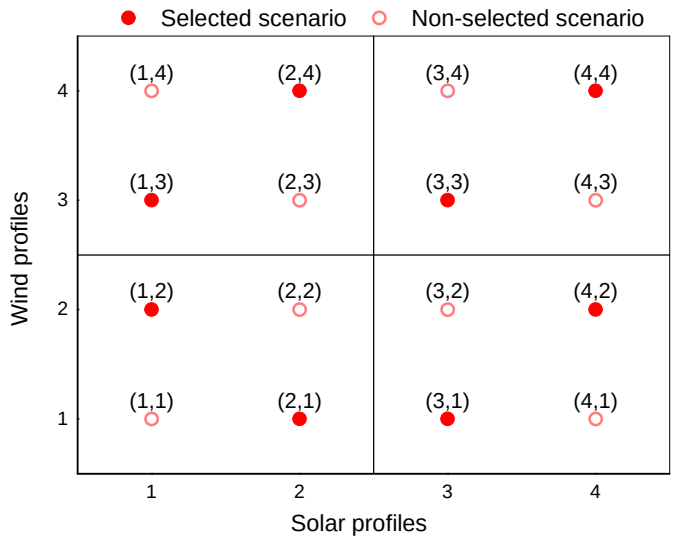

Figure 4.5.: Demonstration of stratified random sampling approach for scenario selection. Each input type (with $n = 4$ profiles each) is divided into $s = 2$ strata, creating $s^2 = 4$ sections for sample selection.

Consider a set of solar and wind input conditions of the same size $n = n_s = n_w$. Each input type is sorted based on the renewables availability level and then divided into d strata of size n/d. Thus, d^2 sections are created from which samples may be selected, with each section containing $(n/d)^2$ scenarios. n/d scenarios are selected randomly from each section such that each renewable input condition is represented exactly once. This means that each point is selected d times in total. The total number of scenarios selected is therefore reduced from n^2 to $n \cdot d$.

To demonstrate this, we consider the case of $n = 4$ solar and wind input profiles as shown in Figure 4.5. There are 16 potential scenarios available for selection. Each input type has been classified into two strata based on the total yearly availability, creating 4 sections to select points from. Each profile is selected (at random) exactly once from each strata it belongs to: the selection of scenario (1,2) means that scenarios (1,1) and (2,2) cannot be selected, and vice versa. The number of scenarios to be considered is reduced from 16 to 8 in this case, with each input condition considered twice.

The approach reduces to pure random sampling when $d = 1$ and becomes the evaluation of the whole space when $d = n$. It becomes more accurate as the number of strata considered is increased ($d \to n$).

The approach ensures that the scenario space is sampled in a structured way, with each input profile adequately represented and each profile combined in quantitatively different types of scenarios. It therefore allows for the exploration of different types of renewable input scenarios while reducing the computational requirements significantly. This is particularly useful where n is large. For example, only 5% of the potential samples will be considered when the approach is applied for $n = 100$ profiles with $d = 5$ strata. While the method has been described here for samples of equal sizes, it can easily be adapted for scenarios with uneven sizes by using different strata sizes for the two input types.

The major limitation of the implementation is that the input profiles are classified based on the yearly totals, thereby assuming that the yearly totals (a quantity-based measure) are representative of the quality of the profiles. This assumption is not necessarily accurate; a solar profile with a good winter but poor summer is qualitatively better than one with a poor winter and good summer, for example. However, there is no simple way of pre-determining the quality of the profiles, making the use of the yearly totals the most suitable alternative.

4.4. Model performance

The previous sections focused on the selection of models for the different renewable input types and the development of a methodology for synthetic data generation. Given that the sizing of renewable energy systems is heavily dependent on the accuracy of the renewables input data, it is necessary to evaluate how well the models and methodology perform in the generation of representative data for any given location. This is important as understanding the capabilities and limitations of the models will provide insights regarding the types of decisions and conclusions which may be drawn from results obtained with the synthetic data.

To do this, the selected models and the renewables data generated from the models are compared to actual historical measurements. Two locations with significant mining activities are selected for investigation: Atacama, Chile and Alberta, Canada. The Atacama region is the hub of significant copper mining activity, while Alberta is known for oil sand and coal mining.

Historical solar radiation data for the Chilean site was obtained from the University of Chile [61]. The dataset obtained contained ten years (2003-2012) of half-hourly measurements of the global horizontal irradiance. Thirty-three years of reconstructed hourly wind velocity data for the location was also obtained from the University of Chile [62]. The databases provide historical wind and solar information for any location (specified by longitude and latitude) within Chile.

For Alberta (Lat. 51.0^o N, Long. 114.0^o W), historical solar radiation data was obtained from the National Renewable Energy Laboratory [160]. The database provides half-hourly solar irradiance measurements for any North American site, with data available from 1998. Wind velocity data covering the same ten years was obtained from the Department of Environmental and Natural Resources, Government of Canada [63].

The monthly statistical properties of the datasets for both locations are presented in Appendix E. For the Canadian site, eight years of data (2005-2012) were used in the computation of the GHI statistical properties. Figures 4.6 and 4.7 show the mean solar and windspeed availability at both locations through the year. The renewables availability at the two locations is widely different, with the Chilean site enjoying much more solar and wind resource. The wind profiles are also qualitatively different: Canada experiences significantly less fluctuation in wind level through the year.

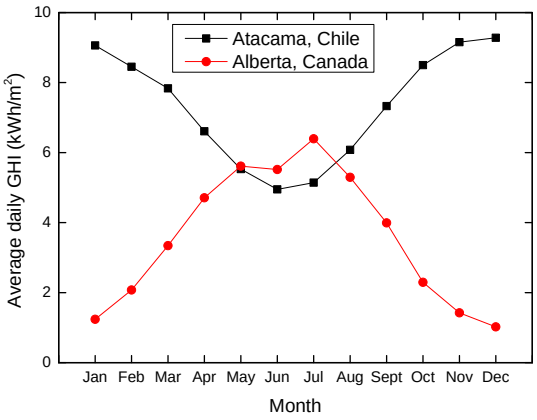

Figure 4.6.: Average daily GHI for both locations

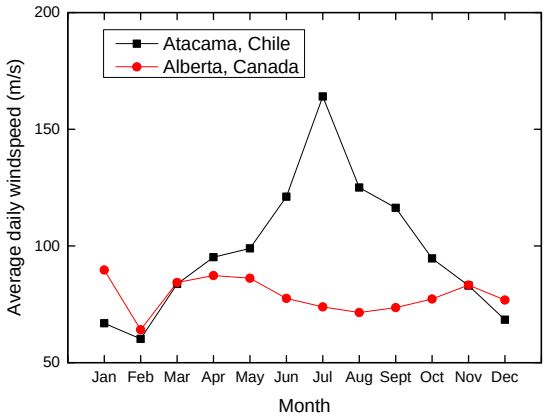

Figure 4.7.: Average daily wind velocity for both locations

The capabilities of the models to generate representative wind and solar data for both locations is investigated. The differences in the properties of renewables at the two locations allow us to test how well the data generation models perform under a variety of conditions.

4.4.1. GHI model performance

Investigation into the capabilities of the GHI model will be done in two parts. First, the ability of the Pearson family of distributions to model (and therefore predict) adequately discrete GHI measurements is demonstrated. The properties of the monthly and yearly GHI profiles generated from the model are then compared to the historical measurements for the locations.

4.4.1.1. Performance of Pearson distributions

To demonstrate the capabilities and advantages of using the Pearson family of distributions for GHI modelling, we consider how well the distributions generated fit the historical data. This can be achieved by comparing the empirical cumulative distribution functions (ECDFs) generated from historical data for a number of measurement points with CDFs of the fitted distributions. For the historical data, the ECDF at the value X is given by

$$\text{ECDF(X)} = \frac{\text{Number of historical values} \leq \text{X}}{\text{Total number of historical values}} \tag{4.20}$$

Sample cases compared for Chile and Canada are shown in Figures 4.8 and 4.9. For each location, the fits generated for one summer and one winter measurement point are presented. For comparison purposes, the PDF and CDF fits obtained with the normal distribution have been included for each case.

The Pearson function produces PDFs which mimic the shapes of the histograms of the historical data closely. The wide range of shapes taken by the distribution demonstrates

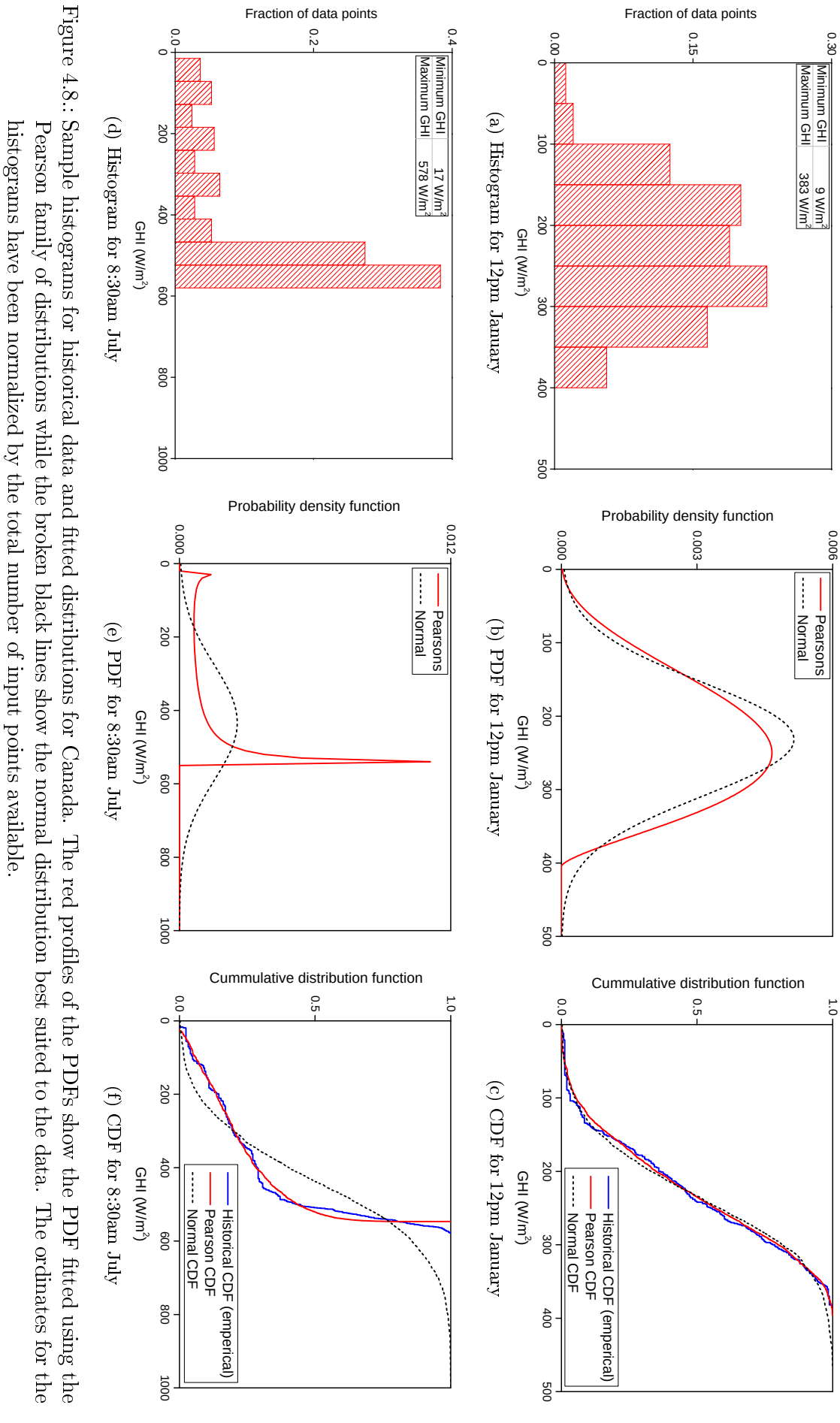

(a) Histogram for 12pm January

(b) PDF for 12pm January

(c) CDF for 12pm January

(d) Histogram for 8:30am July

(e) PDF for 8:30am July

(f) CDF for 8:30am July

Figure 4.8.: Sample histograms for historical data and fitted distributions for Canada. The red profiles of the PDFs show the PDF fitted using the Pearson family of distributions while the broken black lines show the normal distribution best suited to the data. The ordinates for the histograms have been normalized by the total number of input points available.

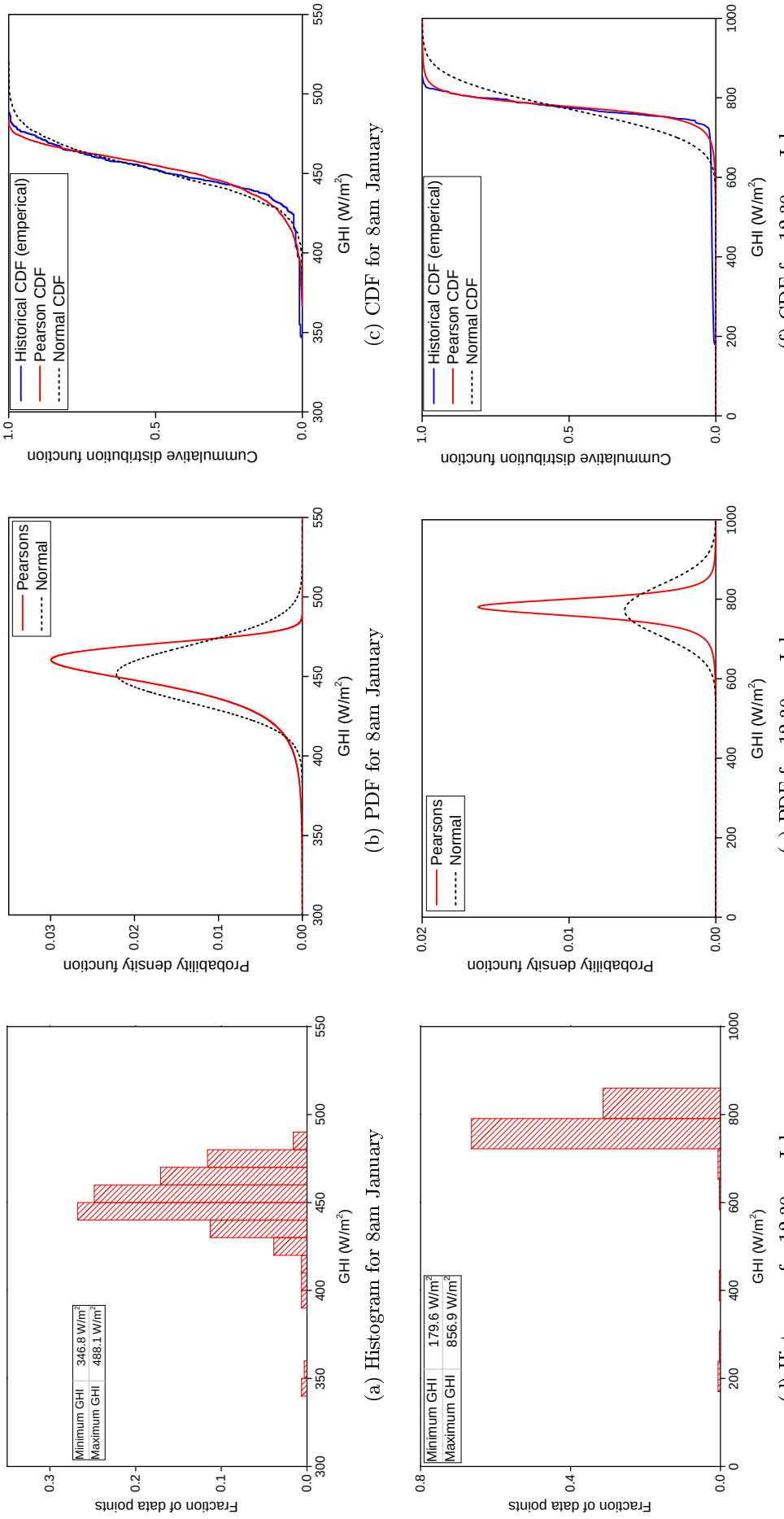

(a) Histogram for 8am January (b) PDF for 8am January (c) CDF for 8am January

(d) Histogram for 12:30pm July (e) PDF for 12:30pm July (f) CDF for 12:30pm July

Figure 4.9.: Sample histograms for historical data and fitted distributions for Chile. The red profiles of the PDFs show the PDF fitted using the Pearson family of distributions while the broken black lines show the normal distribution best suited to the data. The ordinates for the histograms have been normalized by the total number of input points available.

the capability of the family to adapt to the properties of input data. The fits provided by Pearson family outperform the normal distribution in all four scenarios. The normal distribution generates poor models in the cases where the entire weight of the distribution is to one side of the mode, as seen in Figures 4.8d-4.8f. Even in such scenarios, the Pearson function generates good fits. This is important because such profiles are typical for periods with high solar insolation. The Pearson fits perform well in the determination the bounds of the distributions in all the cases. This means that the discrete predictions from the model will be within the bounds if the historical data.

The fits generated are significantly influenced by the presence of outliers, as evidenced by the heavy tails of the distributions. This is expected given that the kurtosis, which determines the heaviness of the tail, is dependent on the fourth power of the deviation from the mean (Equation 4.12). Thus, significant outliers in the historical data cause high kurtosis values. For the cases presented tails are to the left, mimicking the locations of the outliers.

4.4.1.2. Comparison of historical and simulated data

An important factor that must be considered in the data generation process is the range covered by the historical data. Given that the simulated data acts as input into the energy system model for evaluation of reliability, the simulated data needs to cover a similar range to the historical data in order to obtain truly representative reliability information about any location under consideration. The ranges covered by the simulated and historical data for each month can be compared by evaluating the upper and lower bounds of both data sets. To do this, 500 synthetic solar profiles were generated from the Pearson distributions using the methodology described previously (section 4.3) and the maximum and minimum GHI values for each month computed. These values were then compared with those of the historical data. The deviation of the simulated data from the bounds of the historical data were computed as:

$$\text{LBD (UBD)} = \left[\frac{\text{Lowest (highest) simulated value}}{\text{Lowest (highest) historical measurement}} - 1\right] \times 100\% \qquad (4.21)$$

The results for Chile and Canada are presented in Table 4.2. Positive values indicate over-prediction (simulated value > historical measurement) while negative values indicate under-prediction (simulated value < historical measurement).

The results suggest that the solar radiation values obtained from the model are at a similar level to those historically recorded, with all predictions within ±10% of the recorded historical values in all months. In general, the lower bounds are underpredicted while the upper bounds are overpredicted. This is favorable as it allows us to explore a wider range of feasible input conditions in reliability evaluation than pure historical data would ordinarily allow, thereby obtaining more robust designs.

The monthly deviations observed in the Canada case are much higher than those for

Table 4.2.: Deviation of simulated data from historical measurements for total GHI on a monthly basis for Chile and Canada. The lower bound deviations (LBD) and upper bound deviations (UBD) for each month is presented.

Month	Canada		Chile	
	LBD (%)	UBD (%)	LBD (%)	UBD (%)
January	-9.30	1.58	-1.41	-0.57
February	5.62	1.34	-0.39	-0.97
March	-1.51	2.51	-0.89	0.16
April	-4.80	3.00	-4.23	0.65
May	-8.03	-0.17	-1.63	0.90
June	4.44	-4.86	-1.88	-0.79
July	-5.91	0.02	-2.58	0.27
August	-7.87	2.53	-0.24	0.33
September	8.67	-0.75	-1.64	-0.11
October	4.83	0.17	-1.95	0.46
November	-4.31	4.43	-0.32	-0.64
December	-9.09	8.69	-0.36	-0.59
Average	-2.27	1.54	-1.46	0.08

Chile. This occurs for two reasons: the higher variability at the location, and the lower GHI availability at the location (smaller denominators in Eq. 4.21).

The synthetic data generated for full years also agree well with historical data, with the annual maximum and minimum values obtained for the yearly solar radiation within $\pm 0.3\%$ and $\pm 1.8\%$ of the historical data for Chile and Canada respectively. In both cases, the simulated data bounds the region covered by the historical data. This suggests that the implemented GHI model is capable of generating representative data for locations with different degrees of renewables availability.

4.4.2. DNI model performance

To gain an insight into the performance of the Louche model, predictions of the model are compared to actual DNI measurements. Historical GHI data was supplied as input into the model and the predicted DNI values from the model were compared to historical DNI recordings. Figures 4.10 and 4.11 show sample profiles comparing the simulated and actual DNI for Chile and Canada. The model produces good predictions even under cloud cover conditions, as evidenced by the Canadian profiles. However. it is clear that there is some error in the predictions of the model.

To quantify the errors in the predictions of the model, two metrics recommended by the International Energy Agency (IEA) for reporting solar irradiance model accuracy were used: the root mean square error (RMSE), and the mean bias error (MBE). The RMSE is a measure of the magnitude (dispersion) of the errors while the MBE measures the average bias of the model [109]. Typically, both measures report the absolute error between simulated and actual data. To obtain the relative (percent) error, the metrics were normalized by the mean of the actual irradiance measurements as recommended by

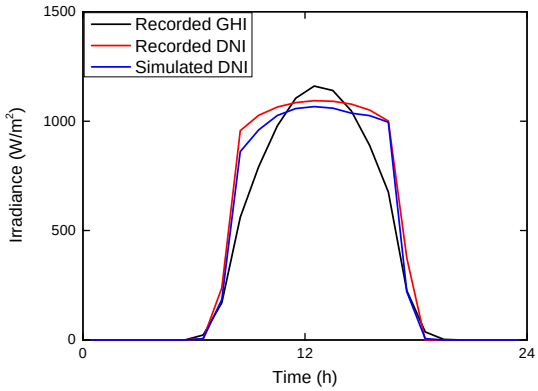

(a) January 1, 2007 (Summer)

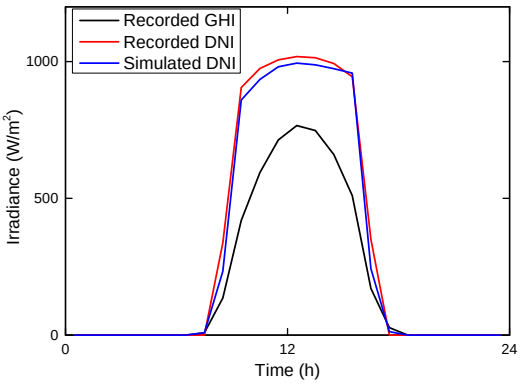

(b) July 1, 2007 (Winter)

Figure 4.10.: Comparison of Louche model predictions with actual data for Chilean site.

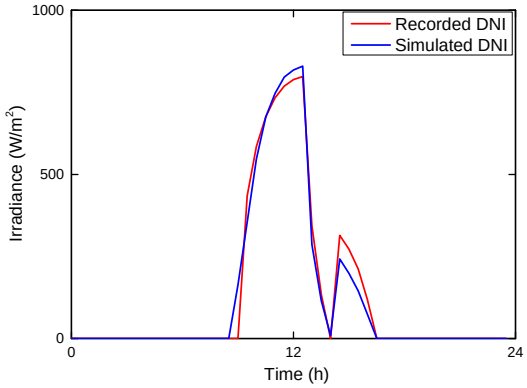

(a) January 1, 2011 (Winter)

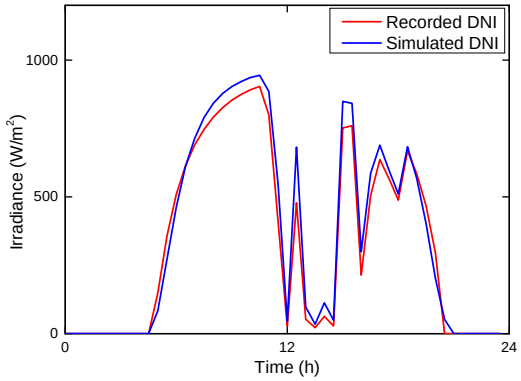

(b) July 1, 2011 (Summer)

Figure 4.11.: Comparison of Louche model predictions with actual data for Canadian site.

Hoff et al. [105]. Thus, the average RMSE is given by [105]:

$$RMSE_{avg} = \left[\frac{\sqrt{N}}{\sum_{\tau=1}^{N} \dot{G}_{\tau}^{m}}\right] \sqrt{\sum_{\tau=1}^{N} \left(\dot{G}_{\tau}^{p} - \dot{G}_{\tau}^{m}\right)^2} \tag{4.22}$$

where $\dot{G}_{\tau}^{p}$ and $\dot{G}_{\tau}^{m}$ are the predicted and actual DNI measurements in $^{W}/_{m^2}$ for the discrete data with measurement intervals $\tau = 1, \ldots, N$. The average MBE is calculated as:

$$MBE_{avg} = \frac{\sum_{\tau=1}^{N} \left(\dot{G}_{\tau}^{p} - \dot{G}_{\tau}^{m}\right)}{\sum_{\tau=1}^{N} \dot{G}_{\tau}^{m}} \tag{4.23}$$

The average errors over six years of historical data are presented in Table 4.3. The RMSE

Table 4.3.: Average errors in Louche model predictions for Chile and Canada, 2005-2011.

	Chile	Canada
RMSE (%)	13.49	18.30
MBE (%)	-7.95	7.86

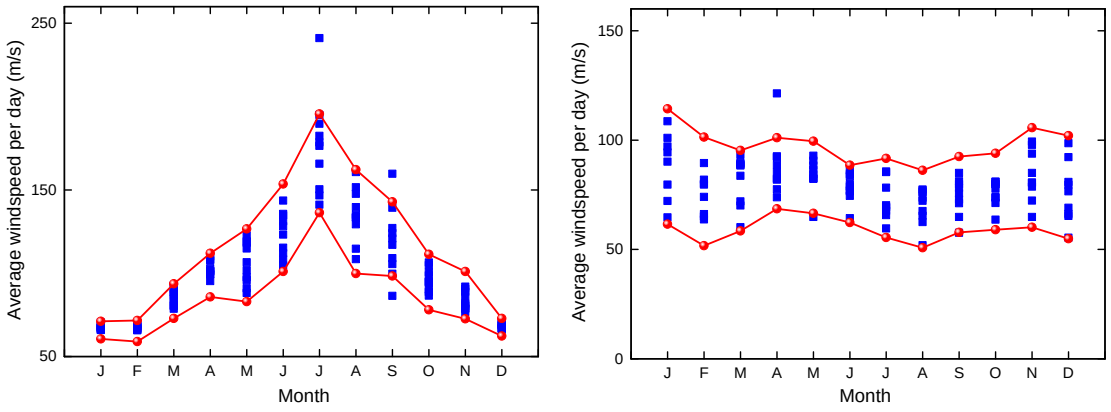

(a) Chile (b) Canada

Figure 4.12.: Comparison of average monthly windspeeds of 500 simulated profiles to 10 years of historical data (2003-2012 for Chile and 2005-2014 for Canada). The blue boxes show the historical data; the red circles show the monthly maximums and minimums of the simulated data.

values are within acceptable range for decomposition models, given that the minimum RMSE reported by Batlles et al. [25] in their comparison of different decomposition models was 20%. The MBE values indicate the predictions for Chile are about 8% below the measured value, while the values for Canada are overpredicted by roughly the same margin. Given that this work focuses on preliminary design and sizing for decision-making, the model is deemed to be sufficiently accurate. For more detailed systems sizing however, a more accurate modelling technique may be required.

4.4.3. Wind model performance

The capability of the Weibull distribution to produce good fits for hourly wind data modelling is well documented in literature [88, 89, 216, 217] and hence will not be repeated. The focus here is to demonstrate that the methodology implemented for wind data generation produces representative profiles for each month of the year.

Figure 4.12 compares the regions covered by 10 years of historical data and 500 simulated wind input profiles for Chile and Canada. The simulated profiles cover and exceed the regions covered by the historical data in most months. However, the model does not reproduce some of the extreme outliers present in the historical data. The synthetic wind profiles also compare well with historical data on an annual basis, with less than 5% difference between the best and worst case scenarios of both datasets for the two locations considered. The fact that the methodology is able to produce statistically good monthly and annual wind profiles for Chile and Canada, despite the quantitative and qualitative differences in the windspeed level at both locations in the different months, is an indication that the implemented method is robust enough to be applied for preliminary sizing at any location.

Summary

A methodology for the stochastic generation of synthetic renewables input scenarios for the energy system model was developed in this chapter. This was achieved by fitting historical data to appropriate probability distributions, from which random renewables input profiles are then generated. The Weibull distribution was selected for wind modelling, while a family of distributions was used for modelling GHI data. The Louche model, which decomposes the GHI into its components, was selected for modelling the DNI. The capabilities of the various models and the implemented methodology were tested by comparing the model predictions to historical data for Chile and Canada, with the results indicating that the models produce renewables profiles which are accurate enough to be used for preliminary sizing purposes. The profiles generated also cover the range of potential input levels present in the historical data except in the most extreme cases, making them representative enough to be used for reliability evaluation.

For each of the renewable input scenarios generated, the optimal design and sizing of the energy system required for a given level of performance can be determined, as has been done in other works in literature and was demonstrated in the single objective case study in the previous chapter. The performance of a given design will change with the level of renewables available: "good" scenarios will lead to higher demand satisfaction, and vice versa. Hence, to evaluate the impact of variability in renewables availability on energy system design and sizing, a suitable measure which takes into account the information provided by the individual scenarios to produce a single index to represent the performance between scenarios is required. This will be the focus of the next chapter.

Chapter 5.

ACCOUNTING FOR CLIMATE-BASED VARIABILITY IN RELIABILITY EVALUATION

This chapter focuses on how chronological simulation can be applied in stochastic reliability evaluation. Two approaches are presented, with the potential advantages and drawbacks of each approach discussed. Development of secondary reliability measures which allow for variability to be accounted for are also discussed.

Previous works on integrated energy systems sizing based on the chronological approach (reviewed in Chapter 2) focused on accounting for variability within fixed input scenarios, typically one year. The reliability measures currently available in literature were specifically designed for this purpose. In order to apply the chronological approach to multiple years of input data, reliability measures which allow for the stochastic nature of renewables input to be accounted for must be developed. This will be the focus of this chapter.

Given a set of renewable input conditions, application of chronological simulation to determine system reliability can be done in two ways.

5.1. Lumping of Renewables Input Data

In this approach, multiple years of input data are simply lumped into a single data set. The conventional reliability measures can then be applied directly for system sizing based on the resultant dataset. Thus, renewables variability is accounted for by applying chronological simulation to a larger dataset. The approach was adopted by Kueh et al. [130] for the sizing of molten salt thermal storage systems. The method provides a single index of reliability which represents the performance of the system over the entire time period.

The main drawback of this approach is that useful information about design performance within individual years is lost due to the aggregated nature of the method: the designer is

unable to tell whether the reliability index obtained provides representative information about each individual year or not. While variability between years is accounted for with this approach, its effect is not quantified.

5.2. Introduction of Secondary Reliability Measures

In this approach, each input scenario is treated independently. The reliability of the energy system within each scenario is evaluated using chronological simulation. This yields a set of reliability indices which must then be combined in some manner to generate a single index of reliability representing overall performance. As such, the individual in-scenario (primary) reliabilities act as an input in the evaluation of a secondary reliability measure. The challenge with this approach is the development of suitable secondary reliability measures with actual physical meanings.

Three secondary reliability measures were considered for extending the conventional reliability measures to account for variability between years: the mean reliability, the minimum reliability and the modified loss of power supply probability.

The descriptions presented in the following sections will be based on a generic measure of reliability R. R may be any of the conventional reliability measures available in literature, some of which which have been described previously (Section 2.1.1).

5.2.1. Mean reliability

In this approach, the reliability of the energy system under each input scenario is evaluated and the values averaged. If the reliability of the design in scenario i is R_i, then the mean reliability over N scenarios is given by

$$\overline{R} = \frac{\sum_{i=1}^{N} R_i}{N} \tag{5.1}$$

The mean reliability reflects the average performance of the given energy system within the period of operation (typically one year). For example, considering the loss of power supply probability, a value of $\overline{LPSP} = 0.05$ indicates that the energy system will, on the average, fail to meet plant demands for 5% of the year.

The equation presented above is based on the assumption that all the input scenarios are equally likely to occur. When this is not the case and some input profiles are more likely than others, the weighted-average can be used. If the reliability in each year is weighted by some factor p_i, Equation 5.1 becomes

$$\overline{R} = \frac{\sum_{i=1}^{N} p_i R_i}{\sum_{i=1}^{N} p_i} \tag{5.2}$$

where p_i is a weight related to the probability of scenario i occurring. The key in the weighted averaging approach is the determination of sufficiently accurate weights for the individual input scenarios.

The mean reliability is straightforward to evaluate and retains a similar meaning to the original reliability measure used in its evaluation, providing information about performance and design choices within the year. The ability to weight each scenario also provides a distinct advantage for this approach.

The main drawback of this approach is the amount of information lost during the averaging process. For systems with low degree of variability, the performance between scenarios will be similar and the measure will provide a good estimate of the performance. For locations with high degree of variability however the performance of the energy system between scenarios may be very different, and any value obtained by this method would be misleading. For example, a design with loss of power supply probabilities of 0.5 and 0.54 in two different years will have $\overline{LPSP} = 0.52$. In reality, the difference in performance between the two scenarios is the equivalent two weeks of design failure (350 h). As such, the mean reliability would be inadequate for such problems.

5.2.2. Minimum reliability

In this approach, the reliability of the energy system under each input scenario is evaluated and the worst case performance selected as representative for the design. For measures whose indices measure the frequency or magnitude of system failure such as the LPSP and EENS, the minimum reliability over N scenarios is given by

$$\overline{R} = \max_i (R_i) \qquad i = 1, 2, \ldots N \tag{5.3}$$

For indices that measure the frequency or magnitude of demand satisfaction such as the EIR,

$$\overline{R} = \min_i (R_i) \qquad i = 1, 2, \ldots N \tag{5.4}$$

This minimum reliability provides information about the worst possible performance that can be expected from the energy system within the period of operation. As such, the method implicitly fixes the reliability between scenarios to 100%. For example, a value of $\overline{LPSP} = 0.1$ means that the primary energy system will, in all scenarios (100% of the time), meet demands for at least 90% of the year.

It should be noted that the scenarios which generate the worst performance for different designs may not necessarily be the same. A design X can perform better than another design Y in one scenario but worse in another. Thus, the minimum reliability approach to design is different from simply designing for the scenario with the least renewables availability.

Multi-objective design with this measure will produce a set of designs guaranteed to produce a certain level of performance $\left(\overline{R}\right)$ irrespective of input scenario. The measure therefore provides information that is suitable for planning and decision-making since

concrete information about the backup system (such as the maximum annual diesel consumption and maximum CO_2 emissions) can easily be inferred. Potential changes in choice of technologies can also be monitored with this approach. However, the method does not take into account the performance in the other years, meaning that significant oversizing of designs can occur due to one extremely poor input scenario.

5.2.3. Frequency-based approach: Modified loss of power supply probability

In this approach, the secondary reliability is measured in terms of the probability of satisfying a preset primary reliability constraint. The performance of the energy system in each input scenario is binary; it either fails or succeeds. A design is said to have failed in a given scenario if the reliability within the scenario is worse than an allowable threshold R'. Based on this, a modified version of the loss of power supply probability (represented by $\overline{LPSP}_m$ throughout this work) is implemented:

$$\overline{LPSP}_m = \frac{\text{Number of scenarios in which design fails } (R_i < R')}{\text{Total number of scenarios}} = \frac{N\,|_{R_i<R'}}{N} \tag{5.5}$$

where $R_i < R'$ is the preset reliability condition (or internal constraint). The expression contains two reliability measures: the primary reliability measure R_i which forms part of the internal constraint and represents the expected level of performance within the year, and a secondary reliability measure $\overline{LPSP}_m$ which represents expected performance between years.

The modified LPSP represents the frequency with which the set internal reliability constraint is violated by the design. As such, the output is probabilistic irrespective of the type of internal constraint implemented. The internal constraint sets the threshold performance for the designs to be generated as each design with $\overline{LPSP}_m < 1$ will have satisfied the constraint at least once. The design reliability is a function of the threshold R': as the constraint is tightened, the reliability decreases. However, the modified LPSP does not account for the degree of failure: a design which fails by 1% in a scenario is no different from a design which fails by 20%, for example.

The measure is fundamentally different from the measures previously presented: the index in this case provides information about design performance between (rather than within) scenarios. It quantifies how frequently a given design will meet the required yearly performance given the potential variability at the location.

The internal (intra-year) reliability constraint may be based on any of the conventional reliability measures. Multi-objective design with this measure will contain a set of designs that have different probabilities of satisfying the preset reliability condition. For example, a value of $\overline{LPSP}_m = 0.1$ for the reliability measure

$$\overline{LPSP}_m = \frac{N\,|_{EIR<80\%}}{N}$$

indicates that the design evaluated will meet at least 80% of the demands in 90% of the

input scenarios. Thus, both the internal reliability measure R_i (which determines the acceptable performance within scenarios) and the secondary reliability measure $\overline{LPSP}_m$ (which represents the system performance between scenarios) can be modified at the design stage. This makes the approach attractive. Design oversizing due to poor input scenarios can also be avoided since this would be reflected on the trade-off curve.

The main drawback with the approach is the need to set the acceptable threshold R' at the start of the optimization process. This is not a problem when there is a specific (minimum) reliability target to be achieved by the design. It however poses a challenge when the aim is to make design decisions based on both the performance between and within years. In such cases, the cost-reliability trade-off curve must be generated for multiple values of R'.

The focus of this work is the development of a methodology for the preliminary design and sizing of energy systems which allows us to account for the stochastic nature of renewables availability at the design stage in some form. While all the measures presented above allow us to do this, the modified loss of power supply probability allows us to actually quantify the effect of climate-based variability, making it the most suitable alternative. It will therefore be used in this work.

Summary

A stochastic measure for quantifying the risk of failure associated with the selection of a given design due to variability in renewables availability was developed in this chapter. Having previously developed an energy system model (Chapter 3) and a suitable methodology for synthetic renewables data generation (Chapter 4), the challenge of developing a sizing methodology for the energy system can now be addressed. This will be the focus of the next chapter.

Chapter 6.

MULTI-OBJECTIVE DESIGN OF INTEGRATED ENERGY SYSTEMS

This chapter focuses on addressing the variability challenge inherent in the design and sizing of stand-alone renewables-based energy systems at the design stage. In order to achieve this, a methodology for solving the bi-objective problem of capital cost minimization and reliability maximization for such an energy system is developed. The framework requires a procedural approach to performance evaluation and the development of an overall operating scheme for the energy system. The modified loss of power supply probability ($\overline{LPSP}_m$) is implemented as the reliability objective. To demonstrate the capabilities of the methodology, the bi-criteria problem is solved for three cases of remotely-located mining operations in Chile and Canada, with approximations to the Pareto-optimal fronts generated using a multi-objective genetic algorithm (NSGA-II). For each study, the performances of the minimum-cost designs generated are investigated. The results provide the decision maker with necessary information about a number of alternative high-performance designs based on which sizing decisions can be made.

The case study presented in Section 3.5 demonstrated how the sizing of energy systems can be done with the assumption of fixed input conditions. The design approach used in the study accounted for daily and seasonal variability, but assumed constant renewables availability between years. This is the same approach adopted by state-of-the-art works on energy system sizing (Chapter 2). In reality however, the availability of renewables can be markedly different between years. While this stochastic nature is expected to cause deviations from the expected performance [241], little is known about how much of an effect variability can have on the sizing and performance of energy systems.

To gain an insight into this, a two-stage approach was initially adopted to investigate how solar resource variability impacted the sizing and performance of the solar-based hybrid energy system considered in the single objective case study (Section 3.5). The approach monitored how feasible designs generated under fixed input conditions for 100% demand

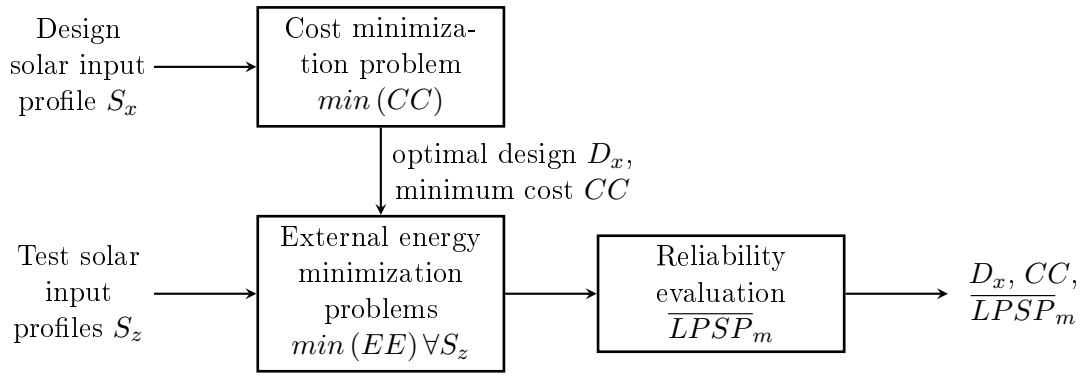

Figure 6.1.: Two-stage approach for investigating the impact of renewables variability on hybrid energy systems design.

satisfaction performed under other feasible input conditions. A schematic representation of the approach for a single design is shown in Figure 6.1.

First, synthetic renewable input scenarios were generated using the methodology presented in section 4.3. The scenarios represent feasible renewable input conditions based on the historical data. NLP cost minimization problems were solved for each of potential input scenarios to generate a set of potential energy system designs. Each of the designs (D_x) generated was optimal for a given renewable input condition (S_x). The impact of renewables variability on the different designs was then investigated by determining how well the generated designs performed when the input conditions were changed. This was measured by how frequently the designs were able to meet the original design target (100% demand satisfaction) under a number of other stochastically generated input scenarios (S_z). In each renewable input scenario, the capability of a given design to meet demand was determined by solving an NLP optimization problem minimizing the external energy (EE) supplied to the mine from outside the renewable energy system. A value of $EE > 0$ indicated the power supplied by the hybrid system was insufficient to power the mine. Based on the information obtained from the different scenarios for each design, the reliability between scenarios was then represented using the $\overline{LPSP}_m$ measure. Details about the approach may be found in Amusat et al. [12].

The approach was applied to two locations with different degrees of variability: Canada and Chile. The NLP optimization problems were implemented in GAMS 24.2 and solved with BARON 12.7.3, while solar radiation modelling, scenario generation and reliability calculations were implemented in MATLAB [150]. Solar input profiles for consecutive mid-winter days were considered. Figures 6.2a and 6.2b show the cost and reliabilities of 250 different designs generated for the locations. Each circle represents a different design. It is clear from the results that variability can have a significant impact on the cost and performance of designs, and that sub-optimal design choices are likely when design decisions are made without taking variability into account. The degree of variability is also important, as is reflected by the difference in the degree of spread of the designs observed in the two cases.

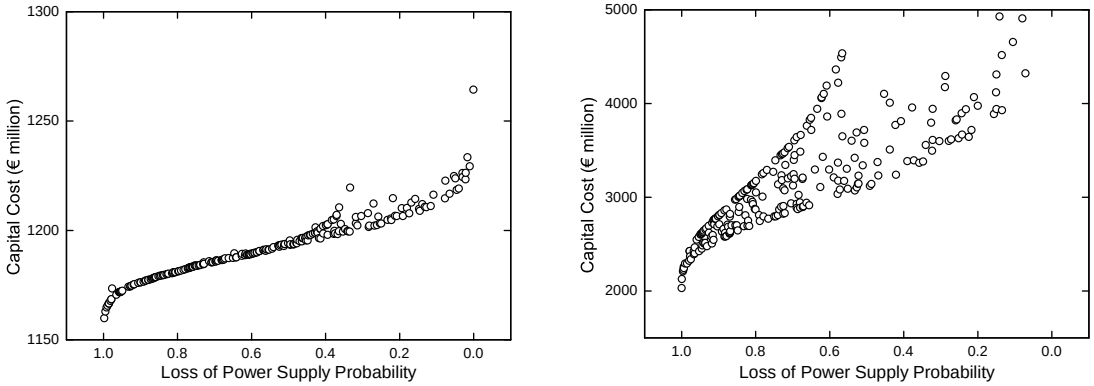

(a) Chile (b) Canada

Figure 6.2.: Cost and reliability information for the different designs generated via two-stage approach. The designs for Canada are more spread out that those for Chile due to the higher degree of variability [12].

The results of the two-stage approach show that the cost and the reliability cannot be treated independently: both need to be considered together as objectives at the design stage. Thus, a multi-objective problem arises. Developing a framework to solve this problem will be the focus of this chapter.

For this, we consider the energy superstructure described in Section 3.2. First, the multi-objective problem is described fully, and the implementation and solution strategies are described. The methodology is then demonstrated using three case studies.

6.1. Problem Definition

The aim of the optimization procedure is to generate a cost-optimal set of designs capable of full thermal and electrical demand satisfaction while taking into account possible variability in renewables availability at the location. The bi-criteria problem may be stated as follows:

Given the energy requirements of the plant, a number of possible renewable input profiles (N) representing potential weather conditions at the plant location, the unit cost data for the generation and storage alternatives ($U_i^{gen}, U_j^s, U_j^{out}$), and the efficiencies for all mechanical units (compressors, turbines, motors, generators and pumps), determine the Pareto-optimal set of designs $\bar{X} = \{\bar{x}_1, \bar{x}_2 \dots \bar{x}_n\}$ which minimize the capital cost $CC(\bar{x})$ of the energy system and maximize reliability $R(\bar{x})$:

$$\min_{\bar{x} \in \bar{X}} z = (F_1, F_2) \begin{cases} F_1(\bar{x}) = CC(\bar{x}) \\ F_2(\bar{x}) = -R(\bar{x}) \end{cases} \tag{6.1}$$

subject to generation, storage and operational constraints.

The cost objective is given by Equation 3.45. For this study, the modified LPSP ($\overline{LPSP}_m$) is implemented as the reliability measure, with the conventional loss of power

supply probability (given by Equation 2.1) enforced as the internal constraint. Given that the aim is to achieve full demand satisfaction from local generation, the designs generated must be capable of operation without external energy support ($LPSP = 0$). Thus, Equation 6.1 may be rewritten as:

$$\min_{\bar{x}\in\bar{X}} z = (F_1, F_2) \begin{cases} F_1(\bar{x}) = \sum_{i=1}^{n_g} U_i^{gen} A_i^{gen}(\bar{x}) + \sum_{j=1}^{n_s} \left[U_j^s C_j^s(\bar{x}) + U_j^{out} C_j^{out}(\bar{x}) \right] \\ F_2(\bar{x}) = \overline{LPSP}_m(\bar{x}) = \frac{N|_{LPSP(\bar{x})>0}}{N} \end{cases} \tag{6.2}$$

where n_g and n_s are the number of available generation and storage options respectively, and N the number of renewable input conditions (number of scenarios) considered.

6.2. Model Discretization: Forward Euler Method

For this study, the differential-algebraic system of equations representing the energy system (presented in Section 3.3) was discretized using Euler's forward differencing technique. For an ordinary differential equation of the form:

$$\frac{\mathrm{d}y}{\mathrm{d}t} = f(t, y)$$

discretization with the forward Euler method gives the approximation at point λ as

$$y_{\lambda+1} = y_\lambda + f(t_\lambda, y_\lambda) \cdot \Delta t \tag{6.3}$$

The scheme was implemented with a uniform time step Δt. The time horizon, $t \in [0, t_{final}]$ is discretised into n_t intervals, $\Delta t = \frac{t_{final}}{n_t}$. We introduce $\tau = 0, \ldots, n_t$ as an index into the discretised time interval. All time dependent continuous variables in the model are replaced by corresponding time-step indexed discrete terms.

The backward Euler method is fully explicit, is simple and direct to implement, and can be applied to nonlinear initial value problems [191]. The method is numerically unstable for stiff problems, requiring very small step sizes [126]. However, it is an approach which has been used frequently in literature for problems involving energy system sizing [68, 120, 241], suggesting that it is sufficient for this work.

The decision to change discretization schemes for this problem was because of the complexity involved in the evaluation of the dynamic equations associated with thermal storage. For example, consider the dynamic equation for the thermal energy store (TES) of the AA-CAES system:

$$\rho c_p V_s \frac{\mathrm{d}}{\mathrm{d}t} T^{TES}(t) = \left[\dot{Q}^{TES,in}(t) - \dot{Q}^{TES,out}(t) - \dot{Q}^{TES,loss}(t) \right]$$

Simplifying the equation by assuming no heat flows into or out of the system and intro-

ducing the convective heat loss expression, the equation becomes:

$$\rho c_p V_s \frac{\mathrm{d}}{\mathrm{d}t} T^{TES}(t) = -UA(T^{TES}(t) - T_{ambient})$$

Applying the Backward Euler method to the equation and re-arranging gives the current temperature of the thermal energy store as:

$$T_{\tau}^{TES} = T_{\tau-1}^{TES} - \frac{UA\Delta t}{\rho c_p V_s}(T_{\tau}^{TES} - T_{ambient}) \qquad \tau = 1, \ldots, n_t$$

The presence of the current TES temperature $\left(T_{\tau}^{TES}\right)$ on both sides of the equation means that an iterative approach (such as the Newton-Raphson method) is required for its solution. This was not a challenge in the single objective case study since the model was implemented and solved in GAMS which performs the iterations automatically. Given that the aim is to develop a general methodology for solving the multi-objective problem which can be applied irrespective of programming platform or software however, it is important to use a discretization approach which can easily be implemented. For some programs such as MATLAB for example, the iterative approach required for the backward Euler method would need to be implemented manually and evaluated using a loop. This would complicate the problem and increase computation time since the iteration for each equation must be evaluated at every time step.

The use of the forward Euler method avoids this problem as the expression is evaluated completely at the previous time step,

$$T_{\tau}^{TES} = T_{\tau-1}^{TES} - \frac{UA\Delta t}{\rho c_p V_s}(T_{\tau-1}^{TES} - T_{ambient}) \qquad \tau = 1, \ldots, n_t$$

The problem therefore becomes a forward-discretized initial value problem.

6.3. Model Implementation for Reliability Evaluation

The discretized model for the hybrid energy system was implemented in MATLAB 8.3 [150]. Hourly time steps were considered for the discretization of the entire model. With the operation starting at midnight, the storage options were initialized to be 60% charged at the start of operation in order to meet the plant demands for the first morning.

The switch from GAMS to MATLAB was required in order to evaluate the system performance based on a full year of renewables input data. The large number of time steps required for a full year, coupled with the nature of the solvers available (gradient-based and branching-based solvers), made the simultaneous solution approach used by GAMS unsuitable for this problem: the model became intractable. With MATLAB, the model is evaluated in a step-wise rather than simultaneous manner, making the problem slightly easier to solve.

For each input scenario, evaluation of system model comprises of the repeating following steps at each time interval τ:

1. The outputs of the generation units $\dot{E}_{i,\tau}^{gen}$ are calculated. The portion of the thermal and electrical loads that could be satisfied directly from the generation, as well as the excess generation, are determined. The electrical generation options are prioritized for power supply. If shortfalls exist, go to step 2. If all demands have been satisfied, go to step 4.
2. The thermal and electrical outputs of the storage units are determined. Due to the number of storage options and energy routes available in the superstructure, the problem of the order in which the options are operated (charged and discharged) within the system must be addressed.

   Ideally, the order is determined at each time step to obtain the best overall performance of the system. In order to achieve this however, separate design variables for the charge and discharge phases would be required for each time step. For example, a year of data with hourly discretization would require 8,760 variables for the discharge phase, with each variable able to take up at least 6 possible values (3! combinations). The combinatorics involved would make such a problem intractable. To address this problem, an overall operating scheme was developed for the discharge phase. This is shown in Algorithm 6.1.

   The implemented scheme prioritizes the satisfaction of thermal demands of the plant. This decision was made because of the fewer number of heat supply alternatives (PHES systems cannot supply heat) and the smaller heat requirements of the plant.

   Two factors were considered in determining the order in which the storage options are charged or discharged:

   - the form in which the energy is stored, and
   - the type of losses associated with the storage.

   For heat supply, the MTS system takes precedence over the AA-CAES system. For electricity storage, the PHES system is discharged after the AA-CAES system due to the use-dependent nature of its losses. Three possible operating schemes emerge once the order of discharge of the AA-CAES/PHES systems is constrained. The alternative schemes are implemented in the model and an extra design variable $\left(\overline{OP}\right)$ is used to select the scheme to use. Thus, the design vector is extended to contain an extra element to select the operating scheme:

$$\overline{x} = \left\{C_i^{gen}, C_j^s, C_j^{out}, \overline{OP}\right\} \qquad \forall i, j$$

   The variable can take integer values between 1 and 3, with each variable corresponding to a different mode of operation. The model therefore not only decides on the optimal energy scheme design; it also determines the best operating scheme for the system.

   The electrical power output of any storage system over interval τ is dependent on the unmet electrical load $\dot{\phi}_{\tau}^{el}$, the current storage state $S_{j,\tau}$, and the dispatch capacity of the storage system C_j^{out}. The unmet load is re-evaluated after the dispatch

Algorithm 6.1 Pseudocode for operating scheme implemented in energy system.

Given: Design specifications $\overline{x} = \left\{C_i^{gen}, C_j^s, C_j^{out}, \overline{OP}\right\}$; demand requirements from storage $\left\{\dot{Q}_\tau^{th}, \dot{E}_\tau^{el}\right\}$.

Output: Storage outputs $\left\{\dot{Q}_{j,\tau}^{heating}, \dot{E}_{j,\tau}^{out}\right\}$; Power shortfalls $\left\{\dot{\phi}_\tau^{th}, \dot{\phi}_\tau^{el}\right\}$

procedure DISCHARGE SUB-MODEL

a) Satisfy thermal demands

- Meet shortfall from MTS system $\dot{Q}_{1,\tau}^{heating}$.
- Evaluate heating requirement shortfall ϕ_τ^{th}. If shortfall exists, try to meet from AA-CAES system $\dot{Q}_{2,\tau}^{heating}$.
- Re-evaluate heating requirement shortfall $\dot{\phi}_\tau^{th} = \dot{Q}_\tau^{th} - \dot{Q}_{1,\tau}^{heating} - \dot{Q}_{2,\tau}^{heating}$.

b) Satisfy electrical demands

- Evaluate storage outputs $\dot{E}_{j,\tau}^{out}$ as specified by the operating scheme selected:
  - If $\overline{OP} = 1$, discharge storage in the order: AA-CAES - MTS - PHES.
  - If $\overline{OP} = 2$, discharge storage in the order: AA-CAES - PHES - MTS.
  - If $\overline{OP} = 3$, discharge storage in the order: MTS - AA-CAES - PHES.
- Evaluate electrical requirement shortfall $\dot{\phi}_\tau^{el} = \dot{E}_\tau^{el} - \sum_{j=1}^{3} \dot{E}_{j,\tau}^{out}$.

end procedure

step to determine what is required from the next storage option. The storage state is also re-evaluated after each discharge step. This procedure continues until either all the storage options have been dispatched or all the demand has been satisfied.

With the approach used for the single objective case study, decisions on the operation of the energy system (such as which storage options to charge/discharge and to what degree) were made at each time step. The implementation of the operating scheme reduces the complexity of the problem significantly as only one extra design variable needs to be optimized: only one decision needs to be made regarding system operation for the entire year. This makes it possible to obtain feasible and resonable solutions. The implication of this however is that the performance of the energy system within each input scenario may be slightly less than optimal. This is because the possibility of switching from one operating scheme to another between time steps to improve overall performance is no longer available to the optimizer. Once a discharge order is selected, it cannot be changed.

3. Evaluate total energy shortfall. Any shortfall (thermal or electrical) left after the dispatch of the all storage options will need to be supplied externally. External energy $E_\tau^{ext} = \left[\dot{\phi}_\tau^{el} + \dot{\phi}_\tau^{th}\right] \cdot \Delta t$ is only required if energy from local generation and storage is insufficient to satisfy demand, thermal or electrical.
4. Evaluate storage end state. The PHES system is charged before the AA-CAES system due to the use-dependent nature of its losses. The storage level at the end

of the time step τ forms the start state at the next time step $\tau + 1$.

5. When storage options become full, dump excess generation.

The steps are repeated for all n_t intervals. The approach mimics how plants are operated in reality as only the previous and current states of generation, storage level and demand are taken into account in decision making at each time step. At the end of each scenario, the $LPSP$ of the system is calculated with Equation 2.1.

After the performance of the design has been evaluated in all the scenarios, the reliability of the design between scenarios can be calculated as shown in Equation 6.2.

Given the design variables (nominal capacities of the generation units, storage and output capacities of storage units, and the choice of operating scheme) and a number of renewable input scenarios, the implemented model returns the cost and reliability of the energy system.

6.4. Solution Methodology

The bi-criteria problem to generate the Pareto-optimal set of designs was solved using NSGA-II [56], a non-dominated sorting-based multiobjective evolutionary algorithm (MOEA) as implemented by Song [205]. Figure 6.3 shows the flowchart for the process.

A typical generic algorithm has 5 major parts: an initial random population generator, a "fitness" evaluation unit and genetic operators for the selection, crossover and mutation operations [77]. NSGA-II is based on the concepts of uncontrolled elitism and non-dominated sorting [57].

Algorithm 6.2 shows the procedure for NSGA-II. The process starts with the generation of an initial random parent population P_0 of size N_{pop}. Non-dominated sorting of the initial population is done. A solution is non-dominated if no other solution exists which improves on one of the objectives without worsening the other objective. Each solution is assigned a rank based on the level of non-domination as illustrated in Figure 6.4. The better the solution, the lower its rank.

A child population of size N_{pop} is created from the parent P_0 using the crossover, mutation and selection operators. This forms a combined parent-offspring population of size $2N_{pop}$. The fitness of the points are evaluated and sorting is done again based on the non-domination principle. This ensures that the fittest candidates from both populations survive. This concept is known as elitism. The best N_{pop} solutions are selected in order of fitness and location relative to other solutions (called the crowding distance) to form the new parent P_1, with the other N_{pop} points discarded. The crowding distance helps to maintain spread of solutions along the front [57]. The genetic operators for selection, mutation and crossover are then used to create a new child population. The iterative process continues until the termination criterion is satisfied, with the final parent population returned as the Pareto front. The quality of the solutions improve with each iteration since only the fittest solutions are retained through the simulation.

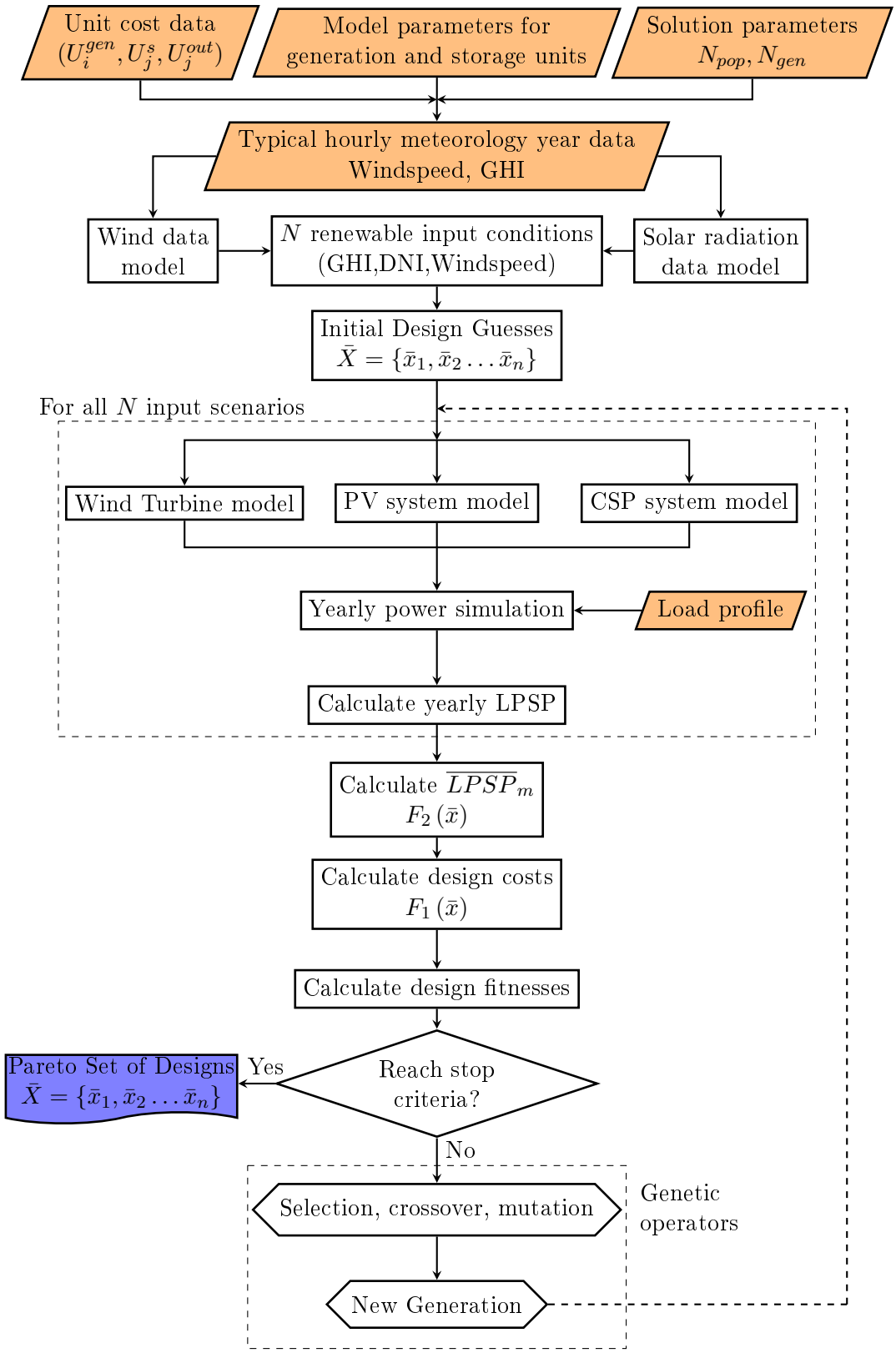

Figure 6.3.: Flowchart for optimal sizing using multi-objective genetic algorithm. The input requirements for the scheme are highlighted in orange.

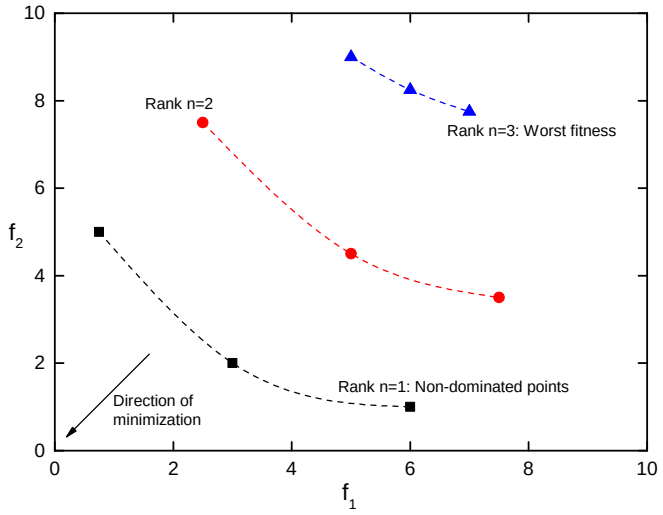

Figure 6.4.: Scatter plot showing example of non-dominated sorting for a minimization problem. The black boxes are the non-dominated solutions with the best fitness values. Together, they form the current approximation to the Pareto front. These points are selected first in the formation of the new parent. The blue triangles are the points with the worst fitness function and are likely to drop out of the population due to elitism.

Algorithm 6.2 NSGA-II algorithm. Adapted from Deb and Goel [57].

Given: N_{pop}, the population size; and N_{gen}, number of generations to perform.
Output: Z, vector approximation to Pareto front

Create random initial parent population P_0
$\mathcal{F} =$ `ND-sort`(P_0) ▷ Non-dominated sorting of initial parent population
$C_0=$ `makepop`(P_0) ▷ Make initial child population from parent initial population
for N_g generations **do**
  $R_t = P_t \cup C_t$ ▷ Combine population of parent and offspring
  $\mathcal{F} =$ `ND-sort`(R_t) ▷ Fast non-dominated sorting of combined population
  $P_{t+1} = \phi$ and $i = 1$ ▷ Start with empty population and non-dominated front
  while $\mid P_{t+1} \mid + \mid \mathcal{F}_i \mid \leq N_{pop}$ **do**
    $P_{t+1} = P_{t+1} + \mathcal{F}_i$ ▷ Add non-dominated front to parent population
    `crowding-distance`$(\mathcal{F}_i)$ ▷ Calculate crowding distance of members
    $i = i + 1$
  end while
  sort $(\mathcal{F}_i, \mathcal{L}_n)$ ▷ Sort current P_{t+1} members based on rank and crowding distance
  $P_{t+1} = P_{t+1} \cup \mathcal{F}_i\,[1 : (N_{pop} - \mid P_{t+1} \mid)]$ ▷ Select remaining members based on crowding distance of last front
  $C_{t+1}=$ `makepop`(P_{t+1}) ▷ Make new child population from parent population
  $t = t + 1$
end for

$Z \leftarrow P$ ▷ Final population is Pareto front approximation

Table 6.1.: NSGA-II parameters for case studies

Population size	$N_{pop} = 100$
Selection	Binary tournament selection
Crossover	Intermediate crossover, Crossover fraction = 0.75
Mutation	Gaussian mutation, mutation fraction = 0.1
Stopping criteria	Maximum number of generations, $N_g = 300$

Genetic algorithms are the most widely used method for solving problems involving hybrid energy system sizing [77], with several variants used in single objective [7, 241] and multi-objective problems [3, 68, 170]. This is because of the ability of genetic algorithms to jump out of local minimas even for large problems with infinite number of design variables [77]. This means that they are quite efficient in finding the global optimum. Genetic algorithms also offer other advantages: they require no derivative information, and they can handle non-continuous problems. However, genetic algorithms can be slow, are relatively hard to code and offer no optimality guarantee [77, 209].

Other approaches which have been used in energy system sizing include particle swarm optimization and simulated annealing. However, both of these approaches are less reliable at finding the global optimum and unsuitable for complex problems with more than three design parameters [77]. A review of stochastic hybrid energy system sizing approaches may found in Erdinc and Uzunoglu [77].

The use of a genetic algorithm for this problem allows us to generate designs and evaluate performance based on full years of renewables input data while avoiding the intractability problem that was encountered with the previous approach. However, the stochastic nature of the solver means that a number of runs may be required to obtain a measure of confidence in the results.

As can be seen from Figure 6.3, the renewable input profiles for performance evaluation are generated before the stochastic solution procedure begins. This is different from the approach adopted by Kaplani and Kaplanis [118] for their PV-battery system where the daily probability distribution sampling was done within the iterative solution algorithm - essentially a Monte-Carlo simulation. Generating a single set of input profiles for design performance evaluation reduces the simulation time and ensures that all the designs are compared on the same basis.

6.5. Case Studies

Three case studies are presented in this work. The first two cases consider the stand-alone design of solar-based renewable energy systems (RES) for locations with different degrees of renewables availability and variability. The third study presents the design of a RES integrating both solar and wind generation alternatives. Together, the studies explore a range of input conditions and technologies, allowing us to stress-test the methodology and the model.

The NSGA-II parameters used for the case studies are presented in Table 6.1. Here, the

Table 6.2.: Statistical properties of generated solar input profiles for Chile.

	Mean[$^{kWh}/_{m^2}$]	Maximum deviation from mean
Global Horizontal Irradiance (GHI)	2672	-0.97% to +0.54%
Direct Normal Irradiance (DNI)	3627	-1.71% to +1.29%

stopping criteria is set as the maximum number of generations: the algorithm terminates after 300 generations. The final generation accepted as the solution to the problem.

The parameters and cost data used in the studies are presented in Appendix B.

6.5.1. Multi-objective design of stand-alone solar-based system for Chile

The first case study considers the multi-objective design of a solar-based renewable energy system for the Chilean mine described in Section 3.5.1. The average power requirement of the mine in July 2013, shown in Appendix B.3, was considered as the power demand data in this study. The thermal demands of the plant were again assumed to be 10% of the electrical demands.

Statistical properties for global horizontal irradiance (GHI) at the mine location may be found in Appendix E. The determination of an adequate number of input profiles to generate in order to obtain a relatively accurate estimate of the reliability provided a challenge. The accuracy of the reliability evaluation increases with the number of renewable input profiles evaluated, but this occurs at the expense of the computational (and time) requirements. A trade-off between the level of convergence and the computational time was therefore required. Tina et al. [217] suggested that 50 simulated years of Monte-Carlo simulation were sufficient to obtain convergence between the chronological (simulation) and analytical approaches to reliability evaluation to within 2% for a PV-wind hybrid system. On the other hand, for the same type of system, Khatod et al. [124] suggested that between 200 and 500 simulated years of Monte-Carlo simulation were required for convergence. The wide difference in values alluded to the system and location-specific nature of the problem.

To determine an adequate number of profiles for this work, 1,000 randomly simulated years were employed for the evaluation of the reliabilities of a number of designs for Canada and Chile, with the reliability after each simulation year monitored for each of the designs. The results obtained suggested that the reliability measure converged to within $\pm 2\%$ of the final value after about 250-280 simulated years. 300 randomly simulated profiles were therefore considered sufficient for reliability evaluation. Further details about about the convergence tests may be found in Appendix C. The GHI and DNI profiles were generated as described in Section 4.3. Table 6.2 shows the statistical properties of the 300 input profiles generated. The low deviations from the mean for GHI and DNI suggests a low degree of variability in solar availability at the location.

The system has nine design variables in this problem. The variable bounds used in the study are shown in Table 6.3.

Table 6.3.: NSGA-II variable bounds for Chilean case study

Variable	C_i^{gen} [MW]	C_j^s [MWh]	C_j^{out} [MW_e]	$\overline{OP}$
Lower bound	0	0	0	1
Upper bound	3,000	10,000	400	3

i = generation technologies $\{PT, PV\}$, j = storage technologies

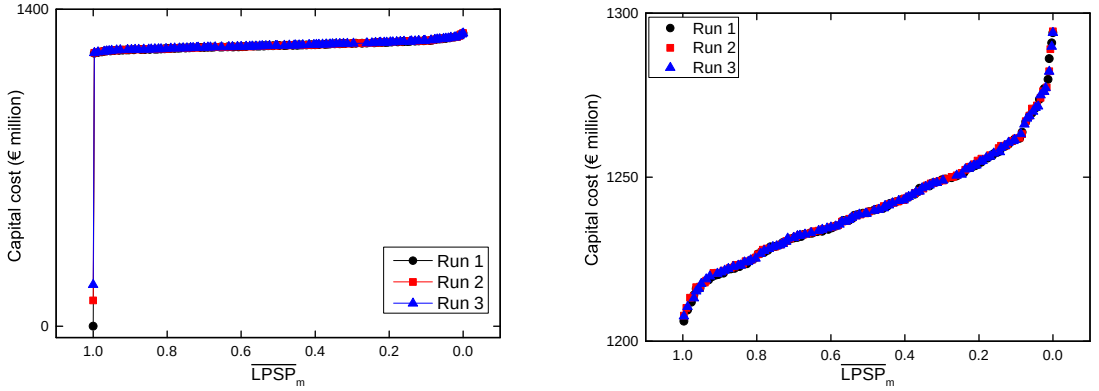

(a) Full Pareto front with trivial ($\overline{LPSP}_m = 1$) solutions

(b) A zoomed in view of Figure 6.5a after removal of trivial solutions

Figure 6.5.: Approximations to Pareto front for Chile from three attempts with NSGA-II

6.5.1.1. Trade-off curve

Figure 6.5 shows the non-dominated objective function values for 3 attempts. The average wall clock time from start to finish for the three parallelized runs was 107.5 h on a Linux based machine with eight 2.4 GHz Intel Xeon processors and 16 GB RAM. There is very little difference between the results of the three runs, giving a measure of confidence that set of non-dominated solutions have been identified well. The minimum cost solution involves doing nothing: powering the mine purely by diesel generation with no renewables generation installed. The Pareto curve can be seen to converge towards this trivial solution $\left(\overline{LPSP}_m = 1, CC = 0\right)$ on the left part of the Figure 6.5a. However, the solution provides no information and will be ignored (Figure 6.5b). The minimum cost design is considered to be the next best solution; $\overline{LPSP}_m \in [0, 1)$. For analysis of the designs, the Pareto front identified from the first run is considered.

Figure 6.6 shows the approximation to cost-reliability Pareto-optimal front. The capital cost varies by 7.3% (€ 88M) over the entire reliability range. The small cost variation reflects the low variability in renewables input for the location.

To understand the shape of the trade-off curve, we look at the properties of the solar input profiles. For each input scenario, the annual direct normal radiation may be obtained from the instantaneous (discrete) DNI as:

$$\text{Annual direct normal radiation } \left(\text{kWh/m}^2\text{.year}\right) = \sum_{\tau=0}^{t_{final}} \dot{G}_{\tau}^{\ DNI} \cdot \Delta t \tag{6.4}$$

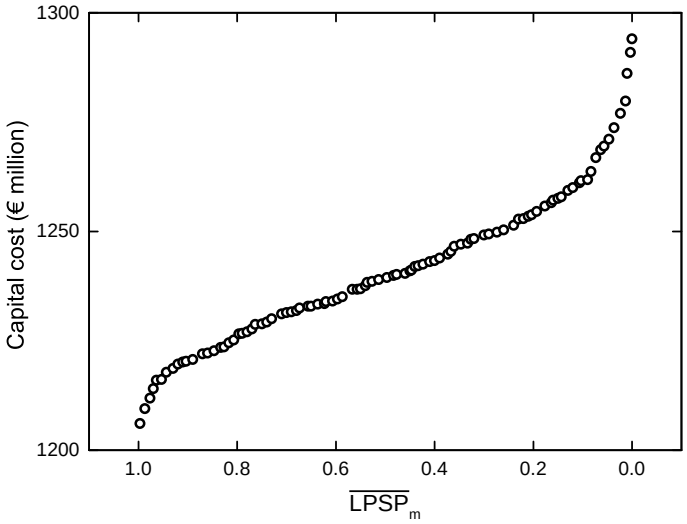

Figure 6.6.: Cost-reliability trade-off curve for solar-based system

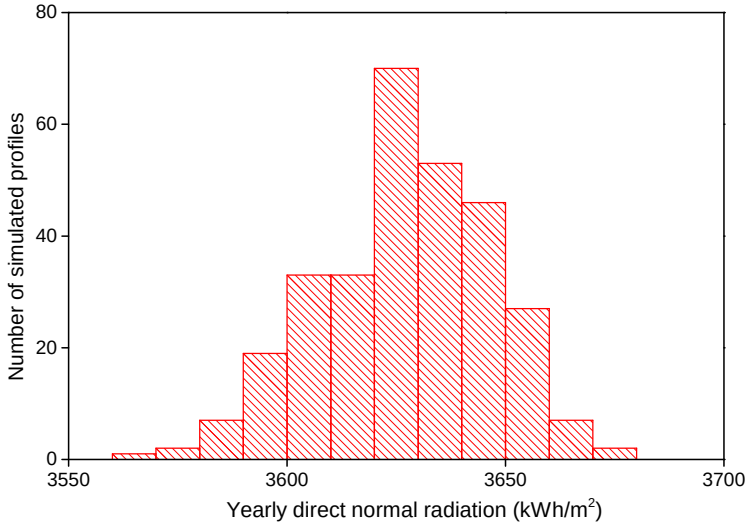

Figure 6.7.: Histogram of 300 solar input profiles for Chile

Figure 6.7 shows the histogram formed by the input profiles generated for the study. The input profiles are normally distributed as expected: the chance of a solar input condition occurring decreases away from the mean, with extreme conditions occurring infrequently. This is reflected in shape of the trade-off curve: the profile becomes steeper and the costs more spread out as we move away from the centre.

Of particular interest is the behaviour of the cost profile at high reliabilities. While the cost profile is near-linear over most of the reliability range, the gradient of the curve increases rapidly over the final 20-30% of the range. The final 20% of the range accounts for 45% of the cost increase. This indicates that oversizing is required to meet 100% of demands all of the time and highlights the problem associated with worst-case designs. However, the small cost difference along the reliability range means that the cost implications of oversizing will not be too significant on the whole.

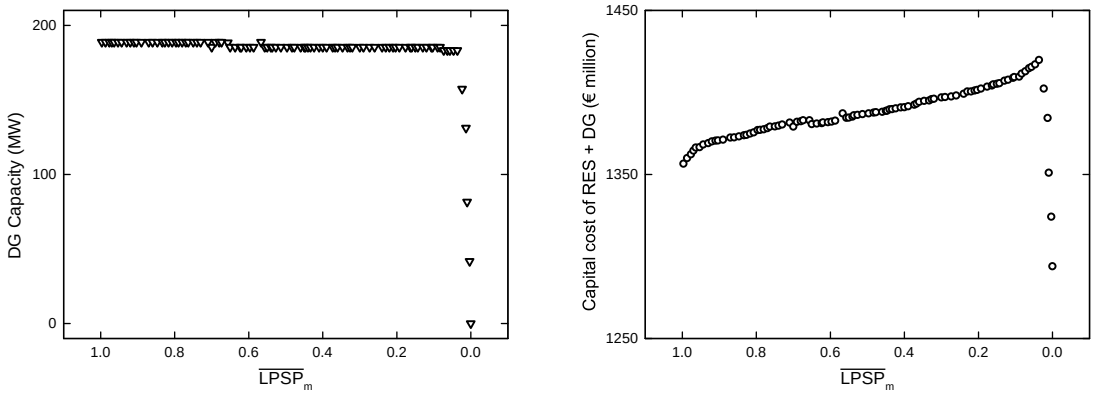

(a) DG backup capacity (b) Total energy system cost for Chile

Figure 6.8.: Effect of DG capital cost on overall cost profile. The diesel generation capacities were estimated as the maximum of the hourly external energy requirements (E_τ^{ext}) in all the input scenarios.

Effect of diesel generation backup costs The cost of diesel generation (capital and operating) can have a significant effect on the design selection. Consider the back-up systems required for each of the Pareto-optimal designs generated in the run. Most of the designs generated require that the installed backup system be large enough to meet almost all of the hourly demands of the mine (Figure 6.8a). This suggests that there are operating time periods in which those designs provide virtually no power: all the energy must be supplied externally. However, the designs with extremely high reliabilities are able to supply a reasonable amount of power in every time period, meaning they require smaller backup systems. This has a significant impact on the overall power system cost as is shown in Figure 6.8b. In this case, the design with the highest reliability (and hence highest RES cost) is actually the cheapest design when the DG cost is taken into account. This is without the addition of the operating costs for diesel generation which can be quite significant.

While this is a special case because of the low cost variability and high demand satisfaction ($LPSP = 0$) demanded from the energy system, it demonstrates why the cost of diesel generation must be taken into account in decision-making.

6.5.1.2. Cost comparison with standalone fossil fuel generation

To obtain a measure of the competitiveness of the costs of the primary (renewable) energy system, we compare the cost of the most reliable system to the cost of diesel generation over the lifetime of a typical mine (taken as 20 years for this study).

Al-Shamma'a and Addoweesh [7] give the expression for annual diesel cost as:

$$F(t) = C_F \sum_{t=1}^{8760} \Big[246 \cdot D^{el}(t) + 84.5 \cdot P_R\Big] \tag{6.5}$$

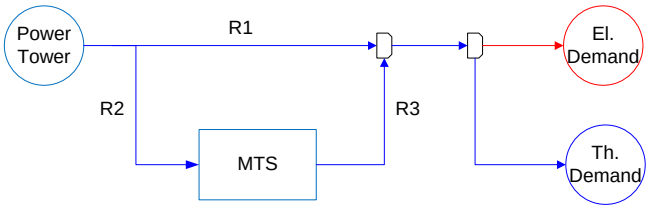

Figure 6.9.: Optimal operating scheme for designs with possible energy routes for Chile case study. The red and blue lines represent the electrical and thermal networks respectively.

where D^{el} is the hourly demand of the plant [MWh], P_R is the rated capacity of the diesel generator [MWh], and C_F the unit cost of diesel per litre. A mine with an average power demand of 171 MWh, peak power demand of 178 MWh and 10% thermal demand consumes $1,507,624.8$ L of diesel daily based on the above expression. For a diesel unit cost of \$ 0.67/L (current diesel cost in Chile), the annual cost of diesel required to run the mine is \$ 368.7 M. Over 20 years, the total cost spent on diesel purchase is \$7.374 billion (€6.7 billion). This is about 5 times the cost of the most expensive renewable energy system generated for Chile and does not account for the cost of diesel generator purchase and replacement, potential diesel cost fluctuations and the potential penalties for greenhouse emissions (carbon taxes, for example) associated with diesel generation.

While there are also other costs associated with renewables generation, the initial capital cost has been shown to be the most significant portion of the financial outlay for renewables-based power systems [117, 179]. Thus, the cost comparison suggests that renewables generation would be significantly cheaper than diesel generation in Chile.

6.5.1.3. Energy system design

The configuration of the energy system is unchanged by variability, with the same set of options selected irrespective of the energy input scenario. For all the scenarios generated, the optimal design involves the installation of a power tower for generation and molten salt two-tank system for thermal energy storage, with photovoltaics eliminated completely.

The optimal design is slightly different from that obtained in the single objective problem in which PVs and PHES were used for peak shaving (see Section 3.5.6). The difference in optimal designs occurs because of the introduction of the pre-defined operating scheme into the solution process. The operating scheme prioritizes power supply to the plant; any power generated by the PV system must be used to satisfy electrical demands first (Algorithm 6.1). This is different from the solution methodology for the single objective case in which the decision was made on an hourly basis by the optimizer, a scenario that meant PHES storage charging could occur while the power tower was supplying power to the plant. The operating scheme prevents that from happening in this case. This loss of freedom in decision-making made peak shaving impossible, leading to the elimination of the PV and PHES systems from the optimal design.

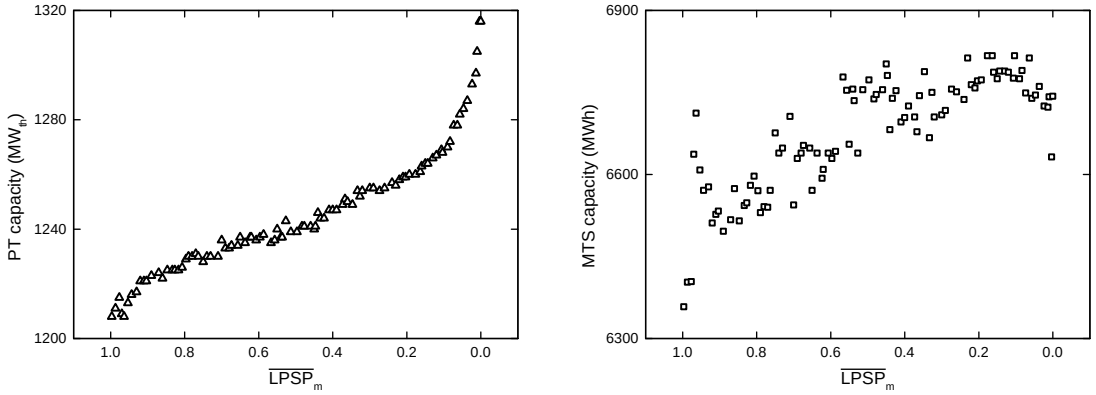

(a) Power Tower (b) Molten salt thermal storage

Figure 6.10.: Variation of installed generation and storage capacities over reliability range

Figure 6.9 shows the optimal system configuration and possible energy pathways within the system. During the day when high solar radiation is available, the demands of the plant are satisfied by direct heat supply from the power tower (R1), with excess generation channeled to the MTS system (R2) until the store is full. When this occurs, only enough thermal energy to meet the demand of the mine is collected, with any excess heat dumped. Once sunlight is unavailable (during the night), the demands of the mine are satisfied solely from storage (R3). During periods of low insolation (early morning, early evening or sudden reduction in solar radiation availability), the demands are satisfied from a combination of direct supply and storage (R1 and R3).

6.5.1.4. Effect of reliability on generation and storage capacities

The effect of reliability on the installed capacities of the PT and MTS units are shown in Figures 6.10a and 6.10b.

The PT profile mirrors the cost profile because the cost of generation (the first term of the cost objective) is the most significant contributor to the capital cost, accounting for roughly 73% of the total cost of each design. The capacity required for generation increases by 108 MW_{th} (9%) over the entire reliability range.

As expected, an increase in the capacity of the installed storage units with increasing reliability is observed. However, the profile is less fully formed because the cost of storage has a much smaller impact on the capital cost ($<$15%). All the optimal designs require the storage units to be capable of delivering 178MW_e. Fully charged, the storage units installed are able to meet the demands of the plant for 14 -15 hours without external supply. This is equivalent to the supply needed for a single night of operation. The results suggest that storage is required for load shifting only; no standby reserve is required.

6.5.1.5. Performance of minimum cost design under worst case input conditions

To understand the type of performance to be expected of the designs within the year, we consider the performance of the minimum cost design (summarized in Table 6.4) under

Table 6.4.: Characteristics of minimum cost design for Chile

PT capacity	MTS capacity	MTS peak output	$\overline{LPSP}_m$	Capital cost
1208 MW_{th}	6358 MWh	178 MW_e	0.9967	€ 1206.06M

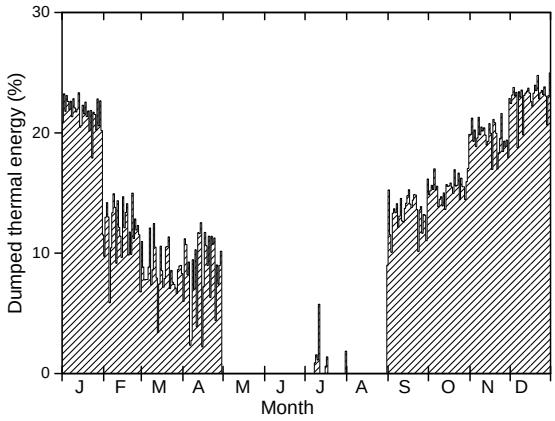

Figure 6.11.: Daily excess thermal generation

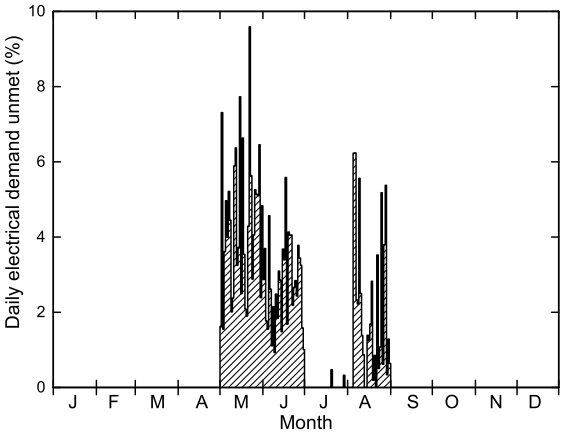

Figure 6.12.: Percentage of daily demand unmet by design

the worst of the input conditions generated. This scenario allows us to make general deductions about performances of the designs.

Figure 6.11 shows the fraction of the thermal generation dumped daily, while Figure 6.12 shows the fraction of the daily demand that that is left unsatisfied by the energy system. From the Figures, we see that:

1. Deficits in energy supply only occur in late Autumn and Winter. For 8 months of the year, the energy system is sufficient to satisfy the demands of the mine. The relatively low dumping levels suggest that energy generation across the year does not change significantly between seasons.
2. The energy system fails for 161 h, translating to 1.9% of the year. Thus, the design is able to meet demands for over 98% of the year. Since it is the least reliable design, this statement can be extended to all the designs generated. Analysis of the total external energy requirements showed that only 0.77% of the annual demand will need to be satisfied externally. This indicates that while the DG system must be sized to meet nearly all the plant demands, it will actually be required very infrequently.
3. On any given day, the design is able to meet more than 90% of the daily demands of the plant. The design will always satisfy demand for at least 21 hours a day.

The results suggest that all the designs perform well even under poor input conditions. The results obtained for the yearly performance can also be a source of information for planning and scheduling. For example, the results obtained here suggest that major refurbishment and maintenance works are best scheduled for the middle of the year for a mine located in Chile.

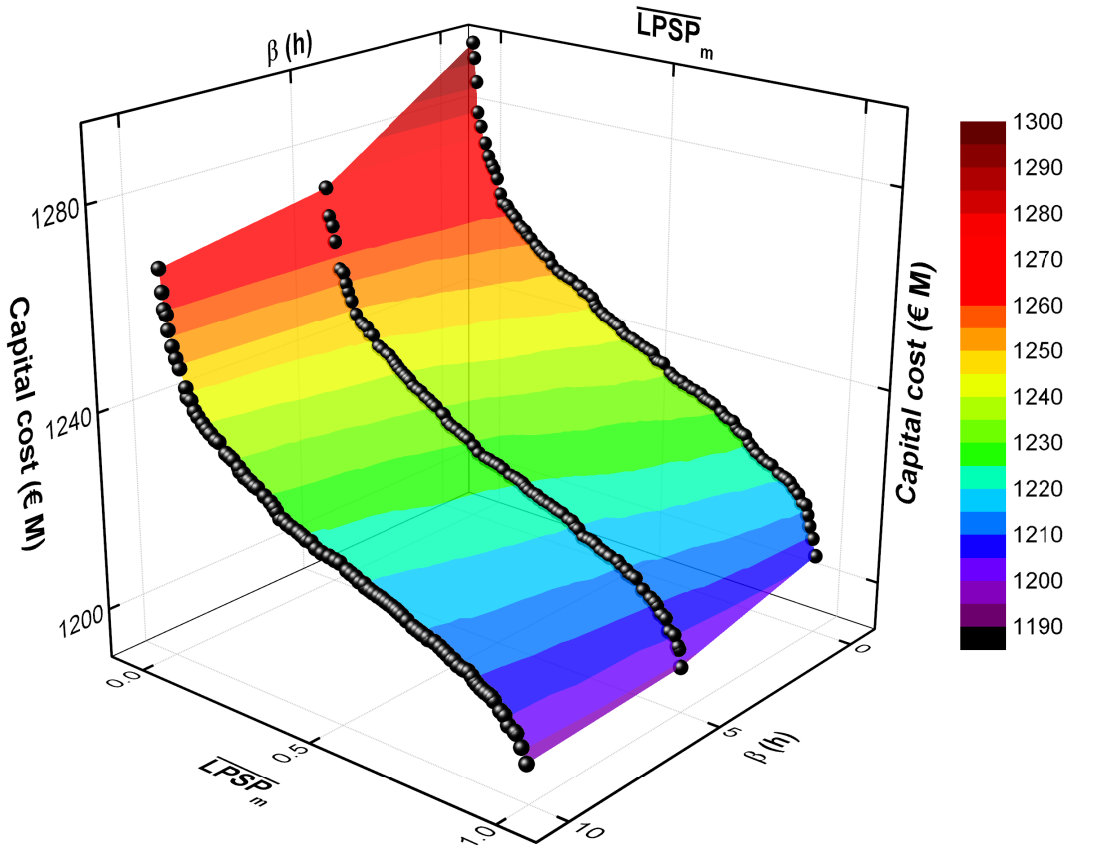

Figure 6.13.: Effect of internal reliability constraint on cost-reliability trade-off curve. The trade-off curves from right to left represent increasing acceptable failure levels of $\beta = 0\text{h}\,(LPSP = 0)$, $\beta = 5\text{h}\,(LPSP = {}^{5}/_{8760})$ and $\beta = 10\text{h}\,(LPSP = {}^{10}/_{8760})$ respectively. The colourbands show designs with similar costs.

6.5.1.6. Relaxation of internal reliability constraint

The results presented so far have considered the scenario in which the internal reliability constraint is set to ensure that the full demands of the mine can be satisfied ($LPSP = 0$). In reality, such a tight constraint may not be required: the mine will not operate continuously at near-peak capacity for a full year. It is therefore useful to consider the impact of relaxing this constraint on design cost.

Consider the scenario in which the decision maker does not insist on 100% demand satisfaction but is willing to allow for a few hours of failure within the year. We solve the optimization problem for two cases in which the acceptable limits for failure β were set at 5 hours and 10 hours respectively. The results are shown in Figure 6.13.

As expected, there is a reduction in the cost of the designs required to produce a given reliability as the internal performance constraint is relaxed, with the cost of the most reliable design (LPSP = 0) reducing by 2.1%. The reduced cost reflects the reduced capacities of the generation and storage units required. The performances of the designs are improved significantly when the constraint is relaxed even slightly: a design costing € 1230M will have a reliability of 71% when 10h of failure is allowed but only 27% when

Table 6.5.: Statistical properties of generated solar input profiles for Canada.

	Mean[kWh/m²]	Maximum deviation from mean
Global Horizontal Irradiance (GHI)	1308	-4.02% to +4.53%
Direct Normal Irradiance (DNI)	1476	-8.35% to +7.75%

Table 6.6.: NSGA-II variable bounds for Canadian case study

Variable	C_i^{gen} [MW]	C_j^s [MWh]	C_j^{out} [MW_e]	$\overline{OP}$
Lower bound	0	0	0	1
Upper bound	15,000	25,000	400	3

i = generation technologies $\{PT, PV\}$, j = storage technologies

100% demand satisfaction is required. Hence, the decision on what level of performance is required within the year is one that must be considered carefully by the decision-maker.

The results from the case study show that locations with low renewables variability have little spread in the capital costs and performance of the designs over the entire reliability range. It is expected that a location with higher variability in renewables input will reveal a larger spread in capacities and costs over the reliability range. This expectation is tested in a second case study.

6.5.2. Multi-objective design of stand-alone solar-based system for Canada

The second case study considers the fictional scenario in which the Chilean mine is relocated to Alberta, Canada. The choice of Canada as an alternative site for the mine was influenced by its signicant mining activities, large variability in renewables availability and the availability of historical solar radiation data. The aim is to solve the same design problem (solar-based generation only) for the same mine at a location with completely different renewable input characteristics, thereby stress-testing the methodology developed and demonstrating it more generally.

The statistical properties for global horizontal irradiance (GHI) at the new location may be found in Appendix E.2. 300 potential GHI and DNI profiles were generated as described in Section 4.3. Table 6.5 shows the statistical properties of the 300 input profiles generated. When compared to Chile (Table 6.2), the values suggest that solar radiation in Canada is less abundant but more variable. The aim is to investigate the effect of these differences on the trade-off between cost and performance.

The variable bounds used in the study are shown in Table 6.6. All other parameters remained the same as in the first study.

6.5.2.1. Trade-off curve

Figure 6.14 shows the non-dominated objective function values for 3 attempts. The average elapsed time for the three parallelized runs was 108.1 h on a Linux based machine

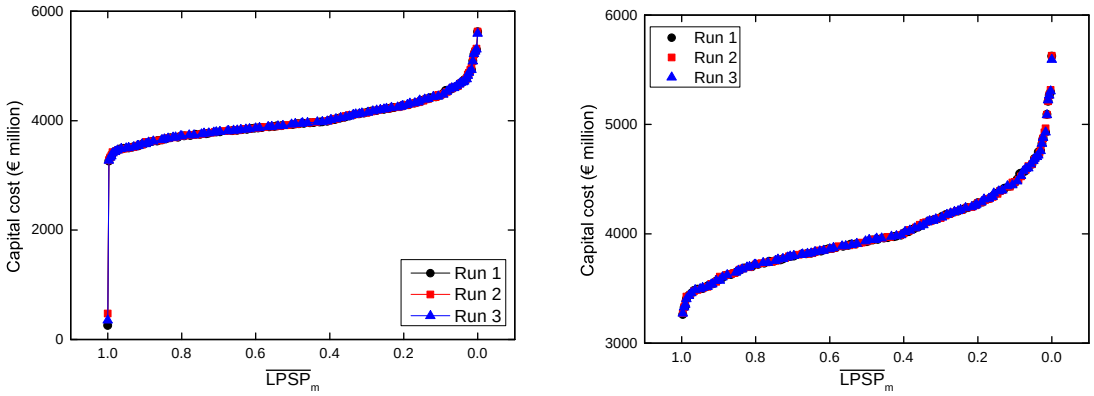

(a) Full Pareto front with trivial ($\overline{LPSP}_m = 1$) solutions

(b) A zoomed in view of Figure 6.14a after removal of trivial solutions

Figure 6.14.: Approximations to Pareto front for Canada from three attempts with NSGA-II

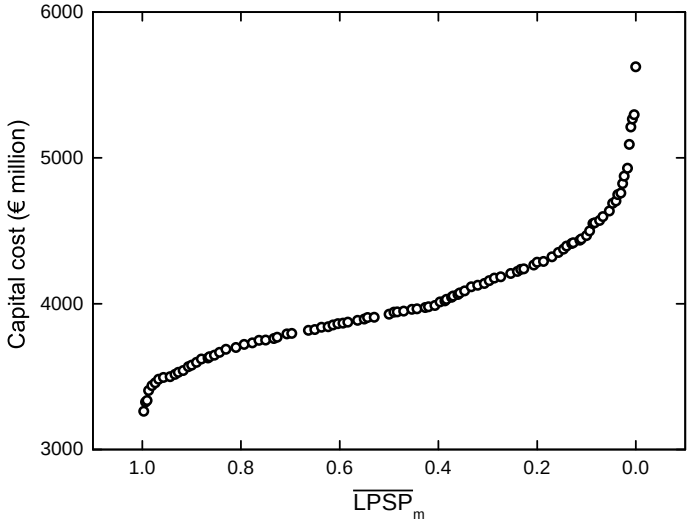

Figure 6.15.: Cost-reliability trade-off curve for solar-based system

with eight 2.4 GHz Intel Xeon processors and 16 GB RAM. Again, there is very little difference between the results of the three runs, giving a measure of confidence that set of non-dominated solutions have been identified well. For analysis of the designs, the Pareto front identifed from the first run is again considered.

Figure 6.15 shows the approximation to cost-reliability Pareto-optimal front. Only 40% of the DNI available in Chile is available in Canada (Table 6.5), and this is reflected in the higher capital costs of the designs. The capital cost varies by 72.5% (€ 2.36bn) over the entire reliability range. The comparatively high cost variation observed compared to the Chile case reflects the significantly higher degree of renewables input variability in Canada.

The higher costs involved for Canada mean that a cost comparison with diesel generation becomes less clear. Equation 6.5 gives the total diesel cost over 20 years as €7.61 billion for a diesel unit cost of $ 0.76/L (current cost in Canada). This is only 26% higher

than the cost of the most reliable renewable energy system. However, given that the operating cost of a solar thermal plant incorporating storage is about 1% of the capital cost annually [161], operating the plant for 20 years on renewables generation is still likely to be slightly cheaper than diesel generation.

Again, the behaviour of the curve at the high end of the reliability range is of interest to the designer. The final 20% of the range accounts for 57% of the cost increase, while increasing the system reliability by 1% from $\overline{LPSP}_m = 0.01$ to $\overline{LPSP}_m = 0$ (essentially accounting for one failure every 100 years) accounts for 17% of the total cost increase. These results suggest that significant oversizing is required to obtain a fully reliable design. Unlike the Chilean case however, the costs involved in system oversizing are significant enough to be a key factor in the decision-making process.

For the decision maker, it raises the question of whether it is essential to attain 100% reliability. Given that the average lifetime of a remote mine is typically about 15 to 20 years [44, 175], such small margins may not be critical. In a case where the reliability requirement is flexible (the mine owner is willing to shut down the plant or run diesel generators for a couple of hours in some years, for example), the designer has a number of slightly less expensive high-performance designs to choose from.

Effect of diesel generation backup costs Figure 6.16 shows the cost profile after the capital and operating costs of the DG backup system have been added. In this case, the cost of the diesel backup system will be a less significant factor in the choice of designs; it has no effect on the cost profile. This occurs because the costs involved are much larger compared to the Chilean case; the cost of the backup system becomes less influential as the renewables availability at the location decreases.

6.5.2.2. Energy system design

The optimal energy system design is the same as for the Chilean case study: installation of a power tower for generation and molten salt two-tank system for thermal energy storage.

6.5.2.3. Effect of reliability on generation and storage capacities

Figure 6.17a shows the variation in PT generation capacity with reliability. The difference in the generation capacities of the least and most reliable designs is 2988 MW_{th}, a 78% increase. This reflects the wide variation in possible input conditions at the location. Generation accounts for between 85% and 87% of the cost of all the designs.

The storage capacity is doubled across the reliability range (Figure 6.17b), with all the designs capable of delivering a maximum of 180 MW_e. When fully charged, the least and most reliable designs are able to power the plant for up to 26h and 43h respectively. Much larger storage capacities are required (compared to Chile) because there is a carry-over of energy between days to prevent shortfall in supply on days that the daily generation is insufficient to meet the demands of the mine. In this case, the storage systems serve

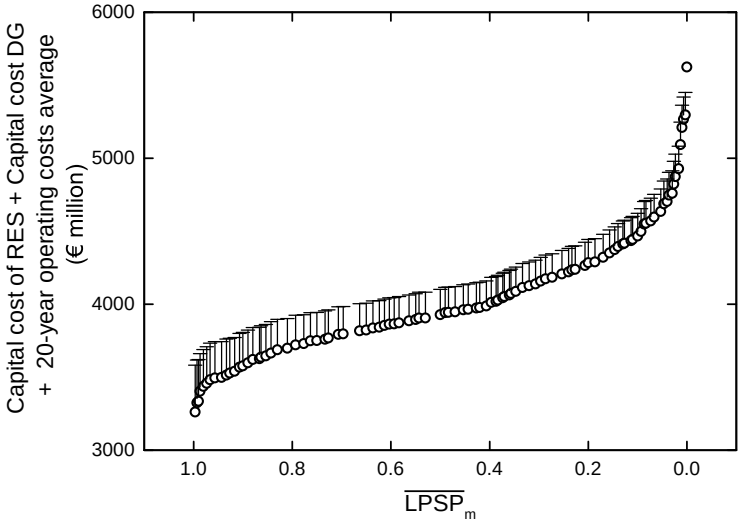

Figure 6.16.: Cost profile for total power system for Canada mine. The circles represent the capital costs of the renewable energy system (Figure 6.15), while the error bars show the costs after the capital and operating costs of diesel generation have been added. The operating costs over the average lifetime of a mine (20 years) were calculated based on the average diesel requirement over all the input scenarios investigated.

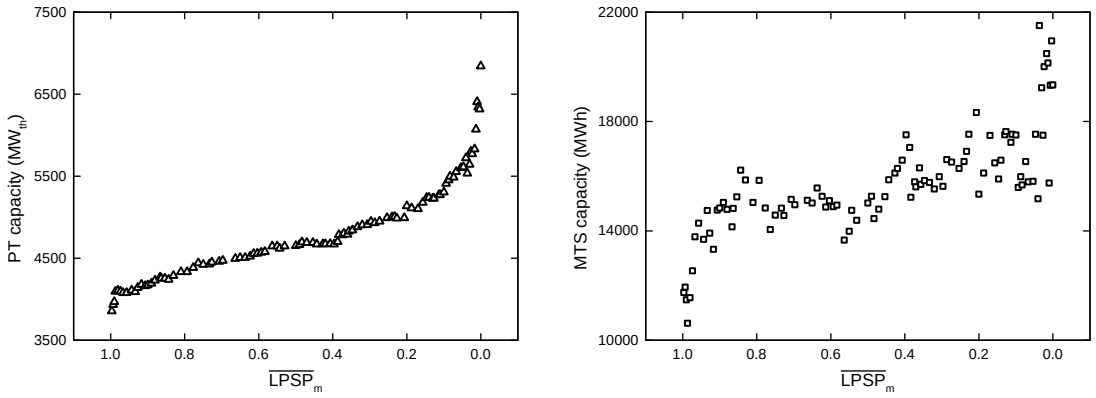

(a) Power Tower (b) Molten salt thermal storage

Figure 6.17.: Variation of installed generation and storage capacities over reliability range

both the purpose of load shifting and standby reserve. The level of standby required increases with the required reliability.

6.5.2.4. Performance of minimum cost design under worst case input conditions

The performance of the minimum cost design for Canada (presented in Table 6.7) under the worst generated solar input conditions was investigated. Figure 6.18 shows the

Table 6.7.: Characteristics of minimum cost design for Canada

PT capacity	MTS capacity	MTS peak output	$\overline{LPSP}_m$	Capital cost
3855 MW_{th}	11744 MWh	180 MW_e	0.9967	€ 3262.12M

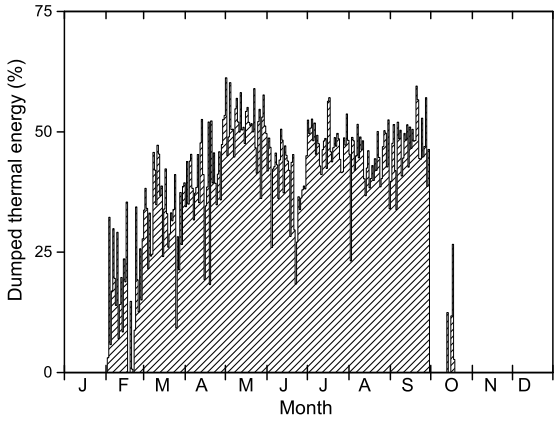

Figure 6.18.: Daily excess thermal generation

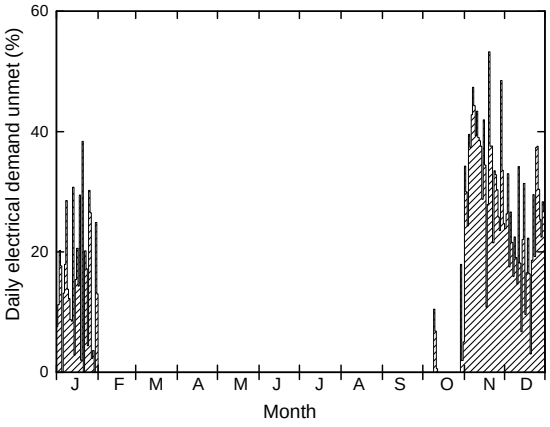

Figure 6.19.: Percentage of daily demand unmet by design

fraction of the thermal generation dumped daily, while Figure 6.19 shows the fraction of the daily demand that that is left unsatisfied by the energy system. From the Figures, the following conclusions can be drawn:

1. The design is able to meet the demands of the plant for 8 months of the year (February through September). During this period, significant energy dumping occurs, with less than half of the energy generated in Summer actually collected for use in the system (Figure 6.18). This suggests that the level of thermal energy generation varies significantly between seasons.

2. The design fails for 6.9% (608 h) of the year, meaning the design (and all others generated) will meet the load demands for over 93% of the year. Analysis of the total external energy requirements revealed that 6.02% of the annual demand will need to be satisfied externally.

3. The design performs poorly in months with low renewables availability, with up to 54% of the load demand (spread over 14 hours) needing to be satisfied from outside the integrated energy system.

The degree of energy dumping required, frequency of power failure and extent of power failure are at higher levels than were observed with the Chilean case study, reflecting the difference in the degree of variability between the locations.

For locations such as Northern Chile where clusters of mining operations exist, the excess generation available for most of the year opens up the possibility of energy trading with neighbouring mines in months with high solar availability to generate extra income to partly or fully cover the cost of external energy supply in the winter months. This would however require that the output capacity of the power block be increased, thereby incurring additional costs.

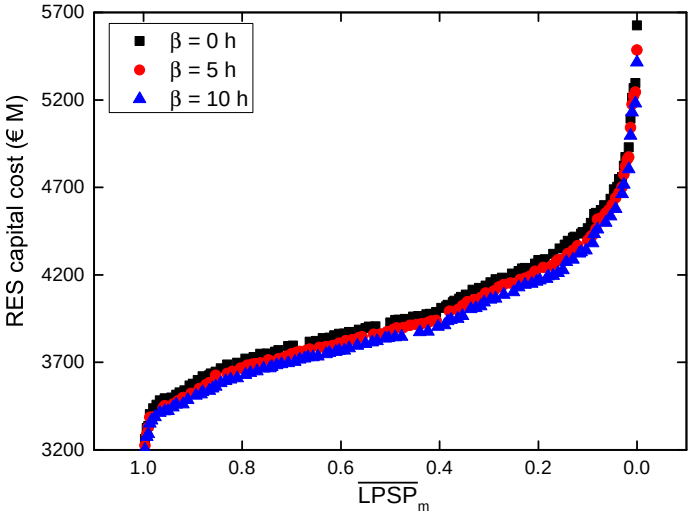

Figure 6.20.: Effect of internal reliability constraint on cost-reliability trade-off curve for Canada.

6.5.2.5. Relaxation of internal reliability constraint

Figure 6.20 shows the effect of relaxing the internal reliability constraint by changing the acceptable degree of failure β. Allowing for failure of up to 10 hours reduces the cost of the most reliable design by 3.7% (€ 210M). In this case, the performance of the energy system is not significantly improved by slightly relaxing the internal reliability constraint: a design costing € 4 bn will have a reliability of around 66% when 10h of failure is allowed and 60% when full demand satisfaction is required. When compared with the Chilean case, the results suggest that designs for low variability systems are more significantly impacted by the relaxation of the internal reliability constraint.

The results raise the question of how important the extra hours of energy security each year is worth to the decision maker and provide an interesting set of alternatives from which a decision can be made based on the designer's definition of reliability.

It is interesting to note that for the two case studies presented so far, the worst energy system performances for the minimum cost designs did not occur under the worst solar input conditions. This highlights another problem in the application of the conventional worst-case approach to energy systems sizing: the worst renewable input conditions (quantitatively) may not necessarily generate the worst case design.

The first two studies consider the case of solar-based generation for two different locations and show that the methodology developed is applicable under different renewable input conditions. Now we wish to demonstrate the capability of the model to handle different technologies.

Table 6.8.: NSGA-II variable bounds for case study integrating wind generation

Variable	C_i^{gen} [MW]	N_T	C_j^s [MWh]	C_j^{out} [MW_e]	$\overline{OP}$
Lower bound	0	0	0	0	1
Upper bound	15,000	7500	25,000	400	3

i = generation technologies $\{PT, PV\}$, j = storage technologies

6.5.3. Multi-objective design of stand-alone solar-wind integrated system for Canada

The third case study also considers the fictional scenario in which the Chilean mine is relocated to Alberta, Canada. In this case however, both solar and wind generation technologies are made available for selection. The aim is to demonstrate the methodology for a larger problem with more technologies available.

The statistical properties for windspeed at the new location may be found in Appendix E.4. 300 potential wind profiles were generated as described in Section 4.3. The wind profiles were paired with the solar profiles generated in the previous case study as described in Section 4.3 using 4 strata, giving a total of 1200 input conditions.

The system requires ten design variables for the problem, with the additional variable representing the number of installed wind turbines from which the nominal wind generation capacity can be computed. The variable bounds used in the study are shown in Table 6.8. All other parameters remained the same as in the first two studies.

6.5.3.1. Trade-off curve

Figure 6.21 shows the non-dominated objective function values for 3 attempts. The average wall clock time from start to finish for the three parallelized runs was 298.8 h on a Linux based machine with twelve 2.4 GHz Intel Xeon processors and 24 GB RAM. Again, there is very little difference between the results of the three runs, giving a measure of confidence that set of non-dominated solutions have been identified well. For analysis of the designs, the Pareto front identified from the first run is considered.

Figure 6.22 shows the approximation to cost-reliability Pareto-optimal front when wind generation is made available. For comparison purposes, the location of the trade-off curve before wind integration is also shown in the figure. Wind integration reduces the cost of the designs required to produce a given performance, with cost of the mid-range designs reducing by about 6% and the cost of the most reliable design reduced by 9.6%. The capital cost varies by 76% (€ 2.19bn) over the reliability range. Thus, while the integration of wind generation affects the cost profile by reducing the cost of the designs required, it has no effect on the spread of designs across the reliability range.

6.5.3.2. Optimal energy system design

The optimal system design involves the installation of a power tower (PT) and wind turbines (WT) for generation, and tank storage (MTS) and pumped hydro (PHES) for

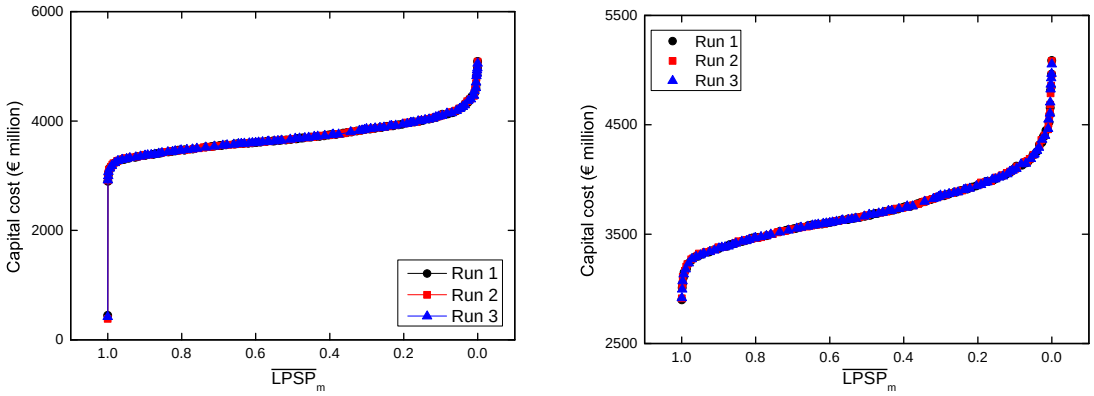

(a) Full Pareto front with trivial ($\overline{LPSP}_m = 1$) solutions

(b) A zoomed in view of Figure 6.21a after removal of trivial solutions

Figure 6.21.: Approximations to Pareto front for Canada after wind integration from three attempts with NSGA-II

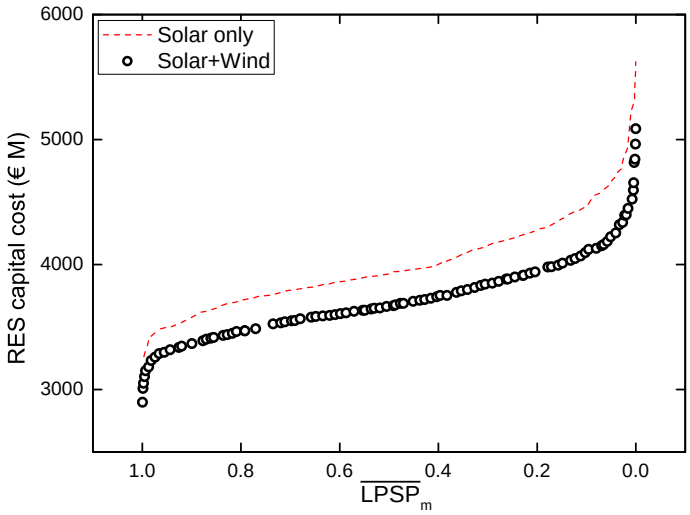

Figure 6.22.: Cost-reliability trade-off curve for solar-wind integrated system. The broken red line shows the location the Pareto front when only solar generation options were allowed.

storage, as is shown in Figure 6.23. The WT and PHES systems satisfy electrical demands only, while the PT and MTS systems satisfy both electrical and thermal demands. The selected operating scheme discharges the PHES before the MTS for power supply. This is logical: discharging less of the MTS for power generation ensures that thermal demands can be satisfied for longer. The order for electrical demand satisfaction is: R1>R4>R3>R6.

The decision to integrate wind and solar power for energy supply takes advantage of the seasonal anticorrelation in the time patterns of the renewable resources [217]. Figure 6.24 shows the monthly average of the solar and wind resources. The inverse relationship between the resources is evident: wind availability (and thus generation) increases between August and November and decreases between April and August; solar availability (and thus generation) is the opposite. Thus, combining generation from the two

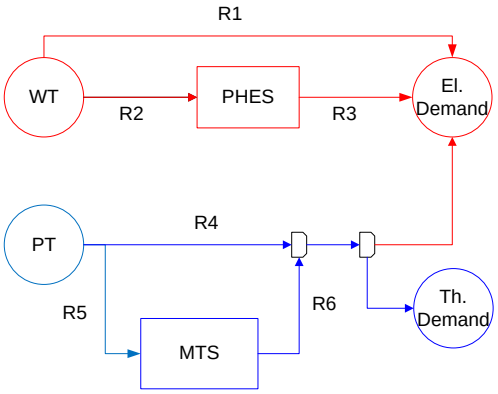

Figure 6.23.: Optimal operating scheme for designs with possible energy routes for Canada case study after wind integration. The red and blue lines represent the electrical and thermal networks respectively.

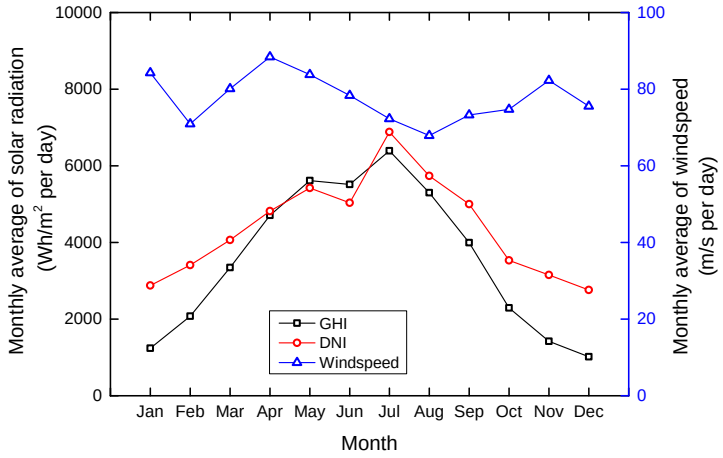

Figure 6.24.: Monthly averages for solar radiation (GHI and DNI) and windspeed in Canada based on the available historical data. Wind and solar radiation are seasonally anticorrelated, with wind availability increasing between August and November (while solar radiation decreases) and decreasing between April and August when solar radiation is at the highest.

resources provides balance to the energy system. This, combined with the poor solar availability at the location (especially in Winter), informed the decision to integrate the two generation options.

6.5.3.3. Effect of reliability on generation and storage capacities

The effect of reliability on the installed generation capacities is shown in Figure 6.25.

The power tower profile mirrors the trade-off curve and is the most significant contributor to the cost, accounting for between 49% and 67% of the capital cost of the design. The installed capacity increases by 2712 MW_{th} (138%) over the entire reliability range.

The installed capacities of the wind turbines remain at the same level across the reliability range. Based on the rated windspeed of 15 m/s, wind generation will produce the

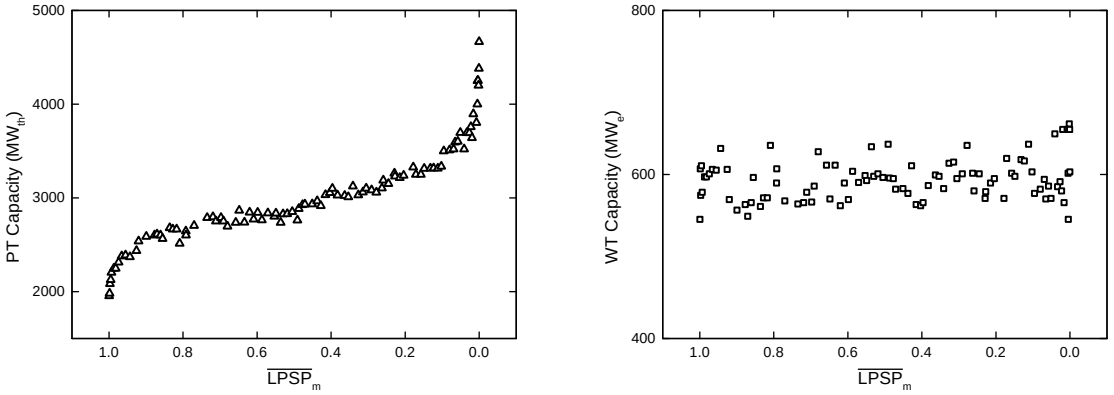

(a) Power Tower (b) Wind Turbines

Figure 6.25.: Variation in power tower and wind generation capacities over reliability range

equivalent of the rated power for between 4 to 6 hours daily. The installed capacities of the wind turbines exceed the peak demand of the plant. Thus, with the current system configuration, the mine will be 100% powered by direct wind generation when wind availability is sufficient. Given the intermittent nature of wind generation, this raises questions about how sudden changes in generation output level will be handled, an issue that will be addressed later.

The effect of reliability on the installed storage capacities is shown in Figure 6.26. Again, the capacity of the MTS is doubled across the reliability range, with all the designs capable of delivering a maximum of 180 MW_e (Figure 6.27). When fully charged, the installed MTS systems are able to provide power to the plant at the nominal capacity (180 MW_e) for between 20h and 34h, suggesting that storage still serves the purposes of load shifting and standby reserve for the system. However, the level of standby required is significantly lower than when only solar generation is available (Section 6.5.2.3), taking advantage of the of the availability of the wind resource throughout the day: some of the electrical demands of the plant at solar off-peak periods (at night) will be satisfied from wind generation (albeit intermittently), meaning less energy is required from storage. Also, the MTS system will only be required to operate near its full capacity when the PHES system is empty, meaning that the MTS system is discharged more slowly.

The installed capacities of the PHES systems remain at roughly the same level irrespective of reliability, matching the behaviour of the charging units (wind turbines).

6.5.3.4. Performance of minimum cost design under worst case input conditions

The performance of the minimum cost design $\left(\overline{LPSP}_m = 0.999\right)$ under the worst generated solar input conditions is again considered. The characteristics of the design are presented in Table 6.9.

Figures 6.28 and 6.29 show the daily and monthly power profiles for the energy system. Direct power supply from wind generation (WT) is the largest single source of power to

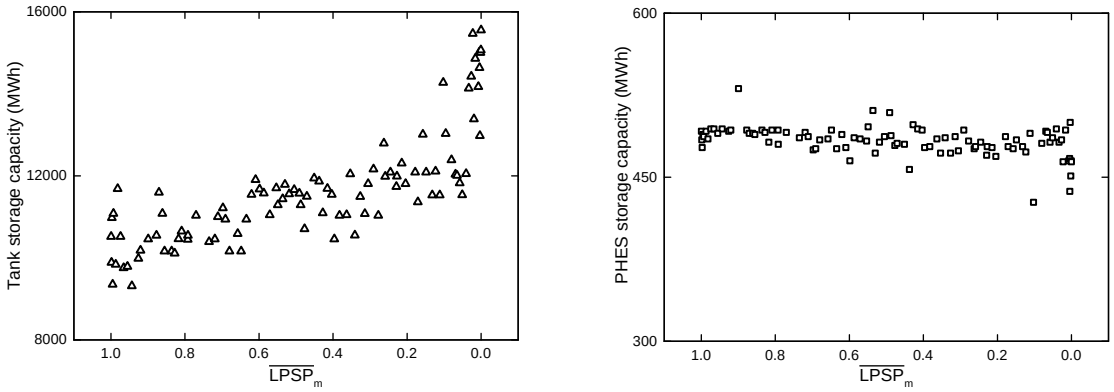

(a) Tank storage capacity (b) PHES capacity

Figure 6.26.: Variation in storage capacities over reliability range

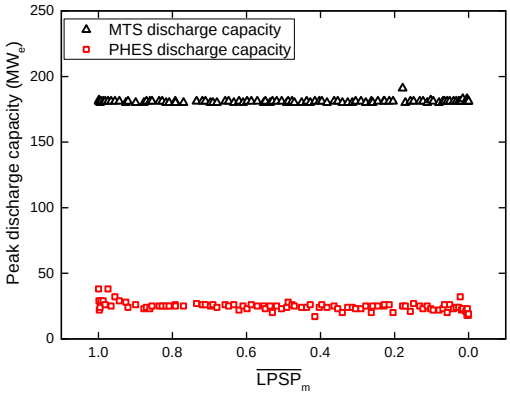

Figure 6.27.: Maximum discharge capacities of installed storage options

the plant, satisfying 33.2% of the annual demand. At its peak, 61% of the daily electrical demand of the mine is met directly from wind generation. WT and PHES combine to meet 37.3% of the annual electrical demand of the mine. The electrical system is most active in the first half of the year with the highest power output occuring in May (56%). The maximum combined output of the two systems for a single day is 68%. The wind turbines were installed primarily for direct demand satisfaction, with the storage unit (PHES) contributing little to the energy mix.

The PT/MTS system combine to supply 53.7% of the annual power demand, with the larger proportion (30%) coming from storage. The thermal route is most active in the Summer months (June to August), with the daily output from the combined system as high as 82% in July.

The design is able to meet the demands of the plant for 6 months of the year (March to May, July through September). During this period significant thermal energy dump-

Table 6.9.: Minimum cost design for Canada after wind integration

C_{PT}^{gen}	C_{wind}^{gen}	C_{MTS}^{s}	C_{MTS}^{out}	C_{PHES}^{s}	C_{PHES}^{out}	Cost
1955 MW_{th}	545 MW_e	10518 MWh	180 MW_e	492 MWh	28 MW_e	€ 2898.15M

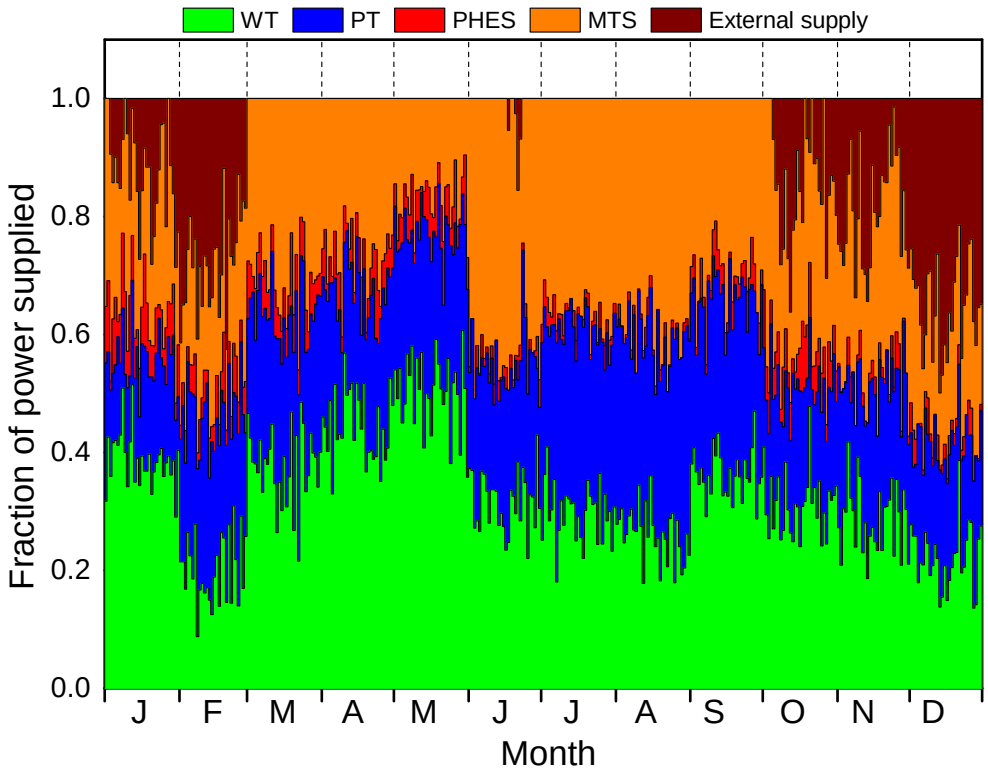

Figure 6.28.: Daily power supply profile for the year.

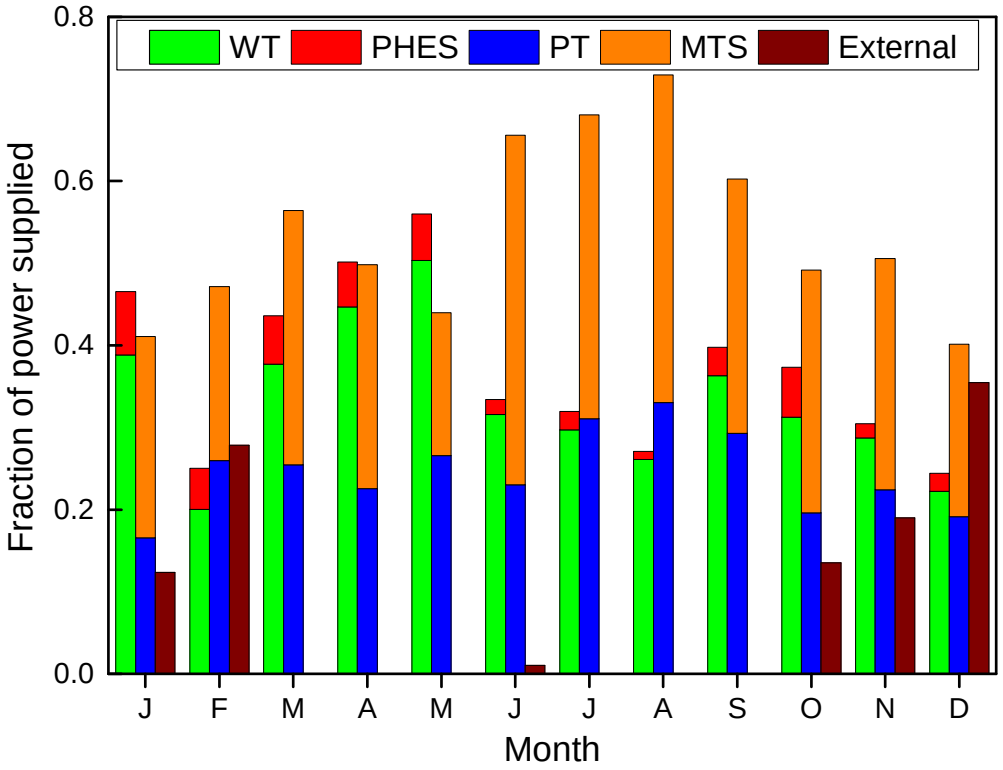

Figure 6.29.: Monthly power supply profile for the year. Four routes are available for power supply from the RES: direct power from wind generation (WT), direct power generation from power tower output thermal energy (PT), power supply from PHES storage (PHES), and power generation from MTS output heat (MTS). External supply (from diesel generators) will be required when the output from these sources are insufficient.

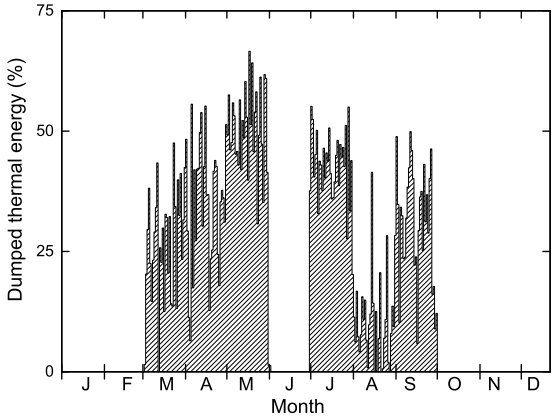

Figure 6.30.: Excess thermal generation

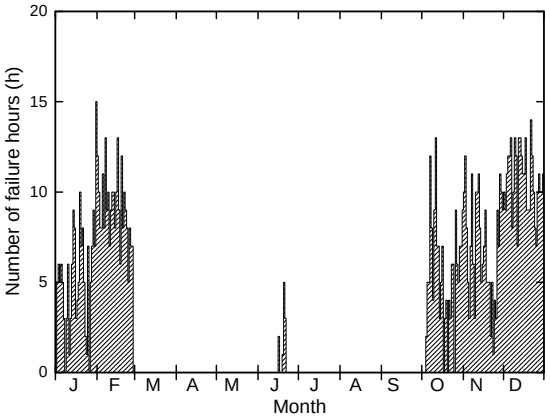

Figure 6.31.: Number of failure hours

ing occurs, with 16.4% of the PT generation within the year unutilized (Figure 6.30). Dumping is highest in May (due to the high wind energy contribution) and July (the month with the highest DNI availability). Almost all the wind generation is used to meet demand, with less than 1% electricity dumping occurring in the year.

The design fails for 13.28% (1193 h) of the year, meaning the design (and all others generated) will meet the load demands for over 86% of the year. Analysis of the total external energy requirements revealed that 8.97% of the annual demand will need to be supplied from an external source. The design performs poorly Autumn and Winter, with up to 50% of the load demand spread over 15 hours (Figure 6.31) needing to be satisfied from outside the renewable energy system.

As the reliability of the energy system is increased, the WT/PHES contribution to the energy mix remains at roughly the same level while the PT/MTS contribution increases, taking over the portion supplied externally. For the same input scenario, the maximum reliability design $\left(\overline{LPSP}_m = 0\right)$ supplied 61% of the power demands from the PT/MTS systems.

The case studies presented demonstrate the capability of the methodology to handle problems with different degrees of renewables variability (making it applicable to different geographies) and technologies. While the studies considered problems in which the daily demand profile was constant throughout the year, the models and methodology are robust enough to handle problems involving variable power demand profiles. This is demonstrated in Appendix D where the problem of the multi-objective design of a solar-wind integrated system for Canada (similar to Section 6.5.3) is considered for a variable power demand profile.

Summary

A techno-economic analysis of a renewables-based energy system integrating thermal and electrical generation with large-scale storage has been presented in this chapter.

The methodology presented shows how inter-year variability can be taken into consideration in the sizing of such systems at the design stage. The results show that the degree of variability is reflected in the range of the costs of the Pareto-optimal designs. An analysis of the designs reveals that significant cost savings are often possible for little loss in reliability and performance. The decision-maker's definition of reliability therefore has a significant impact on the capital cost of the system, with oversizing often required to guarantee energy security. The set of case studies presented demonstrate that the methodology is applicable to any location, can easily be extended to incorporate other generation and storage alternatives, is suitable for any type of demand profile, and provides the decision maker with necessary information about a number of alternative designs based on which sizing decisions can be made. The results also show that the hybridization of thermal and electrical generation and storage systems can be an effective way to reduce costs. While the reliability objective considered here focused on quantifying the climate-based variability effects, the methodology can also be applied to problems with other types of reliability objectives.

The renewable energy system design problems considered so far have focused on storage integration for load shifting and standby reserve purposes. However, the introduction of wind generation into the energy mix increases the variability in the expected system performance as wind is a more intermittent resource. Thus, the challenge of power quality management from storage to handle sudden changes in supply from the renewable energy sources must be addressed in order to ensure smooth and uninterrupted power [78]. This will be the focus of the next chapter.

Chapter 7.

POWER QUALITY MANAGEMENT

This chapter focuses on the development of power quality management strategies to mitigate the effects of the dynamic nature of renewables generation on power supply to the plant. Two approaches are presented in this work. The first approach considers the possibility of using storage as a buffer between generation and supply. With this approach, energy can only be supplied to the plant through storage, thereby ensuring steady power supply to the plant. The second approach involves the incorporation of a new storage alternative with an instantaneous response time (milliseconds) into the energy system to handle transitions between power supply modes. Modifications to the energy system model and solution methodology for both approaches are detailed, with case studies presented to show the impacts of the modifications on the sizing and operation of energy systems.

The work presented in the previous chapter focused on the optimal sizing of integrated energy systems to handle daily, seasonal and inter-year variabilities, with energy storage installed to provide load-shifting and standby reserve capabilities. Implicitly assumed in the design process was that the dynamics of the storage options matched those of the generation technologies, with changes in the outputs of the generation units occurring slowly enough to be countered by storage. In reality, renewables generation is susceptible to sudden (unscheduled) fluctuations in output due to the intermittent nature of resources, and this must be accounted for at the design stage.

While sudden spikes in generation level can be controlled by dumping some of the energy, sudden drops in output will require some form of response from the storage systems. Thus, in order to provide smooth and uninterrupted power to the mine, the storage options must be capable of responding quickly to such fluctuations, typically within milliseconds [78, 140]. For solar-thermal generation technologies integrated with storage, this is not a problem because of the nature of generation-storage integration and the shared power block (Figure 3.10) [142, 182]. Such fluctuations must however be accounted for with electrical generation technologies, particularly wind generation.

Table 7.1 shows the response times of current storage options available in the superstructure for integration with wind and PV generation systems. The storage options do not

Table 7.1.: Comparison of response times of storage options. For the PHES system, the response time is dependent on whether the required generator is already connected to the power system (spinning) or completely switched off (standing).

Storage option	Response time	Source
PHES	10 seconds (spinning) $>$ 1 minute (standing)	Kloess [127], Zach et al. [244]
AA-CAES	15 minutes (cold start)	Kloess [127]

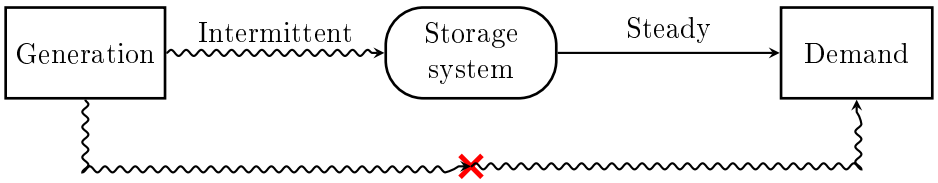

Figure 7.1.: Concept of storage buffering.

respond quickly enough to be used as emergency backup systems. Thus, any designs generated which are heavily dependent on wind or PV generation (as was the case in the Canadian study discussed in Section 6.5.3) will be susceptible to sudden power failure when drops in generation occur as a transitional period is required to switch over from generation to storage for power supply to the mine. This could lead to significant losses in revenue and and possibly even cause equipment damage. In order to ensure that such fluctuations in generation have no impact on power supply to the mine, alternative energy storage options and/or management strategies will be required. This will be the focus of this chapter.

Two approaches to power quality management will be considered. The first approach will investigate the possibility of using storage as a buffer between generation and supply. In the second approach, a new storage option with instantaneous response capabilities will be incorporated into the energy system to provide short-term electrical power during the period of transition. Both approaches will be demonstrated with case studies considering the same sizing problem previously defined in Section 6.1.

7.1. Storage Buffering

In this approach, no energy is sent directly to the plant from generation: all the demands of the plant must be satisfied from storage. This ensures that while the input into the storage system can flunctuate, it does not affect power supply to the plant (Figure 7.1). The storage system therefore acts as a power regulator for the plant, providing a buffer between the variability and intermittency inherent in renewables generation and the stability required in power supply.

With this approach, intermittency is handled from an operational standpoint.

7.1.1. Energy system modelling

The buffering of all generation options (thermal and electrical) for instantaneous heat and electricity supply is considered. Buffering affects the distribution of energy within the system; it does not change the models for the generation or storage units.

7.1.1.1. Balances around generation units

Consider the power regulation system for the electrical generation units shown in Figure 3.7. Since direct supply to the plant is not allowed $\left(\dot{E}^{d}(t) = 0\right)$; instantaneous PV and wind output must either be sent to storage or dumped. Thus, the balance around the regulator (Equation 3.15) becomes

$$\dot{E}^{gen}_{total}(t) = \dot{E}^{in}_{store}(t) + \dot{E}_{dumped}(t) \tag{7.1}$$

Similarly, all thermal energy transferred to the molten salt from the power tower absorber must be sent to storage. The balance around the power tower control system (Figure 3.8) becomes

$$\dot{Q}^{gen}_{PT}(t) - \dot{Q}_{dumped}(t) = \dot{Q}^{in}_{salt}(t) = \dot{Q}^{in}_{mts}(t) \tag{7.2}$$

7.1.1.2. Renewable energy system output

The gross electricity output of the renewable energy system comprises of only the power output from the storage options, thus Equation 3.41 becomes

$$\dot{E}^{RES}(t) = \sum_{j=1}^{3} \dot{E}^{out}_{j}(t) \tag{7.3}$$

The other model equations remain the same. These changes to the model ensure that only power sources which can be controlled by the operator are allowed to supply power to the plant, thereby preventing sudden power failure and ensuring stability.

A case study is considered to understand the impact of these changes on the model.

7.1.2. Case study: Canada

The case study of the multi-objective design of an energy system for a fictional Canadian mine presented in Section 6.5.3 is reconsidered. We investigate how buffering affects the approximate Pareto front and the operating behaviour of the designs. To allow for comparison with the results obtained in the unconstrained case (section 6.5.3), the same input conditions, variable bounds and solution methodology were used in this study.

Optimal energy system design The selected generation and storage options remain the same as the unconstrained case: wind and solar thermal generation integrated with MTS and PHES storage. However, the operating scheme of the system changes to reflect

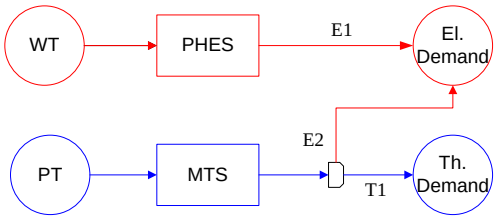

Figure 7.2.: Optimal operating scheme for designs with possible energy routes for buffered system

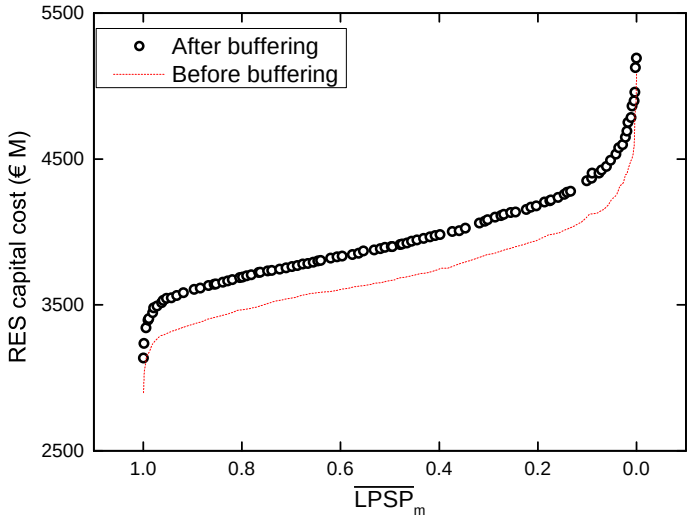

Figure 7.3.: Cost-reliability trade-off curve for buffered system. The broken red line shows the location the Pareto front before system buffering was implemented.

the additional constraints (Figure 7.2). The PHES and MTS systems supply power to the plant while the MTS satisfies the thermal demands. The selected operating scheme discharges the PHES before the MTS for power supply.

Trade-off curve Figure 7.3 shows the Pareto-optimal front when system buffering is enforced. Buffering increases the cost of the designs required to produce a given performance, with the the cost of the most reliable design increased by 2.1%. This is expected as the imposition of additional constraints on a multi-objective problem reduces the feasible design space [155]. The increase in the costs of the designs is a result of the increased dependence on both solar thermal generation and energy storage (reflected in larger installation sizes) to compensate for the loss of direct wind generation as a potential contributor to the energy mix, as will be shown later. Buffering eliminated a cost-effective route for electricity supply, forcing the system to increase its dependence on more expensive electricity supply methods.

The cost varies by 65% across the reliability range.

Effect of buffering on system capacities The effect of reliability on the installed generation capacities is shown in Figure 7.4. The general trend is unchanged from the

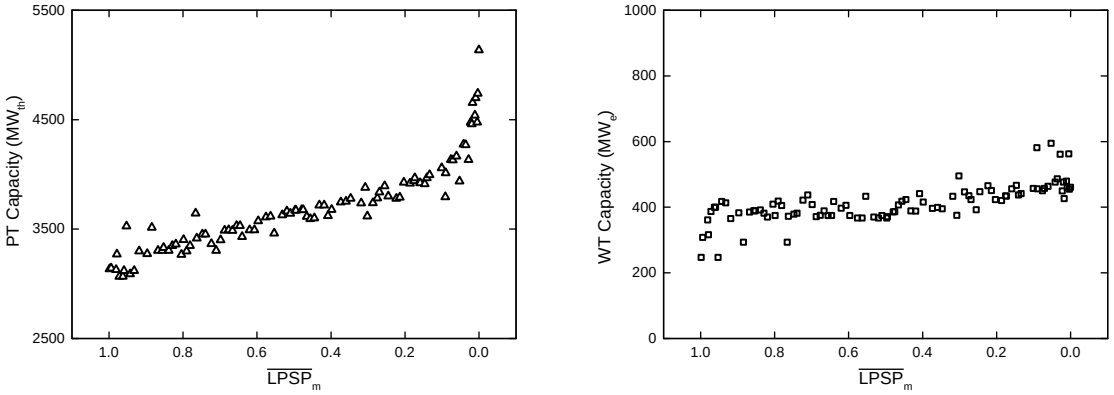

(a) Power Tower (b) Wind Turbines

Figure 7.4.: Variation in power tower and wind generation capacities over reliability range for buffered system

Table 7.2.: Effect of storage buffering on installed generation and storage capacities

	$\overline{LPSP}_m = 0.79$		$\overline{LPSP}_m = 0.20$	
	No buffering	Buffering	No buffering	Buffering
PT (MW_{th})	2,602	3,299	3,239	3,927
WT (MW_e)	607	419	595	423
PHES capacity (MWh)	480	574	469	565
PHES discharge (MW_e)	25	55	22	58
MTS capacity (MWh)	10,546	12,551	11,806	13,174
MTS discharge (MW_e)	181	181	181	181

unconstrained case (Section 6.5.3.3): the installed PT capacity increases with reliability while the wind generation remains at roughly the same level. Similar trends occur for the storage systems each option is integrated with.

To understand the impact of storage buffering on the installed system capacities, the installed capacities for two sets of designs at different ends of the reliability scale are compared before and after buffering. This is presented in Table 7.2.

Buffering reduces the dependence of the system on wind generation. This is logical as the primary reason for installing wind generation is its ability to supply power directly to the plant throughout the day (Section 6.5.3.4), an advantage that is lost when the system is storage-buffered. To achieve the same level of power supply through storage (after buffering), the discharge capacity of the PHES turbine would need to be sextupled to 178 MW_e (peak plant demand). The cost implication of this increase, along with the unavoidable 30% drop in useful power output due to the mechanical losses in the PHES system, make wind generation less unfavorable once buffering is implemented.

Despite the decrease in wind generation, the storage and output capacities of the PHES installation increase when the system is buffered. This is because all the energy generated by the turbines must now pass through the storage system unlike the unconstrained case where very little of the generation went through the PHES (see Figure 6.28). The discharge capacity of the PHES system is more than doubled when the system is buffered.

However, despite the increased capacities, the maximum contribution of wind to the energy mix is still limited by buffering. For the design with $\overline{LPSP}_m = 0.20$ for example, the maximum possible hourly contribution to the power mix from the WT/PHES system is under 35% (minimum demand is 169 MW_e). This is a significant change from the unconstrained case where wind frequently met all of the hourly power demand by bypassing storage.

The reduction in wind energy contribution is compensated for by an increase in the installed PT capacities. Buffering thermal generation through the MTS system incurs no extra losses, and the steam turbine output capacity need not be increased. These factors make increasing the PT capacity more cost-effective than wind. The increased PT capacity is accompanied by an increase in the storage capacity of the MTS system: more energy is generated, so more energy needs to be stored.

In general, a buffered system will always require larger generation and/or storage capacities than an unbuffered system to meet the same level of demand because of the need to compensate for the operational and storage losses incurred when the system is buffered.

7.2. Battery Integration

The second approach considered for handling the difference in dynamics between the generation and storage alternatives is the incorporation of a new storage alternative with fast enough response to match the dynamics of the generation technologies. The new storage option will provide short term power to cover the time interval between sudden failure of generation and the start-up of the other storage alternatives as shown in Figure 7.5. The option will not be considered for long-term use to minimize the size required, as technologies capable of providing such response times are typically very expensive [140].

The key characteristics required for power quality management and emergency backup applications are:

1. instantaneous response time to smooth disturbances on a millisecond scale [78, 140], and
2. the ability to charge and discharge quickly and frequently while maintaining good operating lifetimes [78].

Based on these characteristics, several works reviewing storage options [78, 140, 244] suggest four main storage types for power quality management: flywheels, supercapacitors (SC), battery storage and superconducting magnetic energy storage (SMES). The characteristics of the storage options are shown in Table 7.3. Battery storage was considered to be the most suitable option for this work due to its low self-discharge and long storage duration compared to the alternative technologies.

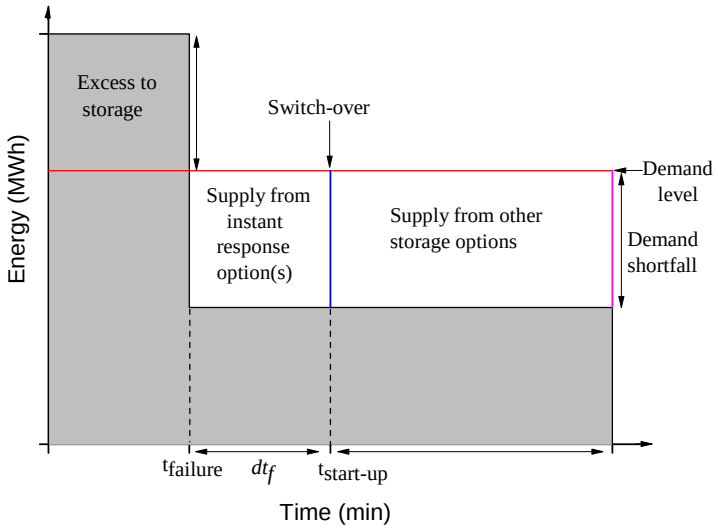

Figure 7.5.: Schematic representation of energy system reaction to sudden drop in generation level. The shaded region shows the output from the generating units while the red line shows the plant demand level. Initially, generation is greater than plant demand and the storage options are in charging mode (no power generation). When the sudden drop in generation occurs at $t_{failure}$, the storage option with instantaneous response takes over for the duration required to start up the AA-CAES and PHES systems (dt_f), thus preventing system failure.

Table 7.3.: Comparison of storage alternatives for power quality management (based on Evans et al. [78], Zach et al. [244] and Luo et al. [140])

Type	Power rating	Efficiency (%)	Daily self discharge (%)	Suitable storage duration
Flywheels	up to 20 MW	90-95	100	Seconds - minutes
SC	$<$ 0.3 MW	85-95	20-40	Seconds-hours
Batteries	up to 50 MW	65-90	0-5	Hours-months
SMES	up to 10 MW	95-98	10-20	Minutes-hours

7.2.1. General description of battery storage

Batteries are electrochemical devices which produce electricity from electrochemical reactions. Batteries are made up of multiple electrochemical cells connected together in series or parallel. Each cell consists of three components: two electrodes (one anode, one cathode) and an electrolyte. The electrodes accept and contribute electrons during reactions, while the electrolyte acts as medium for ion transfer [222].

During discharging, electrons flow from the anode to the cathode through an external circuit, thereby generating electricity to power a load. Ions flow from one electrode to the other through the electrolyte as shown in Figure 7.6. For storage (also called secondary or multiple-cycle) batteries, charging is done by applying an external current to the electrodes in the opposite direction. This forces the reverse reaction and regenerates the original reactants [23, 222], thereby restoring the battery. Batteries are connected in series to give the desired voltage, while parallel connection increases the available current

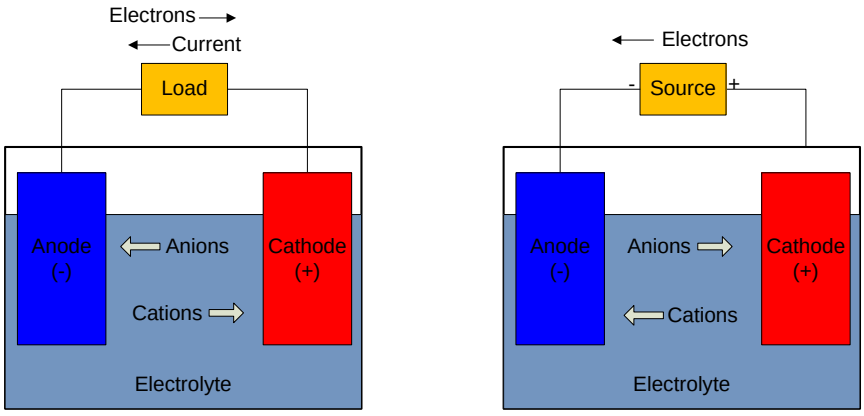

(a) Discharging (b) Charging

Figure 7.6.: Working principle of rechargeable electrochemical cells.

and capacity [29, 195].

Batteries can be used in a variety of applications such as portable systems, power quality, emergency network back-up, renewable-energy storage in isolated areas, energy management, ride-through power and transportation systems [108, 140]. However, the high investment and maintenance costs of battery systems compared to mechanical energy storage technologies have limited the adoption of the technology in large scale applications [140]. The relatively low durability and low cycling times of batteries have also posed problems in the past as it means that batteries need to be replaced frequently [108, 140]. However, advancements in battery technology have led to the development of battery systems capable of cycling times similar to PHES and CAES systems [49, 140].

There are various types of batteries based on the types and phases of the electrolytes and electrodes present in the cells. Most of them have been reviewed extensively [23, 140, 195].

Batteries are the most frequently used type of energy storage in hybrid systems design and sizing. They have been considered in single objective [7, 64, 241] and multi-objective problems [3, 170]. Most of the sizing works consider lead-acid battery banks.

The vanadium redox flow battery (VRFB) will be considered in this work for reasons which will be highlighted in the next section.

7.2.2. Vanadium redox flow battery

A flow battery is a type of storage battery where one or both of the reactants are liquids stored in external tanks and flow through an electrochemical cell consisting of electrodes and separator structures [222]. The schematic of a typical flow battery system shown in Figure 7.7. The electrochemical consists of two half cells [233], with the electrodes in the cell stack separated by a microporous, ion-selective membrane that only allows the flow of ions while preventing electrolyte mixture [195, 222].

During operation, the electrolyte material stored in the tanks are pumped through the electrochemical cell stack which houses the electrodes at which the reactions occur [195].

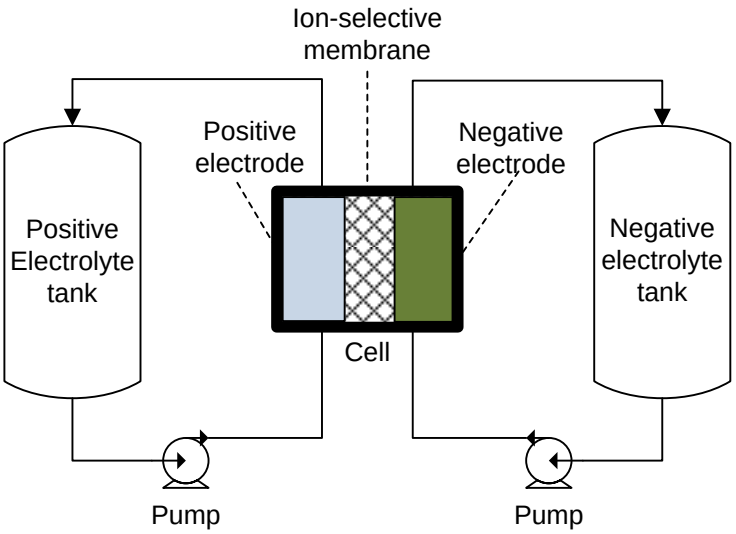

Figure 7.7.: Schematic representation of a flow battery

One of the electrolytes is reduced at the anode while the other oxidized at the anode, thereby converting chemical to electrical energy. This process is reversed during charging.

A crucial advantage of the redox flow battery over other battery types such as lead-acid is that it allows for the decoupling of the energy (storage capacity) and power of the battery [140, 158, 195, 233]. The energy is dependent on the size of the storage tank, while the power is dependent on the pump size and the area of the electrodes in the cell stack [140, 158, 195]. This is key because it allows for the power and energy capacities to be scaled independently of each other, preventing oversizing and allowing greater flexibility in matching power and duration needs for specific applications [158, 233]. With other battery types, the maximum charging and discharging rates are dependent on the battery storage capacity, meaning that the storage capacity may have to be oversized to produce the required power. For this reason, flow batteries easily scalable [78] and are thought to be the future of large-scale battery storage [195].

This characteristic is particularly important when the battery is only required to provide short term power, as is the case in emergency backup and power quality applications. To understand why, consider the lead-acid battery used in the work by Salem and Mahkamov [199] on the sizing of standalone PV-battery systems. The battery used in the work had recommended maximum charging and discharging rates of C/10 and C/5 respectively, where C refers to the battery storage capacity. For such a battery, at least 5 kWh of storage must be installed to produce 1kW of power. Thus, the battery will need to be oversized for any application with less than 5 hours of discharge required. The lead-acid battery system used in the work by Al-Shamma'a and Addoweesh [7] had a recommended discharge rate of C/20, meaning 20 kWh of storage needed to be installed for every 1kW of power required. Similar constraints may be found in batteries used in other works [29, 241]. While such restrictions were fine for those works as the battery systems were expected to have load shifting and standby reserve capabilities (they were the only storage options made available), they would likely be unsuitable for problems

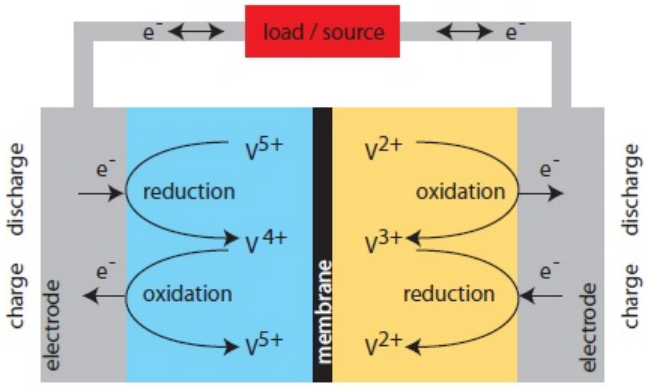

Figure 7.8.: Cell behaviour during charging and discharging of VRFB systems. Source: Türker [222]

in which the battery is only expected to provide short-term power until other electrical storage options come online, as is the case in this work. Such restrictions do not occur with the redox flow batteries since the power and energy are sized separately.

In Vanadium redox low batteries (VRFB), both electrolytes are made up of vanadium ions dissolved in sulphuric acid solutions, taking advantage of multiple oxidation states of vanadium [195, 222]. During discharge, V^{2+} ions are oxidized at negative electrode while V^{5+} ions are reduced at the positive electrode (see Figure 7.8). These reactions are reversed during charging. The battery equations are:

Negative electrode:	$V^{2+} \leftrightharpoons V^{3+} + e^-$
Positive electrode:	$V^{5+} + e^- \leftrightharpoons V^{4+}$
Overall reaction:	$V^{2+} + V^{5+} \leftrightharpoons V^{3+} + V^{4+}$

Round trip efficiencies of up to 85% have been reported for VRFB systems [49, 140]. The same vanadium can be used over and over due to the reversibility of the process, therefore battery lifetime is not a problem. The operating lifetime is expected to be about 20 years [140, 222], making it one of the most durable battery technologies. VRFB systems also have other advantages over other battery types: they have low environmental impact unlike lead-acid and lithium-ion batteries which are enviromentally unfriendly and pose significant disposal problems [222, 233], are fundamentally safe as the electrolytes are non-flammable [233], have significantly longer cycle lifetimes than most other battery types as they do not degrade significantly over time [222, 233], compare well cost-wise with all except lead-acid batteries (Table 7.4), and are more tolerant to overcharging and deep discharge [222]. Merei et al. [154] also suggest that VRFB systems produce better performance than Lithium-ion and Lead-acid batteries for offgrid energy system applications.

However, VRFB systems have low energy density, meaning they are only suitable for stationary applications [49, 140, 222]. Reports about the operating costs are also unclear, with Wilson et al. [233] and Türker [222] suggesting that the systems are low maintenance but Luo et al. [140] reporting a comparatively high operating cost.

Table 7.4.: Comparison of current battery technologies based on works by Chen et al. [49], Evans et al. [78] and Luo et al. [140]. Vanadium redox flow batteries have the longest lifetime, lowest environmental impacts and one of the lowest capital costs of the alternative technologies. They however have the lowest energy density and are more expensive than lead-acid batteries.

Type	Lifetime cycles	Lifetime (years)	Efficiency	Self discharge (%)	Energy density (W h/L)	Enviromental impact	Energy capital cost ($/kW h)	Power capital cost ($/kW)
Lead-acid	2,000	5-15	70-90	0.1-0.3	50-80	High	200-400	200-600
Lithium-ion	10,000	5-15	85-90	0.1-0.3	200-500	Moderate	600-2,500	1,200-4,000
Sodium-Sulphur	4,500	10-15	75-90	∼20	150-300	Moderate	300-500	1,000-3,000
Nickel-Cadmium	3,500	10-20	60-83	0.2-0.6	60-150	Moderate	800-1,500	500-1,500
Vanadium RFB	>12,000	10-20	75-85	very low	25-35	Very small	150-1,000	600-1,500
Zinc-Bromide FB	2,000	5-10	65-80	very low	30-65		150-1,000	700-2,500

7.2.3. System description and battery model

Figure 7.9 shows the proposed energy superstructure for the mine after battery integration. The flow batteries are charged from the output of the wind turbines and photovoltaics, and supply power to the plant when sudden failure occurs. Sudden failure occurs when the outputs of the electrical generation systems are insufficient to meet power demands. When this happens the batteries come online, taking advantage of their instant response capabilities and allowing the required time for the other electrical storage options to power up. During this time, the MTS system may be able to supply power depending on whether the steam turbine is already operational. Once the other options become available, the battery system is switched off. Batteries are installed for power quality purposes only due to the significantly higher capital cost compared to the other storage technologies [140].

Excess electrical generation is now split between three electrical storage systems. Mathematically,

$$\dot{E}^{in}_{store}(t) = \dot{E}^{in}_{PHES}(t) + \dot{E}^{in}_{AA-CAES}(t) + \dot{E}^{in}_{BAT}(t) \tag{7.4}$$

The battery system contributes to the power output of the system. The gross electricity output of the renewable energy system comprises of the power supplied directly from generation and the power output from the four storage options:

$$\dot{E}^{RES}(t) = \dot{E}^{d}(t) + \sum_{j=1}^{4} \dot{E}^{out}_{j}(t) \tag{7.5}$$

where $j = 4$ represents the battery system. Again, the actual (net) electrical power available for supply to the plant may be slightly lower due to parasitic losses.

From the system description, it is clear that the batteries do not operate at the same time as the other electrical storage options. Hence, when shortfall occurs, the energy output of the system is dependent on the state of the system. The energy storage options available are dependent on the elapsed time since the shortfall occured $\mathrm{d}t_f$ (see Fig. 7.5). In the immediate aftermath of the shortfall ($\mathrm{d}t_f < t_{start-up}$), power can only be supplied from the MTS and battery systems. After the PHES and AA-CAES systems become available however, the battery need no longer be used until the next failure. Mathematically,

$$\dot{E}^{RES}(t) = \dot{E}^{d}(t) \qquad \forall\, \mathrm{d}t_f = 0 \tag{7.6}$$

$$\dot{E}^{RES}(t) = \dot{E}^{d}(t) + \sum_{j=3}^{4} \dot{E}^{out}_{j}(t) \qquad \forall\, 0 < \mathrm{d}t_f < t_{start-up} \tag{7.7}$$

$$\dot{E}^{RES}(t) = \dot{E}^{d}(t) + \sum_{j=1}^{3} \dot{E}^{out}_{j}(t) \qquad \forall\, \mathrm{d}t_f \geq t_{start-up} \tag{7.8}$$

where $t_{start-up}$ is the maximum of the start-up times required by the other technologies. It should be noted here that how long the battery is expected to provide instantaneous power before the other options become available ($t_{start-up}$) will have an impact on the

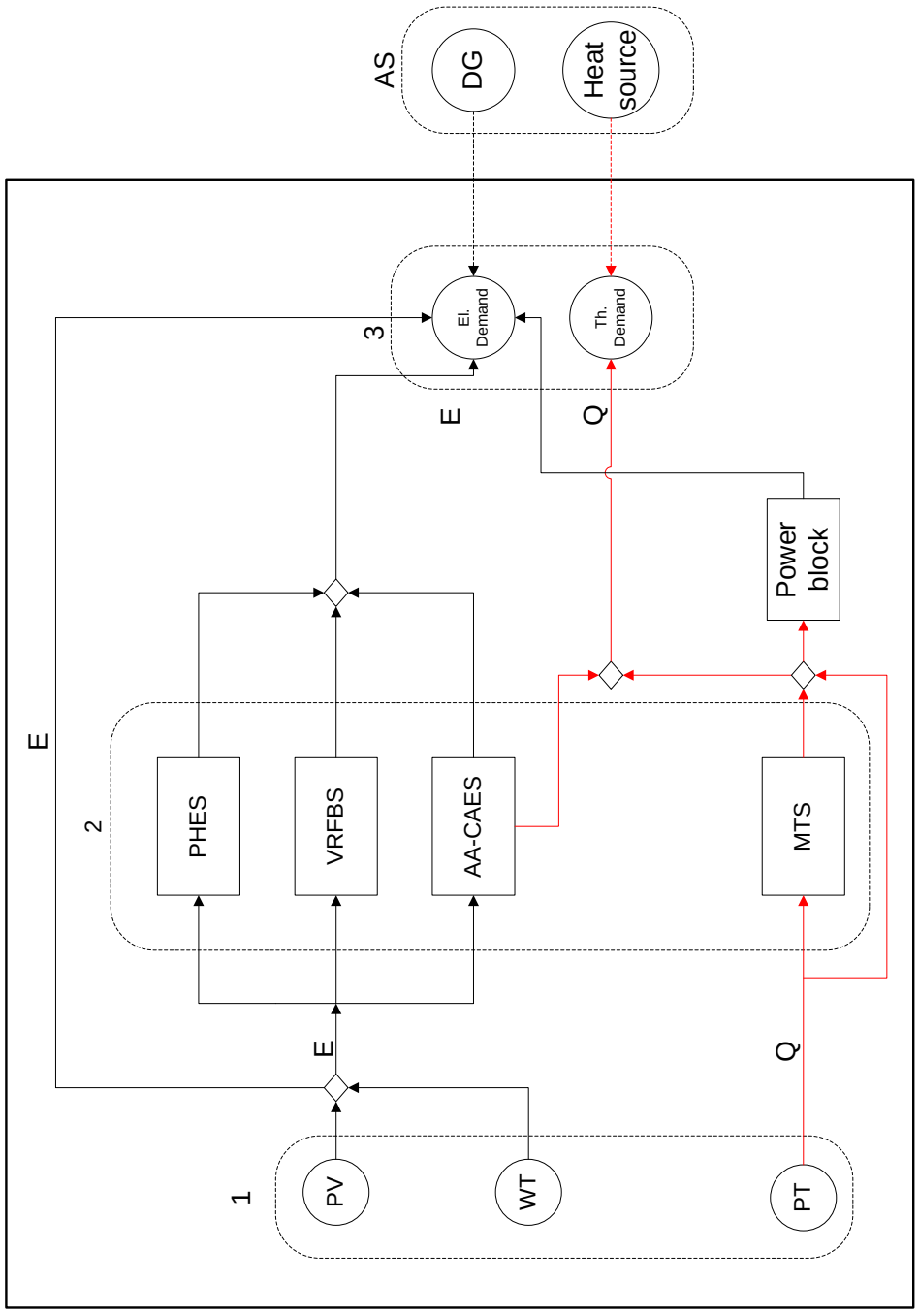

Figure 7.9.: Proposed energy superstructure for the mine after battery integration. The battery system provides intermediate power until the PHES and/or AA-CAES systems become available.

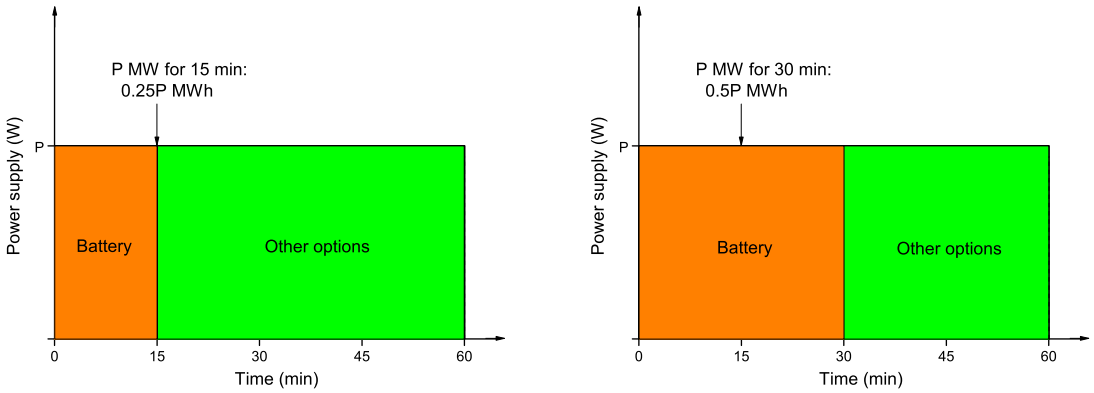

(a) Transition time $t_{start-up} = 15\,\text{min}$ (b) Transition time $t_{start-up} = 30\,\text{min}$

Figure 7.10.: Impact of transition time on battery storage requirements

sizes of the storage capacities required and consequently, the capital costs of the designs. To demonstrate this, consider a one-hour stretch with quarter-hourly time steps in which the first time step requires energy supply from battery storage. The operational profiles for the system when 15-minute and half-hourly transition times are considered are shown in Figures 7.10a and 7.10b respectively.

The total load demand in both cases is $P\,\text{Wh}$, with the storage requirements of each technology given by the area under the curve. When $t_{start-up} = 15\,\text{min}$, a battery of minimum size $0.25P\,\text{Wh}$ is required; the other technologies will need to supply $0.75P\,\text{Wh}$ once they come online. With half-hourly ($t_{start-up} = 30\,\text{min}$) transition times however at least $0.5P\,\text{Wh}$ of battery storage is required, with the other options required to meet less of the load for the hour. Thus, while the power requirement from the battery system is the same in both cases, the energy requirement is different because of the length of discharge: the required battery storage capacity will increase when the battery is operational for longer. This may also influence the capacity requirements of the other storage technologies as well.

What this implies is that the transition time will have an impact on the capital costs (and potentially the configurations) of the designs required. The reliability of the designs will be also affected by $t_{start-up}$: a design which is capable of meeting electrical demands when 15 minutes of battery operation is required after each failure may not do so when 30 minutes of discharge is required, and vice-versa. The selection of $t_{start-up}$ is therefore very important: it must be tailored to the technologies under consideration.

7.2.3.1. Battery model

Figure 7.11 shows a schematic of the battery system. Inverter and efficiency losses are incurred during the charge and discharge phases, while some energy is also lost from the system due to self-discharge. The self discharge rate, κ, is typically dependent on the level of charge of the battery: a fully charged battery will lose more energy through self-discharge than a half-charged battery.

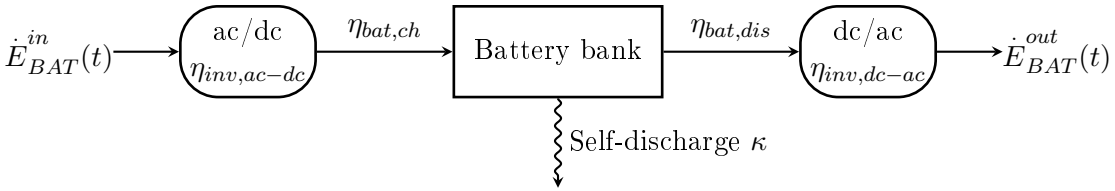

Figure 7.11.: Schematic of battery system showing system losses. The battery bank is made up of series and parallel connections of individual batteries.

Three different measures have been used in energy systems modelling to represent the level of charge of battery banks. The first measure considers the amount of energy stored in the battery S_{BAT} [Wh]. The rate of change of energy within a battery bank [7, 64, 80] is given by

$$\frac{\mathrm{d}}{\mathrm{d}t}S_{BAT}(t) = \eta_{bat,ch}\eta_{inv,ac-dc}\dot{E}^{in}_{BAT}(t) - \frac{\dot{E}^{out}_{BAT}(t)}{\eta_{bat,dis}\eta_{inv,dc-ac}} - \kappa S_{BAT}(t) \tag{7.9}$$

The first two terms represent the rates of energy into and out of the battery bank while the last term gives the rate of energy loss via self discharge as a function of storage level.

The second measure considers the amount of charge stored in the battery $\hat{q}_{BAT}(t)$ [Ah] and can be obtained by dividing the stored energy by the battery bank voltage U_{bat} [Volts]. Hence, based on the above expression, the rate of change of stored charge is given by:

$$\frac{\mathrm{d}}{\mathrm{d}t}\hat{q}_{BAT}(t) = \frac{1}{U_{bat}}\left(\eta_{bat,ch}\eta_{inv,ac-dc}\dot{E}^{in}_{BAT}(t) - \frac{\dot{E}^{out}_{BAT}(t)}{\eta_{bat,dis}\eta_{inv,dc-ac}}\right) - \kappa\hat{q}_{BAT}(t) \tag{7.10}$$

The stored charge was used in place of the stored energy for modelling the battery system by Belfkira et al. [29] and Abbes et al. [3]. The measure is used frequently because battery manufacturers often report the nominal battery capacity in Ah.

The third measure, called the battery state of charge (SOC), expresses the present battery capacity as a fraction (or percentage) of its nominal capacity $\hat{q}^{nom}_{BAT}$ [Ah][46, 80]. From Equation 7.10, the rate of change of the SOC is given by

$$\frac{\mathrm{d}}{\mathrm{d}t}SOC_{BAT}(t) = \frac{1}{\hat{q}^{nom}_{BAT}U_{bat}}\left(\eta_{bat,ch}\eta_{inv,ac-dc}\dot{E}^{in}_{BAT}(t) - \frac{\dot{E}^{out}_{BAT}(t)}{\eta_{bat,dis}\eta_{inv,dc-ac}}\right) - \kappa SOC_{BAT}(t) \tag{7.11}$$

The SOC of a battery will range from 0% (fully discharged battery) to 100% (fully charged battery). This expression used by Yang et al. [241] for a lead-acid battery.

The three expressions provide the same capability to measure battery state. The expressions are based on the assumption that the battery operates at a constant voltage [80]. While this is not strictly true because the voltage varies with hysteresis and nonlinearly with the state of charge [80], the expressions are sufficient for design and sizing purposes [3, 80], although more accurate models which capture the battery voltage variations

would be required for real-time battery control [80].

The first expression (Eq. 7.9) was used to model the battery bank in this work, with the state of charge calculated by dividing by the battery capacity $C^s_{BAT} = \hat{q}^{nom}_{BAT} \cdot U_{bat}$ [Wh].

A battery bank is made up of series and parallel connections of single batteries. Given the nominal voltage $U_{bat,single}$ [Volts] and nominal current capacity $\hat{q}^{nom}_{BAT,single}$ [Ah] of a single battery, the number of batteries required for the bank may be calculated as:

$$N_{bat} = \frac{C^s_{BAT}}{\hat{q}^{nom}_{BAT,single} \cdot U_{bat,single}} = \left[\frac{\hat{q}^{nom}_{BAT}}{\hat{q}^{nom}_{BAT,single}}\right] \cdot \left[\frac{U_{bat}}{U_{bat,single}}\right] \tag{7.12}$$

The first term in the square brackets gives the number of parallel battery connections required to give the desired charge storage capacity in Ah, while the second term gives the number of series connections required to obtain the desired voltage[3, 29].

7.2.3.2. Capacity constraints

The energy accumulated in the battery at any point during operation is limited by the installed storage capacity,

$$S_{BAT}(t) \leq C^s_{BAT} \tag{7.13}$$

For a VRFB system, this is related to the size of the storage tank. Similarly, the instantaneous electrical output from the battery cannot exceed the nominal output capacity,

$$\dot{E}^{out}_{BAT}(t) \leq C^{out}_{BAT} \tag{7.14}$$

For a VRFB system, this is related to the pump size and the area of the cell stack.

7.2.3.3. Constraint on depth of discharge (DOD)

The depth of discharge (DOD) is a measure of how deeply a battery has been discharged [193]. It is typically expressed as a percentage of the nominal (maximum) battery capacity. A battery which has been discharged by 40%, maintaining 60% of its capacity, would have a DOD of 40%. The depth of discharge is inversely proportional to the battery life: a battery typically lasts longer when it it discharged less deeply [241]. Battery manufacturers typically provide information on the recommended lower limit the battery bank should not exceed when discharging in order to preserve battery life. Given a maximum depth of discharge DOD_{max}, the minimum level of discharge of the battery will be [3]

$$S^{min}_{BAT} = (1 - DOD_{max}) \cdot C^s_{BAT} \tag{7.15}$$

When combined with Equation 7.13, we obtain the operating limits for the battery as

$$S^{min}_{BAT} \leq S_{BAT}(t) \leq C^s_{BAT} \tag{7.16}$$

Algorithm 7.1 Operating scheme for energy system with battery integration. The binary variable ψ tracks the state of the storage system.

Given: Design specifications $\overline{x} = \left\{C_i^{gen}, C_j^s, C_j^{out}, \overline{OP}\right\}$; demand requirements from storage $\left\{\dot{Q}_\tau^{th}, \dot{E}_\tau^{el}\right\}$.

Output: Storage outputs $\left\{\dot{Q}_{j,\tau}^{heating}, \dot{E}_{j,\tau}^{out}\right\}$; Power shortfalls $\left\{\dot{\phi}_\tau^{th}, \dot{\phi}_\tau^{el}\right\}$

procedure DISCHARGE SUB-MODEL

1. Satisfy thermal demands
   - Meet shortfall from MTS system $\dot{Q}_{1,\tau}^{heating}$.
   - Evaluate heating requirement shortfall ϕ_τ^{th}. If shortfall exists, try to meet from AA-CAES system $\dot{Q}_{2,\tau}^{heating}$.
   - Re-evaluate heating requirement shortfall $\dot{\phi}_\tau^{th} = \dot{Q}_\tau^{th} - \dot{Q}_{1,\tau}^{heating} - \dot{Q}_{2,\tau}^{heating}$.
2. Satisfy electrical demands

   Determine previous storage state $\psi_{\tau-1}$
   - If $\psi_{\tau-1} = 1$, $\dot{E}_{4,\tau}^{out} = 0$. Evaluate storage outputs $\dot{E}_{j,\tau}^{out}$ as specified by the operating scheme selected:
     - If $\overline{OP} = 1$, discharge storage in the order: AA-CAES - MTS - PHES.
     - If $\overline{OP} = 2$, discharge storage in the order: AA-CAES - PHES - MTS.
     - If $\overline{OP} = 3$, discharge storage in the order: MTS - AA-CAES - PHES.
   - If $\psi_{\tau-1} = 0$, $\dot{E}_{1,\tau}^{out} = \dot{E}_{2,\tau}^{out} = 0$. Determine whether PT supplied plant directly in previous time period:
     - If yes $\rightarrow$ discharge MTS, then battery bank.
     - If no, $\dot{E}_{3,\tau}^{out} = 0 \rightarrow$ discharge battery bank only.
   - Evaluate electrical requirement shortfall $\dot{\phi}_\tau^{el} = \dot{E}_\tau^{el} - \sum_{j=1}^{4} \dot{E}_{j,\tau}^{out}$.

end procedure

These equations, together with the those previously presented for the other system components in Section 3.3, form the energy system model.

7.2.4. Model implementation and solution strategy

The same procedural approach described in Section 6.3 was implemented for this problem. However, the discharge operating scheme was modified to accommodate the battery system as shown in Algorithm 7.1.

For energy supply from storage, the key change from the previous scheme (described in Section 6.3) is the incorporation of the battery system to provide electrical power in the transitional period (one time step) from full supply from generation (photovoltaics/wind turbines) to partial or full supply from storage. This is achieved by introducing a binary variable ψ_τ to track the previous state of the storage systems. A value of $\psi_{\tau-1} = 0$ indicates that none of the storage options was in use at the previous time period, meaning

a transitioning period is required to allow for start-up of the storage systems. During this period, only the battery bank (taking advantage of its instantaneous response) and/or the MTS system (depending on whether the steam turbine it shares with the power tower is already operational from the previous time period) may supply the plant. Supply from the MTS (when available) is preferred over the battery system.

On the other hand, a value of $\psi_{\tau-1} = 1$ means that at least one storage option was active at the previous time step, indicating that sufficient time has elapsed for the main storage systems to become available. In this case, the discharge order is dependent on the pre-defined scheme $\overline{OP}$. An implicit assumption here is that system ramp-up and ramp-down is near-instantaneous: the power output of the storage units can be increased or decreased rapidly as long as the system was already operational.

Since the battery bank may need to be used on short notice at any time, it is charged before the other electrical storage options. Charging the battery bank first also allows us to provide an instant response to sudden spikes in generation, taking advantage of its ability to charge quickly.

External energy E_{τ}^{ext} is only required if energy from local generation and storage is insufficient to satisfy demand, thermal or electrical.

Finer model discretization, smaller population size 15-minute time steps are considered for the discretization of the entire model, corresponding to the maximum start-up time $t_{start-up}$ required by the storage alternatives (see Table 7.1) and the recommended minimum discharge period for electrochemical systems [108]. The smaller time steps mean that the system response to dynamics in generation can be monitored more accurately. However, moving from hourly to 15-minute steps will quadruple the evaluation time for each design. Thus, the optimization model will require significantly more computational time and memory. Given the finite computational resource available, a smaller population size will be considered (compared to previous studies) to keep the solution time manageable.

7.2.5. Case study: Canada

The case study of the design of an energy system for the fictional Canadian mine is again considered. We investigate the impact of the introduced operational constraints on the configuration and cost of the non-dominated set of designs.

Two design variables were introduced to characterize the battery system: number of batteries in the battery bank (N_{bat}) and the storage capacity in hours (N_{st}). Thus, given the nominal capacity of a single battery, the nominal discharge capacity (MW) and storage capacity (MWh) can easily be calculated. In total, twelve design variables were considered for the problem. The variable bounds used are shown in Table 7.5.

The same cost objective presented previously in Section 6.1 was used, with two additional terms representing the storage and discharge capacities of the battery included in the equation. It was assumed that no battery replacement will be required based on the

Table 7.5.: NSGA-II variable bounds for case study integrating battery storage

Variable	C_i^{gen} [MW]	N_T	C_j^s [MWh]	C_j^{out} [MW_e]	$\overline{OP}$	N_{bat}	N_{st} [h]
Lower bound	0	0	0	0	1	0	1
Upper bound	10,000	5,000	25,000	300	3	50,000	3

i = generation technologies $\{PT, PV\}$, j = storage technologies (excluding batteries)

Table 7.6.: NSGA-II parameters for battery study

Population size	$N_{pop} = 40$
Selection	Binary tournament selection
Crossover	Intermediate crossover, Crossover fraction = 0.75
Mutation	Gaussian mutation, mutation fraction = 0.3
Stopping criteria	Maximum number of generations, $N_g = 300$

lifetime information (Table 7.4) and the likely infrequent use. However, the validity of this assumption will be verified once the results have been obtained.

The NSGA-II parameters used for the case study are presented in Table 7.6, while the characteristics and cost data for the battery system considered are presented in Appendix B. The same renewable input scenarios considered in the previous case studies are used, with the same value repeated four times for each hour. All other parameters are unchanged from the previous studies. Given the smaller population size, five runs are considered in this case.

The average time required for the five parallelized runs was 1092 h on a Linux based machine with twelve 2.4 GHz Intel Xeon processors and 24 GB RAM. This is almost quadruple the time required for the solar-wind case considered in section 6.5.3. This increase is despite the fact that the population size was reduced by 60%. The significant increase in computational time reflects how much longer it takes to evaluate a single design because of the increased model size (brought on by the incorporation of an additional technology to be considered at each time step) and finer time discretization (number of time steps increased fourfold).

Figure 7.12 shows the fronts obtained from the runs. Three different fronts have been obtained, with three of the runs converging to the non-dominated front. A difference of 6% is observed in the costs of the most reliable designs obtained from the five runs. While the non-dominated front has been identified, the presence of local fronts suggests that a larger population size or more generations may be more suitable for the problem. However, the presence of local fronts provides the opportunity to explore different potential configurations of the system.

The designs which make up each of the fronts have similar characteristics in terms of technology choices and are different from the designs on the other fronts. However, the results obtained in all the runs integrate solar and wind resources for power generation. This suggests that the advantages provided by solar and wind integration outweigh the intermittency challenges associated with wind generation.

The characteristics of the solutions produced by two of the runs will be explored. First,

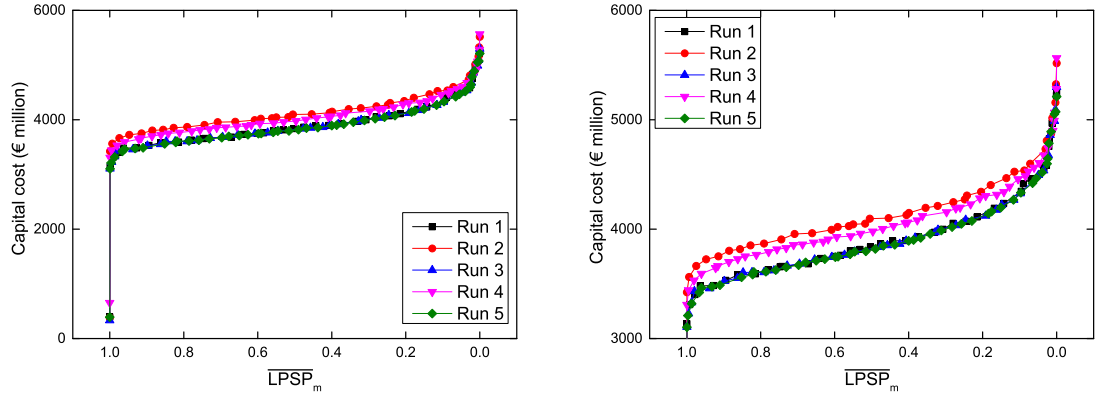

(a) Full Pareto fronts with trivial ($\overline{LPSP}_m = 1$) solutions

(b) A zoomed in view of Figure 7.12a after removal of trivial solutions

Figure 7.12.: Approximations to Pareto front for battery-integrated system obtained in five attempts with NSGA-II. Three distinct fronts are obtained, with three of the runs (1,3 and 5) overlapping on the non-dominated front.

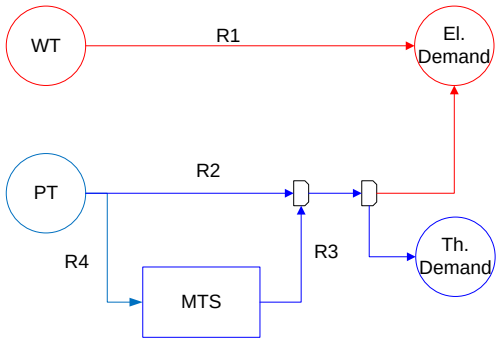

Figure 7.13.: System configuration and operating scheme for designs. The red and blue lines represent the electrical and thermal networks respectively.

the properties of one of the runs on the non-dominated front (run 5) will be discussed. This will be followed by an analysis of the characteristics of the designs on the second front (run 4). The focus here will be on how intermittency impacts the configuration (technology choices, capacities) and operating behaviour of the designs on the fronts.

7.2.5.1. Characteristics of non-dominated front: Run 5

Optimal system configuration In this case, no batteries are installed. The optimal system design involves the installation of a power tower (PT) and wind turbines (WT) for generation, and tank storage (MTS) as shown in Figure 7.13. No electrical storage option is selected. The WT system satisfies electrical demands only, while the PT and MTS systems satisfy both electrical and thermal demands.

Generation capacities Figure 7.14 shows the variations in installed generation capacities with reliability. The general trend remains the same as in previous cases, with the installed wind turbine capacity remaining at the same level and the installed PT capacity increasing across the reliability range. However, significantly less wind generation is

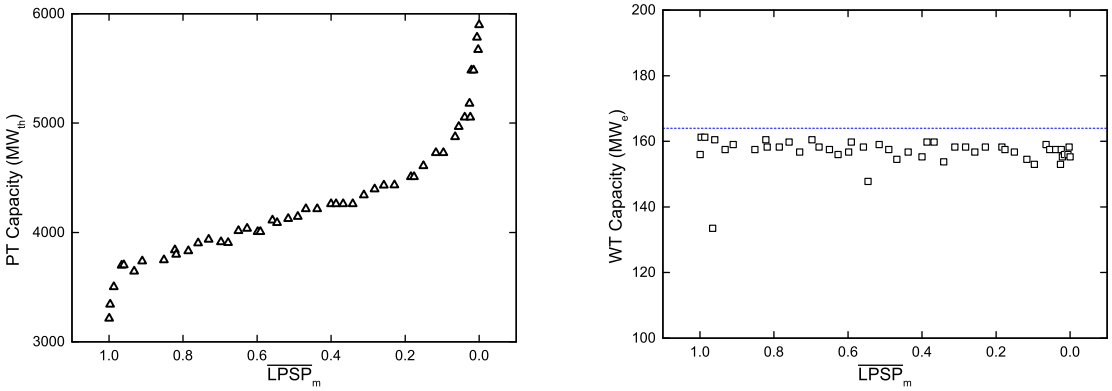

(a) Power Tower (b) Wind Turbines

Figure 7.14.: Variation in power tower and wind generation capacities over reliability range. The broken blue line in Fig. 7.14b shows the minimum power demand for the year.

Table 7.7.: Minimum cost design for Run 5

C_{PT}^{gen}	C_{wind}^{gen}	C_{MTS}^{s}	C_{MTS}^{out}	Cost
3215 MW_{th}	156 MW_e	12103 MWh	187 MW_e	€ 3103.43M

installed compared to the unconstrained case (Figure 6.25b). The nominal wind turbine capacities are just below minimum demand level of the plant (164 MW_e). Thus, the wind turbines generate no excess power: any power generated will be consumed immediately by the mine. This makes sense with no electrical storage option installed. The choice to reduce wind generation and eliminate the PHES system rather than install batteries highlights the high costs associated with battery storage.

The decrease in wind power available is compensated for by increases of about 1250 MW_{th} in the nominal PT capacities compared to the unconstrained case.

Operating behaviour To understand how the intermittency challenge is handled with this system configuration we consider the operating behaviour of the minimum cost design $\left(\overline{LPSP}_m = 0.999\right)$ on a typical day in April, the month with the highest wind availability. The design is shown in Table 7.7.

Figure 7.15 shows the power output profiles from the wind turbine and power tower. Thermal generation is available only during the day (between 6 am and 7pm). Wind generation is available throughout the day, but intermittently.

Figure 7.16 shows the power supply profile to the plant for the same day. The peak generation from wind for the day is 132 MW_e, less than the demand at any point during the day. Thus, the plant is able to absorb all the wind power generated. During the day, wind power is supported by power generated from the power tower output to meet the demands of the mine. At night, the MTS system provides the support. At least one of the PT or MTS systems is always required; the power block is always in operation. This ensures that any sudden drop in wind power output can easily be compensated for.

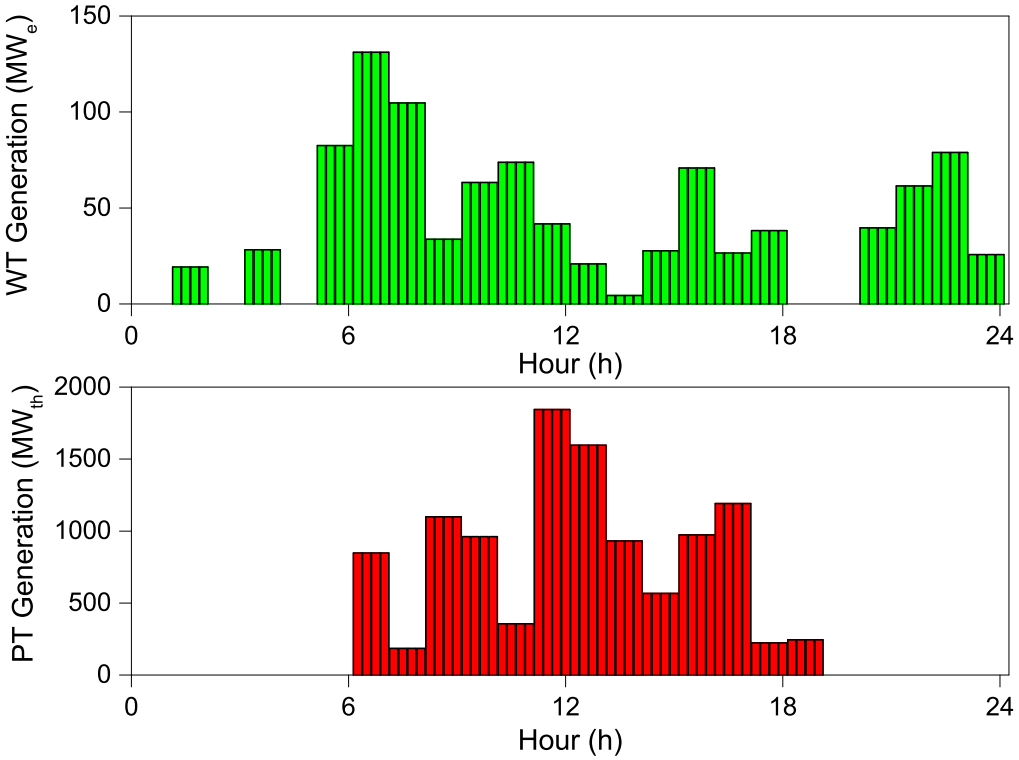

Figure 7.15.: Power generation profiles for typical day in April. The vertical lines represent 15 minute time intervals.

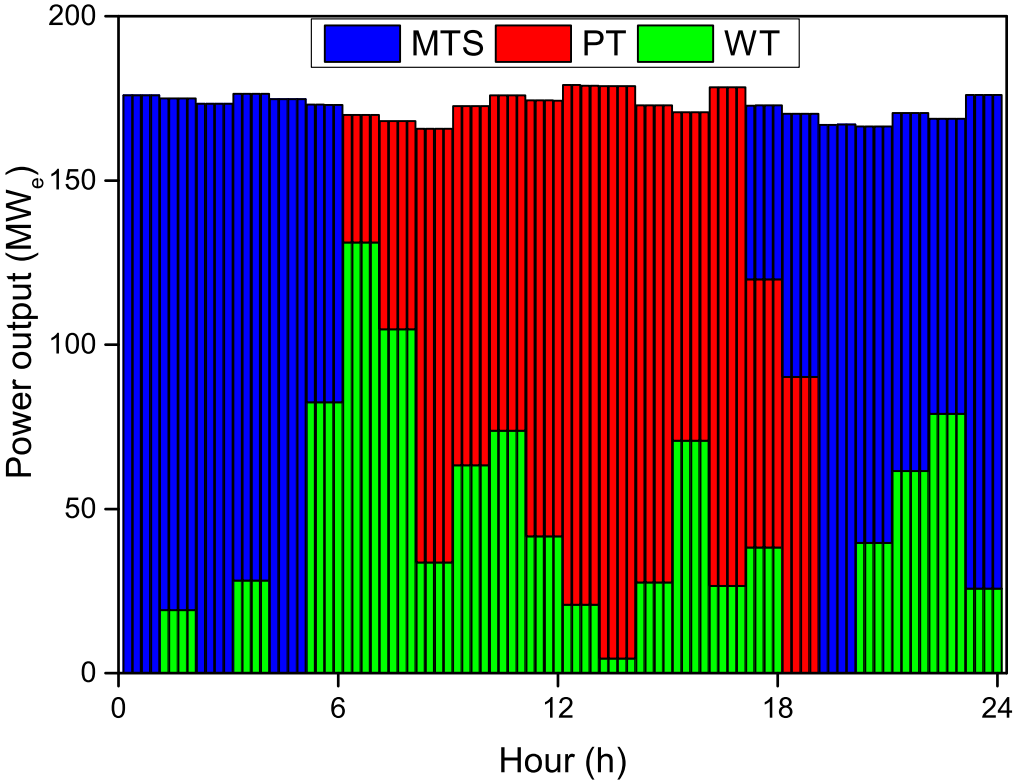

Figure 7.16.: Corresponding power supply profile for the day. The vertical lines represent 15 minute time intervals.

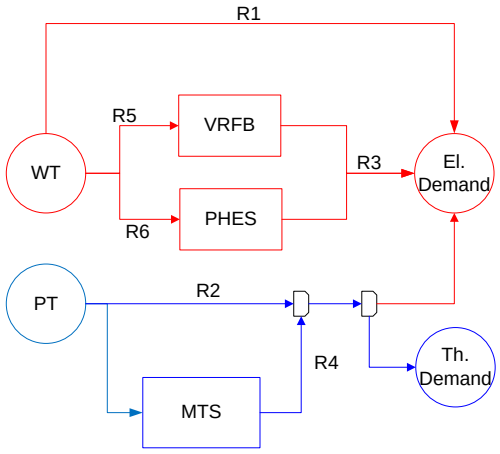

Figure 7.17.: System configuration and operating scheme for designs. The red and blue lines represent the electrical and thermal networks respectively.

Thus, the solution takes advantage of the integrated nature of the solar thermal system and is dependent on the assumption of instantaneous ramping.

It is important to note that with this approach, the maximum allowable wind contribution to the energy mix is dependent on the power demand level of the mine: any significant reduction in the power demand (for example, due to equipment downtime) must be accompanied by a corresponding reduction in the online wind power generation capacity. This is necessary to ensure that the maximum potential wind power output remains insufficient to meet the full power demands of the mine, and can be achieved by simply turning off one or more wind generators. The feasibility of the configuration is therefore dependent on the wind turbines being installed in a way that allows them to be controlled individually or in small clusters.

7.2.5.2. Characteristics of first dominated front: Run 4

System configuration The system design involves the installation of a power tower (PT) and wind turbines (WT) for generation, and three different storage options as shown in Figure 7.17. Batteries have been installed to smoothen out the intermittency of wind generation. The WT, VRFB and PHES systems meet power demands only, while the PT and MTS meet both power and heat loads. The discharge priority for power supply is R1>R2>R3>R4, with the power source for R3 dependent on the previous operating state of the system. Only one of the electrical storage options is discharged at any time. Priority is given to the battery system (R5) during charging.

System capacities Figure 7.18a shows that the installed wind generation capacity does not change significantly across the reliability range. More wind turbines are installed compared to the unconstrained case (Figure 6.25b) because extra power generation is required to charge the batteries. The installed capacities are significantly larger than the peak power demand of the plant; direct generation from wind will be sufficient to meet

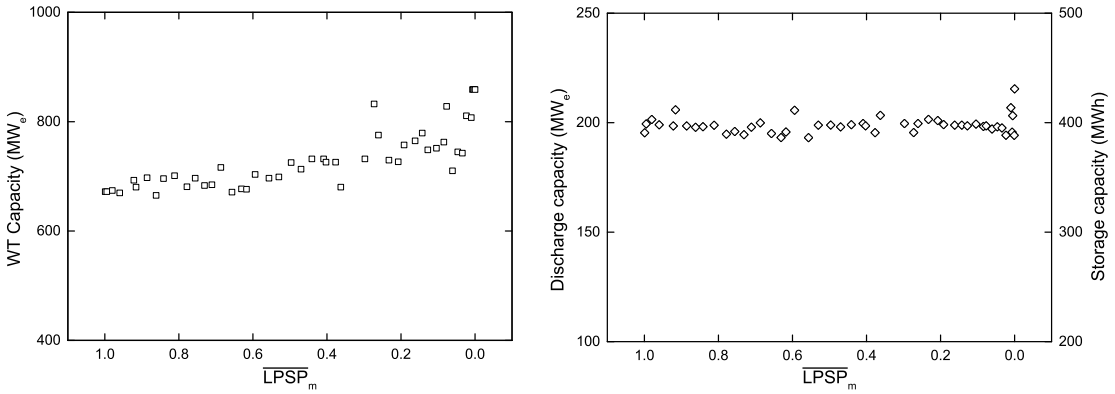

(a) Wind turbine capacities (b) Battery system capacities

Figure 7.18.: Variation in wind turbine and battery storage capacities over reliability range.

Table 7.8.: Characteristics of minimum cost design for battery-integrated system

PT	WT	MTS	PHES	VRFB	Cost
1838 MW_{th}	672 MW_{th}	9612 MWh, 184 MW_e	415 MWh, 42 MW_e	391 MWh, 195.5 MW_e*	€ 3308.84M

* Nominal DC capacity

demand in time periods in which the wind turbines are able to operate at close to their nominal capacities.

The installed capacity of battery storage also remains at the same level across the reliability range (Figure 7.18b). This makes sense given the constant level of the wind installations. The battery is sized to be able to meet the peak power demand of the mine. Two hours of battery storage was deemed sufficient to smoothen out the impact of intermittency. This allows the system roughly eight 15-minute discharges before the battery is emptied.

The capacities of the other system components (PT, MTS, PHES) remain at roughly the same level as for the unconstrained case.

Operating behaviour To show how intermittency is handled with this system configuration, we consider the operating behaviour of the minimum cost design $\left(\overline{LPSP}_m = 0.999\right)$ on the same April day considered previously. The design is shown in Table 7.8.

Figure 7.19 shows the wind generation profile. The wind output exceeds the demand level for 10 hours of the day. At those hours, the mine is run purely on wind generation. As can be seen in Figure 7.20, the battery system provides temporary power for 15 minutes when insufficient wind generation suddenly occurs. This gives the other systems sufficient time to start up. The battery system is only required in 4 time periods (equivalent to one hour) on the day.

Wind power variations below the demand level are managed by increasing or decreasing the power outputs of the other power supply options.

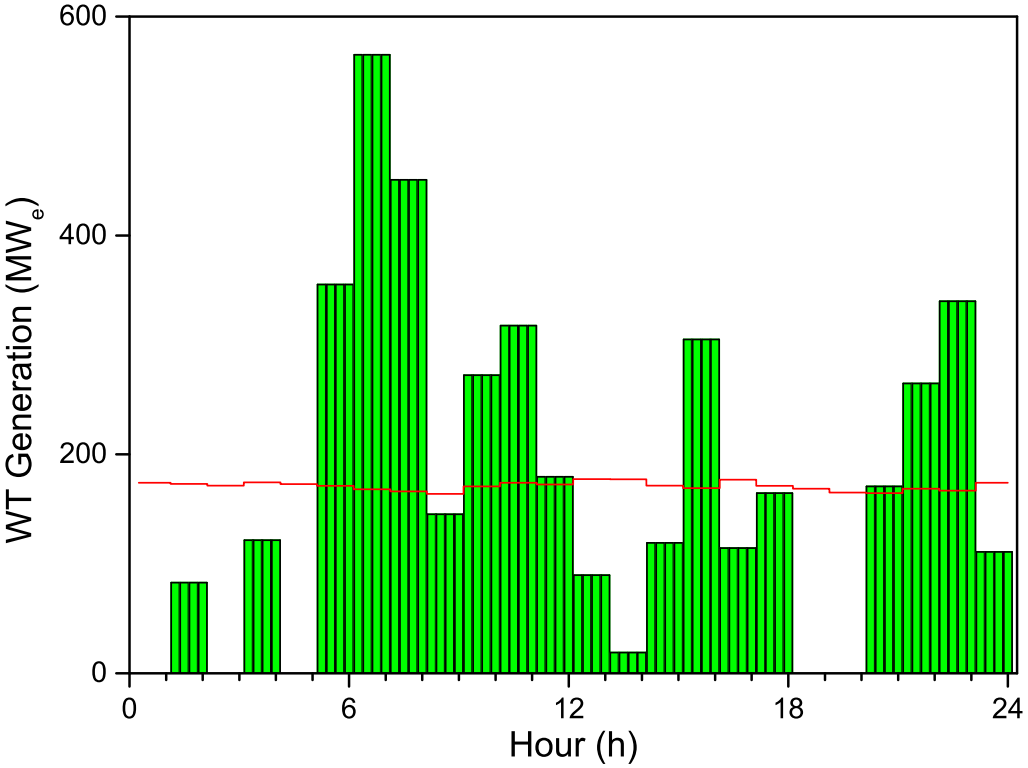

Figure 7.19.: Wind generation profile for typical day in April. The vertical lines represent 15 minute time intervals. The red line represents the demand level.

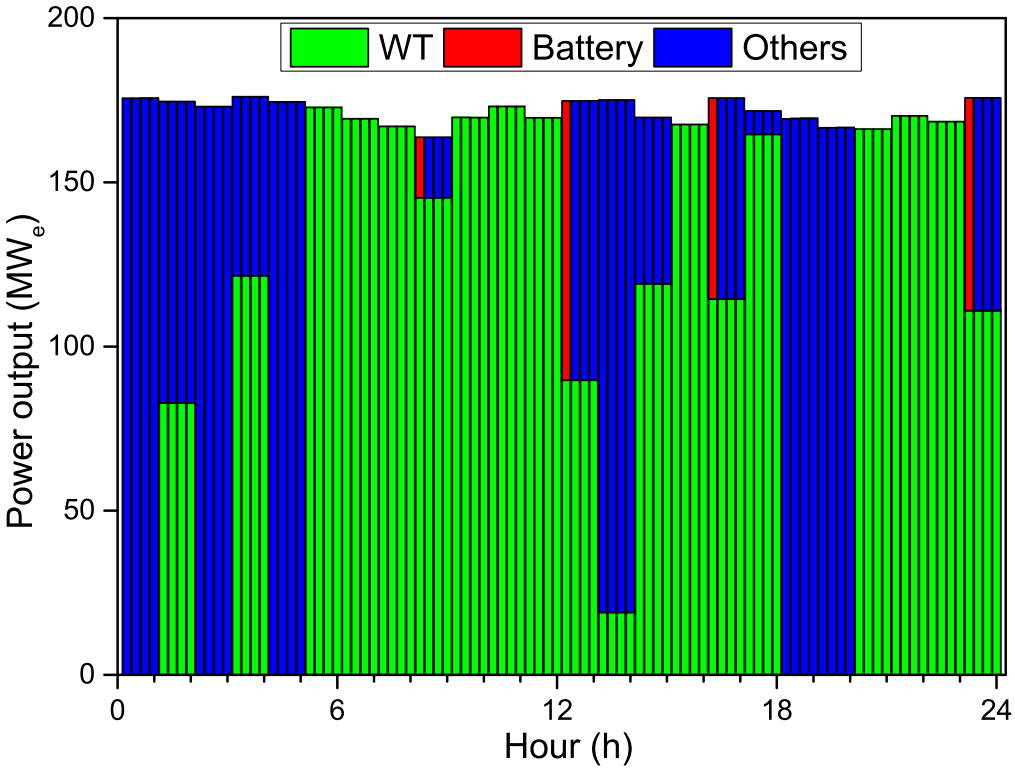

Figure 7.20.: Corresponding power profile for the day. Power supplied from the power tower, MTS system and PHES system have been combined into "others".

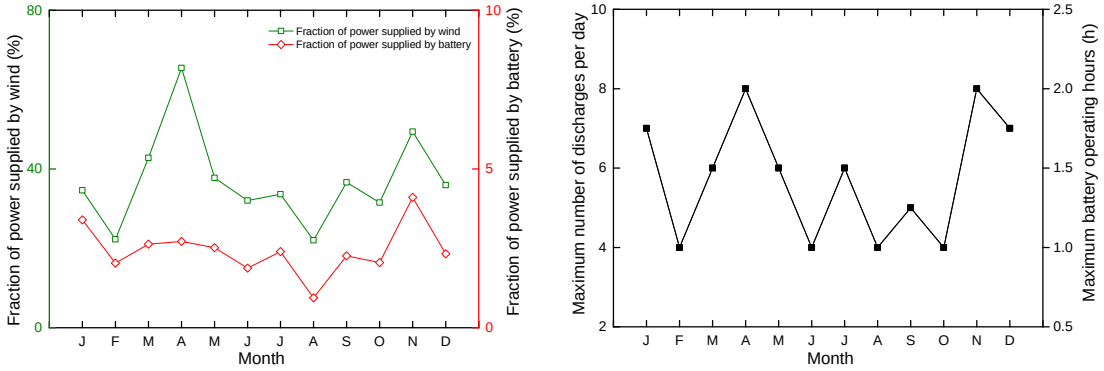

(a) Fraction of monthly power demand met from wind and battery systems.

(b) Maximum number of battery deployments per day in each month.

Figure 7.21.: Battery dispatch and energy behaviour in typical year.

Battery deployment Figure 7.21a shows the battery and wind power dispatch profiles for a typical scenario. The behaviours of the two systems are correlated: less energy is required from the battery system in months where less demand is met directly from wind generation, and vice versa. This makes sense since the battery system is usually required in response to sudden changes in wind generation (see Figure 7.20). Thus, a reduction in the use of wind energy should reduce how frequently the battery system is required, as observed here. It is also clear that batteries supply a very small proportion of the power demands of the mine, about 2.5% over the entire year.

Figure 7.21b shows the battery discharge behaviour in the same scenario. The maximum number of discharges observed on any single day is 8, corresponding to two hours of battery operation. The battery discharges for a total of 291 h (3.3%) in the year in this scenario. The frequency of battery discharge was found to vary from 3.1% - 4.3% over the 1,200 input scenarios considered. This suggests that the frequency of battery dispatch does not change significantly irrespective of the wind availability level. Given that all the designs across the reliability range incorporate a similar level of wind generation (Figure 7.18a), a similar frequency of battery deployment can be expected.

Figure 7.22 shows the depth-of-discharge distribution for the battery in the scenario considered. A total of 1,161 battery cycles occur in the year. However, most of the cycles are partial, with the battery most frequently discharged by only 10-15%.

To evaluate the battery cycle lifetime, the number of full battery cycles (full charge to full discharge to full charge again) is required. This can be evaluated from the partial cycle information available using the equivalent full cycle (EFC) concept developed by Ashari and Nayar [18]. Given a number of partial battery charge-discharge cycles of different depths, the EFC concept gives the equivalent number of full cycles (EFC) for each discharge depth as:

$$EFC = DOD \times \text{Number of cycles}|_{DOD} \tag{7.17}$$

For example, for the scenario under consideration, 163 battery cycles involved discharge

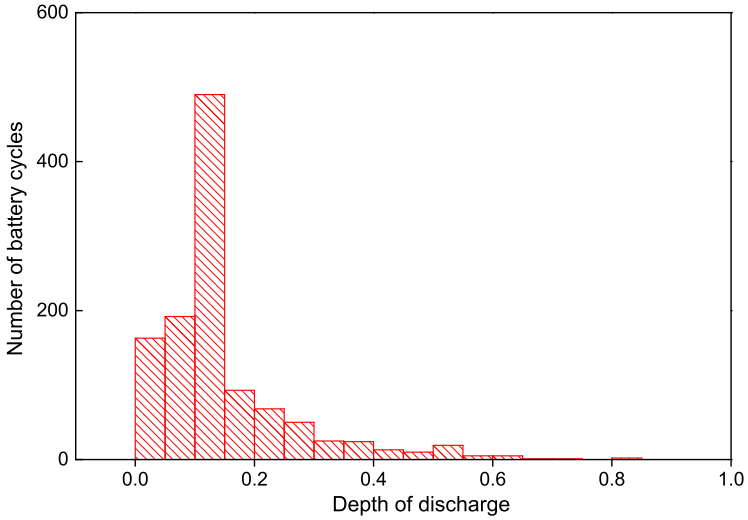

Figure 7.22.: Battery DOD distribution probability for selected scenario

depths of under 5% (Figure 7.22). The equivalent number of full cycles below 5% is:

$$EFC_{5\%} = 163 \times 5\% = 8.15 \text{ full cycles}$$

Applying the same approach to all the ranges shown in the histogram reveals that the battery operates for the equivalent of 201 full cycles in the year. Given that the typical cycle lifetime of Vanadium RFBs is over 12,000 cycles (Table 7.4), the battery will be able to operate at this rate for 60 years before it needs to be replaced. This is more than twice the lifetime of a typical mine. Thus, the assumption that no battery replacement will be required over the lifetime of the mine is valid.

Summary

This chapter focused on the development of power quality management strategies to mitigate the impact of renewables intermittency on power supply to the mine. Two methodologies were presented. In the first approach, the operation of the energy system was redesigned to ensure that the storage systems provided a buffer between renewables generation and power supply to the mine. The second approach was based on the introduction of another storage option to provide power during transitions between power supply modes. Both approaches were demonstrated with case studies, with the results showing that accounting for intermittency will incur extra cost and may affect the optimal system configuration. Despite the intermittency of the wind resource, hybrid systems integrating solar and wind generation were shown to still represent the best opportunity for capital cost minimization.

The work presented in this chapter ensures that the storage options provide the three main functions required to provide smooth and uninterrupted power: load shifting, standby reserve and power quality management [78]. The methodologies developed can easily be applied to hybrid systems incorporating other technologies.

Chapter 8.

CONCLUSION AND FUTURE WORK

This chapter provides a summary of the thesis, discusses its findings and contributions, and outlines possible areas of further research.

8.1. Summary of Thesis and Key Contributions

The main purpose of this work has been to demonstrate the systems modeling and optimum sizing of hybrid renewable energy systems for large-scale off off-grid continuous processes such as mining.

A review of previous works on optimum hybrid energy system sizing was presented in Chapter 2. The review showed that while a lot of works accounted for diurnal and seasonal variability in the sizing of PV-wind-battery-diesel systems, the stochastic nature of renewables availability due to variability in climatic conditions between years had been largely ignored. It was clear that no consideration had been given to the sizing of hybrid systems integrating multiple thermal and electrical generation and storage technologies. The lack of diversity in storage technologies considered was also highlighted. The need to develop methods to address the power intermittency issue during the design and planning was identified. This thesis set out to address these issues.

The work rest of the thesis may be broadly divided into two main parts.

The first part (chapters 3 to 5) focused on the development of the various component models required for the evaluation of system performance.

The development of the integrated energy system model was presented in Chapter 3. The energy superstructure considered incorporated three generation options: photovoltaics for solar to electrical power, power towers for solar to thermal power, and wind turbines for wind to electrical power. Three storage options were made available in the superstructure: pumped hydraulic energy storage (PHES), molten salt thermal storage (MTS) and Advanced Adiabatic Compressed Air Energy Storage (AA-CAES). The storage options were selected based on practical considerations such as technology lifespan, cost, and scale of storage and dispatch. Models for the different technologies were presented,

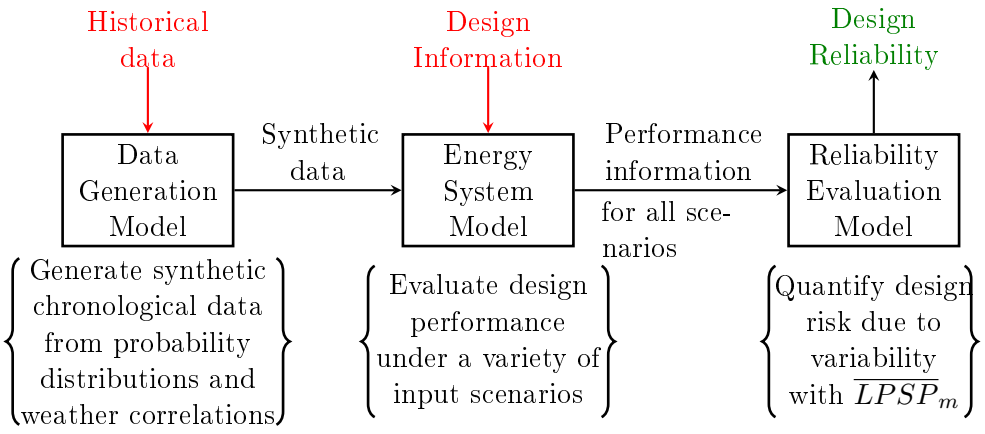

Figure 8.1.: Summary of reliability evaluation process for a single design.

leading to a differential-algebraic system of equations for the entire system. The cost function was also presented. The capability of the model was demonstrated by considering a simple case study of capital cost minimization for a remote mine. The cost and performance data obtained were shown to agree well with literature. The integrated system designed addressed the challenge of thermal and electrical power integration.

A methodology for the stochastic generation of renewables input data for reliability evaluation was developed in Chapter 4. A review of the state of the art methods for solar radiation and wind resource simulation showed distribution-based approaches as the most suitable for investigating the effects of weather-based variability. The Weibull distribution, widely accepted as the best distribution for windspeed modelling, was selected for the wind resource. A novel method for modelling global horizontal irradiance (GHI) using the Pearson family of distributions was presented. A decomposition model for modelling the direct normal irradiance (DNI) was also introduced.

A methodology for renewables data generation was then developed. This involved four stages: historical data pre-processing, random generation of discrete data from probability distributions, generation of continuous renewables input profiles from discrete data, and generation of input scenarios using stratified random sampling. The models and methodology were validated by comparing their predictions to historical measurements.

In Chapter 5, the modified loss of power supply probability $\left(\overline{LPSP}_m\right)$ was introduced. The reliability measure, inspired by the success rate definition given by Kaplani and Kaplanis [118] (Equation 2.11), quantifies the effect weather-based variability on design performance. It represents the probability of a design in meeting a predefined reliability target and requires performance information for several potential renewable scenarios as input. Two other ways of accounting for variability in reliability evaluation – the mean reliability and minimum reliability approaches – were also discussed.

The models developed in the three chapters allow for the reliability of the any given energy system design to be evaluated given historical climate data for the location under consideration. This is summarized in Figure 8.1. The historical data is supplied to the data generation model for the generation of stochastic renewable input scenarios.

The performance of the energy system design in each for the input scenarios is then evaluated for all the input profiles with the energy system model. Based on the results for the individual scenarios, the reliability of the given design can be evaluated.

The second half of the thesis (chapters 6 and 7) focused on the development of methodologies which allow for climate-based variability and renewables intermittency to be accounted for in the system sizing process.

A methodology to solve the bi-criteria sizing problem of cost minimization and reliability maximization was developed in Chapter 6. The methodology required a procedural approach to system performance evaluation for each time interval: first the outputs of the generation units were evaluated, then the heat and power supply routes were determined, and finally the storage units were charged. To reduce the combinatorics of the problem an operating scheme was introduced, with an integer variable used to select between alternative storage dispatch strategies. To demonstrate the flexibility of the methodology, three case studies with different locations and/or generation technologies available were considered. The sizing problems were solved using a multi-objective genetic algorithm. Multiple runs of the cases showed that the non-dominated set of designs was identified in each case. From the results, some conclusions were drawn:

- The degree of energy dumping, frequency of power failure and extent power system failure all increase with the degree of variability in renewables availability,
- Slight reductions in the reliability requirements can lead to significant cost savings,
- Hybrid renewable energy systems compare favourably with diesel generation cost-wise even in locations with relatively poor renewables availability,
- Solar-thermal generation is an excellent alternative for power generation, and
- The integration of thermal and electrical power generation and storage options could provide a way to reduce hybrid system costs.

Finally, the challenge of developing methodologies to mitigate the impact of intermittency in the power outputs of renewable generation technologies was addressed. Two approaches were proposed for this. The first approach was based on system redesign: the storage system was designed to act as a buffer between generation and power demand. This ensured that the intermittent nature of the generation technologies only had an impact on the charging of the storage systems, with storage providing steady power output to the plant (Figure 7.1). This concept was implemented by imposing additional constraints on the energy system. The method was demonstrated with a case study. The results of the case study showed that system buffering will always increase the cost of the system due to the larger generation and/or storage requirements required to compensate for any losses incurred in the energy conversion process.

The second approach proposed was based on the incorporation of a new storage alternative with an instantaneous response time (milliseconds) into the energy system to handle transitions between power supply modes. The vanadium redox flow battery was considered for this work based on a review of suitable technologies. The battery system

supplied power while the other storage systems transitioned from the charge (or dormant) to discharge modes. Two potential storage discharge modes were defined, with the transition between the modes controlled by a binary variable dependent the previous state of the storage system. The methodology was demonstrated by considering a case study. The results of the case study highlighted several feasible configurations of the energy system for handling the intermittency problem. The best configuration was found to avoid battery selection due to the high costs involved, taking advantage of the implicit assumption of instantaneous ramping. A typical design incorporating battery storage was also analyzed.

The thesis therefore contributes to the state-of-the-art in hybrid energy systems sizing in four key areas:

- Renewables modelling and synthetic data generation,
- Systems modelling and technology integration,
- Stochastic reliability assessment for hybrid energy systems sizing, and
- Mitigation of renewables power output intermittency.

8.2. Future Work

The research presented in this work raised several questions and opened up a variety of research directions which could be pursued in the future.

8.2.1. Incorporation of operating costs

The capital cost of the renewable energy system has been the focus of this work. However, as the Canadian case study showed, a more comprehensive cost function incorporating the operating costs of the generation and storage technologies could provide more information to aid decision making, especially for locations with low renewables availability. One such function is the total system cost (TSC), which for this RES will be given by

$$TSC = CC + (20 \text{ years} \times \text{Average operating cost over } N_{year} \text{ scenarios}) \tag{8.1}$$

A potential effect of the changed cost function is on the choice of operating scheme. In the sizing methodology developed in this thesis, a single operating strategy to be adopted throughout the year is optimized. The operating scheme only affected the performance objective: it had no effect on the cost function. This will change with the introduction of operating costs.

Katsigiannis et al. [121] and Merei et al. [154] adopted dispatch strategies which minimized the operating cost at each time step. The approach had several advantages: it ensured that the minimum operating cost was attained and reduced the number of design variables. However, determining the dispatch strategy based on the operating cost alone can have a detrimental effect on system performance. Based on the operating costs

Table 8.1.: Operating costs of storage technologies [127, 140, 244]

	Fixed [€/kW−year]	Variable [€/kWh]
AA-CAES	4	0.01-0.27
PHES	4	0.38
MTS	-	-
VRFB	65	

Table 8.2.: Effect of different dispatch strategies on system performance. Designs A and B were selected randomly from the results of the Canadian case study presented in Section 6.5.3. Both designs integrate MTS and PHES for energy storage. The first column shows the results obtained from the optimization process, while the second shows the performance with the minimum operating cost strategy.

	$\overline{LPSP}_m$	
	Discharge PHES first (Selected strategy)	Discharge MTS first (Cost-optimal strategy)
Design A	0.2450	0.4383
Design B	0.7353	0.9183

presented in Table 8.1 for example, a cost-driven dispatch strategy will give the discharge order for the storage systems as MTS>AA-CAES>PHES. However, while this scheme was made available in the implemented operating scheme, it was not selected in any of the case studies considered. A simple analysis showed that switching the discharge scheme around to reduce the operating costs can siginificantly worsen performance, as can be seen for the two designs shown in Table 8.2. The worsened performance observed when the operating scheme is switched around occurs because discharging the MTS first empties the only thermal store available much more quickly during the night, leaving the energy system with no way to meet the thermal demands of the plant.

Thus, the balance between operating cost, operating strategy and system performance should be the focus of future research.

8.2.2. Tri-criteria optimization with social/environmental impact as objective

A potential direction for this work is tri-criteria design with an environmental or social-related measure treated as the third objective. Different types of environmental objectives have been considered in literature as can be seen from the review in Chapter 2. The measures may be broadly grouped into three classes:

1. Measures related to emissions [121, 179],
2. Measures related to land consumption and potential opportunity cost [69], and
3. Measures related to the energy consumed in the production of the energy system components, such as the embodied energy considered by Abbes et al. [3].

It should be noted that the three measures do not necessarily agree with each other. For example, compared to photovoltaics, wind generators release less greenhouse emis-

sions [198] and require less energy for production [3], but use up significantly more land area[83]. Considering the impact of one or more of these objectives on optimum design choice should be the subject of future research.

Alternatively, a simple objective incorporating all three types can be developed. For example, a simple objective $\Upsilon \in [0,1]$ to be minimized incorporating the average greenhouse emissions (GHG_{avg}), embodied energy (Em) and power plant area (A_p) may be defined as:

$$\Upsilon = w_1 \frac{GHG_{avg}}{\max(GHG_{avg})} + w_2 \frac{A_p}{\max(A_p)} + w_3 \frac{Em}{\max(Em)} \tag{8.2}$$

where w_i are weights for the different objectives, $w_1 + w_2 + w_3 = 1$.

Obtaining the relevant technical data for the solar thermal system and solving the tri-criteria problem to near optimality will be the key challenges for this problem.

8.2.3. Incorporation of emerging grid-scale storage technologies

One of the key achievements of this thesis is the development of an energy system integrating multiple energy storage options. In the future, the energy superstructure developed should be extended to include emerging grid-scale storage technologies. Several technologies which may be of interest for large-scale energy storage for standalone operations are currently at the demonstration and deployment stage.

One technology generating a lot of interest for grid-scale storage is the advanced rock energy storage (ARES). The concept is similar to PHES, but with the system driven by rocks instead of water. Excess electrical generation is used to power a railcar full of rocks up a hill or mountain. When energy is required, the train is allowed to roll down the hill, with the electric motors becoming generators. The technology is expected to be cheaper than PHES. However, the technology requires a significant amount of space and has geographic limitations. Planning for the first commercial scale project (a 50 MW, 12.5 MWh plant to be located in Nevada) is already underway, with construction expected to commence in 2017 [1, 2]. Construction is expected to last for nine months.

Another technology which may be suitable is silicon-based thermal storage. The technology is based on latent heat storage, with excess energy used to heat and melt containers filled with silicon. An advantage of the technology is that storage occurs at over 1400°C, meaning that significantly less storage material and space is required compared to other thermal storage technologies [225, 226]. It also means that the storage technology may be able to provide process heating for continuous processes with high-temperature thermal demands. The technology is ready for commercialization, with a prototype of the technology already demonstrated successfully in Australia [226]. Commercial plants are expected to be able to store over 2,000 MWh of energy.

8.2.4. Development of other approaches for handling intermittency in power output

Two possible methods for mitigating the effect of renewables intermittency on power supply quality were presented in this work. The development of other approaches should be the focus of future research.

LIST OF PEER-REVIEWED PUBLICATIONS

Some of the research leading to this thesis has appeared previously in the following publications:

1. **Oluwamayowa O. Amusat**, Paul R. Shearing, and Eric S. Fraga. On the design of complex energy systems: Accounting for renewables variability in systems sizing. *Computers & Chemical Engineering*, 103:103-115, August 2017.
2. **Oluwamayowa O. Amusat**, Paul R. Shearing, and Eric S. Fraga. Optimal integrated energy systems design incorporating variable renewable energy sources. *Computers & Chemical Engineering*, 95:21-37, Dec 2016.
3. Eric S. Fraga and **Oluwamayowa Amusat**. Understanding the impact of constraints: A rank based fitness function for evolutionary methods. *Advances in Stochastic and Deterministic Global Optimization,* pages 243-254. Springer International Publishing, Cham, 2016.
4. **Oluwamayowa O. Amusat**, Paul R. Shearing, and Eric S. Fraga. Reliable energy systems design for continuous processes incorporating renewables generation. In Zdravko Kravanja and Milo Bogataj, editors, *26th European Symposium on Computer Aided Process Engineering*, volume 38 of *Computer Aided Chemical Engineering*, pages 469-474. Elsevier, 2016.
5. **Oluwamayowa O. Amusat**, Paul R. Shearing, and Eric S. Fraga. Optimal integrated energy systems design incorporating variable renewable energy sources. In Proceedings of the 3rd PRO-TEM Network Conference: *Sustainable Thermal Energy Management in the Process Industries (SusTEM2015)*, pages 245-253, Newcastle upon Tyne, July 2015.
6. **Oluwamayowa O. Amusat**, Paul R. Shearing, and Eric S. Fraga. System design of renewable energy generation and storage alternatives for large scale continuous processes. In Krist V. Gernaey, Jakob K. Huusom, and Raqul Gani, editors, *Computer Aided Chemical Engineering,* volume 37, pages 2279-2284. Elsevier, 2015.

REFERENCES

[1] America's First Commercial-Scale Rail Energy Storage Project Receives BLM Approval - Ares North America. http://www.aresnorthamerica.com/article/8736-americaś-first-commercial-scale-rail-energy-storage-project-receives-blm-approval, Apr 2016. (Accessed 09 December 2016).

[2] Electricity and Power Storage - ARES Nevada. http://www.aresnorthamerica.com/about-ares-north-america, 2016. (Accessed 09 December 2016).

[3] D. Abbes, A. Martinez, and G. Champenois. Life cycle cost, embodied energy and loss of power supply probability for the optimal design of hybrid power systems. *Mathematics and Computers in Simulation*, 98:46–62, Apr 2014. ISSN 0378-4754. doi: 10.1016/j.matcom.2013.05.004. URL http://dx.doi.org/10.1016/j.matcom.2013.05.004.

[4] R. Adinberg. Simulation analysis of thermal storage for concentrating solar power. *Applied Thermal Engineering*, 31(16):3588 – 3594, 2011. ISSN 1359-4311. doi: http://dx.doi.org/10.1016/j.applthermaleng.2011.07.025. URL http://www.sciencedirect.com/science/article/pii/S135943111100384X.

[5] H. Aksoy, Z. Fuat Toprak, A. Aytek, and N. Erdem Unal. Stochastic generation of hourly mean wind speed data. *Renewable Energy*, 29(14):2111–2131, Nov 2004. ISSN 0960-1481. doi: 10.1016/j.renene.2004.03.011. URL http://dx.doi.org/10.1016/j.renene.2004.03.011.

[6] N. Al-Rawahi, Y. Zurigat, and N. Al-Azri. Prediction of hourly solar radiation on horizontal and inclined surfaces for muscat/oman. *Journal of Engineering Research*, 8(2):19–31, 2011. URL http://www.scopus.com/inward/record.url?eid=2-s2.0-84855489697&partnerID=40&md5=0c4c1211394eb886502508eedaec35b3.

[7] A. Al-Shamma'a and K. Addoweesh. Techno-economic optimization of hybrid power system using genetic algorithm. *International Journal of Energy Research*, 38:1608–1623, 2014. URL http://www.scopus.com/inward/record.url?eid=2-s2.0-84908357430&partnerID=40&md5=337663e1dd383316c5c3e8f0d841c55f.

[8] A. Al-Shamma'a and K. Addoweesh. Techno-economic optimization of hybrid power system using genetic algorithm. *International Journal of Energy Research*, 38:1608–1623, 2014.

[9] T. Albanese and J. McGagh. Future trends in mining. In P. Darling, editor, *SME Mining Engineering Handbook*. Society for Mining, Metallurgy, and Exploration Inc., Littleton, CO, USA, 3rd edition, 2011.

[10] C. Amadei, G. Allesina, P. Tartarini, and W. Yuting. Simulation of gemasolar-based solar tower plants for the chinese energy market: Influence of plant downsizing and location change. *Renewable Energy*, 55:366–373, Jul 2013. ISSN 0960-1481. doi: 10.1016/j.renene.2012.12.022. URL http://dx.doi.org/10.1016/j.renene.2012.12.022.

[11] M. Amer, A. Namaane, and N. M'Sirdi. Optimization of hybrid renewable energy systems (hres) using PSO for cost reduction. *Energy Procedia*, 42:318–327, 2013. ISSN 1876-6102. doi: 10.1016/j.egypro.2013.11.032. URL http://dx.doi.org/10.1016/j.egypro.2013.11.032.

[12] O. O. Amusat, P. R. Shearing, and E. S. Fraga. Optimal integrated energy systems design incorporating variable renewable energy sources. *Computers & Chemical Engineering*, 95:21–37, Dec 2016. ISSN 0098-1354. doi: 10.1016/j.compchemeng.2016.08.007. URL http://dx.doi.org/10.1016/j.compchemeng.2016.08.007.

[13] J. S. Anagnostopoulos and D. E. Papantonis. Pumping station design for a pumped-storage wind-hydro power plant. *Energy Conversion and Management*, 48 (11):3009–3017, Nov 2007. ISSN 0196-8904. doi: 10.1016/j.enconman.2007.07.015. URL http://dx.doi.org/10.1016/j.enconman.2007.07.015.

[14] T. Anandharajan, G. A. Hariharan, K. Vignajeth, R. Jijendiran, and Kushmita. Weather monitoring using artificial intelligence. *2016 2nd International Conference on Computational Intelligence and Networks (CINE)*, Jan 2016. doi: 10.1109/cine.2016.26. URL http://dx.doi.org/10.1109/CINE.2016.26.

[15] A. Andreev, A. Kanto, and P. Malo. Simple approach for distribution selection in the pearson system. 2005.

[16] J. Arora, M. Huang, and C. Hsieh. Methods for optimization of nonlinear problems with discrete variables: A review. *Structural optimization*, 8(2-3):69–85, 1994. ISSN 0934-4373. doi: 10.1007/BF01743302. URL http://dx.doi.org/10.1007/BF01743302.

[17] I. Arsie, V. Marano, G. Nappi, and G. Rizzo. A model of a hybrid power plant with wind turbines and compressed air energy storage. *ASME 2005 Power Conference*. doi: 10.1115/pwr2005-50187. URL http://dx.doi.org/10.1115/PWR2005-50187.

[18] M. Ashari and C. Nayar. An optimum dispatch strategy using set points for a photovoltaic (PV)-diesel-battery hybrid power system. *Solar Energy*, 66(1):1–9, May 1999. ISSN 0038-092X. doi: 10.1016/s0038-092x(99)00016-x. URL http://dx.doi.org/10.1016/S0038-092X(99)00016-X.

[19] M. Ashby. Is the mining industry ready to go green? *Mining Engineering*, 60 (11):33–36, 2008. URL http://www.scopus.com/inward/record.url?eid=2-s2.0-57749170419&partnerID=40&md5=5db7efca9e2f0e23aa9dd08808b2d490. cited By (since 1996)0.

[20] A. Askarzadeh. A discrete chaotic harmony search-based simulated annealing algorithm for optimum design of PV/wind hybrid system. *Solar Energy*, 97:

93–101, Nov 2013. ISSN 0038-092X. doi: 10.1016/j.solener.2013.08.014. URL http://dx.doi.org/10.1016/j.solener.2013.08.014.

[21] Y. Atwa, E. El-Saadany, and A.-C. Guise. Supply adequacy assessment of distribution system including wind-based dg during different modes of operation. *IEEE Transactions on Power Systems*, 25(1):78–86, Feb 2010. ISSN 1558-0679. doi: 10.1109/tpwrs.2009.2030282. URL http://dx.doi.org/10.1109/TPWRS.2009.2030282.

[22] Australian Government Department of Resources, Energy and Tourism. Energy-mass balance: Mining. *Energy Efficiency Opportunities*, October 2010. [Online]. Available at: http://energyefficiencyopportunities.gov.au/files/2012/10/Energy-Mass-Balance-Mining.pdf (Accessed 02 December 2013).

[23] V. S. Bagotsky, A. M. Skundin, and Y. M. Volfkovich. Electrochemical power sources. Nov 2014. doi: 10.1002/9781118942857. URL http://dx.doi.org/10.1002/9781118942857.

[24] F. Barnes and J. Levine. *Large Energy Storage Systems Handbook*. Mechanical and Aerospace Engineering Series. Taylor & Francis, 2011. ISBN 9781420086010. URL http://books.google.co.uk/books?id=-j8tOt7VhccC.

[25] F. Batlles, M. Rubio, J. Tovar, F. Olmo, and L. Alados-Arboledas. Empirical modeling of hourly direct irradiance by means of hourly global irradiance. *Energy*, 25(7):675 – 688, 2000. ISSN 0360-5442. doi: http://dx.doi.org/10.1016/S0360-5442(00)00007-4. URL http://www.sciencedirect.com/science/article/pii/S0360544200000074.

[26] T. Bauer, N. Breidenbach, N. Pfleger, D. Laing, and M. Eck. Overview of molten salt storage systems and material development for solar thermal power plants. *Institute of Technical Thermodynamics*, 2011.

[27] A. C. Beath. Industrial energy usage in australia and the potential for implementation of solar thermal heat and power. *Energy*, 43(1):261 – 272, 2012. ISSN 0360-5442. doi: http://dx.doi.org/10.1016/j.energy.2012.04.031. URL http://www.sciencedirect.com/science/article/pii/S0360544212003118. 2nd International Meeting on Cleaner Combustion (CM0901-Detailed Chemical Models for Cleaner Combustion).

[28] O. Behar, A. Khellaf, and K. Mohammedi. A review of studies on central receiver solar thermal power plants. *Renewable and Sustainable Energy Reviews*, 23(0):12 – 39, 2013. ISSN 1364-0321. doi: http://dx.doi.org/10.1016/j.rser.2013.02.017. URL http://www.sciencedirect.com/science/article/pii/S1364032113001184.

[29] R. Belfkira, L. Zhang, and G. Barakat. Optimal sizing study of hybrid wind/PV/diesel power generation unit. *Solar Energy*, 85(1):100–110, Jan 2011. ISSN 0038-092X. doi: 10.1016/j.solener.2010.10.018. URL http://dx.doi.org/10.1016/j.solener.2010.10.018.

[30] H. Belmili, M. Haddadi, S. Bacha, M. F. Almi, and B. Bendib. Sizing stand-alone photovoltaic-wind hybrid system: Techno-economic analysis and optimiza-

tion. *Renewable and Sustainable Energy Reviews*, 30:821–832, Feb 2014. ISSN 1364-0321. doi: 10.1016/j.rser.2013.11.011. URL http://dx.doi.org/10.1016/j.rser.2013.11.011.

[31] L. Biegler. *Nonlinear Programming: Concepts, Algorithms, and Applications to Chemical Processes*. MOS-SIAM Series on Optimization. Society for Industrial and Applied Mathematics (SIAM, 3600 Market Street, Floor 6, Philadelphia, PA 19104), 2010. ISBN 9780898719383. URL http://books.google.co.uk/books?id=VdB1wJQu0sgC.

[32] M. Blanchard and G. Desrochers. Generation of autocorrelated wind speeds for wind energy conversion system studies. *Solar Energy*, 33(6):571–579, Jan 1984. ISSN 0038-092X. doi: 10.1016/0038-092x(84)90013-6. URL http://dx.doi.org/10.1016/0038-092X(84)90013-6.

[33] R. Blonbou, S. Monjoly, and J.-L. Bernar. Dynamic energy storage management for dependable renewable electricity generation. *Energy Storage - Technologies and Applications*, Jan 2013. doi: 10.5772/52411. URL http://dx.doi.org/10.5772/52411.

[34] C. Blum and A. Roli. Metaheuristics in combinatorial optimization. *ACM Computing Surveys*, 35(3):268–308, Sep 2003. ISSN 0360-0300. doi: 10.1145/937503.937505. URL http://dx.doi.org/10.1145/937503.937505.

[35] B. Bobee, L. Perreault, and F. Ashkar. Two kinds of moment ratio diagrams and their applications in hydrology. *Stochastic Hydrology and Hydraulics*, 7(1):41–65, 1993. ISSN 1435-151X. doi: 10.1007/BF01581566. URL http://dx.doi.org/10.1007/BF01581566.

[36] B. Borowy and Z. Salameh. Methodology for optimally sizing the combination of a battery bank and PV array in a wind/PV hybrid system. *IEEE Transactions on Energy Conversion*, 11(2):367–375, Jun 1996. ISSN 0885-8969. doi: 10.1109/60.507648. URL http://dx.doi.org/10.1109/60.507648.

[37] G. E. Box and G. M. Jenkins. *Time series analysis: forecasting and control, revised ed.* Holden-Day, 1976.

[38] R. W. Bradshaw, D. B. Dawson, W. De la Rosa, R. Gilert, S. H. Goods, M. J. Hale, P. Jacobs, S. A. Jones, G. J. Kolb, J. E. Pacheco, and et al. *Final Test and Evaluation Results from the Solar Two Project*. Jan 2002. doi: 10.2172/793226. URL http://www.osti.gov/scitech/servlets/purl/793226.

[39] D. Brus and J. de Gruijter. Random sampling or geostatistical modelling? choosing between design-based and model-based sampling strategies for soil (with discussion). *Geoderma*, 80(1-2):1–44, Oct 1997. ISSN 0016-7061. doi: 10.1016/s0016-7061(97)00072-4. URL http://dx.doi.org/10.1016/S0016-7061(97)00072-4.

[40] C. Bueno and J. Carta. Technical-economic analysis of wind-powered pumped hydrostorage systems. part i: model development. *Solar Energy*, 78(3):382–395, Mar 2005. ISSN 0038-092X. doi: 10.1016/j.solener.2004.08.006. URL http://dx.doi.org/10.1016/j.solener.2004.08.006.

[41] C. Bueno and J. Carta. Technical-economic analysis of wind-powered pumped hydrostorage systems. part ii: model application to the island of el hierro. *Solar Energy*, 78(3):396–405, Mar 2005. ISSN 0038-092X. doi: 10.1016/j.solener.2004.08.007. URL http://dx.doi.org/10.1016/j.solener.2004.08.007.

[42] J. I. Burgaleta, S. Arias, and D. Ramirez. Gemasolar, the first tower thermosolar commercial plant with molten salt storage. In *In: Proceedings of SOLARPACES 2011*, September 2011.

[43] E. Cadenas and W. Rivera. Wind speed forecasting in the south coast of oaxaca, mexico. *Renewable Energy*, 32(12):2116–2128, Oct 2007. ISSN 0960-1481. doi: 10.1016/j.renene.2006.10.005. URL http://dx.doi.org/10.1016/j.renene.2006.10.005.

[44] M. Carvalho, A. Romero, G. Shields, and D. Millar. Optimal synthesis of energy supply systems for remote open pit mines. *Applied Thermal Engineering*, 64:315 – 330, 2014. ISSN 1359-4311. doi: http://dx.doi.org/10.1016/j.applthermaleng.2013.12.040. URL http://www.sciencedirect.com/science/article/pii/S135943111300937X.

[45] Centro de Despacho Economico de Carga del Sistema Interconectado del Norte Grande de Chile. Retiros de energía a clientes. [Online]. Available at: http://cdec2.cdec-sing.cl/. Accessed 04 May 2014.

[46] W.-Y. Chang. The state of charge estimating methods for battery: A review. *ISRN Applied Mathematics*, 2013:1–7, 2013. ISSN 2090-5572. doi: 10.1155/2013/953792. URL http://dx.doi.org/10.1155/2013/953792.

[47] R. P. Charles, K. W. Davis, and J. L. Smith. Assessment of concentrating solar power technology cost and performance forecasts. *Sargent & Lundy LLC, Technical Report*, 2005.

[48] A. Chauhan and R. Saini. A review on integrated renewable energy system based power generation for stand-alone applications: Configurations, storage options, sizing methodologies and control. *Renewable and Sustainable Energy Reviews*, 38:99–120, Oct 2014. ISSN 1364-0321. doi: 10.1016/j.rser.2014.05.079. URL http://dx.doi.org/10.1016/j.rser.2014.05.079.

[49] H. Chen, T. Cong, W. Yang, C. Tan, Y. Li, and Y. Ding. Progress in electrical energy storage system: A critical review. *Progress in Natural Science*, 19(3):291–312, 2009. URL http://www.scopus.com/inward/record.url?eid=2-s2.0-63749132596&partnerID=40&md5=0441bdd26157902684b5648b48d36186.

[50] R. Chenni, M. Makhlouf, T. Kerbache, and A. Bouzid. A detailed modeling method for photovoltaic cells. *Energy*, 32(9):1724–1730, Sep 2007. doi: 10.1016/j.energy.2006.12.006. URL http://dx.doi.org/10.1016/j.energy.2006.12.006.

[51] D. Connolly, H. Lund, B. Mathiesen, and M. Leahy. A review of computer tools for analysing the integration of renewable energy into various energy systems. *Applied Energy*, 87(4):1059–1082, Apr 2010. ISSN 0306-2619. doi: 10.1016/j.apenergy.2009.09.026. URL http://dx.doi.org/10.1016/j.apenergy.2009.09.026.

[52] D. Connolly, S. MacLaughlin, and M. Leahy. Development of a computer program to locate potential sites for pumped hydroelectric energy storage. *Energy*, 35(1): 375–381, Jan 2010. ISSN 0360-5442. doi: 10.1016/j.energy.2009.10.004. URL http://dx.doi.org/10.1016/j.energy.2009.10.004.

[53] D. Connolly, H. Lund, B. Mathiesen, E. Pican, and M. Leahy. The technical and economic implications of integrating fluctuating renewable energy using energy storage. *Renewable Energy*, 43:47–60, Jul 2012. ISSN 0960-1481. doi: 10.1016/j.renene.2011.11.003. URL http://dx.doi.org/10.1016/j.renene.2011.11.003.

[54] A. Daniel and A. Chen. Stochastic simulation and forecasting of hourly average wind speed sequences in jamaica. *Solar energy*, 46(1):1–11, 1991.

[55] J. Deane, B. Gallachoir, and E. McKeogh. Techno-economic review of existing and new pumped hydro energy storage plant. *Renewable and Sustainable Energy Reviews*, 14(4):1293–1302, May 2010. ISSN 1364-0321. doi: 10.1016/j.rser.2009.11.015. URL http://dx.doi.org/10.1016/j.rser.2009.11.015.

[56] K. Deb, A. Pratap, S. Agarwal, and T. Meyarivan. A fast and elitist multiobjective genetic algorithm: Nsga-ii. *IEEE Trans. Evol. Computat.*, 6(2):182–197, Apr 2002. ISSN 1089-778X. doi: 10.1109/4235.996017. URL http://dx.doi.org/10.1109/4235.996017.

[57] K. Deb and T. Goel. Controlled elitist non-dominated sorting genetic algorithms for better convergence. *Evolutionary Multi-Criterion Optimization*, pages 67–81, 2001. ISSN 0302-9743. doi: 10.1007/3-540-44719-9_5. URL http://dx.doi.org/10.1007/3-540-44719-9_5.

[58] P. Delicado and M. Goria. A small sample comparison of maximum likelihood, moments and l-moments methods for the asymmetric exponential power distribution. *Computational Statistics & Data Analysis*, 52(3):1661–1673, Jan 2008. ISSN 0167-9473. doi: 10.1016/j.csda.2007.05.021. URL http://dx.doi.org/10.1016/j.csda.2007.05.021.

[59] P. Denholm and R. Sioshansi. The value of compressed air energy storage with wind in transmission-constrained electric power systems. *Energy Policy*, 37(8): 3149–3158, Aug 2009. ISSN 0301-4215. doi: 10.1016/j.enpol.2009.04.002. URL http://dx.doi.org/10.1016/j.enpol.2009.04.002.

[60] P. Denholm, E. Ela, B. Kirby, and M. Milligan. The role of energy storage with renewable electricity generation. Technical report, National Renewable Energy Laboratory, Jan 2010. URL http://digitalscholarship.unlv.edu/cgi/viewcontent.cgi?article=1005&context=renew_pubs.

[61] Departamento de Geofísica de la Universidad de Chile. Evaluación del recurso solar. [Online]. Available in Spanish at: http://walker.dgf.uchile.cl/Explorador/Solar2/, 2012. Accessed 31 March 2014.

[62] Departamento de Geofísica de la Universidad de Chile. Explorador de energia eólica. [Online]. Available in Spanish at:

http://walker.dgf.uchile.cl/Explorador/Eolico2/, 2016. Accessed 31 March 2014.

[63] Department of Environmental and Natural Resources, Government of Canada. Past weather and climate: Historical Data. [Online]. Available at: http://climate.weather.gc.ca/historical_data/search_historic_data_e.html, 2016. Accessed 19 July 2015.

[64] S. Diaf, M. Belhamel, M. Haddadi, and A. Louche. Technical and economic assessment of hybrid photovoltaic/wind system with battery storage in corsica island. *Energy Policy*, 36(2):743–754, February 2008. ISSN 0301-4215. URL http://www.sciencedirect.com/science/article/pii/S0301421507004788.

[65] F. Diaz-Gonzalez, A. Sumper, O. Gomis-Bellmunt, and R. Villafafila-Robles. A review of energy storage technologies for wind power applications. *Renewable and Sustainable Energy Reviews*, 16(4):2154–2171, May 2012. ISSN 1364-0321. doi: 10.1016/j.rser.2012.01.029. URL http://dx.doi.org/10.1016/j.rser.2012.01.029.

[66] A. S. Drud. CONOPT-A Large-Scale GRG Code. *ORSA Journal on Computing*, 6(2):207–216, May 1994. ISSN 2326-3245. doi: 10.1287/ijoc.6.2.207. URL http://dx.doi.org/10.1287/ijoc.6.2.207.

[67] J. Duffie and W. Beckman. *Solar Engineering of Thermal Processes: Fourth Edition*. John Wiley & Sons, Inc., Solar Energy Laboratory, University of Wisconsin-Madison, United States, 2013. URL http://www.scopus.com/inward/record.url?eid=2-s2.0-84891584184&partnerID=40&md5=a4627e279ca41900c9b4602d84146d08.

[68] R. Dufo-Lopez and J. L. Bernal-Agustin. Multi-objective design of pv-wind-diesel-hydrogen-battery systems. *Renewable Energy*, 33(12):2559–2572, December 2008. ISSN 0960-1481. URL http://www.sciencedirect.com/science/article/pii/S0960148108000724.

[69] R. Dufo-Lopez, J. L. Bernal-Agustin, and F. Mendoza. Design and economical analysis of hybrid PV-wind systems connected to the grid for the intermittent production of hydrogen. *Energy Policy*, 37(8):3082–3095, Aug 2009. ISSN 0301-4215. doi: 10.1016/j.enpol.2009.03.059. URL http://dx.doi.org/10.1016/j.enpol.2009.03.059.

[70] R. I. Dunn, P. J. Hearps, and M. N. Wright. Molten-salt power towers: Newly commercial concentrating solar storage. *Proceedings of the IEEE*, 100(2):504–515, Feb 2012. ISSN 0018-9219. doi: 10.1109/jproc.2011.2163739. URL http://dx.doi.org/10.1109/JPROC.2011.2163739.

[71] T. Edgar, D. Himmelblau, and L. Lasdon. *Optimization of chemical processes*. McGraw-Hill chemical engineering series. McGraw-Hill, 2001. ISBN 9780070393592. URL http://books.google.co.uk/books?id=PqBTAAAAMAAJ.

[72] T. Eglinton, J. Hinkley, A. Beath, and M. Dell'Amico. Potential applications of concentrated solar thermal technologies in the australian minerals pro-

cessing and extractive metallurgical industry. *JOM*, 65(12):1710–1720, 2013. URL http://www.scopus.com/inward/record.url?eid=2-s2.0-84890443566&partnerID=40&md5=c93845ccfbd8fefea2f2152def333adc. cited By (since 1996)0.

[73] EIA.GOV. International Energy Statistics - EIA. [Online]. Available at: http://www.eia.gov/cfapps/ipdbproject/IEDIndex3.cfm, 2014. URL http://www.eia.gov/cfapps/ipdbproject/iedindex3.cfm?tid=44&pid=44&aid=2&cid=ww,&syid=2001&eyid=2012&unit=QBTU. Accessed 09 October 2014.

[74] L. El Chaar, L. Lamont, and N. E. Zein. Review of photovoltaic technologies. *Renewable and Sustainable Energy Reviews*, 15(5):2165 – 2175, 2011. ISSN 1364-0321. doi: http://dx.doi.org/10.1016/j.rser.2011.01.004. URL http://www.sciencedirect.com/science/article/pii/S1364032111000050.

[75] A. A. ElDesouky. Security constrained generation scheduling for grids incorporating wind, photovoltaic and thermal power. *Electric Power Systems Research*, 116 (0):284–292, November 2014. ISSN 0378-7796. URL http://www.sciencedirect.com/science/article/pii/S0378779614002260.

[76] B. Elmegaard and W. Brix. Efficiency of compressed air storage. In *ECOS 2011: 24th International Conference on Efficiency, Cost, Optimization, Simulation and Environmental Impact of Energy Systems*, pages 2512–2523, 2011.

[77] O. Erdinc and M. Uzunoglu. Optimum design of hybrid renewable energy systems: Overview of different approaches. *Renewable and Sustainable Energy Reviews*, 16 (3):1412–1425, Apr 2012. ISSN 1364-0321. doi: 10.1016/j.rser.2011.11.011. URL http://dx.doi.org/10.1016/j.rser.2011.11.011.

[78] A. Evans, V. Strezov, and T. J. Evans. Assessment of utility energy storage options for increased renewable energy penetration. *Renewable and Sustainable Energy Reviews*, 16(6):4141–4147, Aug 2012. ISSN 1364-0321. doi: 10.1016/j.rser.2012.03.048. URL http://dx.doi.org/10.1016/j.rser.2012.03.048.

[79] D. Evans. Simplified method for predicting photovoltaic array output. *Solar Energy*, 27(6):555–560, Jan 1981. ISSN 0038-092X. doi: 10.1016/0038-092x(81)90051-7. URL http://dx.doi.org/10.1016/0038-092X(81)90051-7.

[80] R. L. Fares, J. P. Meyers, and M. E. Webber. A dynamic model-based estimate of the value of a vanadium redox flow battery for frequency regulation in texas. *Applied Energy*, 113:189–198, Jan 2014. ISSN 0306-2619. doi: 10.1016/j.apenergy.2013.07.025. URL http://dx.doi.org/10.1016/j.apenergy.2013.07.025.

[81] F. Figueiredo and P. Flynn. Using diurnal power price to configure pumped storage. *IEEE Transactions on Energy Conversion*, 21(3):804–809, Sep 2006. ISSN 0885-8969. doi: 10.1109/tec.2006.877373. URL http://dx.doi.org/10.1109/TEC.2006.877373.

[82] C. Floudas. *Nonlinear and Mixed-Integer Optimization: Fundamentals and Applications*. Topics in Chemical Engineering. Oxford University Press, USA,

1995. ISBN 9780195100563. URL http://books.google.co.uk/books?id=GJgiUZCMCSEC.

[83] V. Fthenakis and H. C. Kim. Land use and electricity generation: A life-cycle analysis. *Renewable and Sustainable Energy Reviews*, 13(6-7):1465–1474, Aug 2009. ISSN 1364-0321. doi: 10.1016/j.rser.2008.09.017. URL http://dx.doi.org/10.1016/j.rser.2008.09.017.

[84] GAMS Development Corporation. General algebraic modeling system (gams) release 24.2.1, 2013.

[85] A. Garcia, J. Torres, E. Prieto, and A. de Francisco. Fitting wind speed distributions: a case study. *Solar Energy*, 62(2):139–144, Feb 1998. ISSN 0038-092X. doi: 10.1016/s0038-092x(97)00116-3. URL http://dx.doi.org/10.1016/S0038-092X(97)00116-3.

[86] I. L. Garcia, J. L. Ãlvarez, and D. Blanco. Performance model for parabolic trough solar thermal power plants with thermal storage: Comparison to operating plant data. *Solar Energy*, 85(10):2443 – 2460, 2011. ISSN 0038-092X. doi: http://dx.doi.org/10.1016/j.solener.2011.07.002. URL http://www.sciencedirect.com/science/article/pii/S0038092X11002441.

[87] A. Gil, M. Medrano, I. Martorell, A. Lazaro, P. Dolado, B. Zalba, and L. F. Cabeza. State of the art on high temperature thermal energy storage for power generation. part 1 - concepts, materials and modellization. *Renewable and Sustainable Energy Reviews*, 14(1):31 – 55, 2010. ISSN 1364-0321. doi: http://dx.doi.org/10.1016/j.rser.2009.07.035. URL http://www.sciencedirect.com/science/article/pii/S1364032109001774.

[88] P. Gooding, E. Makram, and R. Hadidi. Islanding effects in distributed generation with probability analysis. In *Power Systems Conference (PSC 2013)*, Mar 12-15 2013. URL http://rtpis.org/psc13/files/PSC2013_final_1358372696.pdf.

[89] P. Gooding, E. Makram, and R. Hadidi. Probability analysis of distributed generation for island scenarios utilizing carolinas data. *Electric Power Systems Research*, 107:125–132, Feb 2014. ISSN 0378-7796. doi: 10.1016/j.epsr.2013.09.012. URL http://dx.doi.org/10.1016/j.epsr.2013.09.012.

[90] J. Gordon and T. Reddy. Stationary statistics and sequential properties of normal beam and global solar radiation on tilted surfaces. *Solar Energy*, 42(1):35–44, 1989. ISSN 0038-092X. doi: 10.1016/0038-092x(89)90128-x. URL http://dx.doi.org/10.1016/0038-092X(89)90128-X.

[91] G. Grazzini and A. Milazzo. Thermodynamic analysis of caes/tes systems for renewable energy plants. *Renewable Energy*, 33(9):1998 – 2006, 2008. ISSN 0960-1481. doi: http://dx.doi.org/10.1016/j.renene.2007.12.003. URL http://www.sciencedirect.com/science/article/pii/S0960148107003849.

[92] G. Grazzini and A. Milazzo. A thermodynamic analysis of multistage adiabatic caes. *Proceedings of the IEEE*, 100(2)(2):461–472, 2012. ISSN 0018-

9219. doi: 10.1109/jproc.2011.2163049. URL http://dx.doi.org/10.1109/JPROC.2011.2163049.

[93] N. Gridley and M. Banto. Hydraulic-wind-diesel hybrid system to operate an underground zinc mine at El Toqui, Chile. In *Proceedings of ENERMIN 2010 conference*, pages 46–47, Santiago, Chile, 14-16 November 2010.

[94] A. Grover, A. Kapoor, and E. Horvitz. A deep hybrid model for weather forecasting. In *Proceedings of the 21th ACM SIGKDD International Conference on Knowledge Discovery and Data Mining*, pages 379–386. ACM, 2015.

[95] C. Gueymard. Prediction and performance assessment of mean hourly global radiation. *Solar Energy*, 68(3):285–303, Mar 2000. doi: 10.1016/S0038-092X(99)00070-5. URL http://dx.doi.org/10.1016/S0038-092X(99)00070-5.

[96] A. K. Gupta. *Beta Distribution*, pages 144–145. Springer Berlin Heidelberg, Berlin, Heidelberg, 2011. ISBN 978-3-642-04898-2. URL http://dx.doi.org/10.1007/978-3-642-04898-2_144.

[97] N. Hartmann, O. Vahringer, C. Kruck, and L. Eltrop. Simulation and analysis of different adiabatic compressed air energy storage plant configurations. *Applied Energy*, 93:541–548, 2012. URL http://www.scopus.com/inward/record.url?eid=2-s2.0-84858000179&partnerID=40&md5=fca0cf3aaed3da7cf100798ffea672b2. cited By (since 1996)18.

[98] J. Hernandez-Moro and J. Martinez-Duart. Analytical model for solar PV and CSP electricity costs: Present LCoe values and their future evolution. *Renewable and Sustainable Energy Reviews*, 20:119–132, Apr 2013. ISSN 1364-0321. doi: 10.1016/j.rser.2012.11.082. URL http://dx.doi.org/10.1016/j.rser.2012.11.082.

[99] U. Herrmann and D. W. Kearney. Survey of thermal energy storage for parabolic trough power plants. *Journal of Solar Energy Engineering*, 124(2):145, 2002. doi: 10.1115/1.1467601. URL http://dx.doi.org/10.1115/1.1467601.

[100] U. Herrmann, B. Kelly, and H. Price. Two-tank molten salt storage for parabolic trough solar power plants. *Energy*, 29(5-6):883–893, Apr 2004. doi: 10.1016/S0360-5442(03)00193-2. URL http://dx.doi.org/10.1016/S0360-5442(03)00193-2.

[101] M.-A. Hessami and D. R. Bowly. Economic feasibility and optimisation of an energy storage system for portland wind farm (victoria, australia). *Applied Energy*, 88(8):2755–2763, Aug 2011. ISSN 0306-2619. doi: 10.1016/j.apenergy.2010.12.013. URL http://dx.doi.org/10.1016/j.apenergy.2010.12.013.

[102] T. Hillig. Solar-, wind-diesel hybrid plants at remote mines as a target for investors. *Renewable Energy World*, 4 November 2015. [Online]. Available at: http://www.renewableenergyworld.com/articles/2015/11/solar-wind-diesel-hybrid-plants-at-remote-mines-as-a-target-for-investors.html (Accessed 02 February 2016).

[103] J. Hinkley, B. Curtin, J. Hayward, A. Wonhas, R. Boyd, C. Grima, A. Tadros, R. Hall, K. Naicker, and A. Mikhail. Concentrating solar power–drivers and opportunities for cost-competitive electricity. *Clayton South: CSIRO*, 2011.

[104] C. K. Ho and B. D. Iverson. Review of high-temperature central receiver designs for concentrating solar power. *Renewable and Sustainable Energy Reviews*, 29(0):835 – 846, 2014. ISSN 1364-0321. doi: http://dx.doi.org/10.1016/j.rser.2013.08.099. URL http://www.sciencedirect.com/science/article/pii/S1364032113006394.

[105] T. E. Hoff, R. Perez, J. Kleissl, D. Renne, and J. Stein. Reporting of irradiance modeling relative prediction errors. *Progress in Photovoltaics: Research and Applications*, 21(7):1514–1519, Jun 2012. ISSN 1062-7995. doi: 10.1002/pip.2225. URL http://dx.doi.org/10.1002/pip.2225.

[106] K. Hollands and R. Huget. A probability density function for the clearness index, with applications. *Solar Energy*, 30(3):195–209, 1983. ISSN 0038-092X. doi: 10.1016/0038-092x(83)90149-4. URL http://dx.doi.org/10.1016/0038-092X(83)90149-4.

[107] Y. Hou, R. Vidu, and P. Stroeve. Solar energy storage methods. *Industrial & Engineering Chemistry Research*, 50(15):8954–8964, Aug 2011. doi: 10.1021/ie2003413. URL http://dx.doi.org/10.1021/ie2003413.

[108] H. Ibrahim, A. Ilinca, and J. Perron. Energy storage systems - characteristics and comparisons. *Renewable and Sustainable Energy Reviews*, 12(5):1221 – 1250, 2008. ISSN 1364-0321. doi: http://dx.doi.org/10.1016/j.rser.2007.01.023. URL http://www.sciencedirect.com/science/article/pii/S1364032107000238.

[109] R. H. Inman, H. T. Pedro, and C. F. Coimbra. Solar forecasting methods for renewable energy integration. *Progress in Energy and Combustion Science*, 39 (6):535–576, Dec 2013. ISSN 0360-1285. doi: 10.1016/j.pecs.2013.06.002. URL http://dx.doi.org/10.1016/j.pecs.2013.06.002.

[110] International Energy Agency. Technology roadmap: Energy storage. Technical report, International Energy Agency, Nov 2014. [Online]. Available at: http://www.iea.org/publications/freepublications/publication/WorldEnergyOutlook2016ExecutiveSummaryEnglish.pdf (Accessed 02 December 2016).

[111] International Energy Agency. Key world energy statistics 2016. Technical report, International Energy Agency, 2016. [Online].Available at: http://www.iea.org/publications/freepublications/publication/KeyWorld2016.pdf (Accessed 02 December 2016).

[112] International Energy Agency. World energy outlook 2016: Executive summary. Technical report, International Energy Agency, 2016. [Online].Available at: http://www.iea.org/publications/freepublications/publication/world-energy-outlook-2016---executive-summary---english-version.html (Accessed 02 December 2016).

[113] D. N. Joanes and C. A. Gill. Comparing measures of sample skewness and kurtosis. *Journal of the Royal Statistical Society. Series D (The Statistician)*, 47(1):183–189, 1998. ISSN 00390526, 14679884. URL http://www.jstor.org/stable/2988433.

[114] A. Kaabeche and R. Ibtiouen. Techno-economic optimization of hybrid photovoltaic/wind/diesel/battery generation in a stand-alone power system. *Solar Energy*, 103:171–182, May 2014. ISSN 0038-092X. URL http://www.sciencedirect.com/science/article/pii/S0038092X14000954.

[115] J. Kaldellis, M. Kapsali, and K. Kavadias. Energy balance analysis of wind-based pumped hydro storage systems in remote island electrical networks. *Applied Energy*, 87(8):2427–2437, Aug 2010. ISSN 0306-2619. doi: 10.1016/j.apenergy.2010.02.016. URL http://dx.doi.org/10.1016/j.apenergy.2010.02.016.

[116] S. Kalogirou and G. Panayiotou. Evaluation of a parabolic trough collector performance. volume 3, pages 2085–2091, 2012. URL http://www.scopus.com/inward/record.url?eid=2-s2.0-84871564102&partnerID=40&md5=c204001b8651445c37cdfeed65f35254. cited By (since 1996)0.

[117] S. Kamel. The economics of hybrid power systems for sustainable desert agriculture in egypt. *Energy*, 30(8):1271–1281, Jun 2005. ISSN 0360-5442. doi: 10.1016/j.energy.2004.02.004. URL http://dx.doi.org/10.1016/j.energy.2004.02.004.

[118] E. Kaplani and S. Kaplanis. A stochastic simulation model for reliable PV system sizing providing for solar radiation fluctuations. *Applied Energy*, 97:970–981, Sep 2012. ISSN 0306-2619. doi: 10.1016/j.apenergy.2011.12.016. URL http://dx.doi.org/10.1016/j.apenergy.2011.12.016.

[119] S. Karaki, R. Chedid, and R. Ramadan. Probabilistic performance assessment of autonomous solar-wind energy conversion systems. *IEEE Transactions on Energy Conversion*, 14(3):766–772, 1999. ISSN 0885-8969. doi: 10.1109/60.790949. URL http://dx.doi.org/10.1109/60.790949.

[120] W. Karaki, J. Van Lew, P. Li, C. Chan, and J. Stephens. Heat transfer in thermocline storage system with filler materials: Analytical model. volume 2, pages 725–734, 2010. URL http://www.scopus.com/inward/record.url?eid=2-s2.0-84860292807&partnerID=40&md5=d695e3d407ef7040faf12a9a0e5d617d. cited By (since 1996)0.

[121] Y. Katsigiannis, P. Georgilakis, and E. Karapidakis. Multiobjective genetic algorithm solution to the optimum economic and environmental performance problem of small autonomous hybrid power systems with renewables. *IET Renewable Power Generation*, 4(5):404, 2010. ISSN 1752-1416. doi: 10.1049/iet-rpg.2009.0076. URL http://dx.doi.org/10.1049/iet-rpg.2009.0076.

[122] R. G. Kavasseri and K. Seetharaman. Day-ahead wind speed forecasting using f-arima models. *Renewable Energy*, 34(5):1388–1393, May 2009. ISSN 0960-1481. doi: 10.1016/j.renene.2008.09.006. URL http://dx.doi.org/10.1016/j.renene.2008.09.006.

[123] G. Kear, A. A. Shah, and F. C. Walsh. Development of the all-vanadium redox flow battery for energy storage: a review of technological, financial and policy aspects. *Int. J. Energy Res.*, 36(11):1105–1120, May 2011. ISSN 0363-907X. doi: 10.1002/er.1863. URL http://dx.doi.org/10.1002/er.1863.

[124] D. K. Khatod, V. Pant, and J. Sharma. Analytical approach for well-being assessment of small autonomous power systems with solar and wind energy sources. *IEEE Transactions on Energy Conversion*, 25(2):535–545, Jun 2010. ISSN 0885-8969. doi: 10.1109/tec.2009.2033881. URL http://dx.doi.org/10.1109/TEC.2009.2033881.

[125] Y.-M. Kim, J.-H. Lee, S.-J. Kim, and D. Favrat. Potential and evolution of compressed air energy storage: Energy and exergy analyses. *Entropy*, 14(8): 1501–1521, 2012. URL http://www.scopus.com/inward/record.url?eid=2-s2.0-84867634595&partnerID=40&md5=55235ad6eb3b7ad91211c061c9c8bcb8. cited By (since 1996)4.

[126] M. R. King and N. A. Mody. *Numerical and statistical methods for bioengineering: applications in MATLAB*. Cambridge University Press, 2010.

[127] M. Kloess. Electric storage technologies for the future power system - an economic assessment. *2012 9th International Conference on the European Energy Market*, May 2012. doi: 10.1109/eem.2012.6254729. URL http://dx.doi.org/10.1109/EEM.2012.6254729.

[128] P. Konstantin and J. Kretschmann. Assessment of technology options for development of concentrating solar power in south africa for the world bank. Technical report, The World Bank and ESMAP, Johannesburg, December 2010. URL https://www.climateinvestmentfunds.org/cif/sites/climateinvestmentfunds.org/files/Presentation%20-%20WB%20(Eskom)%20Project%20-%202010_12_07%20.pdf.

[129] E. Koutroulis, D. Kolokotsa, A. Potirakis, and K. Kalaitzakis. Methodology for optimal sizing of stand-alone photovoltaic/wind-generator systems using genetic algorithms. *Solar Energy*, 80(9):1072–1088, Sep 2006. ISSN 0038-092X. doi: 10.1016/j.solener.2005.11.002. URL http://dx.doi.org/10.1016/j.solener.2005.11.002.

[130] K. C. Kueh, G. J. Nathan, and W. L. Saw. Storage capacities required for a solar thermal plant to avoid unscheduled reductions in output. *Solar Energy*, 118: 209–221, Aug 2015. ISSN 0038-092X. doi: 10.1016/j.solener.2015.04.040. URL http://dx.doi.org/10.1016/j.solener.2015.04.040.

[131] R. Kumar, R. Gupta, and A. K. Bansal. Economic analysis and power management of a stand-alone wind/photovoltaic hybrid energy system using biogeography based optimization algorithm. *Swarm and Evolutionary Computation*, 8:33–43, Feb 2013. ISSN 2210-6502. doi: 10.1016/j.swevo.2012.08.002. URL http://dx.doi.org/10.1016/j.swevo.2012.08.002.

[132] S. Kuravi, J. Trahan, D. Y. Goswami, M. M. Rahman, and E. K. Stefanakos. Thermal energy storage technologies and systems for concentrating solar power plants. *Progress in Energy and Combustion Science*, 39(4):285–319, Aug 2013. doi: 10.1016/j.pecs.2013.02.001. URL http://dx.doi.org/10.1016/j.pecs.2013.02.001.

[133] B. Lahcene. On pearson families of distributions and its applications. *African Journal of Mathematics and Computer Science Research*, 6(5):108–117, May 2013.

[134] Lazard. Lazard's levelized cost of energy analysis - version 8.0. [Online]. Available at: http://www.lazard.com/PDF/LevelizedCostofEnergy-Version8.0.pdf, September 2014.

[135] M. Lei, L. Shiyan, J. Chuanwen, L. Hongling, and Z. Yan. A review on the forecasting of wind speed and generated power. *Renewable and Sustainable Energy Reviews*, 13(4):915–920, May 2009. ISSN 1364-0321. doi: 10.1016/j.rser.2008.02.002. URL http://dx.doi.org/10.1016/j.rser.2008.02.002.

[136] S. Lemofouet-Gatsi. *Investigation and optimisation of hybrid electricity storage systems based on compressed air and supercapacitors*. PhD thesis, STI, Lausanne, 2006.

[137] X. Li, W. Kong, Z. Wang, C. Chang, and F. Bai. Thermal model and thermodynamic performance of molten salt cavity receiver. *Renewable Energy*, 35(5):981–988, 2010. URL http://www.scopus.com/inward/record.url?eid=2-s2.0-73249144989&partnerID=40&md5=9430b996525a585d9cff366b2aa16054. cited By (since 1996)17.

[138] A. Louche, G. Notton, P. Poggi, and G. Simonnot. Correlations for direct normal and global horizontal irradiation on a french mediterranean site. *Solar Energy*, 46(4):261–266, 1991. ISSN 0038-092X. doi: 10.1016/0038-092x(91)90072-5. URL http://dx.doi.org/10.1016/0038-092X(91)90072-5.

[139] R. Luna-Rubio, M. Trejo-Perea, D. Vargas-Vazquez, and G. Rios-Moreno. Optimal sizing of renewable hybrids energy systems: A review of methodologies. *Solar Energy*, 86(4):1077–1088, Apr 2012. ISSN 0038-092X. doi: 10.1016/j.solener.2011.10.016. URL http://dx.doi.org/10.1016/j.solener.2011.10.016.

[140] X. Luo, J. Wang, M. Dooner, and J. Clarke. Overview of current development in electrical energy storage technologies and the application potential in power system operation. *Applied Energy*, 137:511–536, Jan 2015. ISSN 0306-2619. doi: 10.1016/j.apenergy.2014.09.081. URL http://dx.doi.org/10.1016/j.apenergy.2014.09.081.

[141] T. Ma, H. Yang, and L. Lu. Feasibility study and economic analysis of pumped hydro storage and battery storage for a renewable energy powered island. *Energy Conversion and Management*, 79:387–397, Mar 2014. ISSN 0196-8904. doi: 10.1016/j.enconman.2013.12.047. URL http://dx.doi.org/10.1016/j.enconman.2013.12.047.

[142] S. H. Madaeni, R. Sioshansi, and P. Denholm. How thermal energy storage enhances the economic viability of concentrating solar power. *Proceedings of the IEEE*, 100(2):335–347, Feb 2012. doi: 10.1109/JPROC.2011.2144950. URL http://dx.doi.org/10.1109/JPROC.2011.2144950.

[143] A. Mahesh and K. S. Sandhu. Hybrid wind/photovoltaic energy system developments: Critical review and findings. *Renewable and Sustainable Energy Reviews*,

52:1135–1147, Dec 2015. ISSN 1364-0321. doi: 10.1016/j.rser.2015.08.008. URL http://dx.doi.org/10.1016/j.rser.2015.08.008.

[144] A. Maleki and A. Askarzadeh. Comparative study of artificial intelligence techniques for sizing of a hydrogen-based stand-alone photovoltaic/wind hybrid system. *International Journal of Hydrogen Energy*, 39(19):9973–9984, Jun 2014. ISSN 0360-3199. doi: 10.1016/j.ijhydene.2014.04.147. URL http://dx.doi.org/10.1016/j.ijhydene.2014.04.147.

[145] A. Maleki and F. Pourfayaz. Sizing of stand-alone photovoltaic/wind/diesel system with battery and fuel cell storage devices by harmony search algorithm. *Journal of Energy Storage*, 2:30–42, Aug 2015. ISSN 2352-152X. doi: 10.1016/j.est.2015.05.006. URL http://dx.doi.org/10.1016/j.est.2015.05.006.

[146] A. Malheiro, P. M. Castro, R. M. Lima, and A. Estanqueiro. Integrated sizing and scheduling of wind/PV/diesel/battery isolated systems. *Renewable Energy*, 83:646–657, Nov 2015. ISSN 0960-1481. doi: 10.1016/j.renene.2015.04.066. URL http://dx.doi.org/10.1016/j.renene.2015.04.066.

[147] T. R. Mancini, B. D. Iverson, W. D. Gary, Jesse A. (U.S. Department of Energy, N. P. Siegel, G. J. Kolb, and C. K. Ho. Development of a power tower technology roadmap for doe. pages –, United States, 2010. Sandia National Laboratories. URL http://www.osti.gov/scitech/servlets/purl/1022213.

[148] T. Markvart. Sizing of hybrid photovoltaic-wind energy systems. *Solar Energy*, 57(4):277–281, Oct 1996. ISSN 0038-092X. doi: 10.1016/s0038-092x(96)00106-5. URL http://dx.doi.org/10.1016/S0038-092X(96)00106-5.

[149] G. M. Masters. *Renewable and efficient electric power systems*. John Wiley & Sons, 2013.

[150] MATLAB. *version 8.3 (R2014a)*. The MathWorks Inc., Natick, Massachusetts, 2014.

[151] A. McIvor. Energy in mining. *Cleantech (special edition fuel cells)*, 5:16–19, 2010.

[152] M. D. Mckay, R. J. Beckman, and W. J. Conover. A comparison of three methods for selecting values of input variables in the analysis of output from a computer code. *Technometrics*, 42(1):55–61, Feb 2000. ISSN 1537-2723. doi: 10.1080/00401706.2000.10485979. URL http://dx.doi.org/10.1080/00401706.2000.10485979.

[153] M. Medrano, A. Gil, I. Martorell, X. Potau, and L. F. Cabeza. State of the art on high-temperature thermal energy storage for power generation. part 2a: Case studies. *Renewable and Sustainable Energy Reviews*, 14(1):56 – 72, 2010. ISSN 1364-0321. doi: http://dx.doi.org/10.1016/j.rser.2009.07.036. URL http://www.sciencedirect.com/science/article/pii/S1364032109001786.

[154] G. Merei, C. Berger, and D. U. Sauer. Optimization of an off-grid hybrid PV-wind-diesel system with different battery technologies using genetic algorithm. *Solar Energy*, 97:460–473, Nov 2013. ISSN 0038-092X. doi: 10.1016/j.solener.2013.08.016. URL http://dx.doi.org/10.1016/j.solener.2013.08.016.

[155] A. Messac and C. A. Mattson. Normal constraint method with guarantee of even representation of complete pareto frontier. *AIAA Journal*, 42(10):2101–2111, October 2004. ISSN 0001-1452. doi: 10.2514/1.8977. URL http://dx.doi.org/10.2514/1.8977.

[156] D. Millar, M. Levesque, G. Lyle, and K. Bullock. Enabling advanced energy management practice for mineral operations. In *Annual General Meeting of the Canadian Institute of Mining, Montreal, PQ, Canada*, pages 22–25, 2011.

[157] E. M. A. Mokheimer, A. Al-Sharafi, M. A. Habib, and I. Alzaharnah. A new study for hybrid PV/wind off-grid power generation systems with the comparison of results from homer. *International Journal of Green Energy*, 12(5):526–542, Dec 2014. ISSN 1543-5083. doi: 10.1080/15435075.2013.833929. URL http://dx.doi.org/10.1080/15435075.2013.833929.

[158] M. A. Moore. A base case design and capital cost analysis of an all vanadium redox-flow battery. Master's thesis, University of Tennessee, 2013. URL http://trace.tennessee.edu/utk_gradthes/2441.

[159] NASA Langley Atmospheric Sciences Data Center. Solar: Average Monthly and Annual Direct Normal Irradiance Data, One-Degree Resolution of the World from NASA/SSE, 1983-2005. NASA Available at: http://purl.stanford.edu/fd535zg0917, 2008.

[160] National Renewable Energy Laboratory. National Solar Radiation Data Base. [Online]. Available at: http://rredc.nrel.gov/solar/old_data/nsrdb/, 2015. Accessed 30 April 2014.

[161] National Renewable Energy Laboratory, NREL. Cost and performance data for power generation technologies. Technical report, prepared by Black & Veatch, 2012. URL http://bv.com/docs/reports-studies/nrel-cost-report.pdf.

[162] National Renewable Energy Laboratory, NREL. Concentrating Solar Power Projects in Chile. http://www.nrel.gov/csp/solarpaces/by_country_detail.cfm/country=CL, 2016. Accessed: 2016-07-25.

[163] National Renewable Energy Laboratory, NREL. Concentrating Solar Power Projects - Crescent Dunes Solar Energy Project. http://www.nrel.gov/csp/solarpaces/project_detail.cfm/projectID=60, 2016. Accessed: 2016-08-01.

[164] National Renewable Energy Laboratory, NREL. Concentrating Solar Power Projects - Gemasolar Thermosolar Plant. http://www.nrel.gov/csp/solarpaces/project_detail.cfm/projectID=40, 2016. Accessed: 2016-06-25.

[165] S. Nielsen. A Solar Mother Lode for Chile's Mines. *Businessweek*, 10 February 2011. [Online]. Available at: http://www.businessweek.com/magazine/content/11_08/b4216012473761.htm (Accessed 06 September 2014).

[166] G. Notton, V. Lazarov, and L. Stoyanov. Optimal sizing of a grid-connected PV system for various PV module technologies and inclinations, inverter efficiency characteristics and locations. *Renewable Energy*, 35(2):541–554, Feb 2010.

ISSN 0960-1481. doi: 10.1016/j.renene.2009.07.013. URL http://dx.doi.org/10.1016/j.renene.2009.07.013.

[167] Organization of the Petroleum Exporting Countries. 2016 OPEC World Oil Outlook. [Online]. Available from: http://www.opec.org/, October 2016. Accessed 24 January 2017.

[168] J. I. Ortega, J. I. Burgaleta, and F. M. Tellez. Central receiver system solar power plant using molten salt as heat transfer fluid. *Journal of Solar Energy Engineering*, 130(2):024501, 2008. ISSN 0199-6231. doi: 10.1115/1.2807210. URL http://dx.doi.org/10.1115/1.2807210.

[169] J. Osborn and C. Kawann. Reliability of the US Electricity System: Recent Trends and Current Issues. *Energy Analysis Department, Ernest Orlando Lawrence Berkeley National Laboratory, LBNL-47043, Berkeley, CA*, 2001.

[170] B. Ould Bilal, V. Sambou, P. Ndiaye, C. Kebe, and M. Ndongo. Optimal design of a hybrid solar-wind-battery system using the minimization of the annualized cost system and the minimization of the loss of power supply probability (lpsp). *Renewable Energy*, 35(10):2388–2390, Oct 2010. ISSN 0960-1481. doi: 10.1016/j.renene.2010.03.004. URL http://dx.doi.org/10.1016/j.renene.2010.03.004.

[171] J. V. Paatero and P. D. Lund. Effects of large-scale photovoltaic power integration on electricity distribution networks. *Renewable Energy*, 32(2):216–234, Feb 2007. ISSN 0960-1481. doi: 10.1016/j.renene.2006.01.005. URL http://dx.doi.org/10.1016/j.renene.2006.01.005.

[172] P. Paliwal, N. Patidar, and R. Nema. Determination of reliability constrained optimal resource mix for an autonomous hybrid power system using particle swarm optimization. *Renewable Energy*, 63:194–204, Mar 2014. ISSN 0960-1481. doi: 10.1016/j.renene.2013.09.003. URL http://dx.doi.org/10.1016/j.renene.2013.09.003.

[173] P. Paliwal, N. Patidar, and R. Nema. A novel method for reliability assessment of autonomous PV-wind-storage system using probabilistic storage model. *International Journal of Electrical Power & Energy Systems*, 55:692–703, Feb 2014. ISSN 0142-0615. doi: 10.1016/j.ijepes.2013.10.010. URL http://dx.doi.org/10.1016/j.ijepes.2013.10.010.

[174] S. V. Papaefthymiou, E. G. Karamanou, S. A. Papathanassiou, and M. P. Papadopoulos. A wind-hydro-pumped storage station leading to high res penetration in the autonomous island system of ikaria. *IEEE Transactions on Sustainable Energy*, 1(3):163–172, Oct 2010. ISSN 1949-3037. doi: 10.1109/tste.2010.2059053. URL http://dx.doi.org/10.1109/TSTE.2010.2059053.

[175] J. Paraszczak and K. Fytas. Renewable energy sources - a promising opportunity for remote mine sites? In *International Conference on Renewable Energies and Power Quality (ICREPQ 12)*, Santiago de Compostela (Spain), 23-30 Mar 2012.

[176] J. Paraszczak and K. Fytas. Renewable energy sources- a promising opportunity for remote mine sites. *Journal of Energy and Power Engineering*, 4:623–632, 2013.

[177] K. Pearson. Mathematical contributions to the theory of evolution. xix. second supplement to a memoir on skew variation. *Philosophical Transactions of the Royal Society of London A: Mathematical, Physical and Engineering Sciences*, 216 (538-548):429–457, 1916. ISSN 0264-3952. doi: 10.1098/rsta.1916.0009.

[178] J. Pellegrino, N. Margolis, M. Miller, M. Justiniano, and A. Thedki. Energy use, loss and opportunities analysis: U.s. manufacturing and mining. [Online]. Available at: `https://www1.eere.energy.gov/manufacturing/intensiveprocesses/pdfs/energy_use_loss_opportunities_analysis.pdf`, Dec 2004. Accessed 21 February 2014.

[179] A. Perera, R. Attalage, K. Perera, and V. Dassanayake. Designing standalone hybrid energy systems minimizing initial investment, life cycle cost and pollutant emission. *Energy*, 54:220–230, Jun 2013. ISSN 0360-5442. doi: 10.1016/j.energy.2013.03.028. URL `http://dx.doi.org/10.1016/j.energy.2013.03.028`.

[180] M. Peters, T. S. Schmidt, D. Wiederkehr, and M. Schneider. Shedding light on solar technologies–a techno-economic assessment and its policy implications. *Energy Policy*, 39(10):6422–6439, Oct 2011. ISSN 0301-4215. doi: 10.1016/j.enpol.2011.07.045. URL `http://dx.doi.org/10.1016/j.enpol.2011.07.045`.

[181] W. F. Pickard. The history, present state, and future prospects of underground pumped hydro for massive energy storage. 100(2):473–483, Feb 2012. ISSN 0018-9219. doi: 10.1109/JPROC.2011.2126030.

[182] K. M. Powell and T. F. Edgar. Modeling and control of a solar thermal power plant with thermal energy storage. *Chemical Engineering Science*, 71(0):138 – 145, 2012. ISSN 0009-2509. doi: http://dx.doi.org/10.1016/j.ces.2011.12.009. URL `http://www.sciencedirect.com/science/article/pii/S0009250911008657`.

[183] A. Prasad and E. Natarajan. Optimization of integrated photovoltaic-wind power generation systems with battery storage. *Energy*, 31(12):1943–1954, Sep 2006. ISSN 0360-5442. doi: 10.1016/j.energy.2005.10.032. URL `http://dx.doi.org/10.1016/j.energy.2005.10.032`.

[184] H. Price and D. Kearney. Reducing the cost of energy from parabolic trough solar power plants. *Solar Energy*, 2003. doi: 10.1115/isec2003-44069. URL `http://dx.doi.org/10.1115/ISEC2003-44069`.

[185] B. Prior. Concentrating solar power 2011: Technology, cost, and markets. *GTM Research*, 2011.

[186] H. D. Purnomo and H.-M. Wee. Soccer game optimization. *Meta-Heuristics Optimization Algorithms in Engineering, Business, Economics, and Finance*, pages 386–420. doi: 10.4018/978-1-4666-2086-5.ch013. URL `http://dx.doi.org/10.4018/978-1-4666-2086-5.ch013`.

[187] C. Qi and Z. Ming. Photovoltaic module simulink model for a stand-alone PV system. *Physics Procedia*, 24:94–100, Jan 2012. doi: 10.1016/j.phpro.2012.02.015. URL `http://dx.doi.org/10.1016/j.phpro.2012.02.015`.

[188] G. R. Raidl and J. Puchinger. Combining (integer) linear programming techniques

and metaheuristics for combinatorial optimization. *Studies in Computational Intelligence*, pages 31–62, 2008. ISSN 1860-949X. doi: 10.1007/978-3-540-78295-7_2. URL http://dx.doi.org/10.1007/978-3-540-78295-7_2.

[189] S. Relloso and E. Delgado. Experience with molten salt thermal storage in a commercial parabolic trough plant; andasol 1 commissioning and operation. In *Proceedings of 15th International SolarPACES Symposium*, pages 14–18, Sept 2009.

[190] REN21. Renewables 2016 Global Status Report. [Online]. Available at: http://www.ren21.net/wp-content/uploads/2016/10/REN21_GSR2016_FullReport_en_11.pdf, 2016. Accessed 02 December 2016.

[191] B. J. Rice and J. D. Strange. *Ordinary Differential Equations: With Applications*. Brooks/Cole Pub Co, 3rd edition, 1993.

[192] H. Rinne. *The Weibull distribution: a handbook*. CRC Press, 2008.

[193] Rolls battery engineering. *Rolls battery user manual*. URL http://rollsbattery.com/wp-content/plugins/rollsbatteries/pdfs/Rolls_Battery_Manual.pdf.

[194] M. Romero, R. Buck, and J. E. Pacheco. An update on solar central receiver systems, projects, and technologies. *Journal of Solar Energy Engineering*, 124(2): 98, 2002. ISSN 0199-6231. doi: 10.1115/1.1467921. URL http://dx.doi.org/10.1115/1.1467921.

[195] M. Root. *The Tab battery book: an in-depth guide to construction, design and use*. McGraw-Hill/Tab Electronics, November 2010. URL https://www.dawsonera.com:443/abstract/9780071739917.

[196] A. Rovira, M. J. Montes, M. Valdes, and J. M. Martinez-Val. Energy management in solar thermal power plants with double thermal storage system and subdivided solar field. *Applied Energy*, 88(11):4055 – 4066, 2011. ISSN 0306-2619. doi: http://dx.doi.org/10.1016/j.apenergy.2011.04.036. URL http://www.sciencedirect.com/science/article/pii/S0306261911002583.

[197] A. D. Sahin and Z. Sen. First-order markov chain approach to wind speed modelling. *Journal of Wind Engineering and Industrial Aerodynamics*, 89(3):263–269, 2001.

[198] A. Saif, K. G. Elrab, H. H. Zeineldin, S. Kennedy, and J. L. Kirtley. Multi-objective capacity planning of a PV-wind-diesel-battery hybrid power system. *2010 IEEE International Energy Conference*, Dec 2010. doi: 10.1109/energycon.2010.5771679. URL http://dx.doi.org/10.1109/ENERGYCON.2010.5771679.

[199] G. Salem and K. Mahkamov. Case study: Modelling and sizing stand-alone pv systems for powering mobile phone stations in libya. *Proceedings of the World Renewable Energy Congress,Sweden, Linköping, Sweden*, 57(11):2891–2898, 8–13 May 2011. URL http://nrl.northumbria.ac.uk/9172/.

[200] A. Sasitharanuwat, W. Rakwichian, N. Ketjoy, and S. Yammen. Performance evaluation of a 10kwp PV power system prototype for isolated building in thailand. *Renewable Energy*, 32(8):1288–1300, Jul 2007. ISSN 0960-1481. doi: 10.1016/j.renene.2006.05.002. URL http://dx.doi.org/10.1016/j.renene.2006.05.002.

[201] A. Sfetsos. A comparison of various forecasting techniques applied to mean hourly wind speed time series. *Renewable Energy*, 21(1):23–35, Sep 2000. ISSN 0960-1481. doi: 10.1016/s0960-1481(99)00125-1. URL http://dx.doi.org/10.1016/S0960-1481(99)00125-1.

[202] M. Sharafi and T. Y. ELMekkawy. Multi-objective optimal design of hybrid renewable energy systems using PSO-simulation based approach. *Renewable Energy*, 68:67–79, Aug 2014. ISSN 0960-1481. doi: 10.1016/j.renene.2014.01.011. URL http://dx.doi.org/10.1016/j.renene.2014.01.011.

[203] Z. Shi, R. Wang, and T. Zhang. Multi-objective optimal design of hybrid renewable energy systems using preference-inspired coevolutionary approach. *Solar Energy*, 118:96–106, Aug 2015. ISSN 0038-092X. doi: 10.1016/j.solener.2015.03.052. URL http://dx.doi.org/10.1016/j.solener.2015.03.052.

[204] J. Smith, H. Van Ness, and M. Abbott. *Introduction to chemical engineering thermodynamics*. McGraw-Hill chemical engineering series. McGraw-Hill, 2005. ISBN 9780073104454. URL http://books.google.co.uk/books?id=3spTAAAAMAAJ.

[205] L. Song. *NGPM - An NSGA-II program in Matlab v1.4*. Aerospace structural dynamics research laboratory, College of Astronautics, Northwestern Polytechnical University, China, 2011. URL http://uk.mathworks.com/matlabcentral/fileexchange/31166-ngpm-a-nsga-ii-program-in-matlab-v1-4.

[206] J. Spelling, M. Jocker, and A. Martin. Annual performance improvement for solar steam turbines through the use of temperature-maintaining modifications. *Solar Energy*, 86(1):496–504, Jan 2012. ISSN 0038-092X. doi: 10.1016/j.solener.2011.10.023. URL http://dx.doi.org/10.1016/j.solener.2011.10.023.

[207] A. Starke, J. M. Cardemil, R. Escobar, and S. Colle. Assessing the performance of hybrid csp+pv plants in northern chile. *AIP Conference Proceedings*, 1734(1):130020, 2016. doi: http://dx.doi.org/10.1063/1.4949230. URL http://scitation.aip.org/content/aip/proceeding/aipcp/10.1063/1.4949230;jsessionid=V2LO8FzXRx4ahihnZpIqzcJf.x-aip-live-03.

[208] F. D. S. Steta. Modeling of an advanced adiabatic compressed air energy storage (aa-caes) unit and an optimal model-based operation strategy for its integration into power markets. Master's thesis, Swiss Federal Institute of Technology (ETH) Zurich, October 2010.

[209] M. Tabassum and K. Mathew. A genetic algorithm analysis towards optimization solutions. *International Journal of Digital Information and Wireless Communications (IJDIWC)*, 4(1):124–142, 2014.

[210] M. Tawarmalani and N. V. Sahinidis. A polyhedral branch-and-cut approach to global optimization. *Math. Program.*, 103(2):225–249, May 2005. ISSN 1436-4646. doi: 10.1007/s10107-005-0581-8. URL http://dx.doi.org/10.1007/s10107-005-0581-8.

[211] I. Tegani, A. Aboubou, M. Ayad, M. Becherif, R. Saadi, and O. Kraa. Optimal sizing design and energy management of stand-alone photovoltaic/wind generator

systems. *Energy Procedia*, 50:163–170, 2014. ISSN 1876-6102. doi: 10.1016/j.egypro.2014.06.020. URL http://dx.doi.org/10.1016/j.egypro.2014.06.020.

[212] The Wind Power. Manufacturers and turbines: NEG Micon NM44/750. [Online], 2016. URL http://www.thewindpower.net/turbine_en_236_neg-micon_750.php. Accessed 19 August 2015.

[213] THEnergy sustainable consulting. Database: Solar & wind systems in the mining industry. http://www.th-energy.net/english/platform-renewable-energy-and-mining/database-solar-wind-power-plants/, 2016. Accessed 10 November 2016.

[214] Y. Tian and C. Zhao. A review of solar collectors and thermal energy storage in solar thermal applications. *Applied Energy*, 104:538–553, Apr 2013. ISSN 0306-2619. doi: 10.1016/j.apenergy.2012.11.051. URL http://dx.doi.org/10.1016/j.apenergy.2012.11.051.

[215] G. Tina and S. Gagliano. Probability analysis of weather data for energy assessment of hybrid solar/wind power system. In *proceedings of 4th IASME/WSEAS international conf. Energy, Environment, Ecosystems and sustainable development*, pages 217–223, 2008.

[216] G. Tina and S. Gagliano. Probabilistic analysis of weather data for a hybrid solar/wind energy system. *Int. J. Energy Res.*, 35(3):221–232, Feb 2011. ISSN 0363-907X. doi: 10.1002/er.1686. URL http://dx.doi.org/10.1002/er.1686.

[217] G. Tina, S. Gagliano, and S. Raiti. Hybrid solar/wind power system probabilistic modelling for long-term performance assessment. *Solar Energy*, 80(5):578–588, May 2006. ISSN 0038-092X. doi: 10.1016/j.solener.2005.03.013. URL http://dx.doi.org/10.1016/j.solener.2005.03.013.

[218] S. Tito, T. Lie, and T. Anderson. Optimal sizing of a wind-photovoltaic-battery hybrid renewable energy system considering socio-demographic factors. *Solar Energy*, 136:525–532, Oct 2016. ISSN 0038-092X. doi: 10.1016/j.solener.2016.07.036. URL http://dx.doi.org/10.1016/j.solener.2016.07.036.

[219] J. Torres, A. Garcia, M. De Blas, and A. De Francisco. Forecast of hourly average wind speed with ARMA models in navarre (spain). *Solar Energy*, 79(1):65–77, Jul 2005. ISSN 0038-092X. doi: 10.1016/j.solener.2004.09.013. URL http://dx.doi.org/10.1016/j.solener.2004.09.013.

[220] T. Tudorache and A. Morega. Optimum design of wind/pv/diesel/batteries hybrid systems. In *Second International Conference on Modern Power Systems, Romania*, 2008.

[221] A. Tuohy and M. O'Malley. Impact of pumped storage on power systems with increasing wind penetration. *2009 IEEE Power & Energy Society General Meeting*, Jul 2009. doi: 10.1109/pes.2009.5275839. URL http://dx.doi.org/10.1109/PES.2009.5275839.

[222] B. Türker. *Modeling and Utilizing a Vanadium Redox Flow Battery for Easier Grid and Market Integration of Wind Power*. PhD thesis, Staats-und Universitätsbib-

liothek Bremen, December 2014. URL http://elib.suub.uni-bremen.de/peid/D00104249.html.

[223] US Department of Energy. U.S. mining industry energy bandwidth study. Technical report, prepared by BCS Inc., 2007.

[224] M. Villalva, J. Gazoli, and E. Filho. Comprehensive approach to modeling and simulation of photovoltaic arrays. *IEEE Trans. Power Electron.*, 24(5):1198–1208, May 2009. ISSN 1941-0107. doi: 10.1109/tpel.2009.2013862. URL http://dx.doi.org/10.1109/TPEL.2009.2013862.

[225] S. Vorrath. Adelaide sand-based energy storage system wins govt grant : ReneEconomy. http://reneweconomy.com.au/adelaide-sand-based-energy-storage-system-wins-govt-grant-28439/, October 2015. Accessed 09 December 2016.

[226] S. Vorrath. SA-made silicon energy storage system "ready to close grid gap" : RenewEconomy. http://reneweconomy.com.au/sa-made-silicon-energy-storage-system-ready-close-grid-gap-23607/, December 2016. Accessed 09 December 2016.

[227] A. Wachter and L. T. Biegler. On the implementation of an interior-point filter line-search algorithm for large-scale nonlinear programming. *Math. Program.*, 106 (1):25–57, Apr 2005. ISSN 1436-4646. doi: 10.1007/s10107-004-0559-y. URL http://dx.doi.org/10.1007/s10107-004-0559-y.

[228] M. Wagner and P. Gilman. Technical Manual for the SAM Physical Trough Model. Technical report, National Renewable Energy Laboratory (NREL), Golden, CO., 2011.

[229] J. Wang, S. Qin, Q. Zhou, and H. Jiang. Medium-term wind speeds forecasting utilizing hybrid models for three different sites in xinjiang, china. *Renewable Energy*, 76:91–101, Apr 2015. ISSN 0960-1481. doi: 10.1016/j.renene.2014.11.011. URL http://dx.doi.org/10.1016/j.renene.2014.11.011.

[230] D. Weisser and R. S. Garcia. Instantaneous wind energy penetration in isolated electricity grids: concepts and review. *Renewable Energy*, 30(8):1299–1308, Jul 2005. ISSN 0960-1481. doi: 10.1016/j.renene.2004.10.002. URL http://dx.doi.org/10.1016/j.renene.2004.10.002.

[231] P. H. Westfall. Kurtosis as peakedness, 1905-2014. R.I.P. *The American Statistician*, 68(3):191–195, Jul 2014. ISSN 1537-2731. doi: 10.1080/00031305.2014.917055. URL http://dx.doi.org/10.1080/00031305.2014.917055.

[232] J. Widen, N. Carpman, V. Castellucci, D. Lingfors, J. Olauson, F. Remouit, M. Bergkvist, M. Grabbe, and R. Waters. Variability assessment and forecasting of renewables: A review for solar, wind, wave and tidal resources. *Renewable and Sustainable Energy Reviews*, 44:356–375, Apr 2015. ISSN 1364-0321. doi: 10.1016/j.rser.2014.12.019. URL http://dx.doi.org/10.1016/j.rser.2014.12.019.

[233] S. D. Wilson, J. Samuel, and G. Simmonds. An energy storage system for the scot-

tish isle of gigha. In *Power in Unity: a Whole System Approach, IET Conference on*, pages 1–5, 2013. doi: 10.1049/ic.2013.0138.

[234] L. Wong and W. Chow. Solar radiation model. *Applied Energy*, 69(3):191–224, Jul 2001. doi: 10.1016/S0306-2619(01)00012-5. URL http://dx.doi.org/10.1016/S0306-2619(01)00012-5.

[235] www.redtenergy.com. Module Datasheet for redT 5-20 energy storage system: 5-20 preliminary specifications. [Online]. Available at: http://www.redtenergy.com/files/5-20%20GEN2%20Prelim%20Datasheet%20-%202%20pp%20v1.3.pdf.

[236] C. Xu, Z. Wang, X. Li, and F. Sun. Energy and exergy analysis of solar power tower plants. *Applied Thermal Engineering*, 31:3904 – 3913, 2011. ISSN 1359-4311. doi: http://dx.doi.org/10.1016/j.applthermaleng.2011.07.038. URL http://www.sciencedirect.com/science/article/pii/S135943111100398X. {SET} 2010 Special Issue.

[237] D. Xu, L. Kang, L. Chang, and B. Cao. Optimal sizing of standalone hybrid wind/pv power systems using genetic algorithms. *Canadian Conference on Electrical and Computer Engineering, 2005.*, 2005. doi: 10.1109/ccece.2005.1557315. URL http://dx.doi.org/10.1109/CCECE.2005.1557315.

[238] X. Xu, K. Vignarooban, B. Xu, K. Hsu, and A. Kannan. Prospects and problems of concentrating solar power technologies for power generation in the desert regions. *Renewable and Sustainable Energy Reviews*, 53:1106–1131, Jan 2016. ISSN 1364-0321. doi: 10.1016/j.rser.2015.09.015. URL http://dx.doi.org/10.1016/j.rser.2015.09.015.

[239] C.-J. Yang and R. B. Jackson. Opportunities and barriers to pumped-hydro energy storage in the united states. *Renewable and Sustainable Energy Reviews*, 15(1):839–844, Jan 2011. ISSN 1364-0321. doi: 10.1016/j.rser.2010.09.020. URL http://dx.doi.org/10.1016/j.rser.2010.09.020.

[240] H. Yang, L. Lu, and W. Zhou. A novel optimization sizing model for hybrid solar-wind power generation system. *Solar Energy*, 81(1):76–84, Jan 2007. ISSN 0038-092X. doi: 10.1016/j.solener.2006.06.010. URL http://dx.doi.org/10.1016/j.solener.2006.06.010.

[241] H. Yang, W. Zhou, L. Lu, and Z. Fang. Optimal sizing method for stand-alone hybrid solar-wind system with lpsp technology by using genetic algorithm. *Solar Energy*, 82(4):354–367, April 2008. ISSN 0038-092X. URL http://www.sciencedirect.com/science/article/pii/S0038092X07001831.

[242] H. Yang, Z. Wei, and L. Chengzhi. Optimal design and techno-economic analysis of a hybrid solar-wind power generation system. *Applied Energy*, 86(2):163–169, Feb 2009. ISSN 0306-2619. doi: 10.1016/j.apenergy.2008.03.008. URL http://dx.doi.org/10.1016/j.apenergy.2008.03.008.

[243] H. Yang, L. Lu, and J. Burnett. Weather data and probability analysis of hybrid photovoltaic-wind power generation systems in hong kong. *Renewable Energy*, 28

(11):1813–1824, Sep 2003. ISSN 0960-1481. doi: 10.1016/s0960-1481(03)00015-6. URL http://dx.doi.org/10.1016/S0960-1481(03)00015-6.

[244] K. Zach, H. Auer, and G. Lettner. Report summarizing the current status, role and costs of energy storage technologies. store-facilitating energy storage to allow high penetration of intermittent renewable energy. [Online], Mar 2012. URL http://www.store-project.eu/documents/results/en_GB/report-summarizing-the-current-status-role-and-costs-of-energy-storage-technologies. Accessed 31 March 2014.

[245] A. Zahedi. Review of modelling details in relation to low-concentration solar concentrating photovoltaic. *Renewable and Sustainable Energy Reviews*, 15 (3):1609–1614, 2011. URL http://www.scopus.com/inward/record.url?eid=2-s2.0-78651098366&partnerID=40&md5=41346026b44dcf47b27244f7a63a03f0.

[246] F. Zaversky, J. Garcia-Barberena, M. Sanchez, and D. Astrain. Transient molten salt two-tank thermal storage modeling for {CSP} performance simulations. *Solar Energy*, 93(0):294 – 311, 2013. ISSN 0038-092X. doi: http://dx.doi.org/10.1016/j.solener.2013.02.034. URL http://www.sciencedirect.com/science/article/pii/S0038092X13001436.

[247] B. Zhao, X. Zhang, P. Li, K. Wang, M. Xue, and C. Wang. Optimal sizing, operating strategy and operational experience of a stand-alone microgrid on dongfushan island. *Applied Energy*, 113:1656–1666, Jan 2014. ISSN 0306-2619. doi: 10.1016/j.apenergy.2013.09.015. URL http://dx.doi.org/10.1016/j.apenergy.2013.09.015.

[248] J. Zhao and X. Yuan. Multi-objective optimization of stand-alone hybrid PV-wind-diesel-battery system using improved fruit fly optimization algorithm. *Soft Computing*, 20(7):2841–2853, Apr 2015. ISSN 1433-7479. doi: 10.1007/s00500-015-1685-6. URL http://dx.doi.org/10.1007/s00500-015-1685-6.

[249] S. Zunft, C. Jakiel, M. Koller, and C. Bullough. Adiabatic compressed air energy storage for the grid integration of wind power. In *Proceedings of the sixth international workshop on large-scale integration of wind power and transmission networks for offshore windfarms*, 26.28 October 2006.

APPENDICES

Appendix A.

Development of heat loss model for storage tanks

The heat loss from the tank is dependent on the exposed surface area, the tank-to-ambient temperature difference and the fill level of the tank [196]. From Equation 3.29, the ratio of heat loss at two different fill levels x and y of the same storage tank is given by

$$\frac{\left(\dot{Q}_k^{loss}\right)_x}{\left(\dot{Q}_k^{loss}\right)_y} = \frac{\left(U_k^{loss} A_{tank} \Delta T_k \cdot (\chi_k)^p\right)_x}{\left(U_k^{loss} A_{tank} \Delta T_k \cdot (\chi_k)^p\right)_y} \tag{A.1}$$

For a given storage tank, the values of A_{tank}, U_k^{loss} and ΔT_k are constant. Thus, the expression reduces to

$$\frac{\left(\dot{Q}_k^{loss}\right)_x}{\left(\dot{Q}_k^{loss}\right)_y} = \frac{\left((\chi_k)^p\right)_x}{\left((\chi_k)^p\right)_y} \tag{A.2}$$

The value of the exponent is determined using measured data from Andasol-1 (Table A.1). Substituting the values for the cold tank into Equation A.2 gives

$$\left(\frac{488}{230}\right) = \left(\frac{1}{0.08}\right)^p$$

Solving this equation gives $p = 0.3$. A similar evaluation using the cold tank data gives the same value. Hence, the value is independent of temperature and can therefore be applied to storage at higher temperatures.

Next, the values of the heat loss coefficients for the cold and hot tanks are determined based on recorded data from the Solar-Two test project (Table A.2). From the given dimensions, the exposed surface areas for the cylindrical tanks were calculated as 517

Heat loss rate	Cold tank (292 °C)	Hot tank (386 °C)
$\dot{Q}_k^{loss}$ at 8% [kW]	225	230
$\dot{Q}_k^{loss}$ at 100% [kW]	483	488

Table A.1.: Measured data from Andasol-1 project [189]

Tank	Dimensions	Measured loss (KW_{th})
Full hot tank at 565 ^{o}C	11.6 m diameter, 8.4 m high	102
Full cold tank at 290 ^{o}C	11.6 m diameter, 7.8 m high	44

Table A.2.: Measured thermal losses from storage tanks at Solar-Two [38]

m^2 and 496 m^2 for the hot and cold tanks respectively. Substituting these values into with the relevant data from Table A.2 into Equation 3.29 give the values of the heat loss coefficients. For the hot tank,

$$U_{HT}^{loss} = \frac{\dot{Q}_{HT}^{loss}}{A_{tank}\Delta T_k \cdot (\chi_k)^p} = \frac{102 \times 10^3}{517 \times (565 - 25) \times (1)^{0.3}} = 0.364\,\mathrm{W/m^2{\cdot}K}$$

A similar approach gives the value for the cold tank as $U_{HT}^{loss} = 0.335\,\mathrm{W/m^2{\cdot}K}$.

The heat loss coefficient U^{loss} is dependent on the thermal conductivity and thickness of the insulation around the tank [246]. As such, the heat loss coefficients obtained above are valid for molten salt storage tanks with the same insulation type and thickness as those for the Solar-Two project.

Appendix B.

Input Information for case studies

B.1. Model parameters for generation and storage technologies

Table B.1.: Parameters used in case studies

Generation/Storage	Description	Source(s)
PV system	Silicon solar panels, $\eta^{inv} = 0.95$	Paatero and Lund [171]
Wind turbine	NEG Micon NM44/750: $P_R = 750$ kW, $H = 56$ m, $\nu_{c,in} = 3.5\,\mathrm{m/s}$, $\nu_r = 15\,\mathrm{m/s}$, $\nu_{c,out} = 25\,\mathrm{m/s}$, power density = $2.03\,\mathrm{m^2/kW}$	Kavasseri and Seetharaman [122], The Wind Power [212]
Power Tower	$\alpha = 0.9, \varepsilon = 0.83, \eta^{hel} = 0.668$, concentration ratio = 1000	Behar et al. [28], Konstantin and Kretschmann [128]
PHES	$z = 700\,m, \eta^{pump} = 0.85, \eta^{tur} = 0.90$	Barnes and Levine [24], Deane et al. [55]
AA-CAES	Design compression and expansion ratio = 50. Concrete TES (T^{TES}_{max}= 620°C). $\eta^{comp} = 0.85, \eta^{motor} = 0.90, \eta^{gen} = 0.90$	Hartmann et al. [97], Kim et al. [125], Zunft et al. [249]
Molten salt system	60/40 $NaNO_3/KNO_3$ salt mixture. Tank operating temperatures of 290°C and 565°C. Power block efficiency between 0.154 and 0.397	Garcia et al. [86], Medrano et al. [153], Ortega et al. [168]
VRF battery bank	Based on RedT 5 KW_e VRFB systems: $\kappa = 0\%$ per month. $U_{bat,single}$= 40 Volts. DC-DC stack efficiency = 0.8. $DOD_{max} = 0.8$. $\eta_{inv,ac-dc} = \eta_{inv,dc-ac} = 0.95$.	Abbes et al. [3], Kear et al. [123], www.redtenergy.com [235]

B.2. Cost data

Table B.2 shows the cost data used for the different components of the energy system.

Table B.2.: Unit costs for generation and storage options in superstructure

Description	Cost	Source	Comment(s)
Photovoltaic modules	173.6 €/m^2	[134]	Converted under nominal conditions
Wind turbines	907.1 €/m^2	[161]	Converted using power density of NEG Micon 750 kW turbine.
Power Tower	410.2 €/m^2	[161]	Combination of heliostat field, tower, receiver and indirect costs.
Energy storage in AA-CAES	70 €/KWh	[127]	-
Power generation from AA-CAES	600 €/KW_e	[127]	-
Energy storage in PHES storage	30 €/KWh	[127]	-
Power generation from PHES	500 €/KW_e	[127]	-
Molten salt tank storage	28 €/KWh	[161]	-
Molten salt electricity generation	884 €/KW_e	[161]	-
Energy storage in VRFB	200 €/KWh	[123, 222]	-
Power generation from VRFB	1,000 €/KW_e	[222]	-
Diesel Generators	797 €/KW_e	[7]	-

B.3. Demand Profile

Figure B.1 shows the average power consumption for Collahuasi mine in July 2013. The thermal demands were assumed to be 10% of the electrical demands.

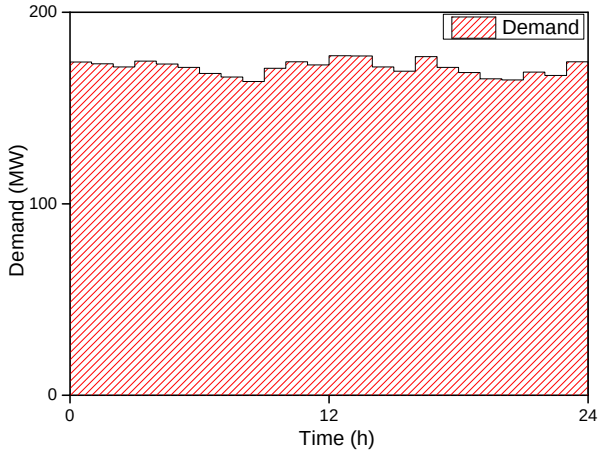

Figure B.1.: Power demand profile for the mine in July 2013. The minimum, average and peak demands are 164 MW_e, 171 MW_e and 178 MW_e respectively. [45]

Appendix C.

Convergence for reliability evaluation

In order to determine the number of renewable input profiles required for convergence, the rate at which the reliability of given designs changed with the number of simulated years was investigated for Chile and Canada. For both locations, random designs generated from solving single objective problems were considered. The designs evaluated are shown in Table C.1. Each of the designs was evaluated for 1,000 randomly generated solar profiles, with the reliability evaluated after each stage.

Figure C.1 shows the results for the designs. In both cases, the reliability measure is seen to converge after a few hundred profiles. In order to select an appropriate number of simulations, a tolerance range for the reliability measure was required. Convergence to within 2% of the final reliability value was considered sufficient based on the work by Tina et al. [217]. The limits in each case are shown as broken lines on the graphs. Both cases require roughly the same number of simulated years to attain the required level of convergence (roughly 280 years). Based on this, 300 profiles were deemed sufficient to give a rough estimate of the reliability.

Table C.1.: Characteristics of evaluated designs for Chile and Canada.

	Canada		Chile	
	Design A	Design B	Design A	Design B
PT capacity (MW)	4875.5	5475.5	1233.9	1243.2
PV Capacity (MW)	-	-	2.1	1.9
MTS Capacity (MWh)	7927.3	8064.0	6421.5	6609.7
MTS Capacity (MW)	181.0	181.0	179.0	179.0
PHES Capacity (MWh)	-	-	3.4	3.0
PHES Capacity (MW)	-	-	1.5	1.3

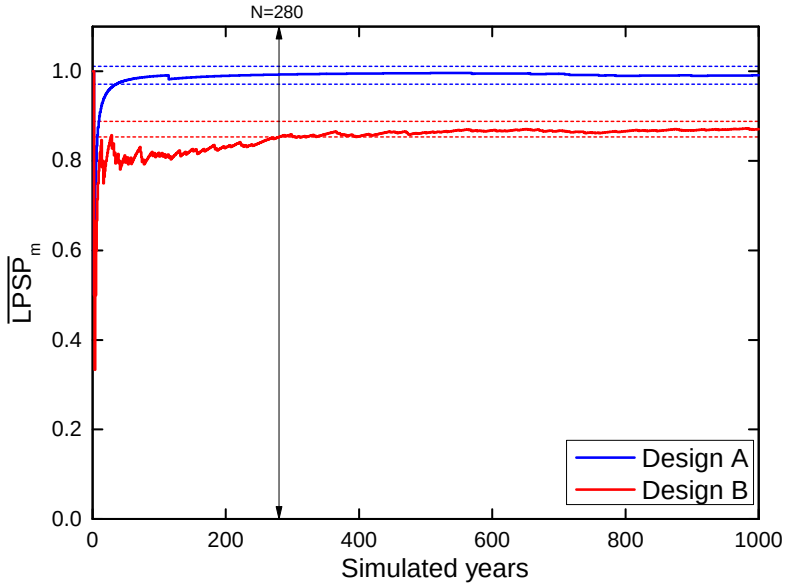

(a) Canada

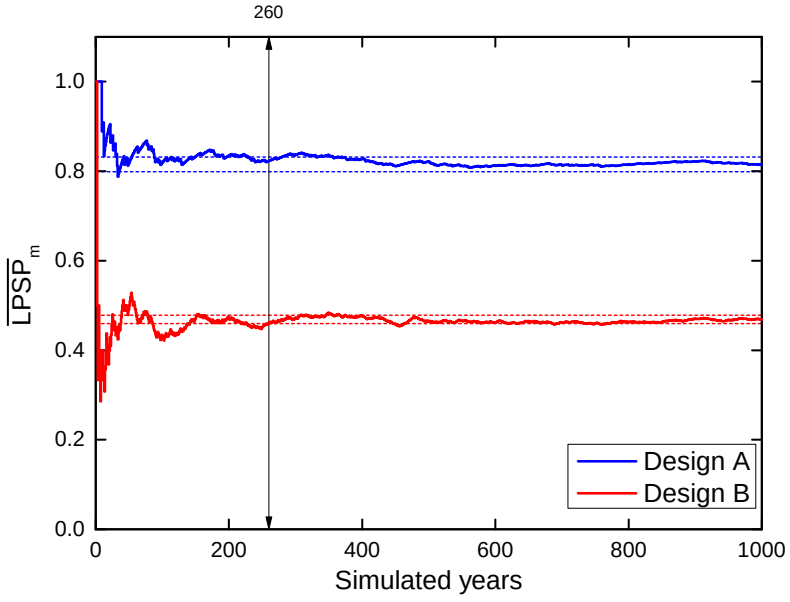

(b) Chile

Figure C.1.: Convergence profiles over 1,000 evaluations for Canada and Chile. The broken lines show the accepted tolerance limits (±2% of final value).

Appendix D.

Multi-objective design of stand-alone solar-wind integrated system system for Canada for variable demand

To demonstrate the capability of the model and methodology to handle different types of demand profiles, the same multi-objective design problem considered in Section 6.5.3 was solved again for a different demand profile (Figure D.1). The demand profile considered in this case is the actual demand profile of the mine in 2013. The demand within the year is more variable than the fixed daily demand case (Figure B.1), with the peak demand slightly higher (186 MW_e). The annual power demand of the mine however is 14.5% lower than the fixed demand case (1,498 GWh for fixed case against 1,281 GWh for variable case). All other inputs (including the solar input profiles) remained the same for the study.

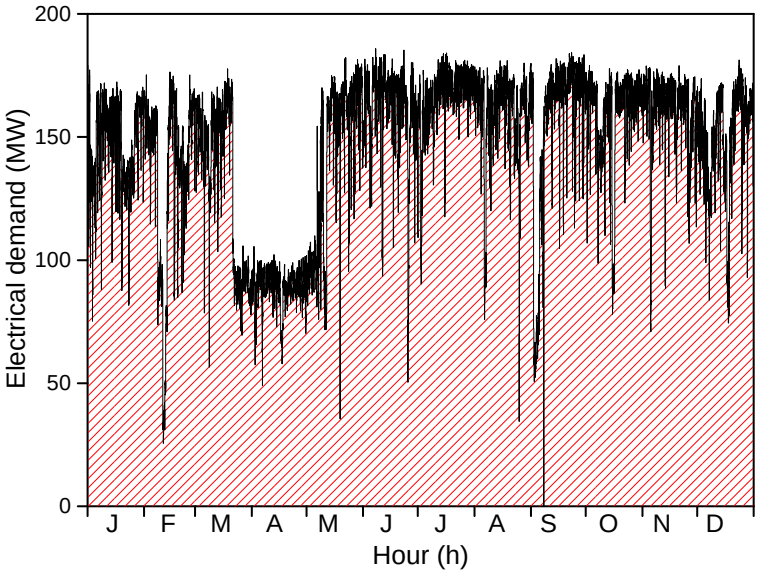

Figure D.1.: Variable demand profile for case study. The profile was generated from the actual power demand of Collahuasi mine in 2013 [45]

Figure D.2 shows the cost-reliability trade-off curve. The costs of the designs required are lower than the fixed demand case, reflecting the lower annual demand. The cost of the mid-range designs reduce by between 6.7% and 7.2% while the cost most reliable

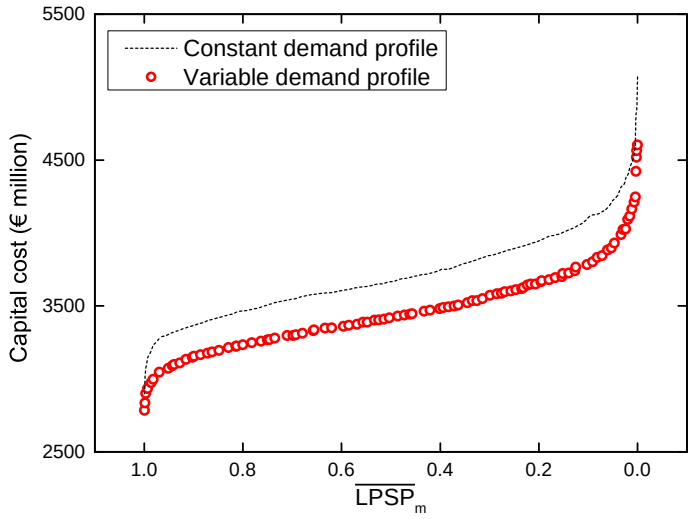

Figure D.2.: Cost-reliability trade off curve. The broken black line shows the location of the trade-off curve for the constant demand case presented in Section 6.5.3.

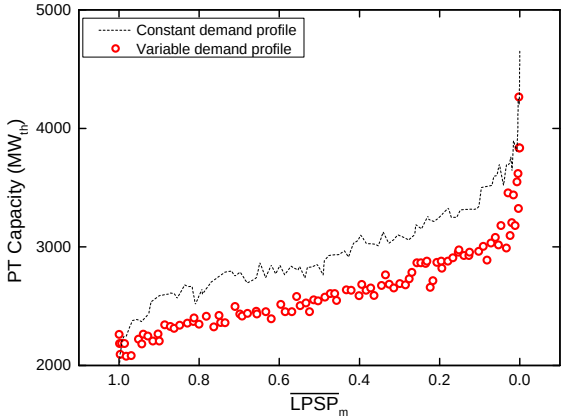

Figure D.3.: Installed PT capacities. The black line shows the PT capacities for the constant demand case.

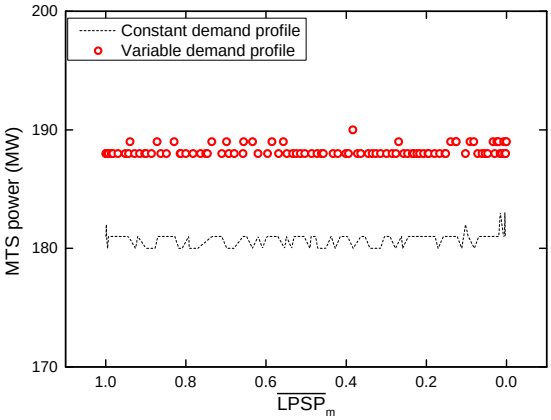

Figure D.4.: Peak discharge capacity of MTS system. The black line shows the PT capacities for the constant demand case.

design reduced by 9.5%. The cost varies by 65% (€ 1.82bn) over the reliability range.

Figure D.3 shows the profile for the installed PT generation capacities across the reliability range. The capacities are significantly smaller than those required for the fixed demand case: the lower demand over the year means that less generation is required through the year. This decrease was accompanied by slight increases in the storage capacities of the MTS. The more variable nature of the demand profile allows for the storage level to be built up on off-peak days. This means that days with poor solar availability are less likely to cause system failure. However, the installed capacities of the WT/PHES systems remained at the same level as in the constant demand case.

Figure D.4 shows the peak discharge capacity of the PT/MTS steam turbine. The installed capacities are slightly higher than those required in the fixed input case, reflecting the higher peak demand.

Appendix E.

Statistical properties of historical solar radiation and wind data

E.1. Monthly statistics of GHI data for Atacama, Chile

The statistical characteristics were calculated from 10 years of historical data (2003-2012) obtained from University of Chile [61].

Hour (h)	Mean $(W \cdot m^{-2})$	S.D. $(W \cdot m^{-2})$	Skew (-)	Kurt (-)	Mean $(W \cdot m^{-2})$	S.D. $(W \cdot m^{-2})$	Skew (-)	Kurt (-)
	JANUARY				FEBRUARY			
6	10.73	9.30	-0.22	1.18	-	-	-	-
6.5	87.21	10.73	-0.11	2.64	53.11	10.27	0.02	3.87
7	200.99	11.96	-0.43	3.53	155.81	17.26	0.15	2.23
7.5	327.45	14.70	0.08	4.71	282.37	22.87	-1.24	13.23
8	451.55	18.00	-1.90	11.82	406.02	32.13	-3.50	28.31
8.5	592.08	14.79	-0.05	2.24	510.16	87.03	-2.75	10.18
9	695.77	42.79	-8.03	78.59	655.66	62.75	-6.12	43.40
9.5	804.51	55.58	-7.62	67.05	761.72	84.92	-4.87	27.98
10	901.36	58.41	-7.74	71.88	861.05	97.39	-4.97	27.46
10.5	984.32	65.03	-8.59	85.68	938.37	116.51	-4.25	21.12
11	1038.99	86.43	-6.30	45.21	1001.47	116.71	-4.32	21.82
11.5	1093.61	81.30	-6.55	47.36	1075.13	79.71	-6.71	49.64
12	1127.69	82.38	-5.95	40.85	1092.62	119.64	-4.41	22.34
12.5	1135.64	98.76	-4.84	26.81	1102.99	119.67	-4.10	20.29
13	1130.87	99.61	-5.60	37.56	1092.53	141.91	-4.19	20.42
13.5	1106.97	86.17	-5.65	37.40	1052.25	159.12	-3.40	14.49
14	1051.78	106.92	-5.46	34.99	1007.72	138.74	-3.80	17.90
14.5	1003.02	91.07	-4.40	24.46	867.12	195.03	-1.75	5.03
15	925.50	88.14	-6.76	51.15	878.65	126.60	-4.02	18.16
15.5	832.62	92.49	-5.17	30.01	788.53	119.23	-4.01	18.29

Hour (h)	Mean ($W \cdot m^{-2}$)	S.D. ($W \cdot m^{-2}$)	Skew (-)	Kurt (-)	Mean ($W \cdot m^{-2}$)	S.D. ($W \cdot m^{-2}$)	Skew (-)	Kurt (-)
16	731.48	68.55	-5.42	35.05	685.66	99.74	-4.34	21.72
16.5	618.36	62.63	-6.83	51.73	568.33	89.84	-4.16	19.71
17	496.12	53.76	-6.27	44.30	451.56	63.04	-4.55	24.79
17.5	369.78	40.04	-6.26	45.91	323.80	41.58	-4.54	28.06
18	245.38	19.05	-4.40	37.02	198.22	24.34	-2.10	13.32
18.5	127.54	11.28	-0.33	9.07	84.51	15.16	0.21	2.29
19	27.88	2.88	-0.37	2.65	7.68	9.64	0.49	1.30

	MARCH				APRIL			
6.5	16.23	18.48	0.35	1.28	-	-	-	-
7	100.13	21.74	0.17	2.30	37.63	16.31	0.63	2.41
7.5	208.05	27.79	0.05	2.64	128.03	23.28	0.08	1.93
8	335.29	28.10	0.02	2.07	245.14	28.61	-0.23	3.07
8.5	472.70	26.45	-0.30	2.36	373.69	31.85	0.21	1.95
9	589.17	30.59	-0.06	2.18	487.34	37.52	-1.69	15.68
9.5	702.38	38.08	-2.39	22.25	598.07	37.85	-0.49	4.09
10	803.75	43.68	-5.38	65.00	696.42	41.82	-1.70	15.20
10.5	887.59	57.87	-6.01	57.02	777.89	52.30	-3.53	31.19
11	950.79	56.93	-6.55	73.21	836.81	62.42	-5.02	47.37
11.5	1009.63	61.13	-8.03	98.42	893.87	59.12	-4.34	36.42
12	1043.39	64.24	-7.74	92.47	925.22	76.89	-5.57	46.32
12.5	1058.03	59.05	-6.77	78.15	937.42	80.35	-5.79	48.97
13	1053.45	48.17	-3.86	31.04	927.49	90.63	-5.09	36.72
13.5	1026.77	40.41	-1.85	13.73	899.03	94.66	-5.33	38.55
14	971.74	57.22	-7.00	78.22	853.05	85.53	-5.88	45.64
14.5	919.23	29.99	-0.34	2.07	778.66	100.48	-3.06	13.29
15	831.30	62.12	-6.42	57.59	719.41	70.10	-5.13	38.84
15.5	739.89	52.07	-6.00	59.08	632.13	51.71	-4.16	39.01
16	631.04	46.88	-5.29	51.21	527.44	44.91	-3.40	31.27
16.5	510.16	38.22	-2.97	28.98	411.17	33.59	-0.29	3.36
17	389.73	28.78	0.13	2.36	300.88	30.40	0.08	2.25
17.5	255.00	26.38	0.07	1.96	169.04	24.99	0.15	1.83
18	131.02	23.27	0.07	1.91	58.82	20.22	-0.02	2.06
18.5	32.15	12.60	1.00	3.04	-	-	-	-

	MAY				JUNE			
7.5	66.97	14.14	0.66	2.55	42.67	7.50	-0.77	21.08
8	169.32	19.72	-0.12	3.65	131.99	9.81	-4.87	41.14
8.5	284.74	22.84	0.36	2.18	240.04	7.51	0.66	4.13

Hour (h)	Mean ($W \cdot m^{-2}$)	S.D. ($W \cdot m^{-2}$)	Skew (-)	Kurt (-)	Mean ($W \cdot m^{-2}$)	S.D. ($W \cdot m^{-2}$)	Skew (-)	Kurt (-)
9	393.77	25.36	0.25	2.07	342.64	10.37	0.57	4.10
9.5	496.12	28.61	0.13	2.32	440.22	13.86	-0.94	9.64
10	588.82	34.65	-2.30	24.22	529.80	12.58	0.63	4.33
10.5	664.58	46.25	-4.55	46.47	603.60	22.84	-5.24	57.11
11	718.76	60.80	-5.34	44.91	656.55	29.73	-8.75	120.26
11.5	774.65	60.05	-6.20	59.16	711.15	10.74	0.28	4.50
12	806.74	56.39	-5.36	49.83	742.62	13.42	0.55	4.67
12.5	819.58	50.90	-4.06	36.44	753.34	25.36	-9.64	140.89
13	816.88	41.90	-2.12	18.41	747.38	39.82	-10.57	130.60
13.5	787.03	51.98	-3.96	30.89	718.24	41.23	-8.84	100.86
14	737.11	58.21	-4.95	38.87	674.67	32.01	-12.00	186.19
14.5	681.75	59.68	-3.68	23.04	628.33	12.82	0.54	3.17
15	613.70	38.95	-3.08	31.41	556.82	10.53	0.62	5.28
15.5	530.43	29.49	0.01	2.99	474.77	9.78	0.48	4.61
16	431.95	25.89	0.32	2.05	379.29	9.28	0.92	7.72
16.5	318.80	23.64	0.22	2.08	268.50	17.70	-7.08	76.26
17	227.03	26.46	0.13	2.13	186.36	20.41	-1.72	13.23
17.5	104.14	24.98	2.44	11.13	69.11	3.54	0.76	3.22
18	21.84	27.86	4.20	22.10	-	-	-	-

	JULY				AUGUST			
7	-	-	-	-	15.30	14.15	0.14	1.58
7.5	52.57	10.68	0.84	6.49	102.65	27.21	0.66	3.09
8	145.42	14.76	-0.85	7.52	207.36	26.28	-0.15	3.06
8.5	259.77	18.68	0.13	1.95	332.06	30.13	0.35	2.54
9	360.86	18.72	0.14	2.70	441.96	31.78	0.17	2.04
9.5	460.09	24.86	-2.89	30.90	547.95	34.85	0.17	2.10
10	549.87	22.34	-0.08	3.65	643.82	36.20	0.18	2.11
10.5	624.19	34.93	-4.63	43.52	720.32	47.90	-2.45	19.79
11	676.47	54.03	-6.51	57.22	778.66	50.57	-3.49	36.61
11.5	728.76	54.53	-7.68	72.31	833.98	58.25	-4.79	46.15
12	759.29	62.77	-6.97	60.84	864.66	74.48	-5.29	42.50
12.5	770.79	64.26	-6.81	58.65	876.45	81.02	-5.37	41.24
13	767.74	53.85	-6.88	64.92	872.29	73.59	-4.73	37.02
13.5	741.40	52.70	-7.60	80.30	841.23	70.79	-4.68	36.29
14	695.83	47.67	-6.49	59.19	796.77	55.57	-3.95	35.92
14.5	647.71	27.13	-0.25	3.24	743.14	60.74	-2.72	16.84
15	574.97	26.98	-2.98	30.82	670.64	43.16	-2.42	24.26
15.5	493.18	22.01	-0.31	5.65	583.46	40.85	-2.62	27.63

Hour (h)	Mean ($W \cdot m^{-2}$)	S.D. ($W \cdot m^{-2}$)	Skew (-)	Kurt (-)	Mean ($W \cdot m^{-2}$)	S.D. ($W \cdot m^{-2}$)	Skew (-)	Kurt (-)
16	396.82	18.79	0.31	2.88	481.04	35.44	-1.08	10.84
16.5	288.99	19.28	0.55	3.78	363.09	35.56	-1.43	15.10
17	199.12	21.24	0.49	3.06	267.44	31.28	0.27	2.07
17.5	80.81	10.17	0.34	2.09	135.91	22.24	0.22	1.82
18	6.52	9.02	0.88	2.92	36.40	14.07	0.64	1.88
	SEPTEMBER				OCTOBER			
6.5	1.07	5.86	5.39	30.47	44.81	8.20	0.30	3.47
7	74.07	22.08	-0.33	3.15	139.89	17.99	-0.20	2.15
7.5	180.40	27.41	-0.84	5.56	263.74	27.64	0.28	2.64
8	296.75	33.85	-1.87	13.43	388.93	27.47	-0.28	2.52
8.5	434.38	28.28	0.01	2.03	529.62	26.04	-0.31	1.89
9	549.47	29.72	0.05	2.20	646.35	27.04	-0.10	2.11
9.5	662.45	31.70	-0.15	3.07	760.19	32.84	-2.87	28.64
10	762.53	31.67	0.09	2.34	860.94	34.41	-3.25	32.00
10.5	838.46	63.17	-5.68	49.52	946.61	39.96	-6.06	76.68
11	900.60	60.43	-6.00	59.70	1008.98	40.80	-6.65	85.89
11.5	962.24	37.85	-2.27	23.14	1064.96	34.70	-5.49	66.91
12	998.35	40.97	-3.10	33.23	1100.41	44.14	-6.80	81.60
12.5	1007.78	62.24	-4.39	30.79	1116.14	34.29	-2.51	21.71
13	998.07	77.62	-5.55	44.41	1111.67	27.59	0.00	2.44
13.5	963.90	87.57	-5.45	41.29	1081.95	31.53	-1.54	14.17
14	917.33	77.66	-5.58	43.43	1027.41	50.67	-9.54	137.43
14.5	873.51	32.28	0.10	2.33	970.66	44.09	-3.75	25.92
15	788.46	46.47	-4.48	40.79	887.28	58.20	-7.34	73.79
15.5	698.97	33.03	-0.30	3.23	796.85	42.47	-7.13	91.29
16	591.75	30.31	0.03	2.06	688.80	37.46	-6.00	74.59
16.5	466.42	44.23	-4.08	36.21	566.90	34.60	-4.99	59.10
17	354.33	37.32	-3.02	25.23	442.76	27.74	0.02	2.17
17.5	220.10	25.40	-0.02	2.07	308.27	24.24	-0.17	2.00
18	100.81	21.23	0.08	1.83	179.05	22.64	-0.14	1.89
18.5	14.40	13.02	0.49	4.41	63.99	20.56	-0.05	2.37
19	-	-	-	-	0.57	3.10	5.30	29.10
	NOVEMBER				DECEMBER			
6	4.26	8.29	2.09	8.37	23.06	4.00	5.58	42.79
6.5	79.43	12.74	0.35	2.58	103.41	5.51	0.84	6.40
7	195.83	14.78	-0.19	2.45	218.54	8.03	-0.12	4.58
7.5	325.66	17.63	0.07	2.91	345.36	11.21	0.14	4.98

Hour (h)	Mean ($W \cdot m^{-2}$)	S.D. ($W \cdot m^{-2}$)	Skew (-)	Kurt (-)	Mean ($W \cdot m^{-2}$)	S.D. ($W \cdot m^{-2}$)	Skew (-)	Kurt (-)
8	452.39	18.25	-0.59	4.76	469.58	16.47	-4.10	40.63
8.5	588.34	17.14	-0.36	2.34	592.31	26.53	-10.81	160.66
9	701.89	31.12	-9.96	144.85	711.08	46.72	-9.14	96.97
9.5	814.01	20.70	-1.69	13.61	818.56	60.35	-8.46	81.33
10	910.74	38.13	-8.38	91.47	914.91	63.69	-9.40	100.00
10.5	995.35	33.22	-7.01	79.05	998.71	59.12	-10.97	136.71
11	1057.18	24.63	-2.96	23.78	1054.51	74.64	-8.76	86.54
11.5	1107.67	48.52	-8.72	88.38	1116.14	37.74	-14.50	239.84
12	1142.02	52.24	-8.87	97.09	1140.87	76.25	-9.78	114.80
12.5	1156.54	53.84	-8.20	77.94	1153.36	79.35	-8.92	93.08
13	1148.13	71.58	-7.96	69.23	1150.80	58.70	-7.63	66.42
13.5	1121.46	67.27	-7.84	71.16	1128.91	31.99	-6.72	72.12
14	1071.43	65.45	-7.80	70.26	1077.85	42.30	-7.47	70.10
14.5	1026.49	15.28	-0.35	2.23	1018.43	53.53	-10.99	134.91
15	937.22	58.48	-8.64	83.63	942.20	62.91	-8.63	87.49
15.5	847.70	48.01	-9.63	107.57	851.51	66.83	-7.26	61.10
16	742.85	34.28	-10.38	144.16	749.57	55.77	-7.96	73.69
16.5	623.77	39.48	-9.18	102.40	637.02	42.55	-9.88	111.70
17	501.20	26.95	-8.32	113.12	515.79	34.67	-10.33	120.98
17.5	370.59	15.24	-0.30	2.67	388.65	26.95	-10.04	116.23
18	241.40	14.93	-0.27	2.41	262.17	18.15	-8.97	100.08
18.5	119.55	14.31	0.37	3.90	142.85	10.87	-0.58	39.12
19	25.55	4.99	2.42	18.94	33.15	7.56	7.34	67.91

E.2. Monthly statistics of GHI data for Alberta, Canada

The monthly statistical characteristics were calculated from 8 years of historical data (2005-2012) obtained from National Renewable Energy Laboratory [160].

Hour (h)	Mean ($W \cdot m^{-2}$)	S.D. ($W \cdot m^{-2}$)	Skew (-)	Kurt (-)	Mean ($W \cdot m^{-2}$)	S.D. ($W \cdot m^{-2}$)	Skew (-)	Kurt (-)
	JANUARY				FEBRUARY			
8	-	-	-	-	9.00	12.58	1.63	5.78
8.5	0.94	2.65	2.87	10.36	41.60	29.03	0.94	3.57
9	23.55	14.29	1.12	3.74	87.26	44.52	0.53	3.07
9.5	63.33	27.16	0.40	3.04	136.70	64.48	0.26	2.72
10	104.99	40.89	0.02	2.81	187.61	85.59	0.00	2.33
10.5	142.31	53.98	-0.10	2.70	238.17	98.23	-0.03	2.22
11	178.81	63.70	-0.12	2.50	278.86	107.74	-0.19	2.24
11.5	210.64	72.65	-0.20	2.35	311.51	122.00	-0.26	2.11
12	231.48	77.56	-0.24	2.43	336.02	134.26	-0.40	2.17
12.5	246.07	80.48	-0.39	2.46	354.23	133.02	-0.49	2.41
13	248.85	75.13	-0.23	2.47	355.65	127.27	-0.43	2.28
13.5	243.62	70.35	-0.32	2.72	353.08	124.96	-0.51	2.48
14	220.45	65.62	-0.34	3.24	329.24	113.40	-0.41	2.42
14.5	186.23	66.40	-0.23	2.89	295.05	107.68	-0.33	2.28
15	155.21	54.19	0.12	2.63	261.78	98.65	-0.24	2.19
15.5	115.41	43.39	0.30	2.66	217.29	88.65	-0.21	2.28
16	70.99	32.94	0.59	2.69	165.41	66.93	0.09	2.39
16.5	28.52	22.02	0.81	2.82	113.24	48.92	0.32	2.56
17	3.02	5.93	1.90	5.63	59.57	33.53	0.54	2.50
17.5	-	-	-	-	17.68	17.96	0.81	2.79
18	-	-	-	-	0.63	2.04	3.34	13.36
	MARCH				APRIL			
5.5	-	-	-	-	0.95	2.43	2.84	10.99
6	-	-	-	-	13.77	15.86	1.15	3.59
6.5	0.58	1.89	3.64	16.53	47.22	33.57	0.80	2.88
7	10.52	15.23	1.62	4.84	94.98	52.08	0.50	2.66
7.5	40.04	34.52	0.97	3.14	150.09	75.50	0.30	2.38
8	84.82	54.56	0.50	2.59	221.36	111.97	-0.20	1.97
8.5	136.45	78.05	0.23	2.47	281.73	141.99	-0.31	1.90
9	192.10	99.66	0.02	2.33	341.55	166.47	-0.37	1.82
9.5	249.09	125.08	-0.08	2.14	411.81	190.05	-0.56	1.99

Hour (h)	Mean ($W \cdot m^{-2}$)	S.D. ($W \cdot m^{-2}$)	Skew (-)	Kurt (-)	Mean ($W \cdot m^{-2}$)	S.D. ($W \cdot m^{-2}$)	Skew (-)	Kurt (-)
10	299.17	145.60	-0.13	2.01	469.53	206.83	-0.62	1.97
10.5	363.55	158.45	-0.29	2.01	514.74	216.71	-0.68	2.08
11	409.55	169.43	-0.35	1.95	544.91	227.49	-0.67	2.12
11.5	443.10	175.93	-0.39	1.97	569.14	231.43	-0.68	2.23
12	475.65	174.90	-0.54	2.23	587.48	230.15	-0.71	2.36
12.5	489.33	173.06	-0.55	2.21	598.83	222.26	-0.71	2.43
13	498.33	170.38	-0.65	2.34	585.03	216.12	-0.54	2.15
13.5	492.34	154.95	-0.73	2.67	571.42	209.22	-0.49	2.12
14	475.19	142.47	-0.66	2.61	556.99	205.44	-0.68	2.35
14.5	441.11	131.04	-0.60	2.54	530.22	195.97	-0.70	2.43
15	407.77	116.81	-0.63	2.66	480.44	187.12	-0.70	2.44
15.5	354.15	109.93	-0.58	2.63	445.40	168.68	-0.66	2.24
16	280.65	100.02	-0.35	2.62	375.24	159.34	-0.59	2.21
16.5	222.15	86.75	-0.16	2.14	324.71	132.57	-0.53	2.14
17	160.50	62.04	-0.03	2.52	262.72	104.03	-0.32	2.03
17.5	103.33	45.82	0.22	2.38	197.23	81.76	-0.17	2.06
18	47.65	30.36	0.58	2.38	133.82	57.75	0.10	2.24
18.5	10.00	12.79	1.13	3.11	74.63	38.70	0.45	2.28
19	-	-	-	-	26.75	21.53	0.79	2.58
19.5	-	-	-	-	3.13	5.40	1.65	4.70

	MAY				JUNE			
5	6.98	8.12	1.07	3.13	23.35	10.20	-0.42	2.25
5.5	36.97	21.90	0.65	2.55	63.83	27.34	-0.53	2.24
6	85.21	38.62	0.15	2.34	114.02	48.60	-0.55	2.23
6.5	142.23	58.95	-0.21	2.27	166.73	74.41	-0.45	1.82
7	202.82	84.49	-0.37	2.08	222.59	103.27	-0.46	1.83
7.5	261.19	114.23	-0.47	1.98	272.60	133.65	-0.37	1.64
8	325.17	151.03	-0.59	1.93	334.18	168.93	-0.50	1.70
8.5	388.53	181.65	-0.69	1.99	388.12	196.48	-0.52	1.76
9	446.26	207.41	-0.70	1.99	439.78	225.15	-0.55	1.82
9.5	503.73	226.12	-0.78	2.17	489.54	253.08	-0.62	1.86
10	556.81	239.17	-0.84	2.28	532.20	266.86	-0.64	1.99
10.5	587.73	249.60	-0.76	2.23	564.24	288.20	-0.64	1.95
11	610.42	274.49	-0.75	2.16	574.28	301.88	-0.48	1.77
11.5	618.29	277.35	-0.63	2.00	568.84	319.71	-0.40	1.67
12	631.20	280.96	-0.64	2.03	562.70	322.87	-0.30	1.66
12.5	630.54	277.46	-0.61	2.03	564.41	326.05	-0.32	1.62
13	631.23	265.04	-0.60	2.05	573.27	308.35	-0.28	1.64

Hour (h)	Mean ($W \cdot m^{-2}$)	S.D. ($W \cdot m^{-2}$)	Skew (-)	Kurt (-)	Mean ($W \cdot m^{-2}$)	S.D. ($W \cdot m^{-2}$)	Skew (-)	Kurt (-)
13.5	611.50	261.48	-0.53	1.94	574.20	296.03	-0.26	1.68
14	584.95	243.18	-0.44	1.86	548.69	279.17	-0.19	1.70
14.5	541.24	250.32	-0.40	1.72	525.40	283.07	-0.23	1.62
15	500.87	237.64	-0.41	1.83	475.49	275.24	-0.14	1.56
15.5	456.06	216.68	-0.36	1.80	436.09	259.88	-0.17	1.57
16	411.40	196.98	-0.37	1.80	405.59	226.57	-0.19	1.65
16.5	361.66	172.97	-0.30	1.77	363.21	205.08	-0.16	1.60
17	319.18	143.60	-0.42	1.99	318.57	175.36	-0.24	1.66
17.5	269.46	114.69	-0.50	2.09	264.98	151.58	-0.13	1.61
18	207.65	86.98	-0.40	2.18	223.60	125.81	-0.29	1.66
18.5	148.37	68.07	-0.32	2.28	181.10	92.04	-0.37	1.83
19	93.26	45.18	-0.06	2.38	133.58	63.99	-0.50	2.06
19.5	43.75	26.28	0.53	2.58	82.71	40.30	-0.44	2.06
20	10.27	11.24	1.09	3.33	38.68	19.80	-0.26	2.00
20.5	-	-	-	-	8.41	5.55	0.08	1.77

	JULY				AUGUST			
5	9.63	8.82	0.55	2.15	-	-	-	-
5.5	45.29	21.04	0.23	2.05	4.46	6.94	1.46	3.98
6	97.88	36.32	-0.28	2.26	32.09	22.50	0.70	2.51
6.5	160.33	53.66	-0.63	2.46	82.82	38.59	0.16	2.34
7	217.30	81.76	-0.70	2.36	143.17	57.14	-0.23	2.38
7.5	290.02	102.19	-0.77	2.31	205.63	84.71	-0.55	2.45
8	364.92	128.91	-1.14	3.01	273.00	120.13	-0.81	2.46
8.5	433.14	155.96	-1.30	3.34	338.76	146.11	-0.88	2.42
9	492.85	184.52	-1.29	3.25	400.83	173.04	-0.85	2.25
9.5	553.17	196.26	-1.32	3.43	461.08	195.87	-0.99	2.52
10	608.37	212.36	-1.38	3.61	515.04	211.78	-1.03	2.64
10.5	653.60	220.23	-1.36	3.63	558.04	227.94	-1.07	2.76
11	668.19	252.42	-1.27	3.30	597.48	235.49	-1.05	2.71
11.5	697.05	260.31	-1.33	3.47	614.35	243.28	-1.00	2.66
12	693.56	272.55	-1.20	3.19	617.33	260.50	-0.90	2.44
12.5	684.97	272.45	-1.06	2.88	630.96	251.58	-0.89	2.46
13	685.98	271.44	-1.01	2.74	621.98	250.00	-0.81	2.28
13.5	671.69	270.36	-0.93	2.59	613.79	243.49	-0.78	2.21
14	646.44	261.29	-0.92	2.62	596.27	236.97	-0.91	2.51
14.5	612.06	252.23	-0.92	2.59	564.60	222.38	-0.86	2.46
15	593.02	237.81	-1.03	2.77	518.22	223.11	-0.82	2.30
15.5	544.00	226.34	-1.02	2.70	470.02	208.14	-0.82	2.30

Hour (h)	Mean ($W \cdot m^{-2}$)	S.D. ($W \cdot m^{-2}$)	Skew (-)	Kurt (-)	Mean ($W \cdot m^{-2}$)	S.D. ($W \cdot m^{-2}$)	Skew (-)	Kurt (-)
16	490.04	206.55	-0.94	2.52	410.77	191.72	-0.68	2.02
16.5	432.75	192.19	-0.88	2.35	358.52	159.39	-0.66	2.18
17	382.55	160.64	-0.89	2.41	303.67	138.35	-0.66	2.17
17.5	321.32	134.16	-0.85	2.40	245.77	111.76	-0.66	2.37
18	265.67	105.14	-0.84	2.39	192.47	78.38	-0.48	2.68
18.5	202.31	84.46	-0.89	2.59	128.42	57.05	-0.16	2.60
19	143.31	57.20	-1.02	3.10	67.28	39.47	0.40	2.25
19.5	84.73	35.54	-0.76	2.80	21.77	21.94	0.85	2.61
20	35.56	17.84	-0.17	2.12	2.46	4.88	1.87	5.33
20.5	5.21	5.47	0.49	1.80	-	-	-	-

	SEPTEMBER				OCTOBER			
6	0.14	0.85	6.09	39.06	-	-	-	-
6.5	14.11	15.64	0.92	2.64	-	-	-	-
7	57.26	34.23	0.37	2.03	2.71	5.44	2.25	7.76
7.5	116.01	54.68	-0.16	2.12	24.74	23.18	0.98	3.21
8	180.60	80.33	-0.49	2.44	68.44	40.93	0.55	2.61
8.5	251.14	100.43	-0.63	2.47	118.99	60.61	0.14	2.39
9	314.59	124.64	-0.85	2.73	166.71	81.37	-0.05	2.19
9.5	370.53	146.75	-0.85	2.53	211.72	101.01	-0.09	2.01
10	415.66	167.24	-0.80	2.43	256.25	116.37	-0.17	1.97
10.5	460.53	175.70	-0.77	2.43	293.52	131.54	-0.25	2.01
11	492.33	191.70	-0.83	2.46	320.67	140.62	-0.20	1.89
11.5	500.50	210.44	-0.77	2.30	335.96	150.19	-0.22	2.00
12	521.82	201.03	-0.71	2.34	351.55	152.37	-0.23	1.91
12.5	535.26	198.29	-0.86	2.67	364.99	153.35	-0.38	2.06
13	527.60	206.22	-0.88	2.60	363.58	148.64	-0.43	2.20
13.5	503.58	205.71	-0.82	2.51	346.00	132.45	-0.36	2.21
14	485.59	190.36	-0.74	2.36	300.73	125.06	-0.42	2.51
14.5	455.39	177.07	-0.81	2.62	288.21	105.26	-0.20	2.62
15	409.12	171.24	-0.74	2.42	250.35	97.70	-0.15	2.36
15.5	364.44	152.41	-0.73	2.48	200.91	84.63	-0.08	2.49
16	323.85	114.62	-0.51	2.43	151.79	66.82	0.04	2.58
16.5	259.50	98.99	-0.42	2.40	100.22	53.02	0.49	2.59
17	197.12	81.35	-0.18	2.34	52.75	40.05	0.84	2.81
17.5	131.59	61.90	0.11	2.16	14.81	19.99	1.40	4.11
18	69.20	45.79	0.47	2.01	0.88	2.82	3.36	13.62
18.5	22.65	25.36	0.90	2.55	-	-	-	-
19	2.55	5.46	2.10	6.29	-	-	-	-

Hour (h)	Mean ($W \cdot m^{-2}$)	S.D. ($W \cdot m^{-2}$)	Skew (-)	Kurt (-)	Mean ($W \cdot m^{-2}$)	S.D. ($W \cdot m^{-2}$)	Skew (-)	Kurt (-)
	NOVEMBER				DECEMBER			
8	6.46	9.85	1.41	3.92	-	-	-	-
8.5	35.31	26.49	0.78	2.55	0.18	1.02	5.88	37.20
9	77.85	40.84	0.43	2.37	20.90	10.47	0.91	3.45
9.5	122.11	55.14	0.10	2.34	59.23	20.67	0.09	2.60
10	162.63	65.11	0.02	2.35	99.26	31.89	-0.23	2.33
10.5	198.69	75.26	-0.15	2.20	135.32	42.32	-0.34	2.24
11	222.59	86.38	-0.27	2.37	165.61	51.69	-0.43	2.22
11.5	251.66	90.20	-0.25	2.13	185.21	57.70	-0.31	2.08
12	264.30	90.07	-0.40	2.60	204.73	62.70	-0.71	2.95
12.5	271.42	90.62	-0.39	2.39	218.09	58.01	-0.84	3.40
13	257.14	90.52	-0.40	2.40	214.50	57.66	-0.88	3.57
13.5	246.12	79.01	-0.46	2.56	204.83	50.12	-0.76	3.19
14	219.97	68.25	-0.51	2.96	178.69	49.41	-0.60	2.37
14.5	186.44	57.67	-0.28	2.86	148.16	40.39	-0.51	2.21
15	148.29	48.42	-0.03	2.68	110.68	30.40	-0.48	2.21
15.5	102.29	37.90	0.26	2.83	68.51	19.12	-0.41	2.21
16	54.71	26.25	0.68	2.88	26.63	8.18	-0.01	2.43
16.5	13.95	14.65	0.98	3.19	-	-	-	-
17	0.28	1.35	4.92	26.19	-	-	-	-

E.3. Weibull parameters for windspeed data in Atacama, Chile

The scale and shape parameters for each month was calculated from 33 years of historical data (1980-2012) obtained from University of Chile [62].

Time (h)	Scale (m/s)	Shape (-)	Scale (m/s)	Shape (-)	Scale (m/s)	Shape (-)	Scale (m/s)	Shape (-)
	JANUARY		FEBRUARY		MARCH		APRIL	
0	2.35	6.65	2.41	6.85	2.75	6.19	2.59	3.87
1	1.61	14.57	1.61	12.29	2.15	4.36	2.22	3.64
2	1.48	10.10	1.21	5.65	1.67	1.67	3.29	2.35
3	1.37	6.15	1.21	3.65	2.38	1.84	3.65	2.54
4	1.34	5.02	1.16	4.17	2.29	2.16	3.97	3.66
5	1.52	6.35	1.22	3.96	2.38	2.20	3.72	3.37
6	1.43	9.05	1.26	6.60	2.44	2.35	4.07	2.91
7	1.20	20.30	1.05	10.95	2.78	2.32	3.98	3.48
8	1.30	9.60	1.28	6.19	2.96	2.26	3.42	2.03
9	1.25	7.50	1.28	7.11	2.62	2.15	3.80	2.56
10	1.24	8.39	1.11	6.07	2.98	2.10	3.98	2.67
11	0.68	∞	0.68	∞	2.76	2.35	4.36	2.85
12	0.38	3.23	0.39	2.79	1.90	2.11	2.71	1.91
13	1.72	13.45	1.66	21.74	1.35	1.34	1.91	1.27
14	2.25	9.54	2.03	8.55	2.45	2.04	3.01	1.72
15	3.99	8.41	3.58	7.67	3.54	2.73	4.14	2.12
16	4.20	6.47	4.82	5.35	5.56	3.78	5.47	2.77
17	5.49	16.56	6.24	5.61	6.25	4.16	7.07	3.60
18	6.83	5.96	7.20	5.13	7.69	4.24	8.61	3.64
19	7.02	4.87	7.24	4.49	7.91	5.49	8.67	4.01
20	6.58	7.27	6.92	6.50	8.15	5.54	8.23	3.82
21	6.08	7.82	6.27	6.94	6.90	6.28	6.85	4.92
22	5.66	6.59	5.59	6.28	5.39	7.41	5.23	5.31
23	3.70	6.68	3.64	6.99	4.43	6.57	4.01	5.73

	MAY		JUNE		JULY		AUGUST	
0	2.80	3.09	4.96	1.66	7.64	2.43	4.86	1.63
1	2.48	2.99	4.14	1.52	7.65	2.50	3.67	1.48
2	2.35	1.63	4.00	1.58	7.25	2.41	3.93	1.81
3	2.83	1.91	3.68	1.50	6.86	2.13	3.36	1.58
4	3.11	2.63	4.92	1.97	7.98	2.64	4.19	1.95
5	2.89	2.29	4.19	1.62	7.67	2.56	3.73	1.80

Time (h)	Scale (m/s)	Shape (-)	Scale (m/s)	Shape (-)	Scale (m/s)	Shape (-)	Scale (m/s)	Shape (-)
6	2.87	2.00	5.53	2.05	8.09	2.49	4.77	1.92
7	3.11	2.63	5.17	1.96	7.47	2.21	4.70	1.99
8	2.78	1.91	4.73	1.82	6.79	1.96	4.75	1.92
9	3.18	2.27	4.40	1.74	6.47	1.89	4.14	1.76
10	3.83	2.42	4.62	1.82	6.50	1.92	4.72	1.92
11	3.51	2.41	4.27	1.72	6.37	1.83	4.56	1.84
12	3.36	2.07	4.47	1.64	7.09	2.10	4.03	1.57
13	2.72	1.61	4.33	1.34	4.81	1.24	5.01	1.45
14	3.69	1.78	4.54	1.29	5.61	1.36	5.31	1.38
15	4.91	2.21	5.59	1.60	5.94	1.42	6.44	1.71
16	6.05	2.78	5.93	1.58	6.06	1.34	6.04	1.55
17	7.80	3.21	7.22	1.67	8.34	1.70	7.89	1.86
18	9.79	3.66	9.42	2.30	10.55	2.29	10.34	2.63
19	9.64	3.69	10.42	2.65	11.37	2.63	10.72	2.79
20	9.34	3.63	10.40	2.84	11.32	2.72	10.70	2.84
21	7.89	4.15	9.74	2.57	10.49	2.55	9.89	2.61
22	5.30	3.78	8.02	2.22	9.70	2.69	6.83	2.06
23	4.09	3.59	5.94	1.83	6.29	1.78	6.11	1.81

	SEPTEMBER		OCTOBER		NOVEMBER		DECEMBER	
0	3.69	3.00	3.01	3.12	2.70	3.65	2.53	6.53
1	2.53	2.68	2.16	2.65	1.85	3.98	1.69	5.04
2	2.47	3.07	2.17	3.38	1.97	5.50	1.94	4.96
3	2.92	2.41	1.68	2.81	1.85	4.39	1.51	7.88
4	3.53	2.02	1.92	1.74	1.34	1.67	1.61	7.99
5	2.62	1.93	1.44	1.57	0.92	1.59	1.81	11.31
6	2.81	2.07	1.72	2.17	1.42	3.15	1.69	14.38
7	3.62	1.91	2.10	1.92	1.61	2.42	1.37	34.26
8	3.97	1.92	2.18	1.77	1.57	2.18	1.52	10.44
9	2.96	1.47	2.53	1.75	2.19	1.88	1.44	8.48
10	3.05	2.54	2.45	2.74	2.26	3.47	1.36	12.79
11	3.97	2.07	2.44	1.88	2.05	1.94	0.69	60.30
12	4.91	1.77	2.96	1.60	2.31	2.05	0.43	2.77
13	4.32	1.40	3.40	1.48	2.70	1.90	1.87	6.34
14	5.51	1.76	4.48	1.88	3.79	2.35	2.35	6.26
15	5.80	2.15	4.85	2.25	4.45	3.03	4.14	6.62
16	7.41	2.24	6.35	2.25	5.58	2.88	3.62	5.11
17	9.29	2.62	7.91	2.54	7.30	3.11	5.66	10.59
18	10.95	3.39	9.62	3.21	10.40	4.00	6.43	9.92

Time (h)	Scale (m/s)	Shape (-)	Scale (m/s)	Shape (-)	Scale (m/s)	Shape (-)	Scale (m/s)	Shape (-)
19	12.76	3.23	10.25	3.62	9.51	3.84	6.66	5.90
20	12.71	3.78	10.64	3.24	9.59	3.35	6.63	5.40
21	10.51	3.38	9.03	3.44	8.18	3.96	6.02	4.85
22	7.69	3.14	6.74	3.25	6.20	3.57	5.83	6.41
23	4.72	2.59	3.95	2.64	3.62	2.95	3.70	7.21

E.4. Weibull parameters for windspeed data in Alberta, Canada

The scale and shape parameters for each month was calculated from 10 years of historical data (2005-2014) obtained from the Department of Environmental and Natural Resources, Government of Canada [63].

Time h	Scale (m/s)	Shape (-)	Scale (m/s)	Shape (-)	Scale (m/s)	Shape (-)	Scale (m/s)	Shape (-)
	JANUARY		FEBRUARY		MARCH		APRIL	
0	3.81	1.28	3.02	1.07	3.22	1.31	3.17	1.18
1	3.69	1.25	3.11	1.12	3.22	1.25	3.26	1.19
2	3.65	1.19	2.83	1.02	3.28	1.43	3.59	1.16
3	3.65	1.18	2.75	0.99	3.30	1.26	4.10	1.53
4	3.32	0.97	2.89	1.03	3.75	1.48	4.30	1.59
5	3.46	1.07	2.93	1.01	4.01	1.56	4.63	1.80
6	3.57	1.10	3.14	1.06	4.23	1.64	4.66	1.83
7	3.72	1.15	3.07	1.05	4.37	1.74	4.89	2.04
8	3.82	1.15	3.33	1.13	4.42	1.75	5.11	2.23
9	3.80	1.17	3.38	1.22	4.50	1.89	5.15	2.09
10	3.78	1.22	3.24	1.12	4.51	2.04	4.94	2.07
11	3.74	1.29	3.18	1.23	4.16	1.93	4.77	2.12
12	3.72	1.29	3.09	1.21	3.77	1.75	4.28	1.88
13	3.63	1.23	2.95	1.12	3.74	1.67	4.01	1.78
14	3.61	1.15	2.96	1.15	3.60	1.61	3.98	1.70
15	3.77	1.30	2.92	1.06	3.47	1.61	3.88	1.65
16	3.58	1.22	2.81	1.03	3.36	1.51	3.74	1.46
17	3.58	1.14	3.03	1.07	3.28	1.43	3.72	1.51
18	3.55	1.05	2.95	1.08	3.32	1.50	3.49	1.32
19	3.66	1.15	2.86	1.04	3.15	1.32	3.46	1.38
20	3.68	1.24	3.04	1.14	3.25	1.43	3.41	1.41
21	3.68	1.19	2.94	1.01	3.23	1.33	3.33	1.31
22	3.58	1.12	3.06	1.09	3.30	1.37	3.55	1.47
23	3.57	1.08	2.93	1.02	3.36	1.50	3.58	1.52

	MAY		JUNE		JULY		AUGUST	
0	3.11	1.29	2.81	1.26	2.38	1.09	2.67	1.43
1	3.28	1.44	3.06	1.38	2.55	1.26	2.52	1.36
2	3.53	1.47	3.31	1.59	2.77	1.35	2.56	1.46
3	3.79	1.55	3.58	1.64	2.98	1.48	2.66	1.50
4	3.97	1.75	3.90	1.88	3.26	1.71	2.99	1.60

Time h	Scale (m/s)	Shape (-)	Scale (m/s)	Shape (-)	Scale (m/s)	Shape (-)	Scale (m/s)	Shape (-)
5	4.06	1.90	4.03	1.83	3.38	1.75	3.29	1.78
6	4.23	1.96	4.29	1.99	3.71	1.83	3.58	1.84
7	4.32	1.95	4.40	2.05	3.97	1.94	3.66	1.78
8	4.40	2.05	4.33	2.12	4.22	2.08	3.81	1.86
9	4.59	2.01	4.41	2.23	4.36	1.92	3.74	1.77
10	4.64	1.93	4.44	2.07	4.22	1.89	3.77	1.79
11	4.53	1.97	4.24	2.03	4.10	2.06	3.65	1.81
12	4.20	1.79	4.15	1.97	3.94	2.21	3.39	1.62
13	4.11	1.86	3.57	1.83	3.71	2.04	3.28	1.66
14	3.91	1.93	3.41	1.79	3.38	1.57	3.15	1.38
15	3.92	1.84	3.50	1.75	3.24	1.50	3.15	1.35
16	3.90	1.80	3.31	1.65	3.17	1.50	3.14	1.42
17	3.83	1.83	3.31	1.65	2.97	1.44	2.84	1.32
18	3.54	1.45	3.23	1.53	2.91	1.29	2.79	1.31
19	3.51	1.52	2.96	1.28	2.91	1.48	2.55	1.25
20	3.52	1.64	2.94	1.20	2.78	1.34	2.59	1.32
21	3.36	1.57	3.12	1.39	2.83	1.35	2.77	1.47
22	3.33	1.58	3.09	1.41	2.74	1.24	2.90	1.64
23	3.22	1.37	2.84	1.17	2.59	1.15	2.88	1.62

	SEPTEMBER		OCTOBER		NOVEMBER		DECEMBER	
0	3.01	1.47	3.08	1.42	3.61	1.56	3.30	1.29
1	2.83	1.26	2.96	1.40	3.55	1.47	3.30	1.22
2	2.73	1.27	2.71	1.20	3.48	1.32	3.34	1.21
3	3.13	1.44	2.85	1.23	3.28	1.23	3.33	1.24
4	3.47	1.60	3.20	1.31	3.55	1.28	3.16	1.29
5	3.57	1.64	3.75	1.57	3.90	1.41	3.14	1.14
6	3.75	1.71	3.91	1.54	4.03	1.46	3.21	1.14
7	3.84	1.67	3.99	1.60	4.03	1.50	3.23	1.13
8	3.88	1.70	4.05	1.68	4.06	1.58	3.29	1.20
9	3.94	1.77	3.97	1.73	3.86	1.59	3.14	1.17
10	3.83	1.60	3.88	1.94	3.92	1.72	3.12	1.13
11	3.58	1.73	3.63	1.77	3.63	1.49	3.35	1.32
12	3.37	1.59	3.64	1.68	3.55	1.41	3.35	1.30
13	3.46	1.70	3.55	1.61	3.58	1.47	3.47	1.41
14	3.65	1.80	3.44	1.68	3.74	1.66	3.50	1.40
15	3.60	2.04	3.29	1.40	3.91	1.77	3.35	1.30
16	3.30	1.52	3.29	1.54	3.94	1.70	3.45	1.26
17	3.19	1.63	3.18	1.52	3.79	1.68	3.37	1.22

Time h	Scale (m/s)	Shape (-)	Scale (m/s)	Shape (-)	Scale (m/s)	Shape (-)	Scale (m/s)	Shape (-)
18	2.91	1.25	3.20	1.54	3.73	1.55	3.37	1.36
19	3.04	1.51	3.22	1.62	3.83	1.81	3.28	1.20
20	2.94	1.47	3.12	1.55	3.70	1.63	3.44	1.42
21	3.09	1.39	3.31	1.72	3.87	1.82	3.42	1.37
22	3.06	1.47	3.16	1.49	3.72	1.57	3.50	1.29
23	2.96	1.38	3.17	1.63	3.72	1.53	3.45	1.41